

Deformation processes and petrophysical properties of subduction channel rocks from the Eclogite Zone of the Tauern Window, Austria

DISSERTATION

Zur Erlangung des Doktorgrades

an der Mathematisch-Naturwissenschaftlichen Fakultät

der Christian-Albrechts-Universität zu Kiel

vorgelegt von

Ruth Keppler

Kiel, 2014

Referent: Professor Jan H. Behrmann

Koreferent: Professor Romain Bousquet

Tagd. mündl. Prüfung:
zum Druck genehmigt:

10.03.2015

16.04.2015

Hiermit erkläre ich, dass ich die vorliegende Doktorarbeit selbständig und ohne Zuhilfenahme unerlaubter Hilfsmittel erstellt habe. Weder diese noch eine ähnliche Arbeit wurde an einer anderen Abteilung oder Hochschule im Rahmen eines Prüfungsverfahrens vorgelegt, veröffentlicht oder zur Veröffentlichung vorgelegt. Ferner versichere ich, dass die Arbeit unter Einhaltung der Regeln guter wissenschaftlicher Praxis entstanden ist.

Kiel, den 10.04.2015 

Ruth Keppler

ABSTRACT:

The exhumation of high pressure metamorphic rocks at convergent plate margins can be explained by the existence of a so-called subduction channel, a shear zone of a few kilometer thickness above the downgoing lithospheric plate, in which material is transported deep into the mantle and exhumed back to crustal depth. The exact processes taking place within these highly dynamic shear zones, however, are still not completely understood. The Eclogite Zone (EZ) of the Tauern Window is an exhumed subduction channel of the Alpine Orogen and provides the opportunity to study subduction channel rocks at the surface. It forms a typical *mélange* consisting of eclogite lenses in a matrix of high pressure metasediments. Crystallographic preferred orientation (CPO) analysis of rocks from the EZ offers the possibility to calculate their elastic properties. This data is valuable for seismic imaging of subduction channels at convergent plate margins active today. CPO analysis of rocks from the EZ furthermore allows drawing conclusions on deformational processes and the tectonic history of subduction channels. This PhD thesis provides CPO data of high pressure subduction channel rocks from the EZ. It gives an overview on the reliability of time-of-flight (tof) neutron diffraction as a method for CPO analysis and uses the obtained data to calculate rock physical properties and to provide a detailed deformational history of subduction channel rocks.

In the first study, Rietveld texture analysis is performed on rock samples of different complexity, using tof neutron diffraction at the SKAT diffractometer in Dubna, Russia. The recently upgraded SKAT provides three interchangeable multidetector-systems, offering the opportunity to use the optimum experimental set-up for different samples. This study illustrates that it is possible to obtain reliable CPO results for mineral phases constituting more than 10 vol.% in complex polymineralic rock samples. A comparison of CPO results with reference pole figures showed coinciding maxima for multiples of a random distribution of crystal lattice planes and similar texture strength, which indicates that the acquired data is suitable for the calculation of rock physical properties, as well as for geological interpretations. This study further showed that the application of full pattern fit methods allows a vast reduction in the number of tof spectra used for CPO calculation. 150 spectra for monomineralic samples and 350 spectra for samples with medium complexity are sufficient. This shows that a vast reduction in measuring positions is possible without loss of information.

In the second study, the CPO of fresh and retrogressed eclogites, as well as metasediments, from the EZ was used to calculate elastic properties of a complete set of subduction channel rocks. The elastic anisotropy of fresh eclogites is fairly low (~1.5%), but increases for progressively higher

grades of retrogression (up to 3.7%). While in fresh eclogites anisotropy is mainly determined by a distinct omphacite CPO, in retrogressed samples the elastic properties are additionally influenced by the CPO of retrograde amphibole. Elastic anisotropies of metasediments in the subduction channel are much higher due to a pronounced quartz and mica CPO (up to 7.5%). V_p/V_s ratios of metasediments (~ 1.5), as well as eclogites with different grades of retrogression (1.70-1.78) yield distinctly different values. The combination of P-wave velocity, elastic anisotropy and V_p/V_s ratios is specific to each rock type found in the EZ and in the future, these results could simplify the detection of internal structures in subduction channels of active subduction zones at depth.

The third study applies CPO and microstructural analyses to the same rocks investigated in the second study to determine the deformational history of the EZ and subduction channel rocks, in general. Electron backscatter diffraction (EBSD) analysis revealed signs of dynamic recrystallization of omphacite in the eclogites during their final stage of subduction. CPO analysis of retrogressed eclogites showed a complex deformation of the rocks within the subduction channel during exhumation. Although plain strain was dominant, locally prolate as well as oblate strain conditions occurred. These local strain variations were consistent from eclogite facies to blueschist facies conditions, as confirmed by matching omphacite and glaucophane CPO in all eclogite samples. Asymmetric quartz CPO in the metasediments points to simple shear. Deformation of the sedimentary matrix was more pervasive and outlasted deformation of the eclogite lenses, which was confirmed by lower silica contents of mica in the metasediments compared to the eclogites. This study elaborates the deformational history of the EZ, illustrating the complexity of processes taking place in subduction channels.

KURZFASSUNG:

Die Exhumation metamorpher Hochdruckgesteine an konvergenten Plattengrenzen kann durch die Existenz eines sogenannten Subduktionskanals erklärt werden. Subduktionskanäle sind wenige Kilometer dicke Scherzonen oberhalb der abtauchenden Lithosphärenplatte, in welchen Material bis tief in den Mantel subduziert und wieder bis in Krustentiefe exhumiert werden kann. Die genauen Prozesse die in diesen äußerst dynamischen Scherzonen stattfinden sind jedoch noch nicht vollständig verstanden. Die Eklogitzone (EZ) des Tauernfensters ist ein exhumierter Subduktionskanal des alpinen Orogens und bietet die Gelegenheit Gesteine aus Subduktionskanälen direkt an der Erdoberfläche zu untersuchen. Sie setzt sich aus einer typischen Mélange von Eklogitlinsen in einer Matrix aus Hochdruckmetasedimenten zusammen. Die Analyse kristallographischer Vorzugsorientierungen (CPO) in Gesteinen der EZ ermöglicht es die elastischen Eigenschaften der Gesteine zu berechnen. Diese Daten sind nützlich für die seismische Erkundung von derzeit aktiven Subduktionskanälen an konvergenten Plattenrändern. Des Weiteren erlaubt eine CPO Analyse von Gesteinen der EZ Rückschlüsse auf Deformationsprozesse und die tektonische Entwicklung von Subduktionskanälen. In der vorliegenden Dissertation werden CPO Daten von Hochdruckgesteinen der EZ präsentiert. Des Weiteren wird die Zuverlässigkeit von „time-of-flight“ (tof) Neutronendiffraktometrie als Methode für die CPO-Analyse ausgewertet. Die ermittelten CPO Daten werden für die Berechnung physikalischer Eigenschaften von Gesteinen aus Subduktionskanälen verwendet.

Im ersten Teil dieser Arbeit wird eine Rietveld Texturanalyse an Gesteinen von verschiedener Komplexität mit Hilfe von tof Neutronendiffraktometrie am SKAT-Diffraktometer in Dubna (Russland) durchgeführt. Das vor kurzem aufgerüstete SKAT ist mit drei austauschbaren Multidetektorsystemen ausgestattet und bietet die Möglichkeit die beste experimentelle Konfiguration für verschiedene Proben zu verwenden. Diese Studie zeigt, dass es möglich ist für komplexe polyphase Gesteine verlässliche CPO-Daten der Mineralphasen zu bestimmen, die einen Volumenanteil von mehr als 10% ausmachen. Ein Vergleich der CPO-Daten mit Referenzpolfiguren weist eine Übereinstimmung der Maxima von Vielfachen der Normalverteilung der Kristallgitterebenen und eine ähnliche Texturstärke auf, was darauf hinweist, dass sich die erlangten Daten sowohl für die Berechnung physikalischer Eigenschaften von Gesteinen, als auch für geologische Interpretationen eignen. Außerdem wird in dieser Studie erläutert, dass es durch die Anwendung dieser Methode möglich ist, die Anzahl der bei der CPO Berechnung verwendeten tof-Spektren erheblich zu reduzieren. 150 Spektren für monomineralische Proben und 350 Spektren für Proben mit einer niedrigen Anzahl an Mineralphasen sind ausreichend. Das bedeutet,

dass eine enorme Reduktion von Messpositionen möglich ist, ohne dass Informationen verloren gehen.

Im zweiten Teil dieser Arbeit wurde sowohl die CPO von frischen und retrograden Eklogiten, als auch die von Metasedimenten der EZ für die Berechnung elastischer Anisotropien von Gesteinen aus Subduktionskanälen verwendet. Die elastische Anisotropie von frischen Eklogiten ist sehr gering (1,5%), nimmt aber bei zunehmend höherer retrograder Überprägung zu (bis zu 3,7%). Während in frischen Eklogiten die Anisotropie hauptsächlich durch die CPO von Omphazit bestimmt wird, trägt in retrograden Eklogiten zusätzlich die CPO von Amphibol dazu bei. Elastische Anisotropien der Metasedimente in Subduktionskanälen sind auf Grund einer ausgeprägten Quartz- und Glimmer-CPO weitaus höher (bis zu 7,5%). Sowohl die V_p/V_s -Verhältnisse der Metasedimente ($\sim 1,5$), als auch die V_p/V_s -Verhältnisse der verschieden stark retrogradierten Eklogite (1,70-1,78), haben deutlich unterschiedliche Werte. Die Kombination von P-Wellengeschwindigkeit, elastischer Anisotropie und V_p/V_s -Verhältnis ist spezifisch für die jeweiligen Gesteinsarten die in der EZ gefunden werden. Zukünftig könnten diese Ergebnisse die Erfassung interner Strukturen in Subduktionskanälen aktiver Subduktionszonen erleichtern.

Im dritten Teil dieser Arbeit wird mit Hilfe einer CPO-Analyse und einer mikrostrukturellen Untersuchung der Gesteine, die bereits Bestandteil der zweiten Studie waren, die Deformationsgeschichte der EZ rekonstruiert. Durch „electron backscatter diffraction“ (EBSD) wurde eine dynamische Rekristallisation von Omphazit während den letzten Subduktionsstadien belegt. Die CPO Analyse der retrograden Eklogite erwies komplizierte Deformationsprozesse der Gesteine im Subduktionskanal bei ihrer Exhumation. Obwohl eine ebene Verformung vorherrscht treten lokal konstriktionale und plättende Verformungen auf. Diese lokalen Unterschiede bei der Verformung halten von der Eklogitfazies bis zur Exhumation in die Blauschieferfazies an, was durch eine Übereinstimmung der CPO von Omphazit und Glaukophan bezeugt wird. Asymmetrische CPO von Quarz in den Metasedimenten deutet auf eine einfache Scherung hin. Die Deformation innerhalb der Metasedimente war durchdringender und überdauerte die Deformation der Eklogite. Dies bezeugt der niedrigere Si-Gehalt des Hellglimmers in den Metasedimenten im Vergleich zu den Eklogiten. In diesem Teil der Arbeit wird somit die gesamte Deformationsgeschichte der EZ veranschaulicht und die Komplexität von Prozessen in Subduktionskanälen verdeutlicht.

CONTENTS

1.	Introduction	1
1.1	Motivation	1
1.2	Aims of this study	3
1.3	Subduction zones	4
1.3.1	Structural elements of subduction zones	6
1.3.2	Exhumation of high pressure rocks	9
1.3.3	Seismic imaging of subduction channels	11
1.4	Geological Overview of the study area	12
1.4.1	Tauern Window	12
1.4.2	The Eclogite Zone	14
1.5	Methods	16
1.5.1	Microprobe analysis	16
1.5.2	Crystallographic preferred orientation analysis	16
1.5.2.1	Time-of-flight neutron diffraction	17
1.5.2.2	Electron backscatter diffraction	19
1.6	Thesis Outline	20
2	Manuscript #1	33
3	Manuscript #2	53
4	Manuscript #3	73
5	Discussion	112
5.1	Manuscript #1	112
5.2	Manuscript #2	113
5.3	Manuscript #3	115
5.4	Synopsis	117
5.5	Outlook	119
6	Appendix	124

List of Tables

Table 1.1: General characteristics of the SKAT	39
Table 1.2: RP values of sample MIX	41
Table 1.3: Texture strengths and RP1 of marble sample	43
Table 1.4: RP1 values of eclogite sample	44
Table 1.5: Variation of texture strength sample MIX	46
Table 1.6: Variation of texture strength of eclogite sample	46
Table 2.1: Modal compositions of the investigated samples	58
Table 2.2: V_p , V_s , and elastic anisotropies of the samples	65
Table 3.1: Location, description and composition of the samples	80
Table 3.2: Mineral analysis of the investigated samples	85
APPENDIX:	
Table 1: Microprobe measurements of omphacite	175
Table 2: Microprobe measurements of amphibole	176
Table 3: Microprobe measurements of garnet	177
Table 4: Microprobe measurements of white mica	179

List of Figures

Fig. 1.1: Pressure-temperature path of the EZ	2
Fig. 1.2: Tomographic images of the mantle	5
Fig. 1.3: Cross section through a subduction zone	6
Fig. 1.4: End-member types of subduction zones	8
Fig. 1.5: Subduction channel mélange	10
Fig. 1.6: Tectonic map of the Tauern window	13
Fig. 1.7: Lithological units of the Eclogite Zone	15
Fig. 1.8: Sample coordinate system for CPO analysis	17
Fig. 1.9: Sketch of the SKAT diffractometer	18
Fig. 1.10: Schematic illustration of EBSD	19
Fig. 2.1: Energy distribution of thermal neutrons	37
Fig. 2.2: General layout of beam line 7 and scheme of the SKAT	38
Fig. 2.3: Experimental resolution of the SKAT	39
Fig. 2.4: Summarized diffraction patterns	39
Fig. 2.5: Recalculated pole figures of sample MIX	42
Fig. 2.6: Difference pole figures of marble sample	43
Fig. 2.7: Omphacite (003) pole figures and difference pole figures	43
Fig. 2.8: Examples for pole figures showing exceptions	44
Fig. 2.9: Individual diffraction patterns	45
Fig. 2.10 Representation of the thinned grids	48
Fig. 3.1: Tectonic maps of the Alps, the Tauern Window and the EZ	56
Fig. 3.2: Geologic map of the EZ	57
Fig. 3.3: Crystal structures and Vp of single crystals	59
Fig. 3.4: Typical BSE microstructures	60
Fig. 3.5: Micrographs of clastic metasediments	61
Fig. 3.6: Recalculated pole figures (retrogressed eclogites)	61
Fig. 3.7: Recalculated pole figures (fresh eclogites)	62
Fig. 3.8: Recalculated pole figures (metasediments)	63
Fig. 3.9: Calculated and experimental Vp	64
Fig. 3.10: Equilibrium assemblage diagram	65

Fig. 4.1: Tectonic maps of the Alps, the Tauern Window and the EZ	78
Fig. 4.2: PT-path and geological maps of the EZ	79
Fig. 4.3: Foliation and lineation of eclogite samples	83
Fig. 4.4: Omphacite and amphibole CPO (from neutron diffraction).	84
Fig. 4.5: Characteristic sample micrographs	87
Fig. 4.6: Orientation maps and EDX maps of omphacite matrix	88
Fig. 4.7: Distribution of misorientation angles	89
Fig. 4.8: Distribution of misorientation axes	90
Fig. 4.9: Orientation map and pole figures of the omphacite matrix	91
Fig. 4.10: EDX maps of a garnet grain	93
Fig. 4.11: Orientation map and EDX map of a retrograde eclogite	94
Fig. 4.12: EDX map of retrogressed eclogite	95
Fig. 4.13: Omphacite and amphibole CPO (from EBSD)	96
Fig. 4.14: PT-path of the EZ including CPO	104

Appendix:

Fig. 1: Pole figures of omphacite	124
Fig. 1: Pole figures of amphibole	125

1. Introduction

1.1 Motivation

Subduction zones are highly dynamic regions, where massive material transfers take place (Vannucchi et al., 2003; Ranero and Weinrebe, 2005; Harders et al., 2012; Herms et al., 2012). Crustal rocks are subducted deep into the mantle and can be exhumed back to crustal levels or even to the earth's surface from depths of over 100 km (e.g. Bebout, 2007). Subduction channels are frequently proposed as a tectonic regime permitting the exhumation of high pressure rocks (e.g. Ernst, 2006). Subduction channels are shear zones of a few km thickness above the subducting lithospheric slab, comprising a mélange of serpentinized mantle rocks, subducted marine sediments and slivers of oceanic crust (e.g. Frederico et al., 2007; Blanco-Quintero et al., 2011). Despite detailed field investigations of exhumed subduction channels and numerous numerical models (e.g. Gerya et al., 2002; Essen et al., 2009), predicting the deformation within these shear zones, the exact processes taking place in subduction channels are still not completely understood.

The Eclogite Zone (EZ) of the Tauern Window is an exhumed subduction channel of the Alpine Orogen forming a high pressure mélange consisting of metabasaltic boudins enclosed in a matrix of metasediments. Its composition and tectonic edifice is comparable to many other exhumed subduction channels around the world and is assumed to be representative of such a tectonic regime. Both the basalts and the sediments experienced eclogite facies conditions of $600^{\circ} \pm 30^{\circ}\text{C}$ and 2.0-2.5 GPa (Stöckhert et al., 1997; Hoschek, 2001; 2004). Recent studies discovered an Oligocene age for peak pressure conditions and a fast exhumation within 1-2 Ma (Glodny et al., 2008; Nagel et al., 2013), making the metabasalts of the EZ the youngest eclogites of the Alps.

Petrographic studies revealed a cold exhumation of the rocks under blueschist facies conditions within the subduction channel and a late high temperature pulse due to continental collision (Fig. 1.1; Zimmermann et al., 1994; Kurz et al., 1998a; Holland and Richardson, 1979).

In addition to ideal outcrop conditions, several other aspects make the EZ an ideal study area to investigate subduction channel rocks and their deformation. Since the

metabasaltic boudins are much more extensive than the usual thickness of a subduction channel (1-2 km), they could not rotate within their sedimentary matrix, as it could be the case in other fossil subduction channels, such as the Franciscan complex of California (e.g. McLaughlin et al., 1988). In the EZ, the metasediments are proven to be part of the high pressure mélangé in the subduction channel (Dachs, 1990) and a coherent deformation of the unit as a whole throughout its subduction, as well as its exhumation history is likely.

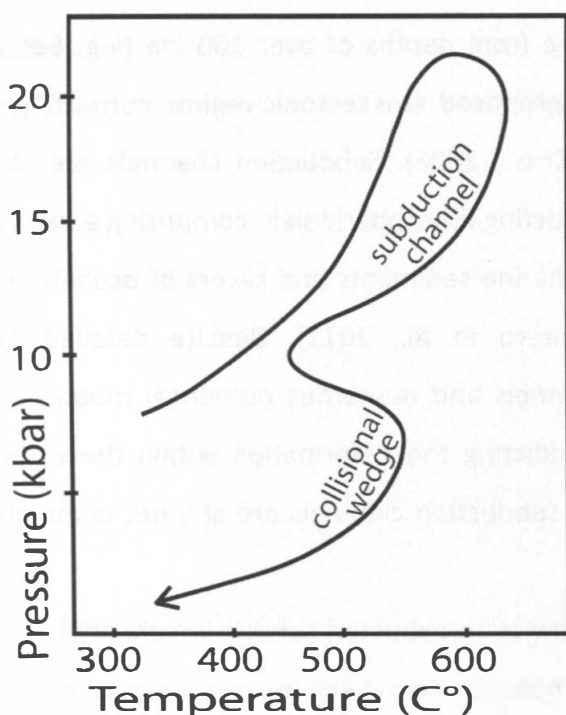


Fig. 1.1: Pressure-temperature path of the EZ (modified after Holland, 1979; Dachs, 1986; Spear and Franz 1986; Dachs, 1990; Zimmermann et al., 1994; Kurz et al., 1998).

Moreover, the metabasalts of the EZ contain a wide spectrum of rocks with different grades of metamorphism. There are fresh eclogites, still exhibiting their high pressure mineral assemblage, and others showing signs of pronounced blueschist facies overprint (Kurz et al. 1998a). Additionally, there are eclogites, which have been completely converted to amphibolites during the late stage high temperature metamorphic overprint. The EZ therefore offers the possibility to study the complete tectonic history from subduction to peak conditions towards the exhumation to crustal levels within in the subduction channel.

1.2 Aims of this study

The deformational processes taking place in subduction channels are not completely understood. So far, the petrophysical properties of subduction channel rocks are not well constrained, which hampers their detection in seismic experiments. The main objective of this study is the analysis of crystallographic preferred orientations (CPO) of polymineralic high pressure rocks from subduction channels, which, on the one hand, allows conclusions on the deformational mechanisms of these rocks and, on the other hand, provides data necessary for the interpretation of seismic data, which permits investigations of active subduction channels at depth. The first aim was a quantitative investigation of the reliability of time-of-flight (tof) neutron diffraction CPO analysis and an improvement in efficiency of this method (A). In the second part (B) of this thesis, the improved tof method presented in the first part was used for CPO analysis of subduction channel rocks and subsequent calculation of their elastic properties. In the third part (C), the CPO and microfabric data was used to reconstruct the deformational processes within the EZ subduction channel.

- A) When it comes to the calculation of physical properties of large coarse grained rocks, tof neutron diffraction is the method of choice. Good grain statistics and large sample volumes result in reliable bulk texture. While neutron diffraction is already a wide spread technique used to acquire the CPO of monomineralic rocks, the reliability of this method analyzing complex polymineralic rock samples has not been quantitatively investigated. It was the aim of this work to obtain an understanding of the dependability of CPO analysis of polymineralic rocks using tof neutron diffraction at the SKAT diffractometer of the Frank Laboratory of Neutron Physics at JINR, Dubna, Russia (Ullemeyer et al., 1998). Since long exposure times are necessary for tof neutron diffraction, a further goal of this work was the quantitative investigation of a possible reduction of exposure time, by progressively reducing the number of measuring positions.
- B) Knowledge of elastic properties of rocks is crucial for seismic imaging of geological structures at depth. One way to obtain this information is the calculation of rock seismic properties with the CPO of the constituent mineral phases and their

experimentally determined single crystal elastic properties. This was done extensively for mostly monomineralic mantle rocks, which led to a better understanding of mantle dynamics (e.g. Montagner and Tanimoto, 1990; Silver, 1996; Montagner and Guillot, 2003; Vauchez et al., 2005; Mainprice et al., 2008). On the other hand, there are only few studies so far, treating seismic properties of polymineralic rocks of the crust, specifically those being subducted to mantle depths and subsequently exhumed. The lack of knowledge regarding elastic properties of subduction channel rocks puts restrictions on seismic imaging of these structures. Therefore, it is the goal of this work to obtain seismic properties of a range of subduction channel rocks and to provide important data, contributing to future seismic investigations of these structures at depth.

- C) The EZ offers the opportunity to study deformational processes of rocks in subduction channels. Both, fresh and retrogressed eclogites are found in this unit and allow a reconstruction of the complete tectonic evolution from subduction to the exhumation of the EZ. Therefore, it is the objective of this study to obtain the CPO of different units within the EZ and perform a microstructural investigation. The metasedimentary rocks were part of the high pressure mélangé and a microfabric analysis of both the metasediments and the eclogites leads to a better understanding of the deformational evolution of the whole unit. In addition, strain and stress analyses offer insights into the tectonic regime at different stages of the EZ during its path in the subduction channel, which can be applied to other fossil and recent subduction channels around the world.

1.3 Subduction zones

Subduction zones are regions at convergent plate margins, where lithospheric plates descend into the mantle (e.g. Jakes and White, 1970; Green and Houston, 1995; Ruff and Tichelaar, 1996; Karason and van der Hilst, 2001). They are often referred to as the world's largest recycling system and play a crucial role in plate tectonics. Oceanic lithosphere forms at mid-ocean ridges and over time moves away from the spreading center. With increasing age the oceanic lithosphere thickens and becomes denser. Davies

(1992) proposed that the oceanic lithosphere is eventually negatively buoyant with respect to the asthenosphere and descends into the mantle creating a new subduction zone. However, the initiation of subduction zones is still strongly debated (e.g. Spence, 1987; Niu et al., 2003). According to Lithgow-Bertelloni and Richards (1995) the largest part of the force needed for plate motion comes from the sinking of dense subducting lithosphere and only a small contribution is made by ridge push at mid-ocean ridges. Although slab buoyancy is a driving force for subduction, newer models illustrate that the interaction of slab and mantle are far from simple (e.g. Doglioni et al., 2007). Royden and Husson (2006) show that viscous stresses in the mantle bear a large influence on subduction dynamics. Karato et al. (2001) suggest that the temperature dependent rheology of the subducting slab strongly influences its behaviour in the mantle.

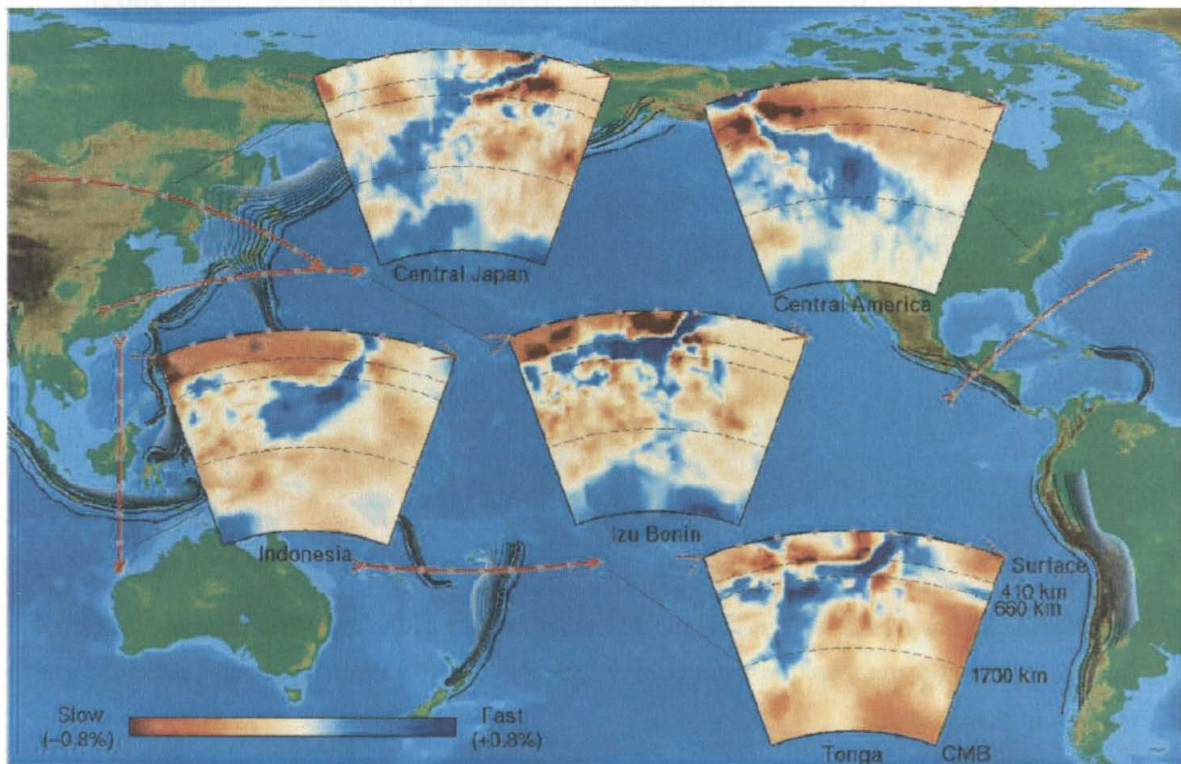


Fig. 1.2: Tomographic images of the mantle showing the descending lithospheric plates, which are defined by high P-wave velocities (blue). CMB: core mantle boundary. Red lines mark location of profiles. In Central America, central Japan, and Indonesia the subducted plate penetrates the 660 km discontinuity and descends into the lower mantle. In Tonga and Izu Bonin on the other hand, the slab is dragged over the 660 km discontinuity (Stern, 2002).

Seismic tomography revealed that the descending plates are either dragged along the 660 km discontinuity, at which the olivine high pressure polymorph ringwoodite breaks down

into perovskite and magnesiowustite, or they penetrate this discontinuity and finally reach the core mantle boundary (Fig. 1.2.; e.g. Helffrich and Wood, 2001; Karason and van der Hilst, 2000).

Apart from the crucial role of subduction zones in plate tectonics, they also have a large impact on society. The world's biggest earthquakes are produced by thrust faulting along subduction zones (e.g. Grevemeyer and Tiwari, 2006; Heesemann et al., 2009; Moscoso et al., 2011; Geersen et al., 2013). The region of seismicity along the descending plate is called Wadati-Benioff Zone (Fig. 1.3; Wadati, 1928; Benioff, 1949). The exact location and the extent of seismicity depend on a number of factors (Protti et al., 1994; Papazachos et al., 1995). One is the dipping angle of the subducting plate. Shallow dipping angles lead to stronger coupling between plates and generally result in higher magnitude earthquakes compared to subduction zones with steeply subducting lithosphere (Stern, 2002).

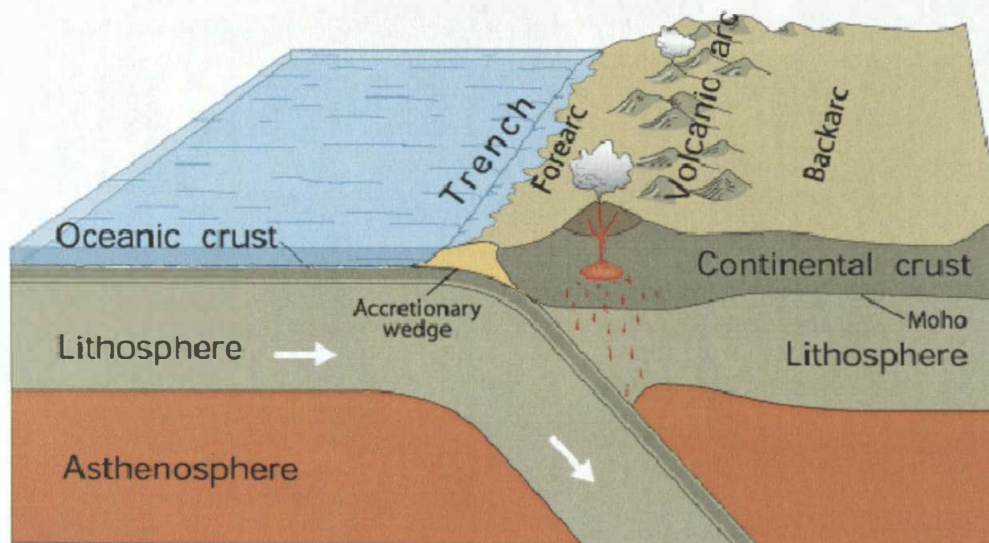


Fig. 1.3: Schematic cross section through a subduction zone illustrating its main structural elements (Kious and Tilling, 1996).

1.3.1 Structural elements of subduction zones

Subduction zones can be divided into several structural elements: the trench, the forearc, the subducting lithosphere, the magmatic arc and the back-arc (Fig. 1.3). At the *trench*, the lithospheric plate descends into the mantle and forms deep depressions at the ocean floor. The deepest trench on earth is the Marianas Trough with a depth of 11.5 km. The

trench can be sediment poor, or filled with turbidites originating from the continental slope (e.g. von Huene and Scholl 1991; Rea and Ruff, 1996; Simpson, 2009). The subduction zone can either be non-accretionary, or accretionary forming a *forearc*, mainly depending on the amount of subducted sediments. Close to continents the sedimentary supply is high, which leads to the formation of accretionary wedges (e.g. von Huene and Scholl, 1991; von Huene et al. 2004; Simpson, 2009). The sedimentary material is added by frontal accretion and deformed by folding and thrusting (Davis et al., 1983). At non-accretionary forearcs on the other hand, significant volumes of material can be eroded from the base of the upper plate and dragged to greater depth (Stern 1991).

The *subducting lithosphere*, specifically the upper layer consisting of oceanic crust and marine sediments undergoes complex mineralogical changes during its descent. With increasing depth the rocks are exposed to high pressure, low temperature metamorphism, which leads to a progressive transformation of the basaltic oceanic crust into blueschists and eclogites. The wide range of subducted sediments can lead to the formation of various rock types at depth. Clastic sediments are mostly transformed into micaschists, quartzites and paragneisses, whereas subducted carbonates give rise to marbles. Many of the mineral reactions result in the release of fluids which migrate into the overlying hot mantle wedge (Pearce and Peate, 1995). These fluids lower the temperature necessary for melting of mantle material and the subducted sediments (Clark and Ringwood, 1964; Paweley and Holloway, 1993; Ulmer and Tromsdorff, 1995). This leads to the formation of magma, which rises in the upper plate and accumulates in subvolcanic magma chambers causing the development of *magmatic arcs*.

Constrained by the thermal structure of the subduction zone, the *magmatic arc* is usually found 150-200 km from the trench axis (England et al., 2004). There are two types of magmatic arcs, depending on whether the upper plate above the subduction zone is mostly oceanic or continental. An *island arc* forms outboard of continental landmasses, like for example in the western Pacific Ocean, while *continental arcs* develop at the edge of continental landmasses, like in the Andes (Murphy, 2006). In the subvolcanic magma chambers the magma differentiates by fractionated crystallization, mixing of magma and an assimilation of crustal material. With increasing maturity (e.g. differentiation) of volcanic arcs, island arc tholeiites, low-K-tholeiites and calc-alkaline basalts are produced. Further, andesites, dacites and rhyolites are widespread at continental arcs due to further

assimilation of the continental crust (Murphy, 2007). A characteristic feature of magma produced at magmatic arcs is an enrichment in large ion lithophile elements (LILE) relative to high field strength elements (HFSE), which confirms their origin at a shallow mantle (Pearce and Peate, 1995). Additionally, the presence of fluids and volatiles verifies dehydration of the subducted slab (Murphy, 2006).

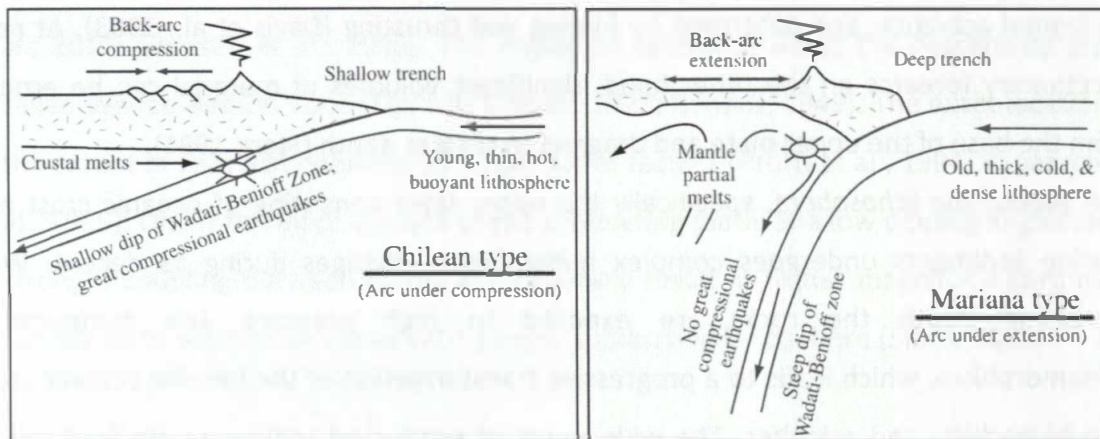


Fig. 1.4: End-member types of subduction zones. According to the model, the age of the subducting plate determines dip angle, seismicity and back arc-tectonics (after Forsyth and Uyeda, 1975).

The *back arc* region is located behind the magmatic arc. Its tectonic regime is highly influenced by the dip angle of the subducting plate. There are two end-members for subduction zones referred to as Chilean-type and Mariana-type. The shallow dip angle of Chilean-type subduction zones results in back-arc compression and the formation of fold and thrust belts. In contrast, the steep dipping angle in Mariana-type subduction zones causes roll-back of the subducting plate and back-arc extension (Stern, 2002; Lallemand et al., 2005). Considering these two end-members Uyeda and Kanamori (1979) came to the conclusion that older denser subducting lithosphere (i.e. the Mariana subduction zone) leads to steep dipping angles and younger warmer subducting lithosphere (i.e. the Chilean subduction zone) leads to shallow dipping angles. Doglioni et al. (1999) assume an influence of a westward drift of the lithosphere with respect to the asthenosphere. According to these authors west-dipping slabs are steeper than east-dipping ones due to this phenomenon. However, there are numerous counterexamples to both theories and recent studies show that a great number of factors influence the dipping angle of subduction zones. Lallemand et al. (2005) suggest that slab dip correlates with the absolute motion of the overriding plate and whether the overriding plate is continental or

oceanic. Furthermore, the authors propose that dipping angles are steeper near the edges of subduction zones (e.g. close to the termination of a slab).

1.3.2 Exhumation of high pressure rocks

Since the discovery of high pressure polymorphs of quartz (coesite) in the Central Alps (Chopin, 1984) and findings of diamond in the Cambrian Kokchetav massif in Kazakhstan (Sobolev et al., 1990), it is clear that exhumation of previously subducted continental crust from depths of over 100 km is possible. For oceanic crust an exhumation depth of up to 80 km has been reported (Angiboust et al., 2009), which is especially impressive considering its high density of $\sim 3.3\text{-}3.4 \text{ g/cm}^3$ after eclogitization (i.e. higher than lherzolite mantle rocks with $\sim 3.2\text{-}3.3 \text{ g/cm}^3$).

For decades researchers investigated the mechanisms responsible for the exhumation of rocks, which have been metamorphosed under high pressure/low temperature conditions. Possible processes are external forcing, by continental fragments entering the subduction zone (e.g. Hacker et al., 1995), slab breakoff (Chemenda et al., 1999), or underplating combined with extensional collapse (Platt, 1986). Additionally slab rollback has been proposed as a mechanism for the exhumation of high pressure rocks during ongoing subduction (Brun and Faccenna, 2008).

The exhumation of dense metabasaltic rocks originating from oceanic crust is difficult to explain and is likely only possible with the aid of more buoyant rocks surrounding them (e.g. Guillot et al., 2001). Slivers of metabasaltic oceanic rocks are usually exhumed within a matrix of lower density metasediments, or serpentinites. The metasediments usually originate from subducted trench fills and pelagic seafloor sediments, whereas the serpentinites are derived from hydrated mantle rocks of the upper and/or lower plates. Together with slivers of oceanic crust these low density rocks form a *mélange*, which is on aggregate more buoyant than the surrounding mantle rocks. Buoyant uplift of this *mélange* is inferred to take place in a subduction channel (Fig. 1.5).

The concept of subduction channels was originally proposed by Cloos (1982) and Cloos and Shreve (1988) for the circulation of sedimentary material in subduction zones to and from up to 30 km depth. Recent subduction channel models further include the

exhumation of subducted oceanic crust from depths of over 70 km (e.g. Agard et al., 2009; Guillot et al., 2009).

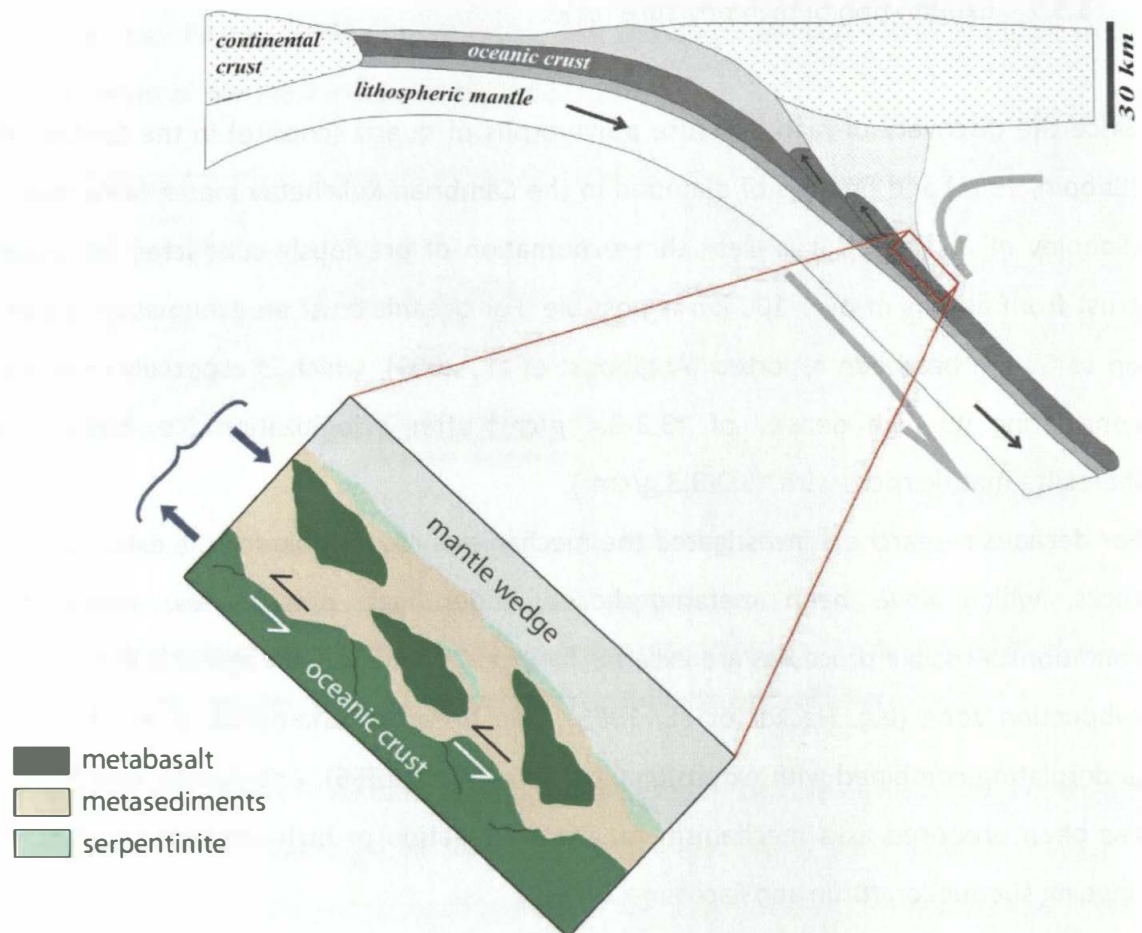


Fig. 1.5: Subduction Zone (Agard et al., 2009) and subduction channel *mélange* incorporating serpentinites and fragments of oceanic crust and marine sediments. Slivers of oceanic basalt and its sedimentary cover detach from the downgoing slab and assemble in the metasedimentary matrix. This *mélange* is more buoyant than the surrounding mantle rocks and exhumes within a few km thin subduction channel.

There are several numerical models describing the conditions for the formation of subduction channels and the exhumation of high pressure rocks (Burov et al., 2001; Gerya et al., 2002; Gerya and Stöckhert, 2006; Warren et al., 2008). Burov et al. (2001) assumes two distinct circulation levels, with slower exhumation in the upper lever (0-30 km) and faster exhumation in the lower level (30-70 km). Gerya and Stöckhert (2006) propose that the formation of a subduction channel depends on the rate of subduction and the rheology of overriding crust. According to these authors, subduction channels most likely

form at moderate subduction rates and moderate brittle strength of the upper plate. Under these conditions, a pronounced return flow of material at high velocities is achieved in their models. While numerical models provide insightful theories for the processes taking place in subduction channels, these theories still need to be confirmed by field studies and by seismic imaging of these structures currently active at depth in recent subduction zones.

1.3.3 Seismic imaging of subduction channels

Geological structures at depth can be imaged by reflection seismic methods. Substantial progress was made in seismic imaging of shallow subduction channels, as defined by Shreve and Cloos (1988), in the last decade (e.g. Eberhard-Philips et al., 2005; Calahorrano et al., 2008; Collot et al., 2011). Seismic observations of the South Ecuador subduction Zone imaged a roughly 1 km thick low velocity channel, interpreted as a continuous sheet of subducted sediment undergoing high shear deformation in the upper 10 km of subduction zones (Collot et al., 2011). Groß et al. (2007) also discussed a zone of high reflectivity between the subducting oceanic Nazca plate and overriding South American plate, which they interpreted as a subduction channel. It exhibits a variable thickness of 2–5 km down to a depth of about 38 km. They furthermore observed reflectivity corresponding to broad band of reflectors of more than 4 km, starting at the upper limit of the mantle wedge and attributed this reflective band to the continuation of the subduction channel.

Even at higher depths, in many subduction zones a low velocity layer of several km thickness has been observed above the downgoing slab (e.g. Langston, 1981; Helffrich and Stein, 1993; Abers et al., 1996; Audet et al., 2010). It is likely caused by serpentinized mantle above the subducted oceanic crust (Davies and Stevenson 1992) and could be part of the subduction channel at depth. However, so far it was not possible to image the internal structure of these low velocity zones, e.g. the existence of slivers of oceanic crust and marine sediments within the subduction channel.

The expected signal of deep subduction channels can be evaluated by numerical modeling of seismic waves. Essen et al. (2009) investigated the possible influence of a deep subduction channel above the slab of the Hellenic subduction zone in the Cyclades. The

authors assume an intermediate velocity and density for the channel, compared to the oceanic crust and the overlying mantle. They come to the conclusion that high amplitudes of guided waves could indicate the existence of subduction channels. Models of Furumura and Kennett (2005), on the other hand show that guided waves are also highly dependent on heterogeneities within the subducted oceanic crust. Recent numerical simulations of seismic wave propagation modeled a more detailed subduction channel structure with eclogite blocks in a serpentinite matrix (Friedrich et al., 2014). The model furthermore incorporates thermodynamic parameters leading to phase transitions of the rocks in the subduction channel. The modeled channel leads to very specific seismic signatures in the simulation and the authors conclude that the detection of such a structure at depth is possible.

1.4 Geological Overview of the study area

1.4.1 Tauern Window

The Tauern Window is a tectonic window in the Eastern Alps - which mainly originate from the Adriatic continent - exposing basement and cover of the European plate, as well as Penninic oceanic units that have been subducted under the Adriatic plate and stacked, during Tertiary continental collision. The exhumation of the Tauern Window was mainly achieved by crustal scale folding, E-W extension, and an indentation of the Adriatic continent (Rosenberg et al., 2007; Schmid et al., 2013). To the east, the Tauern Window is bordered by the Katschberg normal fault (Fig. 1.6 A; Ratschbacher et al., 1989) and the western margin is defined by the Brenner normal fault, which accommodated large amounts of orogen parallel extension (Behrmann, 1988; Selverstone, 1988; Fügenschuh et al., 1997). The southwestern margin of the Tauern Window is bounded by the Sterzing-Steinach mylonite zone, which also exhibits normal displacement (Behrmann, 1988). A large part of the northern edge is formed by the Salzach-Ennstal-Mariazell-Puchberg fault (SEMP), which accommodated about 60 km of sinistral displacement during the Cenozoic (Ratschbacher et al., 1991; Linzer et al., 2002). To the south of the Tauern Window, a system of splay faults that are part of the dextral Periadriatic Line (PL) can be found (Müller et al., 2001; Mancktelow et al., 2001).

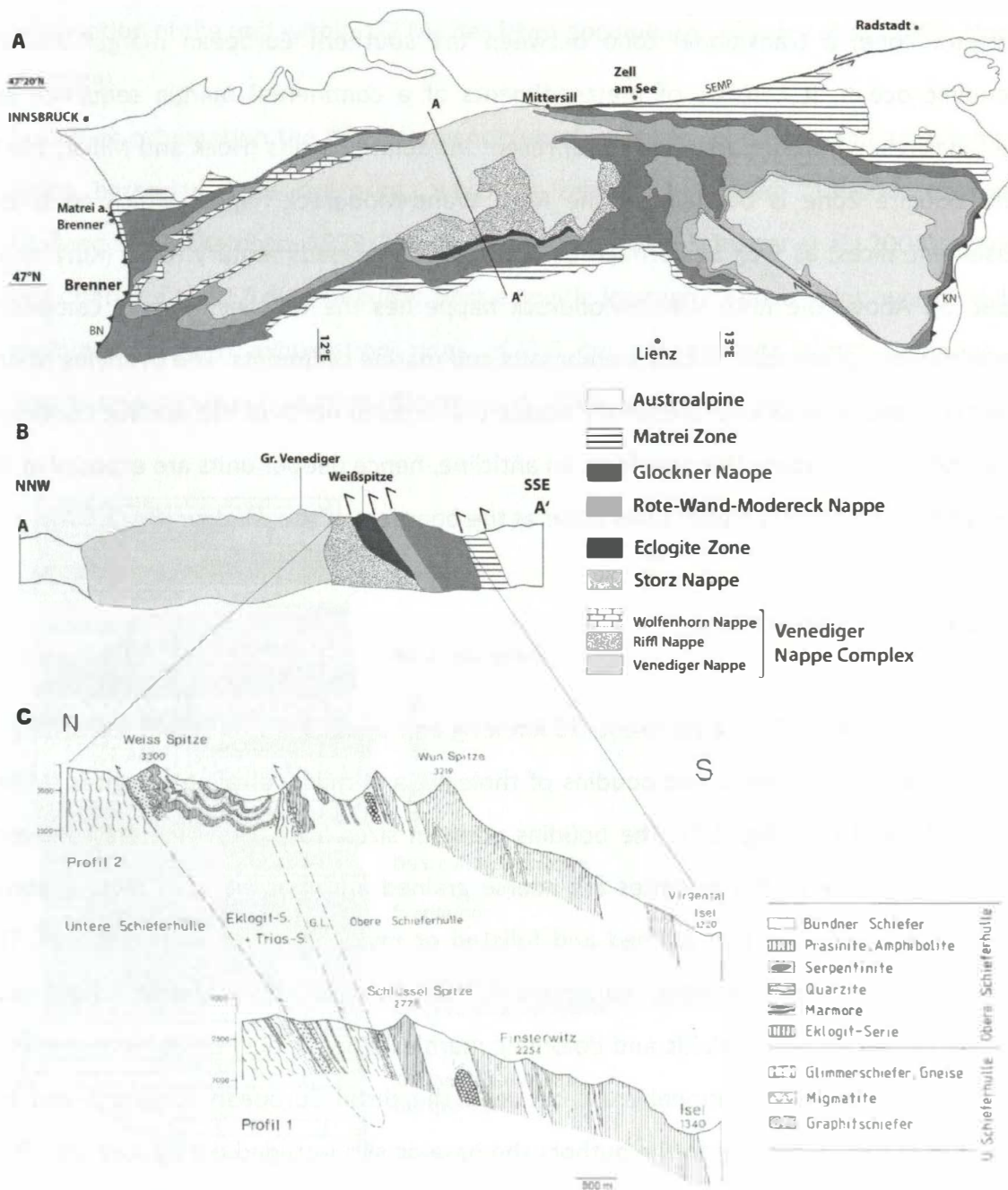


Fig. 1.6: (A) Tectonic map of the Tauern Window. BN: Brenner normal fault; KN: Katschberg normal fault; SEMP: Salzach-Ennstal-Mariazell-Puchberg fault (B) scetch of NNW-SSE cross section of the Tauern Window. Location of cross section is marked on (A) (Kurz et al. 1998b). (C) Cross section of the Eclogite Zone and surrounding nappes (Raith, 1980).

In the Tauern Window, several paleogeographic units have been stacked in a northward fashion (Fig.1.6 B and C). The lowermost unit is the Venediger nappe, which comprises pre-Variscan continental crust from the European margin and Variscian granitic intrusions, as well as Jurassic to Cretaceous metasedimentary cover rocks (Kurz et al., 1998b). In the central southern Tauern Window, the Venediger nappe is overlain by the

Eclogite Zone, a transitional zone between the southern European margin and the Penninic ocean. It consists of metasediments of a continental margin sequence and metabasites, which are assumed to represent intraplate basalts (Höck and Miller, 1987). The Eclogite Zone is overlain by the Rote Wand-Modereck nappe, which comprises basement slices, as well as Permian to Cretaceous metasedimentary rocks (Kurz et al., 1998 b). Above the Rote Wand-Modereck nappe lies the Glockner nappe, comprising serpentinites, greenschist facies metabasalts and marine sediments. The overlying Matri zone is interpreted as an accretionary wedge that formed north of the Adriatic continent. The units of the Tauern Window form an anticline, hence deeper units are exposed in the center and tectonically higher units occur at the borders of the window (Fig. 1.6 A).

1.4.2 The Eclogite Zone

The Eclogite Zone (EZ) is a coherent, 20 km long and up to 3 km thick unit, consisting of eclogite facies sediments, and boudins of tholeiitic and mildly alkaline eclogites (Miller, 1974; Miller, 1977) (Fig. 1.7). The boudins occur in sizes from a few meters to several kilometers. Some of the eclogites are coarse grained and massive with relict gabbroic structures, others are fine grained and foliated or mylonitic (Kurz et al., 1998 a). The metasediments are quartzites, paragneisses, meta-arkosic rocks, garnet micaschists, calcareous micaschists, calcitic and dolomitic marbles. Kurz et al., (1998b) interprets the rocks of the EZ as transitional crust between the distal European continent and the Penninic ocean. According to the authors the basaltic sills intruded during Jurassic rifting of the penninic ocean. On the other hand, some of the eclogites show relictic pillow structures and gabbro structures (Miller et al., 1980). This led Behrmann and Ratschbacher (1989) to the conclusion that the eclogite lenses found in the EZ are slivers of oceanic crust, which got scraped off during subduction of the penninic ocean. The authors interpret the metasediments as the pelagic cover of the oceanic crust, as well as material deposited in the deep sea trench.

The EZ has been buried to a depth of about 70 km and subjected to pressure-temperature conditions of 20-25 kbar and 600+- 30°C (Fig. 1.1; Stöckhert et al., 1997; Hoschek, 2001; 2004). Recently, an Oligocene age for peak metamorphic conditions and a fast

exhumation of the unit within 1-2 Ma has been documented (Glodny et al., 2005; Nagel et al., 2013).

During its exhumation the EZ underwent blueschist facies conditions and an amphibolite facies barrobian type overprint, which is regionally termed “Tauernkristallisation” (Holland and Richardson, 1979; Zimmermann et al., 1994; Schuster et al., 2004). However, large parts of the EZ did not suffer post-eclogitic (retrograde) overprint, which could be explained by high exhumation rates of 3.6 cm per year or a heterogenous fluid distribution during exhumation (Glodny et al., 2005; Kurz et al., 2008).

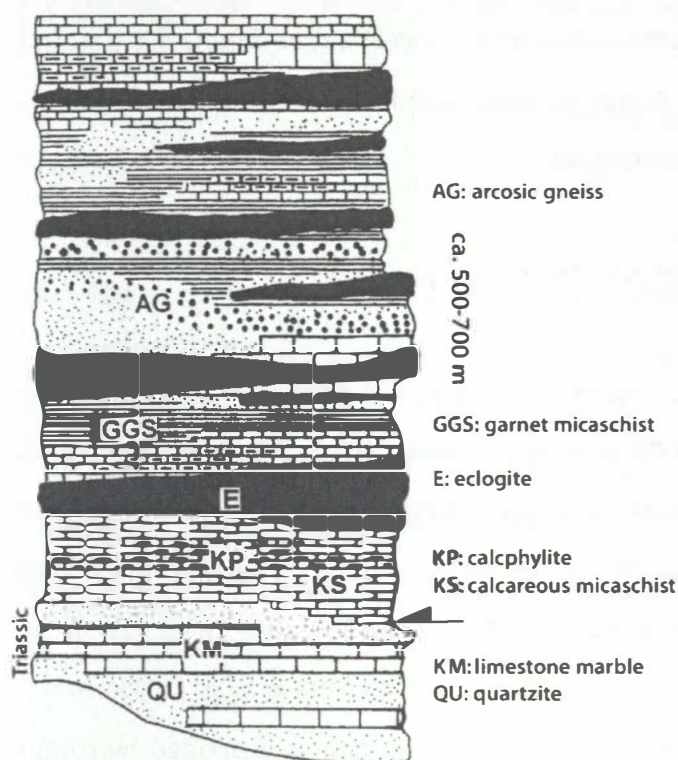


Fig. 1.7: Simplified columnar section documenting the lithological units of the Eclogite Zone (after Kurz et al 1998b).

The foliation of the EZ and its surrounding nappes is generally steeply S to SE-dipping, whereas the lineation mainly SW-plunging to subhorizontally EW-trending (Raith et al., 1980; Behrmann and Ratschbacher, 1989; Kurz et al., 1998a). Folds are large scale and isoclinal with steeply S-SE dipping axial planes (Raith et al., 1980).

1.5 Methods

1.5.1 Microprobe analysis

Mineral assemblages and chemical compositions of the samples in this study were determined by a JEOL JXA 8200 Electron microprobe of the Geomar, Kiel. In microprobe analysis a high voltage electron beam is focused on polished sample surfaces. The electrons produce X-rays, which are characteristic for certain elements. The resulting X-rays are diffracted by analyzing crystals and counted using gas-flow and sealed proportional detectors. Chemical composition of the investigated minerals is determined by comparing the intensity of the X-rays to those produced by standards (natural and synthetic silicates) with a known composition.

1.5.2 Crystallographic preferred orientation analysis

The main method used in this PhD thesis is the analysis of crystallographic preferred orientation (CPO). To describe the CPO of a polycrystalline material, a coordinate system has to be assigned to both the sample and the crystallites (Fig. 1.8 A). The coordinate system of the sample K_A is chosen according to the process geometry, which, in case of geological samples, is the foliation and lineation (Fig. 1.8 B). The coordinate system of the crystallites K_B is determined by the base vectors a , b and c of the Bravais lattice, where $Z_B = c$; $Y_B = c * a$; and $X_B = Z_B * Y_B$. The orientation of the crystal is described by rotations, which transfers the coordinate system of the sample into that of the crystal. Three so called Euler angles describe the minimum set of rotations that can bring one orientation to coincidence with another. In case of a polycrystalline samples, this results in an orientation probability distribution of the lattice planes and is defined by the orientation distribution function (ODF). The ODF is illustrated as equal area projections in polefigures, which are two-dimensional illustrations of the three-dimensional distribution of the pole of a certain lattice plane. They are normalized to multiples of a random distribution and express the probability of finding a lattice plane in a certain direction.

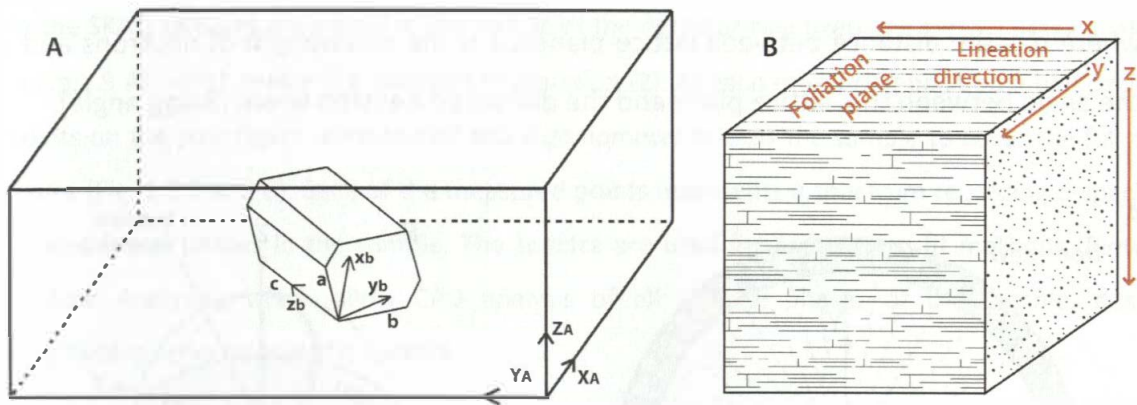


Fig. 1.8: (A) Sample coordinate system X_A , Y_A , and Z_A and crystal coordinate system determined by the base vectors of the crystal (see text for explanation). (B) Lineation direction and foliation plane in geological samples defining X , Y , and Z of the sample coordinate system.

CPO of polycrystalline rocks can be determined through different techniques. The most common one is x-ray or synchrotron diffraction, which is ideal for small, fine grained samples and can be applied even if the water content of the samples is high. Neutron diffraction is the most useful technique for coarse grained samples and when large sample volumes are needed, i.e. for the calculation of rock physical properties from the CPO. This method can be applied to big, coarse grained heterogeneous samples, is however unfitted for samples with high water contents. Another method for CPO investigations is electron backscatter diffraction (EBSD). As opposed to X-ray, or neutron diffraction, where sample volumes are analyzed, EBSD is applied to polished sample surfaces. Grain statistics in this method are low, but it yields the advantage that the orientation relationships between grains can be analyzed, which allows to draw conclusions on the deformation mechanisms.

1.5.2.1 Time-of-flight neutron diffraction

For this work, time-of-flight (tof) neutron diffraction was performed at the SKAT diffractometer of the Frank Laboratory of Neutron Physics at JINR, Dubna, Russia (Ullemeyer et al., 1998). Like x-ray and synchrotron diffraction, tof neutron diffraction takes advantage of the Bragg equation to obtain the CPO (1),

$$(1) \lambda = 2d / \sin(\theta)$$

where d is the distance between lattice planes, λ is the wavelength of neutrons and θ is the angle between the lattice plane and the diffracted neutron beam (Bragg angle).

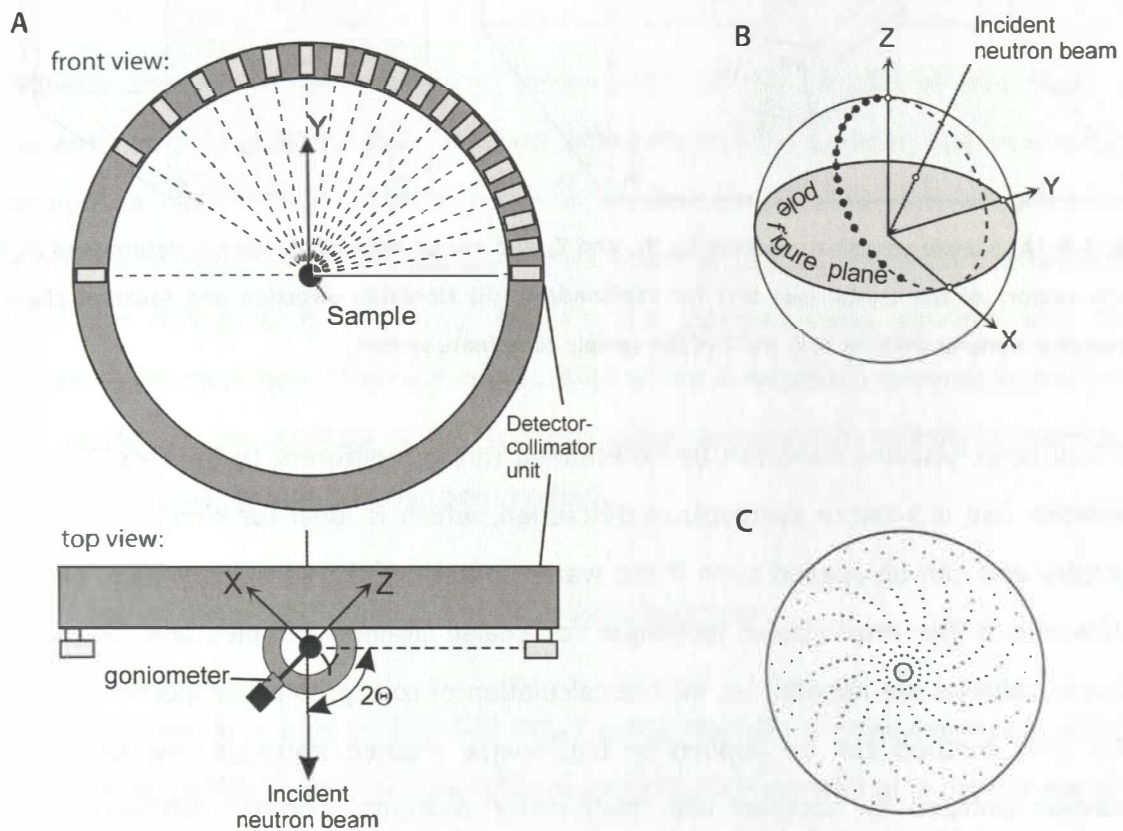


Fig. 1.9: (A) Front and top view of one of the three available detector rings at the SKAT. (B) Points measured at one sample position. (C) Extensively covered pole figure, achieved by a stepwise rotation of the sample through a goniometer.

A reflection of the neutron beam can only be observed if the Bragg equation is fulfilled. Each parallel group of lattice planes (hkl) of any mineral phase has a specific Bragg angle and a specific d -spacing. At the SKAT, d -spacings are recorded by measuring the time of flight of neutrons using equation (2),

$$(2) \quad d = \frac{h}{2m_n s \sin \theta} t$$

which combines (1) with mechanical properties of neutrons, whereas h is the Planck's constant, m is the mass of neutrons, s is the flight path and t is the time of flight.

At the SKAT, samples are placed in the middle of the detector-ring fixed at a certain Bragg angle (θ in Fig. 1.9 A), which makes θ a constant in equation (2). At each measuring position a half circle of points on the pole figure is measured and a goniometer rotates the sample to cover the full pole figure (Fig. 1.9 B and C). Each of the measured points represents a spectrum recording d-spacings of all mineral phases in the sample. The spectra are used for full pattern fit methods (Rietveld Texture Analysis), which allow CPO analysis of all mineral phases of the sample, despite overlapping reflections in the spectra.

1.5.2.2 Electron backscatter diffraction

Another method applied in this study was EBSD analysis with a scanning electron microscope (SEM) at the Bayerisches Geoinstitut, Universität Bayreuth. In this method a polished sample is placed at a shallow angle to an incident electron beam with an accelerating voltage of 10–30 kV (Fig. 1.10 A). The electrons are diffracted on the sample surface, interacting with the crystal lattice of the constituent minerals (Fig. 1.8 B).

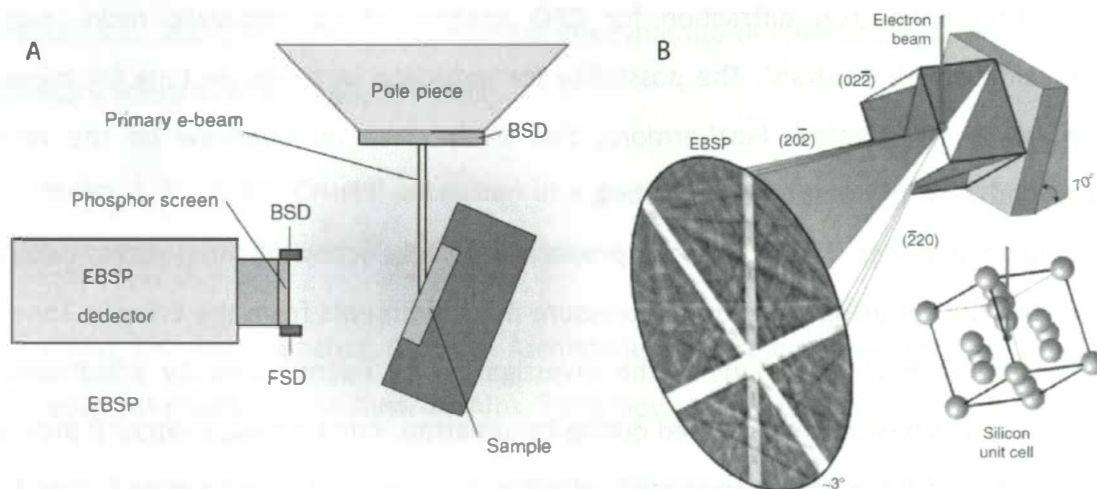


Fig. 1.10: (A) Schematic illustration of EBSD using a scanning electron microscope. (B) Kikuchi bands produced by the diffracted electrons interacting with crystal lattice planes.

The diffracted electrons display specific patterns on a phosphor screen in short distance to the sample. The patterns are called Kikuchi bands and are specific to different mineral phases, reflecting their lattice symmetry (Schwartz et al., 2009). Specialized computer software can use the detected Kikuchi bands to identify the mineral phase and its orientation within the sample coordinate system. With systematic point measurement on

the sample the CPO of different mineral phases can be obtained. Individual areas on the sample can be scanned with small step sizes and high resolution to produce orientation maps, which reveal even small differences in orientation of the crystal lattice planes. These maps can be used for microstructural investigations as they illustrate the grain structures and grain boundary characters.

1.6 Thesis Outline

Chapters 2, 3, and 4 are individual articles, which are either published (chapter 1), submitted for publication (chapter 3), or in preparation (chapter 4). They all focus on CPO analysis of polycrystalline high pressure rocks. Samples investigated in the three studies originate from the Tauern Window subduction channel (Eclogite Zone). In *chapter 5* the main results of the individual studies are summarized and discussed. Furthermore an outlook on prospective continuative work in this research area is given.

In *chapter 2*, a methodical study is presented, which illustrates the reliability and limits of time-of-flight neutron diffraction for CPO analysis of polymineralic rocks, applying 'Rietveld Texture Analysis'. The possibility for reduction in exposure time for measured samples is investigated. Furthermore, this study gives an overview on the recently upgraded SKAT diffractometer in Dubna.

Chapter 3 provides data for elastic properties of subduction channel rocks, calculated from the CPO of eclogites and high pressure metasediments from the Eclogite Zone. The novel approach of this study is the investigation of seismic velocity anisotropies of eclogites, which were retrogressed during exhumation. Additionally, chapter 3 provides a comparison of fresh and retrogressed eclogites. Data presented in chapter 3 were finally used to calculate the elastic properties of the metasediments in the subduction channel.

In *chapter 4*, CPO and microstructures of high pressure rocks from the Eclogite Zone are investigated to gain insights on their deformational history. As in chapter 2, fresh and retrogressed eclogites, as well as metasediments are analyzed to cover the full spectrum of subduction channel rocks and unravel the complete deformational path of the Eclogite Zone from its subduction to high pressure towards its exhumation to crustal depths.

REFERENCES:

- Agard, P., Yamato, P., Jolivet, L., and Burov, E., 2009. Exhumation of oceanic blueschists and eclogites in subduction zones: Timing and mechanisms. *Earth and Science Review*, 92, 53-79.
- Angiboust, S., Agard, P. Jolivet, L. and Beyssac, O. 2009. The Zermatt-Saas ophiolite: the largest (60-km wide) and deepest (c. 70–80 km) continuous slice of oceanic lithosphere detached from a subduction zone? *Terra Nova*, 21, 171–180.
- Audet, P., Bostock, M.G., Christensen, N.I. and Peacock, S.M., 2009. Seismic evidence for overpressured subducted oceanic crust and megathrust fault sealing. *Nature*, 457, 76-78.
- Audet, P., Bostock, M.G., Boyarko, D.C., Brudzinski, M.R., Allen, R.M., 2010. Slab morphology in the Cascadia forearc and its relation to episodic tremor and slip. *Journal of Geophysical Research*, 115, doi:10.1029/2008JB006053.
- Bebout, G.E., 2007. Metamorphic chemical geodynamics of subduction zones. *Earth and Planetary Science Letters* 260, 373–393.
- Behrmann, J. H., 1988. Crustal extension in a convergent orogen: The Sterzing-Steinach mylonite zone in the Eastern Alps. *Geodynamica Acta*, 2, 63-73.
- Behrmann, J.H., Ratschbacher, L., 1989. Archimedes revisited: a structural test of eclogite emplacement models in the Austrian Alps. *Terra Nova* 1, 242–252.
- Benioff, H., 1949. Seismic evidence for the fault origin of oceanic deeps. *Geological Society of America, Bulletin*, 60, 1837-1856.
- Brun, J.P. and Faccena C., 2008. Exhumation of high-pressure rocks driven by slab rollback. *Earth and Planetary Science Letters* 272, 1–7.
- Calahorrano A.B., Sallarès, V., Collota, J.Y., Sagea, F. and Ranero C.R., 2008. Nonlinear variations of the physical properties along the southern Ecuador subduction channel:

Results from depth-migrated seismic data. *Earth and Planetary Science Letters* 267, 453–467.

Chemanda, A.I., Burg, J.-P., and Mattauer, M., 1999. Evolutionary model of the Himalaya-Tibet system : geopoem based on new modelling, geological and geophysical data. *Earth and Planetary Science Letters*, 174, 397-409.

Chopin, C., 1984. Coesite and pure pyrope in high grade blueschists of the Western Alps: a first record and some consequences. *Contributions to Mineralogy and Petrology*, 86, 107-118.

Clark, S.P. and Ringwood, A.e., 1964. Density distribution and constitution of the mantle. *Reviews of Geophysics*, 2, 1, 35-88.

Cloos, M., 1982. Flow mélanges – numerical modeling and geological constraints in their origin in the Franciscan Complex, California. *Geological Society of America*, 93, 4, 330-345.

Cloos, M. and Shreve, R. L., 1988. Subduction-Channel Model of Prism Accretion, Melange Formation, Sediment Subduction, and Subduction Erosion at Convergent Plate Margins: Implications and Discussion, *Pure and Applied Geophysics* 128, 314, 501-545.

Collot, J.-Y., Ribodetti, A., Agudelo, W. and Sage, F., 2011. The South Ecuador subduction channel: Evidence for a dynamic mega-shear zone from 2D fine-scale seismic reflection imaging and implications for material transfer. *Journal of Geophysical Research*, 116, 1-20.

Dachs, E., 1986. High-pressure mineral assemblages and their breakdown products in metasediments South of the Grossvenediger area (Tauern Window, Austria). *Journal of Metamorphic Geology*, 8, 217-230.

Dachs, E., 1990. Geothermobarometry in metasediments of the southern Grossvenediger area (Tauern Window, Austria). *Journal of Metamorphic Geology*, 8, 217–230.

Davies, G. F., 1992. On the emergence of plate tectonics, *Geology*, 20, 963–966.

Davies, J.H., Stevenson, D.J., 1992. Physical model of source region of subduction zone volcanics. *J. Geophys. Res.* 97, 2037–2070.

Davis, D., Suppe, J. and Dahlem F. A., 1983. Mechanics of Fold-and-Thrust Belts and Accretionary Wedges. *Journal of Geophysical Research*, 88, 1153-1172.

Dogliani, C., Carminati, E., Cuffaro, M., Scrocca, D., 2007. Subduction kinematics and dynamic constraints. *Earth-Science Reviews* 83, 125-175.

Dogliani, C., Hrabaglia, P., Merlini, S., Mongelli, F., Peccerillo, A., and Piromallo, C., 1999. Orogens and slabs vs. their direction of subduction. *Earth Science Review*, 45, 167-208.

Eberhart-Phillips, D., Reyners, M., Chadwick, M. and Chiu, J.M., 2005. Crustal heterogeneity and subduction processes: 3-D Vp, Vp/Vs and Q in the southern North Island, New Zealand. *Geophysical Journal International*, 162, 270–288.

England, P., Engdahl R. and Thatcher, W., 2004. Systematic variation in the depths of slabs beneath arc volcanoes. *Geophysical Journal International*, 156, 377–408.

Ernst, W.G., 2006. Preservation/exhumation of ultrahigh-pressure subduction complexes. *Lithos* 92, 321–335.

Ernst, W.G., Maruyama. S. and Wallis S., 1997. Buoyancy-driven, rapid exhumation of ultrahigh-pressure metamorphosed continental crust. *Proc. Natl. Acad. Sci.*, 94, 9532–9537.

Essen, K., Braatz, M., Ceranna, L., Friederich W. and Meier, T., 2009. Numerical modelling of seismic wave propagation along the plate contact of the Hellenic Subduction Zone—the influence of a deep subduction channel. *Geophysical Journal International* 179, 1737–1756.

Evans, B.W., Trommsdorff, V. and Richter, W., 1979. Petrology of an eclogite-metarodingite suit at Cima de Gagnone, Ticino, Switzerland. *American Mineralogist*, 64, 15-31.

- Exner, C., 1979. Geologie des Salzachtales zwischen Taxenbach und Lend. *Jahrbuch der Geologischen Bundesanstalt*, 122, 1, 1-73.
- Friederich, W., Lambrecht, L., Stöckhert, B., Wassmann, S. and Moos, C., 2014. Seismic visibility of a deep subduction channel – insights from numerical simulation of high-frequency seismic waves emitted from intermediate depth earthquakes. *Solid Earth*, 5, 141–159.
- Fügenschuh, B., Seward, D., and Mantckelow, N. S., 1997. Exhumation in a convergent orogen: the western Tauern Window. *Terra Nova*, 9, 213–217.
- Furumura, T. and Kennett, B.L.N., 2005. Subduction zone guided waves and the heterogeneity structure of the subducted plate: Intensity anomalies in northern Japan. *Journal of Geophysical Research*, 110, B10302.
- Geersen, J. M., Völker, D., Behrmann, J. H., Kläschen, D., Weinrebe, W., Krastel-Gudegast, S. und Reichert, C., 2013. Seismic rupture during the 1960 Great Chile and the 2010 Maule earthquakes limited by a giant Pleistocene submarine slope failure. *Terra Nova*, 25, 472-477.
- Glodny, J., Ring, U., Kühn, A., Gleissner, P., Franz, G., 2005. Crystallization and very rapid exhumation of the youngest Alpine eclogites (Tauern Window, Eastern Alps) from Rb/Sr mineral assemblage analysis. *Contributions to Mineralogy and Petrology*, 149, 699 – 712.
- Green, H. W., and H. Houston, The mechanics of deep earthquakes, *Annual Reviews of Earth and Planetary Science*, 23, 169 – 213.
- Grevemeyer, I. und Tiwari, V. M., 2006. Overriding plate controls spatial distribution of megathrust earthquakes in the Sunda-Andaman subduction zone. *Earth and Planetary Science Letters*, 251, 3-4, 199-208.
- Groß, K., Micksch, U. and TIPTEQ Research Group, 2007. The reflection seismic survey of project TIPTEQ—the inventory of the Chilean subduction zone at 38.2° S. *Geophysical Journal International*, 172: 565–571.

Guillot, S., Hattori, K., Sigoyer, J., Nägler, T., Auzende, A.L., 2001. Evidence of hydration of the mantle wedge and its role in the exhumation of eclogites. *Earth Planet Scientific Letters* 193: 115–127.

Harders, R., Ranero, C. R. und Weinrebe, R. W., 2012. An overview of the role of long-term tectonics and incoming plate structure on segmentation of submarine mass wasting phenomena along the Middle America Trench In: *Submarine Mass Movements and Their Consequences : 5th International Symposium. Advances in Natural and Technological Hazards Research* . Springer Verlag, Heidelberg, pp. 391-402.

Heesemann, M., Grevemeyer, I. und Villinger, H., 2009. Thermal constraints on the frictional conditions of the nucleation and rupture area of the 1992 Nicaragua tsunami earthquake. *Geophysical Journal International*, 179, 3, 1265-1278.

Helfrich, G. R., and B. J. Wood, 2001. The Earth's mantle. *Nature*, 412, 501–507.

Helfrich, G., Stein, S., 1993. Study of the structure of the slab-mantle interface using reflected and converted seismic waves. *Geophys.J.Int.* 115, 14–4072.

Herms, P., John, T., Bakker, R. J. und Schenk, V., 2012. Evidence for channelized external fluid flow and element transfer in subducting slabs (Raspas Complex, Ecuador) *Chemical Geology*, 310/311, 79-96.

Höck, V. a. Miller, C., 1980. Chemistry of mesozoic metabasites in the middle and eastern part of the Hohe Tauern. *Mitteilungen der österreichischen geologischen Gesellschaft*, 71/72, 81-88.

Holland, T.B.J., 1979. High water activities in the generation of high pressure kyanite eclogites in the Tauern Window, Austria. *Journal of Geology*, 87, 1-27.

Hoschek, G., 2001. Thermobarometry of metasediments and metabasites from the Eclogite zone of the Hohe Tauern, Eastern Alps, Austria. *Lithos*, 59, 127-150.

Hoschek, G., 2004. Comparison of calculated P-T pseudosections for a kyanite eclogite from the Tauern Window, Eastern Alps, Austria. *European Journal of Mineralogy* 16, 59-72.

Jakes, P. and White A.J.R., 1970. K/Rb ratios of rocks from island arcs. *Geochimica et Cosmochimica Acta*, 34, 849-856.

Karason, H., and R. D. van der Hilst, Tomographic imaging of the lowermost mantle with differential times of refracted and diffracted core phases (PKPP-diff). *Journal of Geophysical Research*, 106, 6569 – 6587.

Kárason, H., and van der Hilst, R. D., 2000. Constraints on mantle convection from seismic tomography, in *The History and Dynamics of Global Plate Motion*. Geophysical Monograph 121, edited by M. A. Richards, R. Gordon, and R. D. van der Hilst, pp. 277–288.

Karato, S. Riedel, M.R., and Yuen, D.A., 2001. Rheological structure and deformation of subducted slabs in the mantle transition zone: implications for mantle circulation and deep earthquakes. *Physics of the Earth and Planetary Interiors*, 127, 83-108.

Kious, W.,J. and Tilling R.I., 1996. *This dynamic Earth: The Story of Plate Tectonics*. U.S. Geological Survey.

Kurz, W., Neubauer, F. a. Dachs, E., 1998a. Eclogite meso- and microfabrics: implications for the burial and exhumation history of eclogites in the Tauern Window (Eastern Alps) from P-T-d paths. *Tectonophysics*, 285, 183-209.

Kurz, W., Neubauer, F., Genser, J., Dachs, E. 1998b. Alpine geodynamic evolution of passive and active continental margin sequences in the Tauern Window (eastern Alps, Austria, Italy): a review. *International Journal of Earth Sciences*, 87, 225–242.

Lallemant, S., A. Heuret, and D. Boutelier, 2005. On the relationships between slab dip, back-arc stress, upper plate absolute motion, and crustal nature in subduction zones. *Geochemistry, Geophysics and Geosystems*, 6, doi:10.1029/2005GC000917.

Langston, C.A.,1981.Evidence for the subducting lithosphere under southern Vancouver island and western Oregon from teleseismic P wave conversion. *J. Geophys.Res.*86,3857–3866.

Linzer, H. G., Decker, K., Peresson, H. a. Frisch, W., 2002. Balancing lateral orogenic float of the Eastern Alps. *Tectonophysics*, 354, 211-237.

Lithgow-Bertelloni, C. and Richards, M. A., 1995. Cenozoic plate driving forces. *Geophysical Research Letters*, 22, 11, 1317-1320.

Mainprice, D., Tommais, A., Ferré, D., Carrez, P., Cordier, P., 2008. Predicted glide systems and crystal preferred orientations of polycrystalline silicate Mg-Perovskite at high pressure: Implications for the seismic anisotropy in the lower mantle. *Earth and Planetary Science Letters*, 271, 135–144.

Mancktelow, N. S., Stöckli, D. F., Grollmund, B., Müller, W., Fügenschuh, B., Viola, G., Seward, D. a. Villa, I. M., 2001. The DAV and Periadriatic fault systems in the Eastern Alps south of the Tauern window. *International Journal of Earth Sciences (Geologische Rundschau)*, 90, 593-622.

McLaughlin, R. J., Blake, M. C., Jr., Griscom, A., Blome, C. D., and Murchey, B., 1988, Tectonics of formation, translation and dispersal of the Coast Range ophiolite of California: *Tectonics*, 7, 1033–1056.

Miller, C., 1974. On the metamorphism of the eclogites and high-grade blueschists from the penninic terrane of the Tauern Window, Austria. *Schweizerische Mineralogische und Petrologische Mitteilung*, 54, 371-384.

Miller, C., 1977. Chemismus und phasenpetrologische Untersuchungen der Gesteine aus der Eklogitzone des Tauernfensters, Österreich. *Tschermaks Mineralogische und Petrologische Mitteilung*, 24, 221-277.

Miller, C., Satir, M., a. Frank, W., 1980. High-pressure Metamorphism in the Tauern window. *Mitteilung der österreichischen geologischen Gesellschaft*, 71/72, 89-97.

Montagner, J.-P., Guillot, L., 2003. Seismic Anisotropy and global geodynamics. *Mineralogical Society of America*, 51, 353-385.

- Montagner, J.-P., Tanimoto, T., 1990. Global Anisotropy in the Upper Mantle Inferred From the Regionalization of Phase Velocities. *Journal of Geophysical Research*, 95, B4, 4797-4819.
- Moscoso, E., Grevemeyer, I., Contreras-Reyes, E., Flueh, E. R., Dzierma, Y., Rabbel, W. und Thorwart, M., 2011. Revealing the deep structure and rupture plane of the 2010 Maule, Chile earthquake (Mw=8.8) using wide angle seismic data. *Earth and Planetary Science Letters*, 307, 147-155.
- Müller, W., Prosser, G., Mancktelow, N. S., Villa, I. M., Kelley, S. P., Viola, G. a. Oberli, F., 2001. Geochronological constraints on the evolution of the Periadriatic Fault System (Alps). *International Journal of Earth Sciences (Geologische Rundschau)*, 90, 623-653.
- Murphy, J.B., 2006. Arc Magmatism I: Relationship between tectonic evolution and petrogenesis. *Geoscience Canada*, 33, 4, 145-167.
- Murphy, J.B., 2007. Arc Magmatism II: Geochemical and Isotopic Characteristics. *Geoscience Canada*, 34, 1, 7-35.
- Nagel, T. J., Herwartz, D., Rexroth, S., Münker, C., Froitzheim, N., Kurz, W., 2013. Lu-Hf dating, petrography, and tectonic implications of the youngest Alpine eclogites (Tauern Windo, Austria). *Lithos* 170-171, 179-190.
- Niu, Y., O'Hara, M.J., Pearce, J.A., 2003. Initiation of subduction zones as a consequence of lateral compositional buoyancy contrast within the lithosphere: a petrological perspective. *Journal of Petrology*, 4, 5, 851-866.
- Papazachos, B.C., Karakostas V.G., Papazachos, C.B.,and Scordilis, E.M., 1995. The geometry of the Wadati–Benioff zone and lithospheric kinematics in the Hellenic arc. *Tectonophysics*, 319, 275–300.
- Pawely, A.R. and Holloway, J.R., 1993. Water sources for subduction zone volcanism: New experimental constraints. *Science*, 260, 664-667.

Pearce, J.A. and Peate, D.W., 1995. Tectonic Implications of the Composition of volcanic arc magmas. *Annual Review in Earth and Planetary Science*, 23, 251-285.

Platt, J.P., 1986. Dynamics of orogenic wedges and the uplift of high pressure metamorphic rocks. *Bulletin of the geological Society of America*, 97, 1037-1053.

Protti, M., Gündel, F. and McNally, K., 1994. The geometry of the Wadati-Benioff zone under southern Central America and its tectonic significance: results from a high-resolution local seismographic network. *Physics of the Earth and Planetary Interiors*, 84, 1-4, 271-287.

Raith, M., Mehrens, C., and Thöle W., 1980. Gliederung, tektonischer Bau und metamorphe Entwicklung der penninischen Serien im südlichen Venediger-Gebiet, *Osttiroler Jahrbuch der Geologischen Bundesanstalt*, 123, 1-37.

Ranero, C. R. und Weinrebe, R. W., 2005. Tectonic processes during convergence of lithospheric plates at subduction zones In: *Sound Images of the Ocean: In Research and Monitoring*. Springer-Verlag, Berlin, pp. 85-105.

Ratschbacher, L., Frisch, W., Linzer, H. G. and Merle, O., 1991. Lateral extrusion in the eastern Alps, Part 2: structural analysis. *Tectonics*, 10, 2, 257-271.

Ratschbacher, L., Frisch, W., Neubauer, F., Schmid, S. M. a. Neugebauer, J., 1989. Extension in compressional orogenic belts: The eastern Alps. *Geology*, 17, 404-407.

Rea, D.K. and Ruff, L.J., 1996. Composition and mass flux of sediment entering the world's subduction zones: Implications for global sediment budgets. *Great earthquakes and volcanism. Earth and Planetary Science Letters*, 140, 1-4.

Rosenberg, C.L., Brun, J.P., Cagnard, F. and Gapais, D., 2007. Oblique indentation in the Eastern Alps: Insights from laboratory experiments. *Tectonics*, 26, TC2003.

Royden, L.H. and Husson, L., 2006. Trench motion, slab geometry and viscous stresses in subduction systems. *Geophysical Journal international*, 167, 881-905.

- Ruff, L. J., and B. W. Tichelaar, 1996. What controls the seismogenic plate interface in subduction zones? in *Subduction: Top to Bottom*, Geophysical Monographic Series, 96, edited by G. E. Bebout et al., 105 – 112, AGU, Washington, D.C.
- Schmid, S.M., Scharf, A., Handy, M.R., and Rosenberg, C.L., 2013. The Tauern Window (Eastern Alps, Austria): a new tectonic map, with cross-sections and a tectonometamorphic synthesis. *Swiss Journal of Geoscience*, 106, 1-32.
- Schwartz, A.J., Kumar, M., Adams, B.L., Field, D. (Eds.), 2009. *Electron Backscatter Diffraction in Materials Science*, 41-75.
- Selverstone, J., 1988. Evidence for east-west crustal extension in the eastern Alps: implications for the unroofing history of the Tauern Window. *Tectonics*, 7, 1, 87-105.
- Silver, P.G., 1996. Seismic anisotropy beneath the continents: probing the depths of geology. *Annual Review: Earth and Space Science* 24, 385.
- Simpson, G.D.H., 2009. Formation of accretionary prisms influenced by sediment subduction and supplied by sediments from adjacent continents. *Geology*, 38, 2, 131-134.
- Sobolev, N.V. and Shatsky, V.S. 1990. Diamond inclusions in garnets from metamorphic rocks: a new environment for diamond formation. *Nature* 343, 742 - 746.
- Spear and Franz, 1986. P-T evolution of metasediments from the Eclogite one, south-central Tauern Window, Austria. *Lithos* 19, 219-234.
- Spence, W., 1987. Slab pull and the seismotectonics of subducting lithosphere. *Reviews in Geophysics*, 25, 1, 55-69.
- Stern, R., 2002. Subduction Zones. *Reviews of Geophysics*, 40, 3-1 - 3-13.
- Stöckhert, B., Massonne, H.-J., Nowlan, E. U., 1997. Low differential stress during high-pressure metamorphism: the microstructural record of a metapelite from the Eclogite Zone, Tauern Window, Eastern Alps. *Lithos*, 41, 103-118.
- Ullemeyer, K., Spalhoff, P., Heinitz, J., Isakov, N. N., Nikitin, A. N., Weber, K., 1998. The SKAT texture diffractometer at the pulsed reactor IBR-2 at Dubna: Experimental layout

and first measurements. *Nuclear Instruments and Methods of Physical Research*, 412, 80–88.

Ulmer, P. and Trommsdorff, V., 1995. Serpentine Stability to Mantle Depths and Subduction-Related Magmatism. *Science*, 268, 858-861.

Uyeda, S. and Kanamori, H., 1979. Back-arc opening and the mode of subduction. *Journal of Geophysical Research*, 84, 1049-1061.

Vannucchi, P., Ranero, C. R., Galeotti, S., Straub, S., Scholl, D. W. und McDougall-Ried, K., 2003. Fast rates of subduction erosion along the Costa Rica Pacific margin: implications for non-steady rates of crustal recycling at subduction zones *Journal of Geophysical Research - Solid Earth*, 108 (B11), doi:10.1029/2002JB002207.

Von Huene, R., Ranero, C.R., and Vannucchi, P., 2004. Generic model of subduction erosion. *Geology*, 32, 10, 913-916.

von Huene, R., and Scholl, D.W., 1991. Observations at convergent margins concerning sediment subduction, subduction erosion, and the growth of continental crust. *Reviews in Geophysics*, 29, 279–316.

Vauchez, A., Dineur, F., and Rudnick, R., 2005. Microstructure, texture and seismic anisotropy of the lithospheric mantle above a mantle plume: Insights from the Labait volcano xenoliths (Tanzania). *Earth and Planetary Science Letters*, 232, 295–314.

Wadati, K., 1928. A shallow and deep earthquakes. *Geophysical magazine* 1, 162-202.

Zimmermann, R., Hammerschmidt, K., Franz, G., 1994. Eocene high pressure metamorphism in the Penninic units of the Tauern Window (Eastern Alps): evidence from ⁴⁰Ar-³⁹Ar dating and petrological investigations. *Contributions to Mineralogy and Petrology*, 117, 175–186.

Potential of full pattern fit methods for the texture analysis of geological materials: implications from texture measurements at the recently upgraded neutron time-of-flight diffractometer SKAT

Ruth Keppler¹, Klaus Ullemeyer¹, Jan H. Behrmann² and Michael Stipp²

(1) Department of Geosciences, University of Kiel, Otto-Hahn-Platz 1, D-24118 Kiel

(2) GEOMAR Helmholtz Centre for Ocean Research, Wischhofstr. 1-3, D-24148 Kiel

Journal of Applied Crystallography 47, doi:10.1107/S1600576714015830

Potential of full pattern fit methods for the texture analysis of geological materials: implications from texture measurements at the recently upgraded neutron time-of-flight diffractometer SKAT

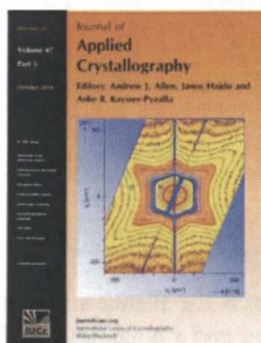
Ruth Keppler, Klaus Ullemeyer, Jan H. Behrmann and Michael Stipp

J. Appl. Cryst. (2014). **47**, 1520–1534

Copyright © International Union of Crystallography

Author(s) of this paper may load this reprint on their own web site or institutional repository provided that this cover page is retained. Republication of this article or its storage in electronic databases other than as specified above is not permitted without prior permission in writing from the IUCr.

For further information see <http://journals.iucr.org/services/authorrights.html>



Many research topics in condensed matter research, materials science and the life sciences make use of crystallographic methods to study crystalline and non-crystalline matter with neutrons, X-rays and electrons. Articles published in the *Journal of Applied Crystallography* focus on these methods and their use in identifying structural and diffusion-controlled phase transformations, structure-property relationships, structural changes of defects, interfaces and surfaces, etc. Developments of instrumentation and crystallographic apparatus, theory and interpretation, numerical analysis and other related subjects are also covered. The journal is the primary place where crystallographic computer program information is published.

Crystallography Journals **Online** is available from journals.iucr.org

Potential of full pattern fit methods for the texture analysis of geological materials: implications from texture measurements at the recently upgraded neutron time-of-flight diffractometer SKAT

Ruth Keppler,^{a*} Klaus Ullemeyer,^a Jan H. Behrmann^b and Michael Stipp^b

^aDepartment of Geosciences, University of Kiel, Otto-Hahn-Platz 1, Kiel, D-24118, Germany, and
^bGEMAR Helmholtz Centre for Ocean Research, Wischhofstrasse 1-3, Kiel, D-24148, Germany.
Correspondence e-mail: rkeppler@geomar.de

The application of Rietveld texture analysis (RTA) to time-of-flight (TOF) neutron diffraction data allows complex materials with many diffraction peaks to be investigated, for example, rocks composed of different minerals. At the recently upgraded SKAT texture diffractometer at the JINR in Dubna (Russia), which provides three alternative multidetector systems, resolution and accessible range of lattice d spacings can be adapted to sample requirements. In order to infer the optimum experimental setup and the reliability of texture estimates from complicated TOF patterns, the influence of counting statistics and various spectral resolutions on texture deconvolution was investigated. Comparing the results obtained at different resolutions and from different sections of the d patterns indicates that the textures of a four-phase sample can be determined, but using a section at small d spacings with a larger number of peak overlaps leads to smoother textures. A complex seven-phase sample shows orientation differences in addition to the smoothing effect. Weak textures and textures of the minor rock constituents are inaccurate owing to multiple peak overlaps. Consequently, good resolution is essential for RTA on such samples. Grid thinning tests confirmed that no more than 150 diffraction spectra are needed to characterize the texture of a monomineralic sample, and approximately 350 spectra are sufficient for a four-phase sample. The irregular grid point arrangement caused by the SKAT geometry has no negative consequences.

© 2014 International Union of Crystallography

1. Introduction

Neutron diffraction has proven to be the most suitable and promising method for texture analysis of polymineralic rock samples (e.g. Brokmeier, 1994; Siegesmund *et al.*, 1994; Wenk, 1991; Wenk *et al.*, 2001; Leiss *et al.*, 2002; Xie *et al.*, 2003; Pehl & Wenk, 2005; Müller *et al.*, 2010). Because of the low attenuation of thermal neutrons in matter large sample volumes can be investigated and good counting statistics are achieved. The texture calculated from neutron diffraction data is, therefore, an optimal representation of the bulk rock. This is particularly important when predicting physical anisotropies from the textures in medium- to coarse-grained rocks (e.g. Siegesmund *et al.*, 2000; de Wall *et al.*, 2000; Ullemeyer *et al.*, 2006, 2010; Kern *et al.*, 2008).

In addition to this principal advantage of working with neutrons, the energy-dispersive time-of-flight (TOF) method provides the possibility of measuring the complete diffraction patterns for each sample direction. The detector is installed at a fixed scattering angle (2θ) and records the time of flight (t) of

neutrons with different wavelengths (λ) from their point of creation at a pulsed reactor or a spallation source. From Bragg's law,

$$\lambda = 2d \sin \theta, \quad (1)$$

and de Broglie's quantum law,

$$\lambda = \frac{h}{m_n v} = \frac{ht}{m_n s}, \quad (2)$$

it follows that

$$d = \frac{ht}{2m_n s \sin \theta}, \quad (3)$$

where d is the lattice spacing, h is the Planck constant, m_n is the neutron mass, v is the speed and s is the total flight path (Windsor, 1981). Since θ and s are fixed, λ and d depend on t only, *i.e.* recording the neutrons as a function of their arrival time at the detector directly leads to neutron intensity as a function of d spacing. Once the TOF spectra are acquired, full

pattern fit methods like the so-called Rietveld texture analysis (RTA) for texture evaluation (Matthies *et al.*, 1997; Von Dreele, 1997) can be applied. This method is advantageous for texture investigations of polymineralic rocks, because the separation of nonoverlapped pole figures for quantitative texture analysis (QTA) using a classical pole figure inversion method (*e.g.* Matthies & Vinel, 1982; Dahms & Bunge, 1989; Hielscher & Schaeben, 2008) is difficult and often impossible owing to multiple peak overlaps. Besides the texture evaluation, RTA offers the possibility of refining lattice parameters, grain size and microstrain, and of performing quantitative phase analysis (Lutterotti *et al.*, 1997).

The accessible range of lattice spacings is determined by the pulse repetition rate of the neutron source and by the diffraction angle θ . The resolution ($\Delta d/d$) depends on flight time uncertainty ($\Delta t/t$), uncertainty of the total flight path ($\Delta s/s$) and θ :

$$\frac{\Delta d}{d} = \left[\left(\frac{\Delta s}{s} \right)^2 + \left(\frac{\Delta t}{t} \right)^2 + (\Delta\theta \cot\theta)^2 \right]^{1/2} \quad (4)$$

The neutrons are slowed down to thermal energies in a moderator, which causes a Maxwellian energy distribution. This leads to the highest intensities at small wavelengths, tailing off rapidly at higher wavelengths, *i.e.* counting statistics become worse with increasing λ and also d (Fig. 1). Larger diffraction angles θ generate higher resolution, but because of the energy distribution of the neutron beam, the counting statistics are very low at high d spacings. Smaller diffraction angles, on the other hand, have the opposite effect. In addition, there are many peak overlaps at small d spacings. This will be explained in detail in §3. It follows that the quality of texture analysis with TOF neutrons and RTA depends on

several factors, which have so far not been investigated comprehensively.

In order to extend the possibilities for QTA of polymineralic rock samples from TOF spectra, the SKAT texture diffractometer at the pulsed neutron source IBR-2M in Dubna (Russia) has recently been upgraded. In addition to the already existing multidetector system with the detectors positioned at $2\theta = 90^\circ$ (Ullemeyer *et al.*, 1998), two more detector arrangements at other diffraction angles were installed. This offers the opportunity to select the most suitable instrument geometry, *i.e.* to adapt the accessible d range and resolution to the sample state. For texture evaluation from complicated spectra, RTA is introduced as the standard method.

The aim of this paper is, first, to give a short description of the upgraded SKAT and its main characteristics and, second, to develop criteria for selecting the optimum detector geometry for texture analysis from diffraction spectra of polymineralic geological samples. We also address the question to what extent exposure time can be reduced when using RTA for texture evaluation. In contrast to classical QTA based on the inversion of only a few pole figures, RTA uses a large number of Bragg reflections for the texture computations. This directly implies that the number of sample orientations and, by this means, bulk exposure time can be reduced without loss of information. The limits of such optimization have not yet been investigated. Answering all these questions will, first of all, characterize the SKAT diffractometer and delineate its potential applications. However, the results of the investigation presented here are of general interest and may be helpful to judge the results obtained at other TOF instruments, which have already been successfully operated for texture investigations [HIPPO (Wenk *et al.*, 2003) and GEM (Hannon, 2005)] or are under construction (POWTEX; Conrad *et al.*, 2008).

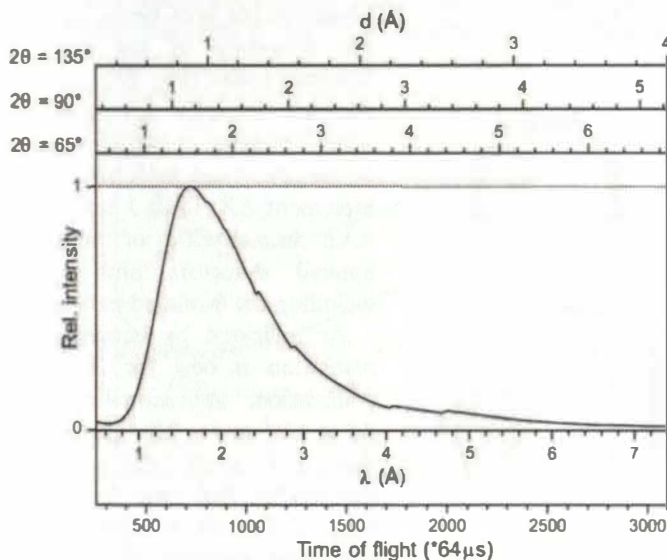


Figure 1 Energy distribution of thermal neutrons at the IBR-2M reactor applying a water moderator at ambient conditions; the time of flight and wavelength range of the SKAT related to the accessible d ranges for various diffraction angles 2θ .

2. The upgraded SKAT

The early SKAT (Ullemeyer *et al.*, 1998) at beamline 7A2 of the IBR-2M reactor in Dubna (Russia) was placed at the end of an over 100 m long flight path and the detectors were arranged at a diffraction angle of $2\theta = 90^\circ$. Along with the pulse repetition rate of 5 s^{-1} , this limited the accessible d range to $d_{\text{max}} \approx 5 \text{ \AA}$ with a resolution of $\Delta d/d = 5 \times 10^{-3}$ at $d = 2.5 \text{ \AA}$ at best (Ullemeyer *et al.*, 1998). Owing to the usually large sample dimensions, the contribution of the θ -dependent term in equation (4) is large; hence, high resolution can be achieved only by collimation of the secondary beam. Two sets of collimators with angular dispersions of $18'$ and $45'$ are available, allowing adaptation of the resolution, the width of the pole figure window and the level of diffracted intensity to some extent. High resolution and consistent detector geometry (*i.e.* avoidance of λ - and θ -dependent intensity corrections) were the main demands when designing the early SKAT; an accompanying loss of luminosity was accepted. Owing to these characteristics and to the large beam cross section of $50 \times 95 \text{ mm}$, many materials – including coarse-

grained rocks – could be successfully investigated applying classical QTA, but the investigation of complicated poly-mineralic rock samples was mostly impossible. The application of RTA leads to an enormous improvement; however, other restrictions have to be considered. As already pointed out by Matthies *et al.* (1997), the deconvolution of overlapping diffraction peaks may be ambiguous, especially in the case of multiple overlaps. This corresponds to our experience from many experiments and led to the conclusion that instrumental upgrading is the only way for further improvements of the SKAT. From equations (1) and (4) above it follows that (a) decreasing the diffraction angle θ expands d_{\max} at the expense of resolution. As many minerals have large volume cells,

access to more well separated diffraction peaks is possible, and (b) increasing the diffraction angle θ improves resolution, but leads to a decrease of d_{\max} .

Both possibilities were realized with the installation of two new detector systems at diffraction angles of $2\theta = 65^\circ$ and 135° . In order to keep the advantage of constant diffraction geometry, the detector systems were designed for alternative use. The technical realization is such that the detector-collimator units can be exchanged without making subsequent adjustment of the collimators necessary. As a further advantage of consistent detector geometry, d range and resolution are the same for all detectors during an experimental run. The relation of particular d ranges to the wavelength range and to the energy distribution is shown in Fig. 1, and Fig. 2 illustrates the general layout of beamline 7A2 at the IBR-2M reactor (Fig. 2a) and the detector arrangements at various diffraction angles 2θ (Fig. 2b). The position of the detector-collimator units on the rings is arbitrary; the example arrangements for $2\theta = 65^\circ/90^\circ$ with 19 units correspond to a constant pole angle step size of 5° . Related spherical representations indicate that a single sample revolution around the Z axis is sufficient to measure complete pole figures (Fig. 2b). In contrast, the $2\theta = 135^\circ$ configuration requires two sample revolutions at goniometer positions Y_1 and Y_2 to obtain complete pole figures. The example arrangement with 13 detector-collimator units is such that repeated measurements in the center and at the boundary of the pole figure, as well as at the boundary of the two Debye-Scherrer cones (Fig. 2b), are avoided. For all detector arrangements the overall number of sample directions to be measured can be selected *via* the Z increment ΔZ . Table 1 summarizes the main characteristics of the SKAT and applied detectors and collimators, including the θ -related parameters.

As indicated by equation (4), the resolution is best for $2\theta = 135^\circ/18'$ collimation, approximating $\Delta d/d \approx 3.5 \times 10^{-3}$ at $d = 2.5 \text{ \AA}$. It decreases to $\Delta d/d \approx 11 \times 10^{-3}$ ($2\theta = 65^\circ/45'$ collimation) in the least favorable case (Fig. 3). For all detector systems, the resolution applying $45'$ collimation is about 25% less compared with $18'$ collimation. However, the intensity gain at the collimator exit is about 2.5 times. In comparison with the resolution prior to upgrading of the SKAT, the resolu-

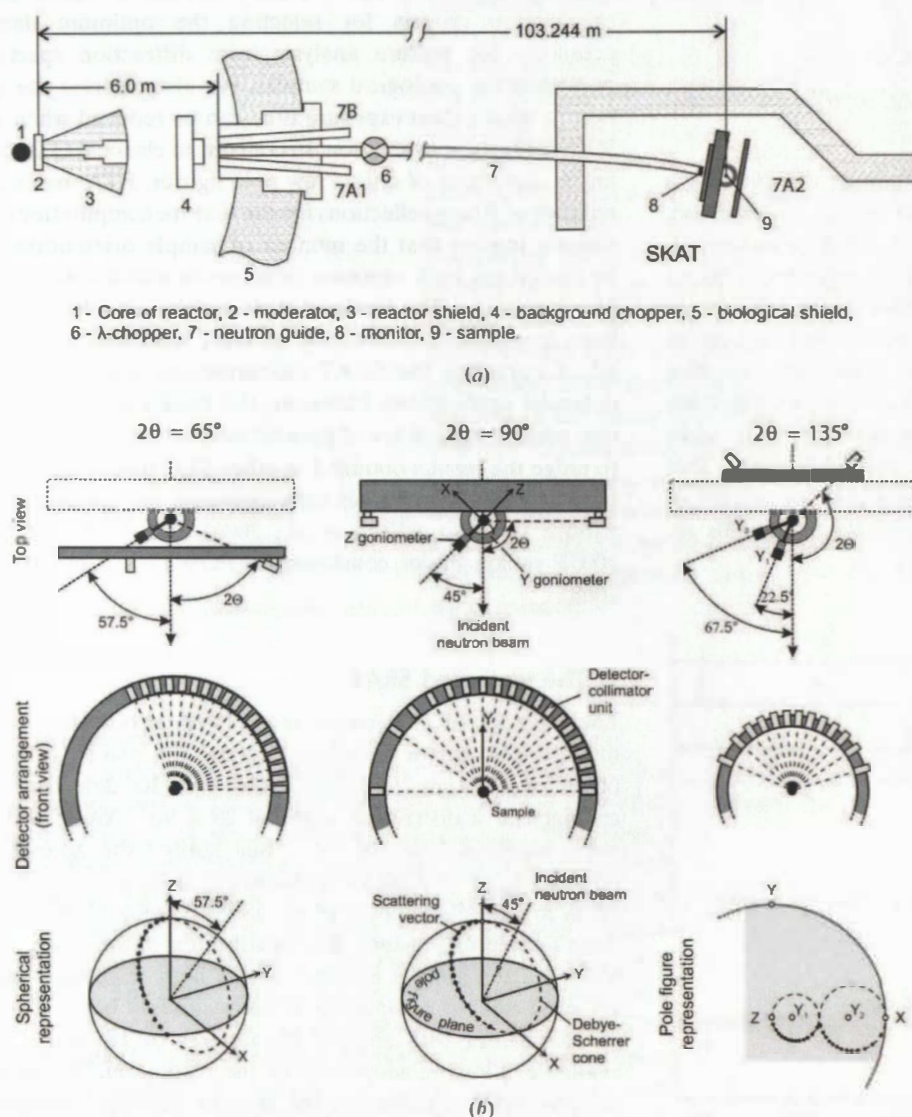


Figure 2

(a) General layout of beamline 7 at the IBR-2M reactor; 7A1, 7A2 and 7B represent the neutron guides of adjacent beamlines. (b) Scheme of the SKAT detector arrangements at various diffraction angles 2θ for alternative use. The mounting ring of the active detector system is shaded gray. Dots in the spherical and pole figure representation indicate scattering vectors at starting position $Z = 0^\circ$. In case of $2\theta = 135^\circ$ comprising two goniometer positions Y_1 and Y_2 , the pole figure representation (equal angular projection) is shown for better visualization of the more complicated spatial relationships.

Table 1

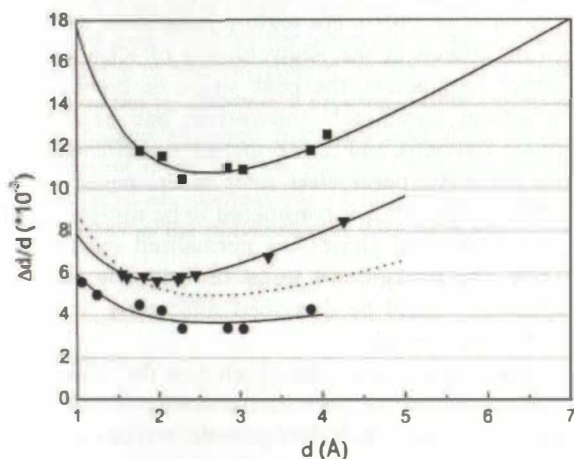
General characteristics of the SKAT diffractometer.

Moderator-sample distance	103.244 m		
Neutron guide	Cross section: 50 (width) × 95 mm (height) Bent, radius: 13 400 m Coating: natural Ni ($m = 1$) Option: λ -chopper covering every second neutron pulse		
Detectors	^3He single tube, $P = 4.5 \text{ bar} = 450 \text{ kPa}$, $\varnothing 60 \text{ mm}$		
Collimators	Soller-type, Gd coated, cross section: 55 × 55 mm Two sets with angular dispersions 18' and 45'		
λ_{max}	7.4 Å		
Flux at sample position	$\sim 10^6 \text{ n cm}^{-2} \text{ s}^{-1}$		
	θ -related parameters		
	$2\theta = 65^\circ$	$2\theta = 90^\circ$	$2\theta = 135^\circ$
Sample-detector distance (m)	1.041	1.000	1.060
d_{max} (Å)	6.8	5.2	4.0
d_{max} (Å) applying λ -chopper option	13.8	10.6	8.2

tion at present ($2\theta = 90^\circ/18'$ collimation) shows a small decrease and a shift of the resolution function to smaller d values (Fig. 3). Both effects can be attributed to the replacement of the formerly straight neutron guide by a curved one, while the diffracted beam geometry remains unchanged. The decrease of resolution is small and corresponds to predictions from neutron guide simulations (Manoshin *et al.*, 2009). For this reason, the small decrease was accepted when planning the upgrade of the SKAT.

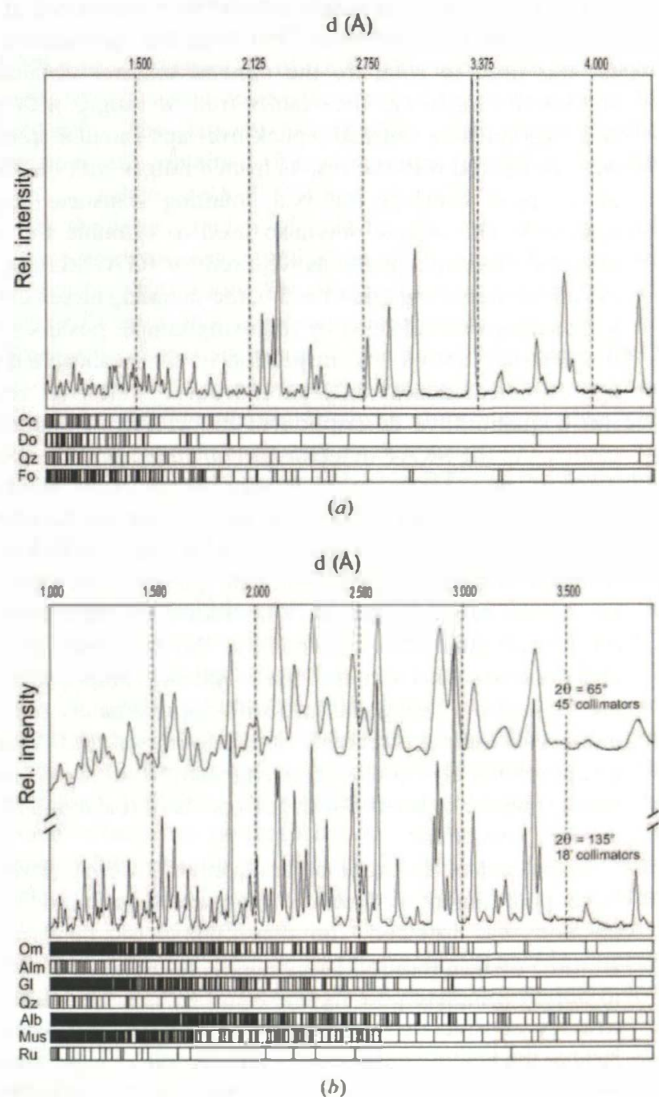
3. Analytical methods

As mentioned above, the objective of this work is to assess the influence of resolution, multiple peak overlaps and variability of counting statistics in the TOF neutron spectra on the

**Figure 3**

Experimental resolution of the SKAT. Dots refer to the best possible resolution function ($2\theta = 135^\circ/18'$ collimators), squares to the worst one ($2\theta = 65^\circ/45'$ collimators). For comparison, the resolution prior to upgrading of the SKAT (dotted line; Ullemeyer *et al.*, 1998) and the current resolution function for $2\theta = 90^\circ/18'$ collimators (triangles) are given.

reliability of RTA-based QTA. RTA allows the exposure time to be decreased by reducing the number of sample positions. So, some effort was made to define the minimum number of sample positions necessary to ensure reliable results for RTA. For this purpose three geological samples were investigated. Two samples are natural rocks originating from the Eclogite Zone of the Tauern Window in Austria (*e.g.* Raith *et al.*, 1980), a monomineralic calcite (Cc) marble (RK17) and a poly-mineralic eclogite (RK20). The latter has seven mineral phases identifiable in thin section. The sample volumes applied in the neutron experiment were 43 and 60 cm³, respectively. In both cases the exposure time was 30 min per sample position. The two samples were taken to represent the lower and upper bounds of spectrum complexity. The third sample, termed MIX, was artificially created by summing up the TOF spectra of two monomineralic rocks [a quartzite and

**Figure 4**

Summarized diffraction patterns of (a) the artificial (MIX) and (b) the eclogite (RK20) sample, normalized with respect to the energy distribution. For the eclogite, diffraction patterns with the highest and lowest resolution are given. The line patterns indicate peak positions.

a dunite consisting solely of forsterite (Fo)] and a marble-containing calcite and dolomite (Do). The resulting four-phase TOF pattern is of intermediate complexity with a moderate number of peak overlaps (Fig. 4a), and from the point of mineralogical complexity is representative of a large number of real rocks, although rocks with the above composition do not occur in nature. The reason for creating such an artificial sample was that well defined reference textures from the monomineralic samples were accessible. RTA performed on the individual measurements is considered to approximate the true texture in the best possible way, which is, therefore, used as a reference for comparison with the results obtained from the artificial sample. In the case of the marble it should be mentioned that calcite and dolomite do not exhibit overlapping reflections at d spacings greater than 1.6 Å (Fig. 4a), *i.e.* setting this lower limit for RTA avoids mutual influences between the two phases.

The MIX individual measurements were performed at $2\theta = 90^\circ$, applying 18' collimation. First of all, the summarized data set was used to compare the mineral textures obtained at various d ranges, *i.e.* the results from d ranges with good counting statistics but many peak overlaps (small d spacings) were compared with the results from d ranges with only a few or no peak overlaps but bad counting statistics (large d spacings). The sample was also used to examine the minimization of sample positions required for RTA. Starting with the initial measuring grid ($5 \times 5^\circ$), the sampling increment ΔZ was successively enlarged by removing sample positions from the data set, until visual inspection of the recalculated pole figures indicated clear differences from the reference texture (for a quantitative description of differences in texture see below). As the SKAT detectors occupy fixed positions on the detector ring, large sampling increments cause scattering vector arrangements on the pole sphere that are far from an equal area arrangement (compare with Fig. 2b). Hence, the results of grid thinning are, first of all, specific to the SKAT and grid effects cannot be excluded. In order to obtain information on possible grid effects, thinning of the measuring grid was also done in such a way that the remaining sample directions are closest to a hexagonal grid with approximately the same number of sample directions as the optimized grid. Thereby, an approximately equal area arrangement is achieved and the results may be compared with the results of the standard grid thinning procedure.

In the case of the monomineralic marble sample (RK17), a large potential to reduce the number of required sample positions was expected. The measurement was performed at $2\theta = 135^\circ$, which requires two goniometer positions Y_1 and Y_2 to obtain complete pole figures (see Fig. 2b). The measuring strategy considered that position Y_1 covers approximately 30% of the pole sphere surface, and position Y_2 approximately 70%. Consequently, the sampling increment ΔZ in the central part of the pole figure was twice the increment in the outer part (30 and 15°), and the reduction of sample positions was done accordingly. Likewise, as for sample MIX, the starting grid was also thinned to approximate a hexagonal grid in order to assess grid effects.

The eclogite sample (RK20 mainly consists of omphacite (Om), almandine (Al) and glaucophane (Gl), and to a lesser extent of quartz (Qz), muscovite (Mus), albite (Alb) and rutile (Ru). The large number of phases and, in part, their low crystal symmetries lead to many peak overlaps in the spectra at small d spacings (Fig. 4b). To give examples, the d range 1.2–2.4 Å hosts 1424 reflections but the d range 2.1–4.0 Å a much smaller number (294) of reflections. In order to detect texture differences between high- and low-resolution measurements, the sample was measured twice with the highest and lowest resolution applying detector configurations $2\theta = 135^\circ/18'$ collimation and $2\theta = 65^\circ/45'$ collimation, respectively (see Fig. 2b). In contrast to sample MIX no reference textures were available. In order to define a reference measurement in the best possible way, we checked R indices of the high-resolution RTA fits on various d ranges in order to find a reference (for details refer to §4.3). Subsequently, the reference textures were compared with the other texture estimates.

RTA was performed using the MAUD software (Lutterotti *et al.*, 1997; Wenk *et al.*, 2010). Initially, the significant instrument parameters – total flight path, accuracy of the collimator alignment, detector efficiency and instrumental peak shape – were calibrated using precipitated calcite as a standard. The lattice parameters were proven independently by means of Rietveld refinement on X-ray diffraction data. A vanadium sample was used to determine the energy distribution (Fig. 1), which is used to normalize the diffraction spectra prior to RTA. For the texture evaluation the EWIMV algorithm was applied (Wenk *et al.*, 2003). EWIMV is able to handle irregular pole figure grids and, for this reason, was the method of choice for our investigations. The resolution in Euler space was selected close to the angular resolution of the SKAT, and always below or equal to 15°. This ensured an orientation distribution function (ODF) coverage of 100%; however, one should be aware that in the case of extremely thinned measuring grids the number of ODF hits may differ greatly (Wenk *et al.*, 2010). For texture evaluation, useful parameters to be refined in the Rietveld step of RTA were the crystal lattice parameters, the peak shape by means of the microstructural parameters microstrain and crystallite size, the phase fractions, and the temperature coefficient B [for details on particular parameters refer to the paper by Wenk *et al.* (2010)]. The latter is considered to be isotropic and equal for all atoms of all phases. As normalized spectra are used for RTA, the background trend (individually adapted to each spectrum) could be described sufficiently well by a second-order polynomial.

Textures are mostly interpreted on the basis of pole figures. Consequently, the quantitative description of texture differences is based on pole figure differences ('difference pole figures')

$$\Delta P_{hkl}(\alpha, \beta) = P_{hkl}^{\text{ref}}(\alpha, \beta) - P_{hkl}(\alpha, \beta) \quad (5)$$

(α, β are the inclination, azimuth of sample directions) and mean RPI values (%)

Table 2

RP1_{mean} values (%) of sample MIX, based on the pole figures in Fig. 5(a).

Values in parentheses indicate the RP1 range; $\bar{\varnothing}$ is the average RP1_{mean} of all phases. (a) Obtained from RTA applying various d ranges. (b) Results of grid thinning, related to sampling increment ΔZ and bulk number of sample directions (n).

(a)						
d range (Å)	Quartz	Calcite	Dolomite	Forsterite	$\bar{\varnothing}$	
1.0–4.3	8.5 (6.3–11.7)	5.2 (4.2–6.4)	4.3 (2.4–7.2)	5.5 (2.2–10.1)	5.9	
1.0–2.3	25.9 (13.9–54.2)	9.8 (6.8–14.7)	15.9 (7.1–29.5)	16.7 (12.5–20.5)	17.1	
1.7–3.0	17.6 (7.2–45.8)	8.3 (4.6–11.7)	4.9 (3.3–7.7)	5.9 (4.3–9.1)	9.2	
2.2–4.3	9.1 (6.6–14.2)	5.4 (3.2–7.3)	5.7 (3.6–8.5)	6.8 (4.2–11.4)	6.8	
(b)						
ΔZ	n	Quartz	Calcite	Dolomite	Forsterite	$\bar{\varnothing}$
10°	684	16.5 (10.5–33.4)	9.5 (5.0–13.1)	5.0 (3.3–7.8)	5.4 (4.0–7.5)	9.1
20°	342	20.4 (13.0–38.5)	10.3 (6.3–15)	6.1 (4.4–10.3)	6.9 (5.8–8.8)	10.9
30°	228	29.7 (20.7–49.4)	10.3 (7.1–13.5)	6.0 (4.5–8.5)	8.7 (6.7–10.3)	13.7
45°	152	29.0 (19.9–47.0)	10.6 (6.9–16.4)	6.5 (4.8–9.4)	8.9 (5.8–10.9)	13.8
Hexagonal	301	24.4 (20.6–28.2)	8.4 (5.5–12.5)	6.2 (4.4–9.7)	11.8 (11.7–12.0)	12.7

$$RP1_{\text{mean}} = \sum_{i=1}^I RP1_i / I \quad (6)$$

(I is the number of pole figures considered). RP1 values are derived from relative deviations $r_{hkl}(\alpha, \beta)$ of the pole figures to be compared:

$$r_{hkl}(\alpha, \beta) = |P_{hkl}^{\text{ref}}(\alpha, \beta) - P_{hkl}(\alpha, \beta)| / P_{hkl}(\alpha, \beta), \quad (7)$$

$$RP1 = \theta(x)r_{hkl}(\alpha, \beta), \quad (8)$$

where $\theta(x)$ represents a selecting function,

$$\theta(x) = \begin{cases} 0 & \text{for } x \leq 1 \\ 1 & \text{for } x > 1 \end{cases} \quad (9)$$

(1 is the random pole density). For the definition of RP values in general refer to the paper by Matthies *et al.* (1988). The unique estimation of RP1_{mean} should consider all recalculated pole figures of a mineral phase. In practice, only a few pole figures that are important for the interpretation of the texture were used (refer to the description of the results). Indirect information on the reliability of RTA comes from variations of the texture indices obtained from different RTA runs, and from parameters related to the Rietveld refinement step in MAUD, as there are fluctuations of lattice parameters and volume fractions in the polymineralic rock samples.

4. Results

4.1. MIX sample

All reference textures derived from the individual measurements show clearly preferred orientations of the lattice directions used for the computation of difference pole figures (Fig. 5a). The weakest textures are evident for calcite and dolomite, as indicated by texture indices f^2 (Matthies *et al.*, 1988) of 2.21 and 1.67, respectively, and pole density maxima mostly less than 2.0 multiples of random distribution (m.r.d.). Rather strong textures are shown by quartz ($f^2 =$

12.23) with pole density maxima always exceeding 3.0 m.r.d. and forsterite ($f^2 = 3.01$) with pole density maxima always greater than 2.0 m.r.d.

Judging RP1_{mean} values obtained from RTA on various d ranges, the best results are achieved using the whole d range (1.0–4.3 Å), yielding magnitudes of 4.3–8.5% and an average $\bar{\varnothing}$ of 5.9% (see Table 2a). For several Bragg reflections, the intermediate section (1.7–3.0 Å) leads to lower RP1 values compared with the whole d range [Qz (110), Do (110), Fo (002), Fo (010)]. However, this never holds true for RP1_{mean}, which is always minimal for RTA considering the whole d range. Nonetheless, RTA using the intermediate section also yields good results, with RP1_{mean} ranging from 4.9 to 17.6% and $\bar{\varnothing} = 9.2\%$. Considering the d range from 2.2 to 4.3 Å produces RP1_{mean} values ranging from 5.4 to

9.1% and an average $\bar{\varnothing}$ of 6.8%. This is close to the magnitudes obtained when using the whole d range (see Table 2a). Generally, the largest discrepancies with the reference textures are obtained for the range 1.0–2.3 Å, yielding RP1_{mean} values of 9.8–25.9% and $\bar{\varnothing} = 17.1\%$.

As the large number of pole figures and difference pole figures prevents easy visualization of all results, Qz (110) was chosen for illustration. The principal characteristics of particular difference pole figures are representative for most other Bragg reflections; exceptions will be noted. Moreover, the Qz (110) pole density distribution has several maxima and, therefore, displays textural changes more clearly than pole density distributions with only a single maximum. Mostly, the reference pole figure generated from RTA of the individual sample (Fig. 5a) bears a strong resemblance to the pole figures and difference pole figures generated from RTA of the MIX sample (Fig. 5b). Positive deviations in the difference pole figures usually yield intensities greater than 1.0 m.r.d., *i.e.* the degree of preferred orientation obtained from the MIX sample is smaller than the reference. Exceptions are Fo (002) and Fo (200), where the relationship is *vice versa* (see Discussion). The positive variations in the difference pole figures are always found at the location of the maxima of the pole figures, whereas the smaller negative variations are also found at locations varying from the maxima, *e.g.* close to the center of the pole figure (Fig. 5b). The difference pole figures reflect the RP1_{mean} magnitudes and exhibit fairly low differences of the textures gained at intermediate and high d spacings, as well as RTA using the whole d range. In contrast, usage of only small d spacings produces the largest differences, usually in the positive range (Fig. 5b).

Grid thinning by increasing the sampling increment ΔZ generally creates higher RP1_{mean} values (Table 2b). The best results are achieved for a starting grid with $\Delta Z = 5^\circ$, corresponding to 1368 sample directions (RP1_{mean} = 4.3–8.5%, $\bar{\varnothing} = 5.9\%$; Table 2a), while the highest values are yielded for $\Delta Z = 45^\circ$ (RP1_{mean} = 6.5–29.0%, $\bar{\varnothing} = 13.8\%$). The only exception is

quartz, where 30° increments cause the highest magnitudes of $RP1_{\text{mean}}$. Remarkably, the wide range of $RP1$ values for quartz

are caused by the (003) lattice plane, which always produces the maxima of $RP1$. $RP1_{\text{mean}}$ values for a comparable hexagonal grid comprising 301 sample directions show magnitudes similar to the one obtained for 20 and 30° sampling increments, for which 342 and 228 grid points, respectively, were used for the calculation.

All pole figures up to a sampling increment of $\Delta Z = 20^\circ$ display a fairly strong visual similarity to the reference pole figures, but the pole density maximum is slightly weaker. Correspondingly, the maxima in the difference pole figures agree with the maxima in the pole figures (Fig. 5c). There is also a visual similarity for sampling increments greater than 20°, but the pole density maxima are much weaker and, consequently, the maxima in the difference pole figures are higher. This holds true for the quartz reflections (Fig. 5c) and Fo (040) and Fo (200) only, while all other reflections do not show a clear trend. Do (012) and Do (104) show progressively higher maxima when using a more thinned-out grid, *i.e.* the trend is inverted, as well as the pole density distributions in the difference pole figures. Furthermore, with increasing sampling increments, the maxima always broaden and become less precise (Fig. 5c).

4.2. Marble sample RK17

The results obtained from sample MIX indicated that a rather small number of diffraction spectra should be sufficient for a reliable texture evaluation of monomineralic samples. Thus, the marble sample was initially measured with 15° increments in the outer part of the pole figure and 30° increments in the center (in the following abbreviated as 15°/30°). This full grid results in 468 spectra employed for the RTA, and this particular texture was used as baseline for the grid thinning. Just as for sample MIX, $RP1_{\text{mean}}$ calculation of calcite is based on reflections (006), (012), (104) and (110). The reference texture is weak ($f^2 = 1.23$) and the type of texture is the same as for sample MIX (refer to Fig. 5a) and, therefore, not shown here.

As expected, $RP1_{\text{mean}}$ increases with increasing sampling increment ΔZ and, correspondingly, fewer spectra (Table 3). Applying $\Delta Z = 30^\circ/60^\circ$ (234 spectra) and $\Delta Z = 45^\circ/90^\circ$ (156 spectra) yields very low $RP1_{\text{mean}}$ values of 2.2 and 3.5%, respectively. Further reduction using $\Delta Z = 60^\circ/120^\circ$ (117 spectra) provides $RP1_{\text{mean}} = 4.6\%$, and for $\Delta Z = 90^\circ/180^\circ$ (78 spectra) a rather low $RP1_{\text{mean}}$ of 7.0% is achieved (Table 3).

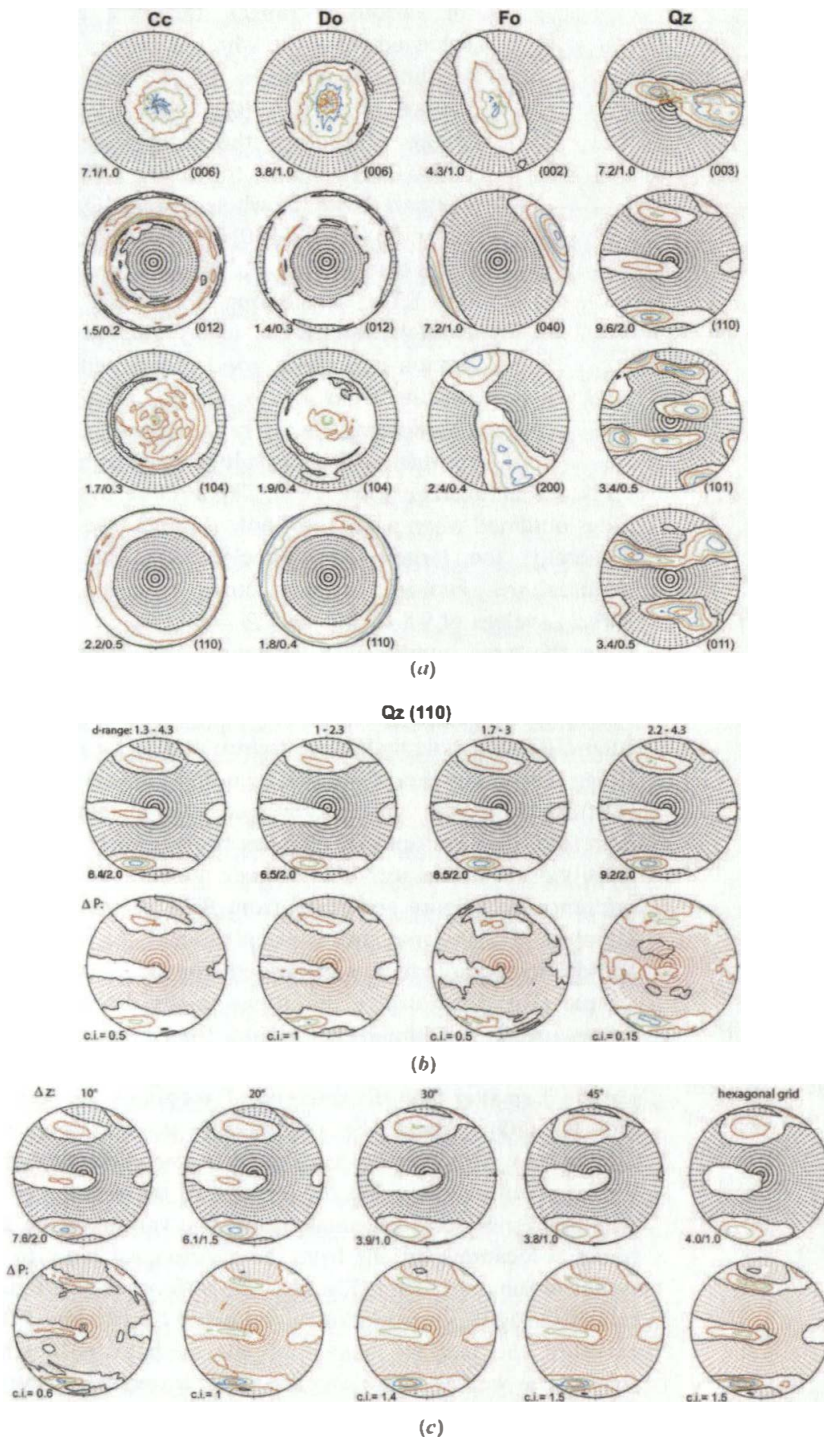


Figure 5 (a) Recalculated pole figures of the artificial sample (MIX) representing the reference textures of calcite (Cc), dolomite (Do), forsterite (Fo) and quartz (Qz). The maximum pole density and/or the contour interval are given at the bottom left of the pole figures; grid points indicate intensities <1.0 m.r.d. (b) Recalculated and difference pole figures of quartz (110) applying different d ranges; c.i. indicates contour intervals. In the difference pole figures (ΔP), grid points indicate intensities <0.0 m.r.d. (c) Recalculated and difference pole figures (ΔP) of quartz (110) resulting from grid thinning tests. Always, intensities are multiples of a random distribution (m.r.d.) and the pole figures are given for a regular $5 \times 5^\circ$ grid.

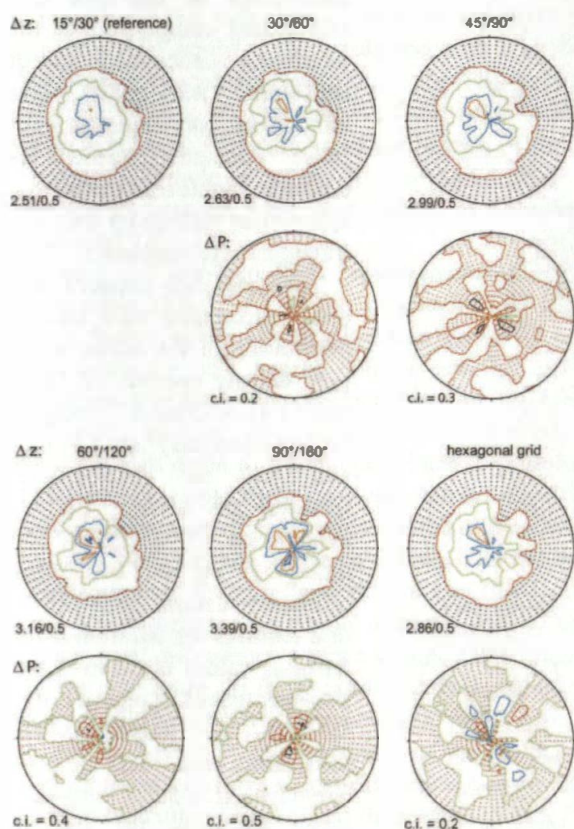
Table 3

Texture strengths f^2 and $RP1_{\text{mean}}$ values (%) of the calcite marble sample (RK17) for various grids.

Values in parentheses indicate $RP1$ ranges. The grid thinning is described by the sampling increment ΔZ in the outer/inner part of the pole figure and the bulk number of sample directions (n).

ΔZ (°)	n	f^2	$RP1_{\text{mean}}$
15/30	468	1.23	
30/60	234	1.25	2.2 (1.5–4.3)
45/90	156	1.35	3.5 (2.2–6.3)
60/120	117	1.44	4.6 (2.4–8.4)
90/180	78	1.55	7.0 (4.5–11.8)
Hexagonal	127	1.31	4.5 (3.0–6.5)

Calcite (003) was chosen to illustrate the effects of grid thinning. The reference pole figure of Cc (003), for which 15°/30° sampling increments were used, shows a single pole density maximum of 2.5 m.r.d. slightly to the left of the center (Fig. 6). The maximum pole density increases using a progressively thinned-out grid. This is the case for reduced sample increments, as well as for reduced hexagonally arranged grid points. It also holds true for all other relevant pole figures of the sample. The pole figures calculated for a

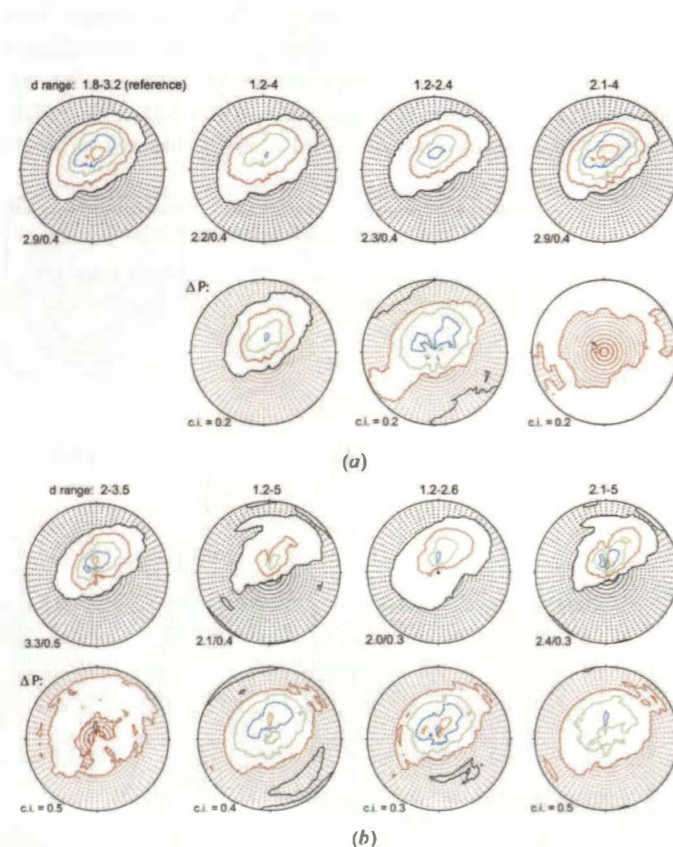
**Figure 6**

Calcite marble sample: recalculated and difference pole figures (ΔP) of calcite (006) for successively thinned-out measuring grids. The sampling increment in the outer/inner section of the starting (= reference) grid was $\Delta Z = 15^\circ/30^\circ$. The maximum pole density and/or the contour interval are given at the bottom left of the pole figures; c.i. indicates the contour interval, and grid points in the recalculated and difference pole figures indicate intensities <1.0 and <0.0 , respectively.

thinned grid using 30°/60° and 45°/90° sampling increments exhibit a strong visual similarity to the reference with the same location of the pole density maximum. For the grid with 60°/120° sampling increments, the calculated pole figure displays a second maximum to the lower left of center. A third maximum to the upper right of the center is produced using the 90°/180° grid. For the hexagonally thinned-out grid, the pole figure is visually similar to the reference (Fig. 6).

Difference pole figures exhibit larger positive as well as negative ranges for progressively larger sample increments. For sampling increments of 90°/180° and 60°/120°, the negative ranges are larger than the positive. This is also the case for other pole figures, with the exception of (104), where negative and positive ranges are of similar magnitude in all difference pole figures.

The hexagonal grid comprises 127 spectra and is close to the number of sample directions resulting from 45°/90° and 60°/120° sampling increments (156 and 117, respectively; Table 3). It yields an $RP1_{\text{mean}}$ value of 4.5% (Table 3). The pole figure exhibits a visual similarity to the reference, but the maximum is likewise higher for the reference (Fig. 6). Furthermore, equally larger negative and positive ranges occur in the difference pole figure.

**Figure 7**

Omphacite (003) pole figures and respective difference pole figures (ΔP) of the eclogite sample. Results obtained from different d ranges at high (RK20 HR) and low (RK20 LR) resolution were compared. The maximum pole density and/or the contour interval are given at the bottom left of the pole figures; c.i. indicates contour interval, and grid points in the recalculated and difference pole figures indicate intensities <1.0 and <0.0 , respectively.

Table 4

RPI_{mean} values (%) of the main constituents of the eclogite sample (RK20).

Values in parentheses indicate the RPI range. \emptyset is the average of all phases. HR and LR indicate the high- and low-resolution measurements, respectively.

<i>d</i> range (Å)	Omphacite	Glaucophane	Quartz	\emptyset
HR				
1.2–4.0	7.8 (5.5–11.5)	2.3 (1.1–4.3)	10.3 (3.3–15.4)	6.8
1.2–2.4	10.0 (5.4–14.6)	6.5 (2.4–10.2)	5.1 (3.4–9.0)	7.2
2.1–4.0	5.5 (4.4–8.5)	3.7 (2.0–5.3)	8.5 (6.2–12.5)	5.9
LR				
1.2–5.0	19.9 (12.0–26.4)	9.1 (7.7–11.9)	14.0 (5.3–20.9)	14.3
1.2–2.6	14.9 (9.8–24.7)	15.1 (6.6–22.5)	6.4 (4.8–9.7)	12.1
2.0–3.5	10.8 (5.8–15.9)	7.8 (5.5–9.8)	16.7 (7.7–29.5)	11.8
2.1–5.0	20.8 (16.8–23.2)	8.9 (8.4–9.6)	12.7 (6.1–17.1)	14.1

4.3. Eclogite sample RK20

As has been mentioned above, identification of the reference textures for comparison of the high- and low-resolution measurements of the eclogite sample (RK20) is largely based on judgment of the residuals of RTA. In the following R_{wp} values are used because of their independence of scattered intensity (e.g. Von Dreele, 1997). The much better peak separation of the high-resolution measurement must lead to better results (see Fig. 4*b*); hence, we compared R_{wp} values of RTA fits on various *d* ranges of the high-resolution measurement in order to identify the reference. The intermediate *d* range (1.8–3.2 Å) yielded the best results ($R_{\text{wp}} = 20.9\%$), whereas the other fits delivered somewhat higher residuals (1.2–4.0 Å: $R_{\text{wp}} = 24.2\%$; 2.1–4.0 Å: $R_{\text{wp}} = 27.3\%$).

Use of the *d* range between 1.2 and 2.4 Å yielded an $R_{\text{wp}} = 14.9\%$, but because of many overlaps the texture calculations are not considered very reliable (see later discussion). As other independent criteria are missing, the intermediate *d* range is taken to provide the reference textures. However, it has to be emphasized that the reference textures do not necessarily correspond to the true textures. For subsequent comparison of the textures, omphacite, glaucophane and quartz were considered (with quartz representing a minor rock constituent of approximately 10%). Almandine, which has random crystallographic orientation in the ample, and phases making up only small volume fractions were neglected.

The reference textures of omphacite and glaucophane show clearly preferred orientation of the lattice directions, with pole density maxima of 1.62–2.76 m.r.d. and 1.41–3.75 m.r.d., respectively. The texture strengths f^2 are 1.57 for omphacite and 1.70 for glaucophane. Weaker textures are evident for quartz with maxima of 1.17–1.41 m.r.d. and texture indices f^2 up to 1.07. Comparing the reference textures to other high-resolution textures for different *d* ranges yields RPI_{mean} values between 2.3 and 10.3%. The averages of all phases are in the range 5.9–7.2% (see Table 4). There is no consistency concerning the best value. For omphacite it is 5.5% derived from the *d* range 2.1–4.0 Å, for glaucophane the minimum of 2.3% refers to the whole spectrum (1.2–4.0 Å), while quartz shows 5.1% for the *d* range 1.2–2.4 Å (Table 4). With regard to low-resolution textures, the general range of RPI_{mean} is 6.4–20.8%. The averages of the phases have a range 11.8–14.3%. This is approximately

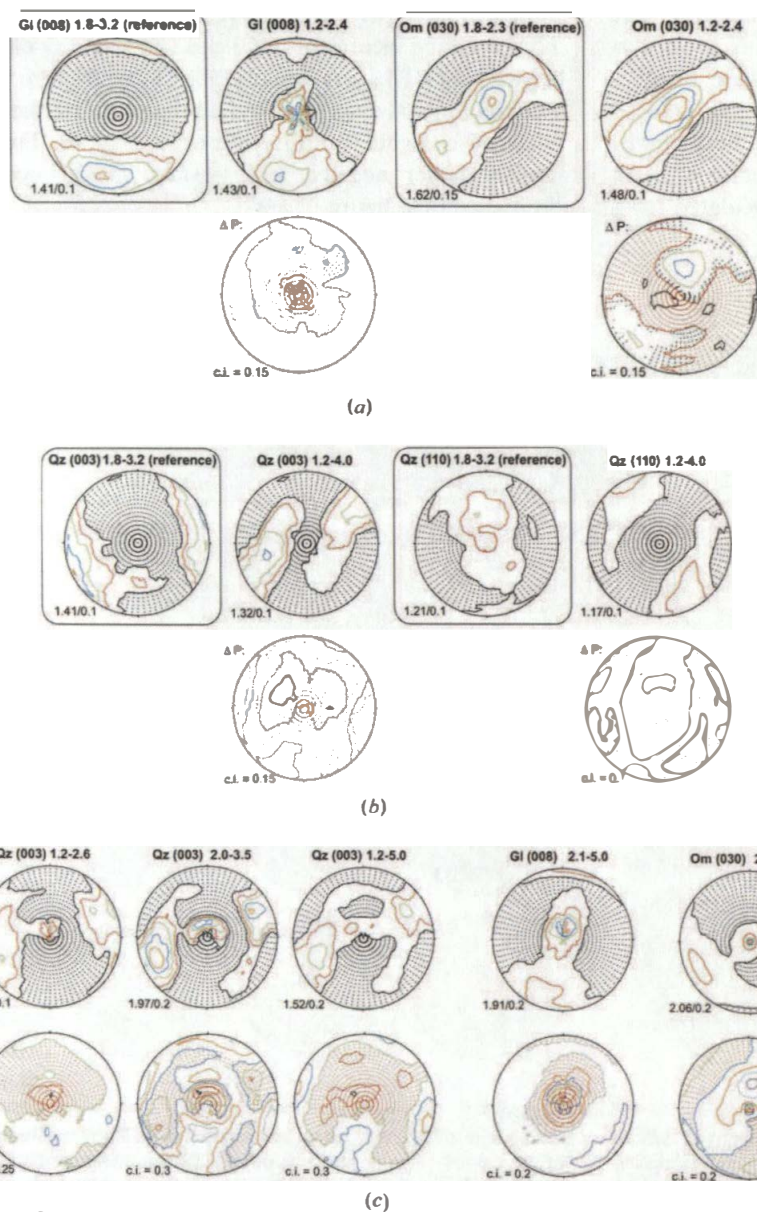


Figure 8

Examples for pole figures showing inconsistent pole density distributions. (a) Gl (008) and Om (030) from the eclogite high-resolution experiment. (b) Qz (003) from the eclogite high resolution experiment. (c) Qz (003), Gl (008) and Om (030) from the eclogite low resolution experiment.

twice the value of the high-resolution measurements. The lowest RPI_{mean} values are mostly seen when considering the intermediate d range (omphacite: 10.8%; glaucophane: 7.8%), except for quartz with an RPI_{mean} value of 6.4% for the d range 1.2–2.6 Å (Table 4).

The omphacite (003) pole figure with a clear maximum close to the center is appropriate to illustrate that the maximum pole density in the difference pole figures of high-resolution measurements frequently coincides with the maximum pole density in the reference pole figure, whose pole density is generally higher (Fig. 7). The smallest deviations from the reference are obtained for the d range 2.1–4.0 Å, which also finds its expression in the difference pole figure (Fig. 7). For other d ranges, deviations are up to 0.6 m.r.d. from the reference. This similarity holds true for most other pole figures of omphacite and glaucophane, with the exception of Gl (008), which sometimes develops a second maximum in the center of the pole figure, and Om (030), which exhibits a secondary maximum in the reference. The latter is missing in the pole figures recalculated from the whole d range and high d range RTA runs (Fig. 8a).

At high resolution, quartz (011) and (101) textures reveal strong visual similarities for all d ranges. In contrast, the Qz (003) reference pole figure displays the maximum pole density at the margin of the pole figure, whereas the maximum resulting from RTA applying the whole spectrum (1.2–4.0 Å) is shifted towards the center. Accordingly, Qz (110) displays a single maximum close to the center of the reference pole figure and, in contrast, a maximum at the margin of the pole figure when the whole d range is considered (Fig. 8b). However, the textures are weak, as indicated by pole density maxima around 1.2 m.r.d.

Concerning the low-resolution measurements, the intermediate d range (2.0–3.5 Å) of the omphacite and glaucophane pole figures exhibits a strong visual similarity to the respective reference pole figures. This is not the case for quartz. The example difference pole figure of Om (003) shown in Fig. 7 yields positive deviations up to 0.52 m.r.d. and negative deviations down to -0.86 m.r.d. Such deviations are typical for the other pole figures as well. All the other RTA runs show obvious visual discrepancies and the difference pole figures usually yield higher positive deviations. This holds true for all other relevant Bragg reflections. For Om (030) and Gl (008), the pole figures for particular d ranges display extremely strong visual discrepancies with a strong maximum in the center of the pole figure. Qz (003) exhibits discrepancies to the reference for all d ranges at low resolution. In all cases, the maxima are no longer at the periphery of the pole figure. However, the quartz textures in low-resolution measurements are similar to each other (Fig. 8c) and the texture indices f^2 are generally higher than the reference (f^2 up to 1.33).

5. Discussion

For the evaluation of textural differences it has to be kept in mind that several sources contribute to RPI magnitudes. These are differences in texture strength, orientation differ-

ences and superimposed noise. Hence, the global parameter RPI carries only limited information on texture differences, except when it is very small. Difference pole figures are capable of providing more detailed information on texture variations: if the contour pattern of the difference pole figure resembles the pole figure patterns to be compared, RPI magnitudes are largely due to differences in texture strength. If not, orientation differences contribute to particular magnitudes. The discussion now focuses mainly on these reflections, but, as stated above, parameters like f^2 magnitudes, estimated volume fractions and fluctuations of the lattice parameters bear information on the reliability of RTA as well and will also be considered in the following.

This paper does not include a general discussion of counting statistics, which applies to any diffraction experiment. As the use of neutrons is very expensive, the exposure time is usually selected to be close to the minimum required to obtain sufficient counting statistics. The individual spectra of two of our samples given in Fig. 9 illustrate the level of noise, which according to our experience is acceptable for the purpose of texture analysis at the SKAT. However, in a strict sense, the transfer of our results to other TOF neutron instruments implies a comparable level of noise for particular measurements. The comparison of texture measurements on a gneiss rock sample at the SKAT and HIPPO reveals that, despite significantly worse R_{wp} indices of the RTA fit performed on the SKAT data, the textures are very similar (Wenk *et al.*, 2012). We, therefore, suppose that variation in counting statistics has only a slight effect on the estimated textures.

5.1. RTA using various d ranges

For sample MIX, only minor variations of texture strength f^2 are observed, except for the d range 1.0–2.3 Å, which

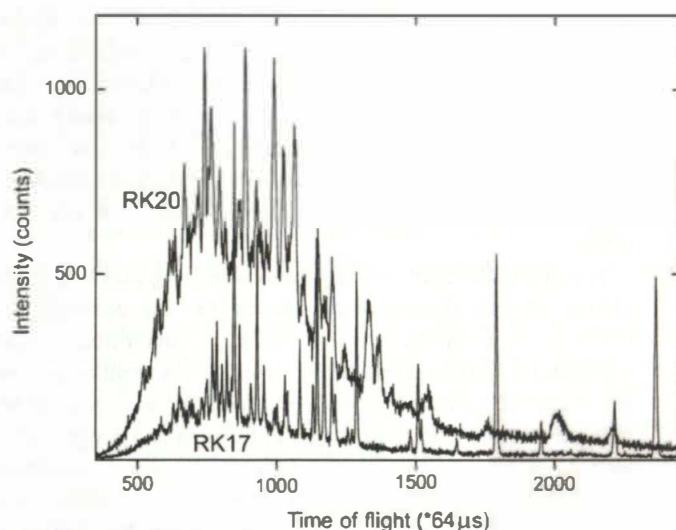


Figure 9 Individual diffraction patterns of the monomineralic marble (RK17) and the polymineralic eclogite (RK20), illustrating the noisy patterns and the high background level of the eclogite. The exposure time was 30 min. Because of the different diffraction angles, the intensity is given as a function of time of flight instead of d spacing.

Table 5

Variation of texture strength f^2 and volume fractions of sample MIX as a function of the applied d range and grid step size ΔZ .

Fo: forsterite; Qz: quartz; Cc: calcite; Do: dolomite. n is the bulk number of sample directions.

	f^2	Vol. %			
		Fo	Qz	Cc	Do
Reference	3.01	12.23	2.21	1.67	
d range (Å)					
1.0–4.3	2.76	7.66	1.88	1.51	25.8 32.1 27.8 14.4
1.0–2.3	1.82	4.59	1.13	1.60	23.6 31.0 28.2 17.2
1.7–3.0	3.26	9.06	2.08	1.60	26.6 34.8 24.8 13.9
2.2–4.3	3.45	9.55	2.46	1.80	29.7 31.2 26.5 12.6
ΔZ	n				
10°	684	3.08	9.12	2.01	1.49 26.8 34.2 25.1 14.0
20°	342	3.02	8.11	1.89	1.47 27.1 34.0 24.8 14.1
30	228	3.36	5.74	1.91	1.45 26.8 31.3 27.2 14.6
45	152	3.24	5.38	2.04	1.49 27.5 30.6 27.2 14.7
Hexagonal	301	2.53	5.34	1.80	1.37 27.2 28.2 30.1 14.4

generally indicates much weaker magnitudes of f^2 (Table 5). The only exception is dolomite, showing arbitrary scattering of f^2 . This is probably due to the rather low volume fraction of dolomite (12.6–17.2%; Table 5). It appears that the large number of peak overlaps (the d range 1.0–2.3 Å contains 312 Bragg reflections), or in other words the absence of isolated peaks, reduces texture strength. Texture factors derived from overlapping peaks are generally not unique (Matthies *et al.*, 1997). However, texture strength does not necessarily diminish as a consequence of peak overlaps. Variance tests confirm that the applied Rietveld algorithm does not constrain the texture factors of overlapping peaks (Matthies *et al.*, 1997). Consequently, there is no implied explanation for the observed consistent reduction of texture strength. The variation in volume fractions of the different phases obtained from various RTA runs is 3.4–6.1%. Variations are arbitrary (Table 5) and, therefore, do not allow any correlation. The lattice parameters exhibit a maximum deviation of 0.026 Å from the reference. Such a small deviation should not be interpreted in terms of strain because of the low counting statistics of the texture experiment (see discussion below), but indicates that the Rietveld refinement did not get out of control.

Judging difference pole figures, coinciding maxima apply to almost all pole figures of all phases [see the example of Qz (110) in Fig. 5(b)], so that RPI_{mean} magnitudes mainly represent differences in texture strength. As mentioned above, the smallest deviations from the reference occurred when using the intermediate and high lattice spacing ranges (1.7–3.0 and 2.2–4.3 Å), whereas the d range 1.0–2.3 Å consistently leads to higher RPI_{mean} values. The only exceptions to this observation are Cc (012) and Cc (104), where the intermediate d range exhibits slightly higher values than the small d spacing range. The increase of RPI_{mean} corresponds to decreases of the texture strength f^2 . The d range 1.0–4.3 Å includes 344 Bragg reflections in total with an average RPI_{mean} of 5.9%, whereas the range 1.0–2.3 Å includes 312 reflections with an

Table 6

Variation of texture strength f^2 (Om, Gl, Qz) and volume fractions of all constituents of the eclogite sample (RK20) as a function of the applied d range.

HR and LR indicate the high- and low-resolution measurements, respectively. Om: omphacite; Gl: glaucophane; Qz: quartz; Gt: garnet; Rut: rutile; Mus: muscovite; Alb: albite.

d range (Å)	f^2			Vol. %						
	Om	Gl	Qz	Om	Gl	Qz	Gt	Rut	Mus	Alb
HR										
1.2–4.0	1.37	1.65	1.07	42.3	19.7	7.2	24.1	1.1	2.4	3.1
1.2–2.4	1.26	1.44	1.02	43.7	20.2	6.5	26.8	0.9	0.6	1.4
1.8–3.2	1.57	1.70	1.07	38.9	18.3	6.9	21.6	1.0	6.0	7.3
2.1–4.0	1.58	1.74	1.17	42.4	19.7	6.7	23.9	1.1	3.5	2.7
LR										
1.2–5.0	1.10	1.42	1.13	38.2	23.4	4.1	20.7	2.4	10.1	1.2
1.2–2.6	1.29	1.15	1.04	38.6	18.5	9.2	22.6	3.5	0.3	7.4
2.0–3.5	1.68	1.66	1.33	41.8	19.8	7.2	24.1	4.6	0.5	2.0
2.1–5.0	1.15	1.58	1.33	38.9	24.3	3.8	20.0	3.3	8.2	1.5

average RPI_{mean} of 17.1%. The overall number of reflections is comparable, but in the second case isolated reflections are almost completely absent (see Fig. 4a). Obviously, the lack of isolated reflections for the RTA has a significant influence on the results of RTA.

In summary, it appears that almost all examined d ranges of sample MIX are suitable to derive the textures of all constituents with sufficient accuracy. Care must be taken when the number of peak overlaps becomes very large and no, or only a few, isolated peaks are accessible. This is generally the case for the d range 1.0–2.3 Å. Despite higher diffracted intensities, *i.e.* better counting statistics (see Fig. 1), the large number of overlaps appears to be a limitation, as indicated by significantly worse RPI_{mean} magnitudes and diminishing texture strength. Weak textures might still be useful for geological interpretations, since maxima positions are usually interpreted in terms of strain geometry and deformation kinematics (*e.g.* Schmid & Casey, 1986; Law *et al.*, 1990; Trullenque *et al.*, 2006; Keller & Stipp, 2011). However, the prediction of anisotropic physical rock properties depends on such quantities and may be influenced in a negative way.

For the high-resolution RTA runs of the eclogite sample (RK20), the texture strength f^2 of the main rock constituents omphacite, glaucophane and quartz is minimal for the small lattice spacing range (1.2–2.4 Å). The texture strength shows the same relationship with the number of peak overlaps as sample MIX (Table 4). Such a consistency was not observed for the low-resolution runs, where the minimal texture strength of omphacite (the dominant rock constituent) belongs to the d range 1.2–5.0 Å ($f^2 = 1.10$, see Table 6). The scattering of estimated volume fractions seems acceptable for the main constituents; however, the minor rock constituents muscovite and albite show much larger variabilities. In particular, the muscovite volume fractions range from 0.3 to 10.1%, both extreme values in association with low-resolution RTA (see Table 6). The observations on texture strength and estimated volume fractions indirectly indicate that RTA on polymineralic materials has limitations, in particular, if the

resolution is low. In contrast, such an obvious conclusion cannot be drawn from the small variability of lattice parameters of the main rock constituents, which is $\leq 0.06 \text{ \AA}$ for the crystallographic axes and $\leq 0.36^\circ$ for the monoclinic angles of omphacite and glaucophane. The maximum variability is always associated with low-resolution RTA, supporting the notion that good spectral resolution is advantageous.

Hence, it is not surprising that pole figure differences for the eclogite sample (RK20) are considerably larger than for sample MIX. Regarding high-resolution RTA performed on various d ranges, the recalculated pole figures exhibit coinciding maxima in the majority of cases [see the example of Om (003) in Fig. 7]. In this case texture strength is always comparable to the reference, although generally a bit higher. However, there are some exceptions [see examples in Figs. 8(a) and 8(b)]. The causes of such differing pole figure maxima are not necessarily true texture differences. For example, the pole density maximum in the center of the Gl (008) difference pole figure (considered d range: 1.2–2.4 \AA) might be an artifact caused by the weighting scheme, which is applied to balance the large number of sample directions in this pole figure region (Fig. 8a). The differences found in the quartz pole figures are less well interpretable (Fig. 8b). Bearing in mind that the quartz texture is not very strong and the volume fraction is approximately 10%, this texture estimation may be erratic. The similarity of Qz (003) textures derived from the whole d range (1.2–5.0 \AA) RTA with Qz (003) pole figures recalculated from low-resolution data may indicate that the reference texture (high resolution, d range: 1.8–3.2 \AA) is not the true texture.

For the low-resolution measurement, the pole figure differences of omphacite and glaucophane become significant [see the examples in Fig 8(c)]. Several pole figures exhibit maxima that do not coincide with the reference, or exhibit additional maxima missing in the reference pole figure. Gl (008) and Om (030), which also showed larger differences in the high-resolution measurements, exhibit such maxima in the center of the pole figures; this holds true for all d ranges. As above, we have to state that such maxima may be artifacts. Qz (003) displays a visual similarity to the pole figure obtained from the whole d range RTA at high resolution, which in this case might in fact be the better texture estimate.

As expected, texture analysis of a seven-phase sample containing several phases with low crystal symmetries is not as consistent as in the case of sample MIX. Mostly, coinciding maxima, relatively low variations of f^2 values and similar lattice parameters for all d ranges, however, show that for the main constituents the results of texture analysis are reliable, if the measurement is made at high resolution. Many deviations in the texture analyses measured at low resolution, however, show that this setup is not suitable for a sample of such complexity.

5.2. The effect of grid thinning

The grid thinning tests are independent of counting statistics and the effect of overlapping peaks, because the d range

used for RTA is always the same. There are two possible reasons why the removal of sample directions goes along with smoother textures. Firstly, the resolution in orientation space has been reduced in order to approximate the angular resolution of the instrument. Secondly, texture maxima are not necessarily hit, or poorly characterized by the thinned grid. In particular, sharp textures can be falsified in the case of excessive grid thinning. In contrast to classical QTA, RTA uses a very large number of Bragg reflections for the texture computations. This significant increase of input information may be able to compensate the effects of incompletely described pole figures, as discussed in the following.

For sample MIX, the effect of grid thinning on the textures can be demonstrated best by means of the forsterite and quartz textures with rather different texture strength of the reference textures ($f^2 = 3.01$ and 12.23, respectively, Table 5). All the important pole figures of forsterite show broad maxima (Fig. 5a), and the effect of grid thinning on texture strength is minor (3.02–3.36, Table 5). In contrast, the quartz texture is more complicated, displaying several sharp maxima in the pole figures (Fig. 5a). The grid thinning leads to a consistent decrease of texture strength down to $f^2 = 5.38$ for $\Delta Z = 45^\circ$ (Table 5). The correlation of f^2 and ΔZ is obvious and reasonable. The variability of estimated volume fractions as a function of ΔZ is small (Table 5) and disparities of the lattice parameters are of the order of 10^{-3} \AA , indicating that the fit did not get out of control. The difference pole figures should deliver significant information to decide whether the texture estimates are similar or not. For all phases, sampling increments ΔZ up to 20° exhibit strong similarities to the reference textures, and only small deviations from the maximum intensities in the pole figures are apparent [see the example of Qz (110), Fig. 5(c)]. Exceptions are Do (012) and Do (104), where inconsistent scattering of the pole figure maxima as a function of ΔZ are observed. This probably results from the low volume fraction of dolomite. For sampling increments greater than 20° all phases show abrupt drops in the maximum pole density of most pole figures (Fig. 5c). Correspondingly, the maximum in the difference pole figure increases and the maxima of the pole density distributions appear to be significantly wider (Fig. 5c). These observations let us conclude that a sampling increment of $\Delta Z = 20^\circ$ appears to be a reasonable limit, which ensures reliable texture estimates for samples constituting a medium number of mineral phases.

The monomineralic calcite marble sample (RK17) produces low f^2 values and very small fluctuations of the lattice parameters with variations of ΔZ . In contrast to sample MIX, f^2 consistently increases with increasing sampling increment (Table 3). The same holds true for RP1_{mean} (Table 3) and the pole density maxima of the recalculated pole figures. Another important observation is some correlation between the sampling increment ΔZ and the symmetry of the pole density distributions in the difference pole figures (Fig. 6). This is illustrated best by means of the difference pole figure resulting from sampling increments $\Delta Z = 45^\circ/90^\circ$. An eightfold repetition of pole density maxima (Fig. 6) in agreement with the

accumulation of grid points at these positions (see Fig. 10) is observed at the periphery of the difference pole figure. In the center of the pole figure the symmetry appears to be fourfold. The same observation is made for sampling increments of $\Delta Z = 30^\circ/60^\circ$ and $\Delta Z = 60^\circ/120^\circ$, leading to a sixfold symmetry of the pole density distributions in the difference pole figures (best visible in the center of the $30^\circ/60^\circ$ difference pole figure in Fig. 6). Remarkably, such dependence on the grid point arrangement could not be observed in the case of the calcite reference texture of sample MIX (Fig. 5a), although the type of texture and its relation to the sample coordinate system are the same (the texture is axially symmetric with the symmetry axis at or close to the center of the pole figure). This means that the algorithm used for the texture evaluation can be sensitive to irregular grid arrangements. As other causes like anisotropy effects due to irregular sample shape can be excluded, the only reasonable source for the observed differences of the marble sample (RK17) and the artificial sample (MIX) appears to be the texture strength, leading to pole figure maxima of the order of two to three times random (RK17) and six to seven times random (MIX) for the calcite (006) pole figure. In the case of the weaker texture, the relative contribution of artifacts is larger and becomes obvious in the difference pole figures. Hence, grid effects on the texture cannot be definitely excluded, and the recommendation is to check the textures for such features in order to avoid misinterpretation. All the parameters and characteristics discussed above deliver no clear criteria to recommend an optimum grid for the marble sample (RK17). The only clues come from the visual inspection of the difference pole figures. The inference that the grid with increments of $\Delta Z = 45^\circ/90^\circ$ seems to be the optimum one is largely based on the observation that single

pole density maxima in several pole figures – in particular the (110) pole figure – split into submaxima for larger sampling increments.

Comparing the MIX textures obtained for the optimized grid with $\Delta Z = 20^\circ$ with the textures from the closest hexagonal grid (see Fig. 10 for illustration of the grids) leads to similar $RP1_{\text{mean}}$ values, the variability of a few percentage values appears to be acceptable (Table 2). Significant differences are due to the texture strength f^2 , which is always weaker for the hexagonal grid (Table 5). The drop is small for most textures; however, the comparatively strong quartz texture shows a decrease of f^2 from 8.11 down to 5.34, similar to those for sampling increments of $\Delta Z = 30$ and 45° . The texture weakening finds its expression in both the recalculated pole figures and difference pole figures. For the quartz (110) pole figure, which is given as an example in Fig. 5(c), the maximum pole density of 6.14 m.r.d. decreases down to 3.98 m.r.d. and corresponds to the maximum pole density observed for larger sampling increments. Concurrently, the difference from the reference pole figure is large. This large drop holds true for all quartz reflections, while for the other mineral phases it is less pronounced but visible in the pole figures and difference pole figures. At least, we attribute this observation to the fact that the quartz texture is more complicated than the textures of the other phases, leading to multiple sharp maxima in most pole figures (see Fig. 5a). The hexagonal grid with an approximately equal area distribution of sample directions is not able to describe the maxima arrangement and the outlines of the maxima in all detail. In contrast, the optimized grid with closely spaced grid points along the circles belonging to a single sample direction obviously delivers more detail about the shape of the maxima than the hexagonal grid does, despite the large sampling increment of $\Delta Z = 20^\circ$. The consequence is a more precise texture description; in other words, the smoothing effect of the hexagonal grid on the quartz texture is more pronounced. For the forsterite texture the effect is less pronounced because of the somewhat simpler texture, which is characterized by broad elongated maxima in the considered pole figures (see Fig. 5a). The related drop of texture strength f^2 is from 3.02 to 2.53 (Table 5).

The even simpler textures of calcite and dolomite, displaying almost perfect axial symmetry (see Fig. 5a), are least affected. In summary, it appears that the irregular, optimized grid contains more detailed information on the textures than the hexagonal grid does, and the textural discrepancies caused by these two types of grids largely depend on the complexity of the texture. Moreover, the irregular grid point arrangement of the optimized SKAT grid obviously produces no artifacts or falsification of the textures. The optimized grid of the calcite sample (RK17) contains 156 sample directions and the closest hexagonal grid 127 sample directions (see Fig. 10). The texture type is axially symmetric and corresponds to the textures of calcite and dolomite in sample MIX. Hence, we expect only minor differences between particular texture approximations, which, in fact, is the case. $RP1_{\text{mean}}$ values are similar and texture strengths f^2

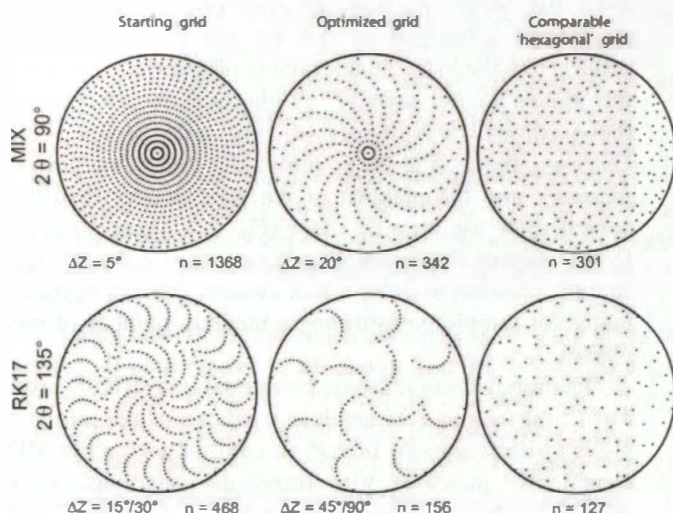


Figure 10

Representation of the grids used for grid thinning tests of sample (MIX) and the marble sample (RK17). Starting grid refers to the measurement grid and optimized grid to the grid causing only insignificant variation of the starting textures. The hexagonal grid comprises the starting grid sample directions, which are closest to a hexagonal grid with approximately the same number of sample directions as the optimized grid. n is the number of sample directions and ΔZ it the sampling increment.

are almost identical (Table 3). In the pole figures, the layout of the pole density distributions and the maximum pole densities are nearly the same. For the Cc (006) pole figure, given as an example in Fig. 6, the particular magnitudes are 2.99 and 2.86 m.r.d., respectively. These observations confirm the above finding that for simple axially symmetric textures no differences between the optimized and hexagonal grids are valid, and that the irregular arrangement of sample directions has no negative effects.

6. Summary and conclusions

The upgraded SKAT with three interchangeable detector arrangements offers the possibility of adapting the resolution and accessible d range to the sample state. Owing to a large beam cross section of 50×95 mm, the analysis of sample volumes of up to 65 cm^3 is possible.

Investigation of the potentially limiting factors of RTA, such as the resolution $\Delta d/d$, the dependence of the variable counting statistics on d and the number of peak overlaps, indicates that the texture estimates of a four-phase compound (sample MIX) are largely independent of the d range applied for RTA. The outlines of the textures can be reproduced very well, but using only reflections with small d spacings, thereby accepting many peak overlaps, reduces texture strength significantly. This holds true despite better counting statistics at small d spacings. We correlate the smoothing effect with the large number of peak overlaps, *i.e.* improving the resolution delivers better results.

RTA of the eclogite sample (RK20) comprising several low-symmetry phases yielded more complications. The coincidence described above of the texture maxima when using different d ranges is valid for many pole figures, but orientation differences frequently occur as well. This holds true in particular for low-resolution measurements. In polyphase geological samples, when phases constitute a volume fraction greater than 10% and the texture strength f^2 is greater than 1.5, orientation differences are missing and textural differences are due to texture strength only. The correlation between the number of peak overlaps and decreasing texture strength applies in the same way as for the low d spacing range of sample MIX, but for RTA of the eclogite sample (RK20) with seven mineral phases high resolution is indispensable. It is important to recall that no true reference textures were available for this sample; the comparison with the textures derived from the intermediate d range of the high-resolution measurement indicates only the range of possible solutions. Consequently, we must be aware that the textural results we get from such complex samples are approximations of the true textures. The missing orientation differences of sufficiently strong textures from mineral phases comprising large volume fractions let us predict that these textures better resemble the true textures.

The experimental effort to obtain reliable results by means of RTA, especially exposure time, can be reduced, depending on the complexity of the diffraction patterns. A monomineralic sample of medium to low symmetry requires no

more than 150 sample directions. The irregular grid point arrangement of the minimized SKAT grid leads to a more detailed texture description than the comparable hexagonal grid does, when the texture is sharp and pronounced. Hence, the irregular grid arrangement of the SKAT is not a disadvantage but can be advantageous for this texture type. More complex samples bearing few phases require approximately 350 sample directions. As the results were obtained from diffraction spectra with rather low counting statistics, we conclude that the numbers given above are upper limits and can be smaller, if counting statistics are significantly improved.

The general conclusion is that TOF neutron diffraction in combination with full pattern fit methods can be used to evaluate the textures of the rock constituents with good reliability even in polymineralic materials. The complexity of the diffraction patterns is the limiting factor, *i.e.* high resolution is essential, provided that a minimum of statistical significance is achieved. It was demonstrated that access to many Bragg reflections compensates the need for measuring a large number of sample directions and, therefore, far reaching reduction of exposure time is possible. Although the direct transfer to other TOF instruments is not possible, our results can be helpful to define the experimental conditions in relation to the complexity of the material to be investigated. The concept of creating an artificial sample from individual measurements is useful to find out the specific limitations of, in principle, any diffraction instrument delivering diffraction patterns suitable for RTA.

We are thankful for constructive comments from the two reviewers and their help improving the manuscript. Funding by the German Federal Ministry of Education and Research (BMBF) through grants 05K09FKA and 05K13FKB is gratefully acknowledged. We are also grateful to the Frank Laboratory of Neutron Physics (FLNP) in Dubna (Russia) for support in the texture measurements.

References

- Brokmeier, H.-G. (1994). *Textures of Geological Materials*, edited by H. J. Bunge, S. Siegesmund, W. Skrotzki & K. Weber, pp. 327–344. Oberursel: DGM Informationsgesellschaft-Verlag.
- Conrad, H., Brückel, T., Schäfer, W. & Voigt, J. (2008). *J. Appl. Cryst.* **41**, 836–845.
- Dahms, M. & Bunge, H. J. (1989). *J. Appl. Cryst.* **22**, 439–447.
- Hannon, A. C. (2005). *Nucl. Instrum. Methods Phys. Res. Sect. A*, **551**, 88–107.
- Hielscher, R. & Schaeben, H. (2008). *J. Appl. Cryst.* **41**, 1024–1037.
- Keller, L. M. & Stipp, M. (2011). *J. Struct. Geol.* **33**, 1491–1500.
- Kern, H., Ivankina, T. I., Nikitin, A. N., Lokajiček, T. & Pros, Z. (2008). *Tectonophysics*, **457**, 143–149.
- Law, R. D., Schmid, S. M. & Wheeler, J. (1990). *J. Struct. Geol.* **12**, 29–45.
- Leiss, B., Gröger, H. R., Ullemeyer, K. & Lebit, H. (2002). *Deformation Mechanisms, Rheology and Tectonics: Current Status and Future Perspectives*, Geological Society, London, Special Publications, Vol. 200, edited by S. De Meer, M. R. Drury, J. H.

- P. De Bresser & G. M. Pennock, pp. 219–238. London: Geological Society.
- Lutterotti, L., Matthies, S., Wenk, H.-R., Schultz, A. S. & Richardson, J. W. (1997). *J. Appl. Phys.* **81**, 594.
- Manoshin, S. A., Belushkin, A. V., Kulikov, S. A., Shabalin, E. P., Walther, K., Scheffzueck, C. & Zhuravlev, V. V. (2009). *Nucl. Instrum. Methods Phys. Res. Sect. A*, **608**, 447–453.
- Matthies, S., Lutterotti, L. & Wenk, H. R. (1997). *J. Appl. Cryst.* **30**, 31–42.
- Matthies, S. & Vinel, G. W. (1982). *Phys. Status Solidi B*, **112**, K111–K114.
- Matthies, S., Wenk, H.-R. & Vinel, G. W. (1988). *J. Appl. Cryst.* **21**, 285–304.
- Müller, A., Leiss, B., Ullemeyer, K. & Breiter, K. (2010). *Int. J. Earth Sci.* **100**, 1515–1532.
- Pehl, J. & Wenk, H.-R. (2005). *J. Struct. Geol.* **27**, 1741–1749.
- Raith, M., Mehrens, C. & Thöle, W. (1980). *Jahrb. Geol. Bundesanst. Austria*, **123**, 1–37.
- Schmid, S. M. & Casey, M. (1986). *AGU Geophys. Monogr.* **36**, 263–286.
- Siegesmund, S., Helming, K. & Kruse, R. (1994). *J. Struct. Geol.* **16**, 131–142.
- Siegesmund, S., Ullemeyer, K., Weiss, T. & Tschegg, E. K. (2000). *Int. J. Earth Sci.* **89**, 170–182.
- Trullenque, G., Kunze, K., Heilbronner, R., Stünitz, H. & Schmid, S. M. (2006). *Tectonophysics*, **424**, 69–97.
- Ullemeyer, K., Leiss, B. & Stipp, M. (2010). *Solid State Phenom.* **160**, 183–188.
- Ullemeyer, K., Siegesmund, S., Rasolofosaon, P. N. J. & Behrmann, J. H. (2006). *Tectonophysics*, **414**, 97–116.
- Ullemeyer, K., Spalhoff, P., Heinitz, J., Isakov, N. N., Nikitin, A. N. & Weber, K. (1998). *Nucl. Instrum. Methods Phys. Res. Sect. A*, **412**, 80–88.
- Von Dreele, R. B. (1997). *J. Appl. Cryst.* **30**, 517–525.
- Wall, H. de, Bestmann, M. & Ullemeyer, K. (2000). *J. Struct. Geol.* **22**, 1761–1771.
- Wenk, H.-R. (1991). *J. Appl. Cryst.* **24**, 920–927.
- Wenk, H.-R., Cont, L., Xie, Y., Lutterotti, L., Ratschbacher, L. & Richardson, J. (2001). *J. Appl. Cryst.* **34**, 442–453.
- Wenk, H.-R., Lutterotti, L. & Vogel, S. (2003). *Nucl. Instrum. Methods Phys. Res. Sect. A*, **515**, 575–588.
- Wenk, H.-R., Lutterotti, L. & Vogel, S. C. (2010). *Powder Diffr.* **25**, 283–296.
- Wenk, H.-R., Vasin, R. N., Kern, H., Matthies, S., Vogel, S. C. & Ivankina, T. I. (2012). *Tectonophysics*, **570–571**, 123–134.
- Windsor, C. G. (1981). *Pulsed Neutron Scattering*. London: Taylor and Francis.
- Xie, Y., Wenk, H.-R. & Matthies, S. (2003). *Tectonophysics*, **370**, 269–286.

**Crystallographic preferred orientations of exhumed
subduction channel rocks from the Eclogite Zone of the
Tauern Window (Eastern Alps, Austria), and implications
on rock elastic anisotropies at great depths**

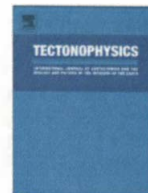
Ruth Keppler ¹, Klaus Ullemeyer ¹, Jan H. Behrmann ², Michael Stipp ², Robert
M. Kurzawski ², Tomas Lokajíček ³

(1) Department of Geosciences, University of Kiel, Otto-Hahn-Platz 1, D-24118 Kiel

(2) GEOMAR Helmholtz Centre for Ocean Research, Wischhofstr. 1-3, D-24148 Kiel

(3) Institute of Geology ASCR, Rozvojova 269, CZ-165 00 Praha 6

Submitted to Tectonophysics



Crystallographic preferred orientations of exhumed subduction channel rocks from the Eclogite Zone of the Tauern Window (Eastern Alps, Austria), and implications on rock elastic anisotropies at great depths

Ruth Keppler^{a,*}, Klaus Ullemeyer^a, Jan H. Behrmann^b, Michael Stipp^b, Robert M. Kurzawski^b, Tomas Lokajčiček^c

^a Department of Geosciences, University of Kiel, Otto-Hahn-Platz 1, D-24118 Kiel, Germany

^b GEOMAR Helmholtz Centre for Ocean Research, Wischhofstr. 1-3, D-24148 Kiel, Germany

^c Institute of Geology ASCR, Rozvojova 269, CZ-165 00 Praha 6, Czech Republic

ARTICLE INFO

Article history:

Received 14 October 2014

Received in revised form 25 January 2015

Accepted 15 February 2015

Available online xxx

Keywords:

Crystallographic preferred orientation

Subduction channel

Elastic properties

P-wave anisotropy

Eclogite Zone

Retrogression of eclogites

ABSTRACT

Crystallographic preferred orientations (CPO) of rocks from an exhumed subduction channel of the Alpine orogen were determined using time-of-flight neutron diffraction. This method allows the investigation of large polymineralic samples and, more importantly, the application of full pattern fit methods to constrain CPOs of mineralogically complex rocks. Samples studied include intensely deformed fresh and retrogressed eclogites, as well as metasediments, which are interleaved with the eclogites in the subduction channel. From the CPO, seismic properties of the samples were calculated. P-wave anisotropies of the eclogite samples are fairly low, with an average of about 1.5%, and mainly constrained by pronounced omphacite CPO. Growth and deformation of retrograde amphibole in the eclogites also led to a pronounced CPO, which has a large impact on seismic anisotropies by raising them to up to 3.7% and changing the orientations of velocity maxima. Elastic anisotropies of the subducted metasediments are higher (up to 7.4%) and constrained by quartz and mica CPO in clastics and by calcite CPO in marble. V_p/V_s ratios may help to distinguish fresh eclogites from retrogressed ones, and both rock types from mantle peridotites of downgoing lithospheric slabs in seismic imaging. Our data also indicate that subducted terrigenous sediments not only are strongly anisotropic, but also have low V_p/V_s ratios. This way there may be the potential to image them by seismic tomography at depth in active subduction channels.

© 2015 Published by Elsevier B.V.

1. Introduction

The interface of convergent plate boundaries is a highly dynamic tectonic environment, featuring deep subduction, offscraping of lower plate materials, underplating, and eventual exhumation by return flow towards the Earth's surface. The general concept is that of rocks moving in a subduction channel, first established by Shreve and Cloos (1986) and Cloos and Shreve (1988). These authors mainly describe the movement of material to and from depths of 30 km. More recent subduction channel models include the exhumation of previously subducted oceanic crust and sedimentary cover from depths of over 70 km (e.g. Agard et al., 2009; Angiboust et al., 2009). The generally invoked driving mechanisms are buoyancy of surrounding low-density rocks (e.g. Guillot et al., 2001; Kurz and Froitzheim, 2002), external forcing by continental fragments entering the subduction zone (e.g. De Franco et al., 2008), slab breakoff (e.g. Ratschbacher et al., 2004), or the changeover to an extensional regime in the overriding plate (e.g. Behrmann and Ratschbacher, 1989; Platt, 1986). There is a large number of recent

regional studies of exhumed subduction channel rocks, which yield information on their petrology and tectonic history. Examples are the Franciscan Complex of California (e.g. Anczkiewicz et al., 2004), the Mesohellenic subduction zone in the Cyclades (e.g. Schmaedicke and Will, 2003), the Western (e.g. Bousquet, 2008) and the Eastern Alps (e.g. Kurz et al., 1998). Common to all these subduction zones are the thickness of only a few kilometres and their lithologies comprising metabasic lenses of variable size embedded in a matrix of lower-density metasediments or serpentinites.

Despite detailed field investigations and numerous models for subduction channels, the exact processes taking place within are far from being completely understood. High resolution seismic imaging – a promising tool for the deconvolution of small-scale structures at depth – is still hampered by inadequate knowledge regarding the velocity structure and elastic anisotropies. Elastic anisotropy data of rocks incorporated in subduction zones are an important source of information for the interpretation of (high resolution) seismic sections, and have been used to aid the understanding of mantle dynamics (e.g. Montagner and Guillot, 2003; Montagner and Tanimoto, 1990; Silver, 1996). In this context crystallographic preferred orientation (CPO) of the rock constituents can be used as a powerful tool to predict the elastic anisotropy of

* Corresponding author.

E-mail address: rkeppler@geomar.de (R. Keppler).

deformed subduction channel rocks. However, the acquisition of CPO data and, thus, obtaining first-hand information on elastic anisotropies of polymineralic rocks is not straightforward. Most studies on polymineralic rocks were conducted on materials from the upper and lower crust (e.g. Ivankina et al., 2005; Kitamura, 2006; Ullemeyer et al., 2006), or on rocks originating from above and below the continental Moho (e.g. Barruol and Kern, 1996; Llana-Fúnez and Brown, 2012; Pros et al., 2003; Ullemeyer et al., 2010). Elastic data for subduction channel rocks were provided by Mauler et al. (2000), Bascou et al. (2001), and Worthington et al. (2013), who investigated mineral CPOs of eclogites using EBSD (electron backscatter diffraction) and bulk rock elastic anisotropies calculated from the CPO data. However, these studies neither include metasedimentary rocks in the subduction channel nor retrogressed eclogites, which yield information on the processes and changes in state during exhumation. Furthermore, a methodical drawback of EBSD is the poor grain statistics due to limited sample size, which has consequences when calculating rock physical properties from CPO data.

To overcome these methodical limitations, and to offer a more comprehensive insight into the petrophysics of rock associations in a subduction channel, we present CPOs and bulk rock elastic anisotropies of principal rocks from an exhumed subduction channel: the Eclogite Zone (EZ in the following) of the Tauern Window in the Eastern Alps. The CPOs were acquired from time-of-flight neutron diffraction spectra applying the full pattern fit method for the texture evaluation, which permits a fully quantitative investigation of large rock samples with complex mineralogy. From the CPO data, we have modelled elastic anisotropies. In addition, two eclogite samples were the subject of direct

P-wave velocity measurements on spherical samples, giving an impression of the crack influence on the elastic rock properties at shallow and intermediate crustal depths. Our results allow to make inferences regarding the seismic attributes of subduction channels, especially acoustic anisotropy, and guide future visualization of subduction channel structure and physical properties.

2. Geological overview of study area

The EZ is located at the southern margin of the Tauern Window in the Eastern Alpine Orogen (Fig. 1A and B). The Tauern Window is a tectonic window exposing basement and cover of the lower European plate, as well as Penninic oceanic units that were initially subducted beneath the Adriatic plate and subsequently incorporated in the Alpine stack of tectonic nappes during continental collision in the Tertiary. The EZ is considered to represent the ocean-continent boundary at the distal European margin. Its general character is a volcano-sedimentary sequence formed during Jurassic rifting of the Penninic ocean (Kurz et al., 1998). Driven by the negative buoyancy of the downgoing Penninic oceanic slab, the EZ entered the subduction channel in the course of Adria–Eurasia convergent movements. The rocks were subjected to PT conditions of 2.0–2.5 GPa and 600 ± 30 °C (Dachs, 1990; Hoschek, 2001, 2004; Stöckhert et al., 1997). Rb–Sr dating by Glodny et al. (2005) and Lu–Hf dating by Nagel et al. (2013) indicate an Oligocene age for the peak PT conditions, and a fast exhumation thereafter within 1–2 Ma. Because of the fast exhumation from great depths, only part of the rocks suite was severely affected by retrograde metamorphism. With large coherent sheets of eclogite and interleaved metasediments preserved, the area offers the

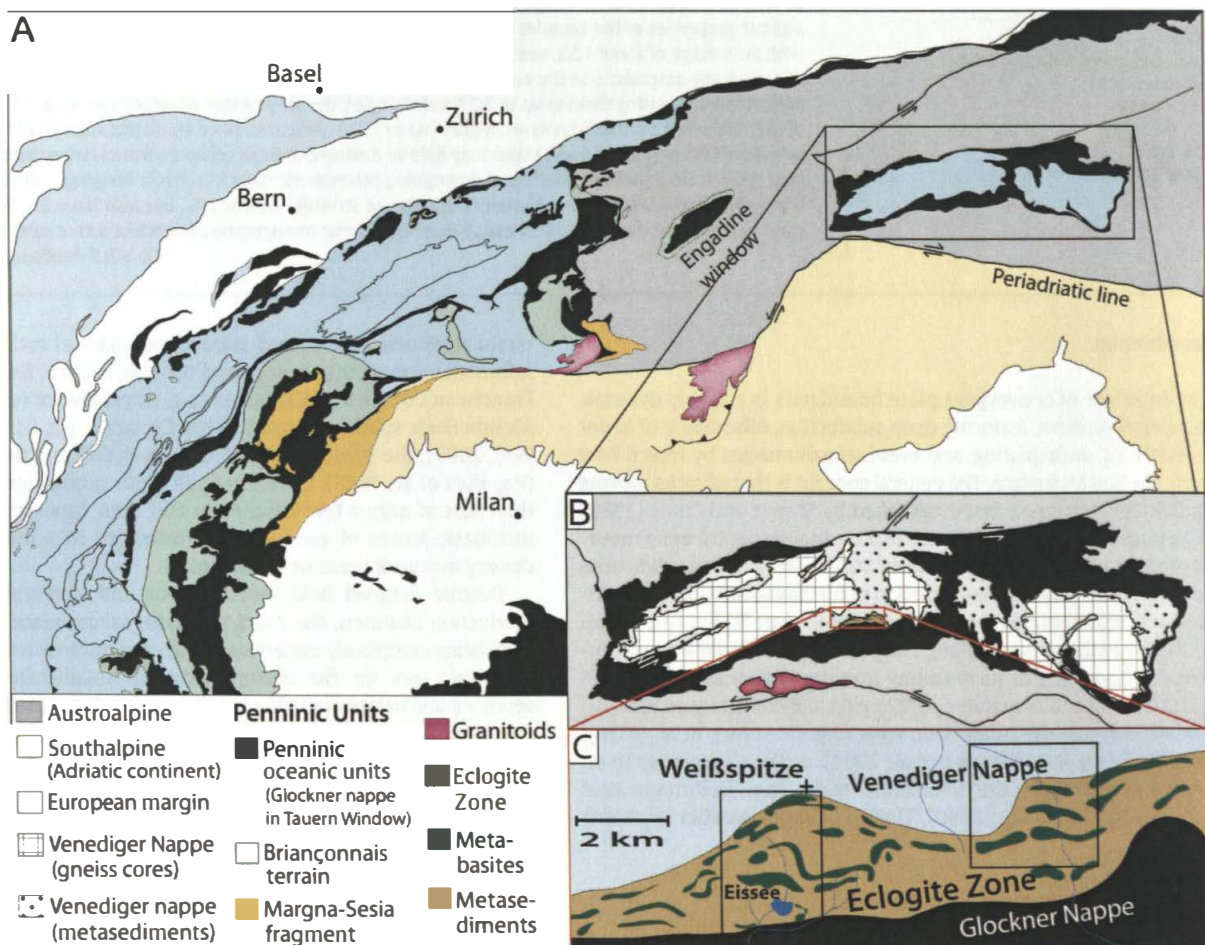


Fig. 3.1. Tectonic maps of A) the Alps, B) the Tauern Window (after Schmid et al., 2013) and C) the Eclogite Zone (after Neufeld et al., 2008). The location of the field area is indicated by a frame.

opportunity to study the effects of retrogression along intensity gradients in the field, and make predictions about the changes in petrophysical behaviour as rocks are being progressively exhumed.

Currently, the EZ is sandwiched in between European continental units to the north (Venediger nappe) and Penninic oceanic units to the south (Glockner nappe), and is dipping steeply to the SSE (Figs. 1C and 2). The EZ comprises eclogite lenses of various sizes, surrounded by a matrix of gneisses, micaschists, quartzites, marbles, and metaconglomerates (Fig. 2).

3. Methods

CPO measurements were performed at the neutron time-of-flight (TOF) texture diffractometer SKAT at the Frank Laboratory of Neutron Physics at JINR, Dubna, Russia (Keppeler et al., 2014; Ullemeyer et al., 1998). The high penetration capability of neutrons in matter together with the large beam cross section of the SKAT ($50 \times 95 \text{ mm}^2$) allows

the application of large-volume samples in the neutron experiment, e.g. of spherical samples with volumes of about 65 cm^3 . This is an important prerequisite, because the investigated samples are usually coarse-grained. Moreover, since complete diffraction patterns are recorded in a TOF experiment, highly sophisticated methods like the so-called 'Rietveld Texture Analysis' (RTA) can be used for the texture evaluation, allowing the simultaneous determination of all mineral textures even for samples with complex mineralogy (Von Dreele, 1997; Matthies et al. 1997). We used the MAUD software for the texture evaluation (Lutterotti et al., 1997; Wenk et al., 2010), for the discussion of practical limitations refer to Wenk et al. (2012) and Keppeler et al. (2014). Since RTA requires knowledge of the mineral structures present in the sample, mineral assemblages and chemical compositions were determined by means of microprobe analysis on a JEOL JXA 8200 Electron microprobe.

From the CPOs of the main rock constituents and particular single crystal elastic constants and volume fractions the elastic moduli of

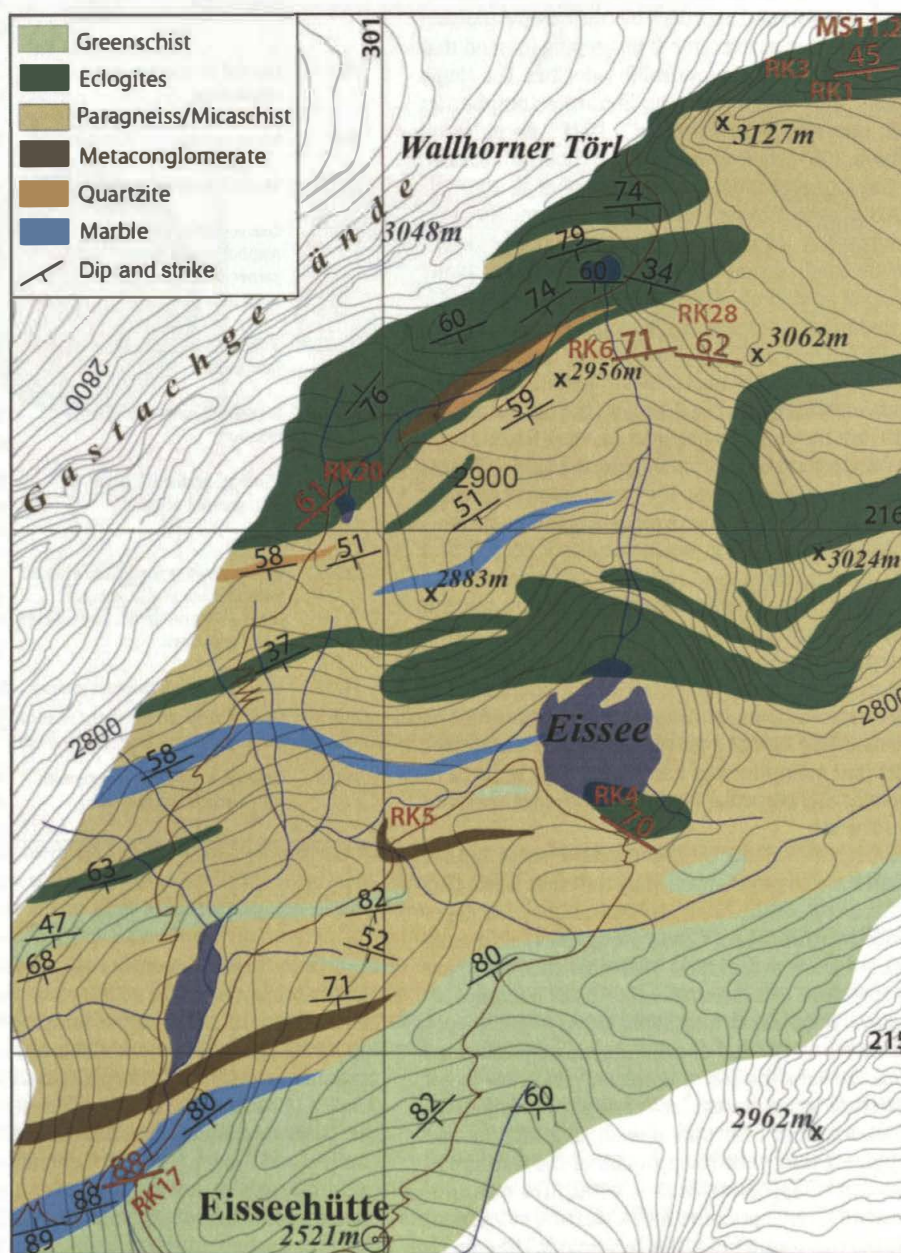


Fig. 32. Geologic map of the Eclogite Zone in the area of the Tirmeltal (own mapping completed by map of Raith et al., 1980). Sample locations and corresponding dipping angles are indicated in red. (For interpretation of the references to colour in this figure legend, the reader is referred to the web version of this article.)

bulk rock were calculated by using the Christoffel equation (e.g. Christoffel, 1874; Mainprice and Humbert, 1994),

$$\text{Det}|\Gamma_{ij} - V^2 \delta_{ij}| = 0, \quad (1)$$

where V is the phase velocity of the P-, S_1 or S_2 waves, δ_{ij} is the Kronecker delta, and Γ_{ij} is the Christoffel tensor,

$$\Gamma_{ij} = a_{ijkl} x_k x_l. \quad (2)$$

Parameters a_{ijkl} represent the density-corrected elastic (stiffness) moduli, and $x_k x_l$ are the direction cosines of the wave propagation direction. Hill (1952) has shown that the widely used Voigt (1928) and Reuss (1929) averaging schemes deliver upper and lower bounds of the elastic moduli, respectively. Other averaging schemes were proposed (e.g. Matthies, 2011; Matthies and Humbert, 1995), however, the true values of parameters a_{ijkl} are still somewhat uncertain. Therefore, we decided to use the most straightforward approach by consistently applying the Voigt averaging scheme, and at the same time keeping in mind that the recalculated velocities obtained are maximum velocities. The single crystal elastic constants were taken from the literature (omphacite: Bhagat et al., 1992; garnet: Babuska et al., 1978; hornblende: Aleksandrov and Ryzhova, 1961; glaucophane: Bezacier et al., 2010; muscovite: Vaughan and Guggenheim, 1986; quartz: Heyliger et al., 2003; albite: Brown et al., 2006; epidote/zoisite/clinozoisite: Aleksandrov et al., 1974; calcite: Dandekar, 1968). Whereas the elastic constants of quartz, muscovite and albite are confirmed to be reliable, the elastic constants of some other minerals are at least questionable. This holds in particular true for hornblende, the main constituent of the amphibolite TW32 (see Table 1). Microprobe analyses revealed glaucophane as the amphibole phase in most samples. Its chemical formula shows differences compared to the glaucophane individual of Bezacier et al. (2010), but the elastic data of Bezacier et al. (2010) are the only available and we were forced to use them. The omphacite composition varies from $\text{Di}_{65}\text{Jd}_{35}$ to $\text{Di}_{45}\text{Jd}_{55}$; Bhagat et al. (1992) report $\text{Di}_{38}\text{Jd}_{62}$ for their sample. The composition of garnet is close to the almandine end member in the pyrope–almandine–spessartine system, which justifies the use of the almandine elastic constants of Babuska et al. (1978). Nevertheless, we conclude that for some main rock constituents the elastic constants may differ from the ‘true’ mineral constants in our samples. Elastic data of chlorite, not present in excess of 5% in any of the samples, were approximated by the muscovite elastic constants. In this case and for other minerals like epidote/zoisite/clinozoisite contents in the samples studied are lower than the 10% threshold that would make the CPO of a particular mineral relevant for the physical properties (see Mainprice and Ildfense, 2009). In Fig. 3, P-wave velocity distributions and particular P-wave anisotropies are given for the main rock constituents.

Many experiments have shown that the elastic properties of rocks at small confining pressures are largely controlled by the crack fabric (e.g. Ivankina et al., 2005; Kem et al., 2002, 2008; Pros et al., 2003; Ullemeyer et al., 2006). The unique experiments of Christensen (1974) on mantle rocks confirmed crack influence to pressures of about 1 GPa, and there is evidence from low-pressure measurements that crack influence up to 1 GPa (or more) is valid for other rock types as well (Ullemeyer et al., 2011). We, therefore, accept that our texture-based predictions of the elastic constants are valid for great depths only. In order to get an impression on the crack influence at smaller depths, complete P-wave velocity distributions were determined on an amphibolite and an eclogite sample applying the pressure apparatus of the Institute of Geology ASCR, Prague, Czech Republic (Pros et al., 1998). The measurements were performed at various pressure levels starting at ambient conditions (0.1 MPa), the maximum pressures achieved in the experiments (300 and 400 MPa, respectively) are sufficient to close most open microcracks, allowing in particular the judgement of anisotropy differences to the crack-free medium.

Table 1

Description and modal compositions of the investigated samples, derived from RTA. RK4HP and RK20HP are model compositions calculated by means of the THERIAK/DOMINO thermodynamic modelling tool.

Sample	Description	Composition
RK1	Layered, mica-rich eclogite with medium grain size. Alternating omphacite, garnet, and mica layers of 0.5–4 mm.	37% omphacite, 19% zoisite, 15% garnet, 15% phengite, 7% quartz, 4% dolomite, 3% rutile
RK3	Fine-grained eclogite with weak layering.	43% omphacite, 22% garnet, 15% paragonite, 10% glaucophane, 9% quartz, 1% rutile
RK4	Retrogressed eclogite with pronounced carbonate-rich layers. Medium grain size and layers of about 1–5 mm thickness.	37% barroisite, 25% omphacite, 12% phengite, 9% garnet, 8% albite, 6% dolomite, 3% calcite
RK4HP	Simulated HP equivalent of sample RK4	38% omphacite, 33% garnet, 12% phengite, 8% quartz, 6% magnesite (MgCO_3), 3% dolomite
RK5	Layered micaschist, containing clinozoisite.	71% quartz, 24% muscovite, 5% clinozoisite
RK6	Micaquartzite	92% quartz, 8% muscovite
RK17	Medium-grained, foliated marble	99% calcite, 1% dolomite
RK20	Coarse-grained eclogite with omphacite-dominated and garnet-dominated layers of 5–10 mm.	43% omphacite, 24% garnet, 20% glaucophane, 7% quartz, 3% albite, 2% paragonite, 1% rutile
RK20HP	Simulated HP equivalent of sample RK4	52% omphacite, 23% garnet, 13% phengite, 11% quartz, 1% rutile
RK28	Paragneiss with strong mica foliation.	50% quartz, 31% albite, 19% muscovite
RK49	Medium-grained, layered, retrogressed eclogite.	25% omphacite, 33% albite, 14% garnet, 12% phengite, 8% quartz, 8% glaucophane
MS11.2	Fine-grained, mylonitized eclogite with pronounced layering of omphacite and garnet. Layers are 0.5–2 mm thick.	45% omphacite, 24% almandine, 15% quartz, 6% phengite, 5% albite, 4% glaucophane, 1% rutile
TW32	Weakly layered, medium grained amphibolite.	51% hornblende, 20% paragonite, 8% garnet, 6% albite, 5% dolomite, 5% chlorite, 3% omphacite, 2% quartz
TW33	Layered, mica-rich eclogite with fine to medium grain size.	38% omphacite, 24% garnet, 19% phengite, 10% albite, 5% glaucophane, 4% quartz

In order to help quantification of the effects of retrogression on the elastics properties of the eclogite samples, bulk chemical compositions of the retrogressed eclogite samples RK4 and RK20 were used to model the pristine equilibrium mineral assemblages and modal mineral amounts at peak metamorphic conditions of 600–630 °C and 2.0–2.5 GPa (Hoschek, 2001, 2004; Stöckhert et al., 1997). For this purpose the thermodynamic modelling tool THERIAK/DOMINO is used (de Capitani and Brown, 1987; de Capitani and Petrakakis, 2010). The equilibrium assemblage was calculated utilizing a modified Holland & Powell database (Holland and Powell, 1998). To avoid interferences of different implemented amphibole solid solution models, only the two-endmember glaucophane model was applied. Such an adjustment is reasonable as only the relevant high-pressure realm is considered, and therefore only blueschist facies amphiboles are expected. Bulk

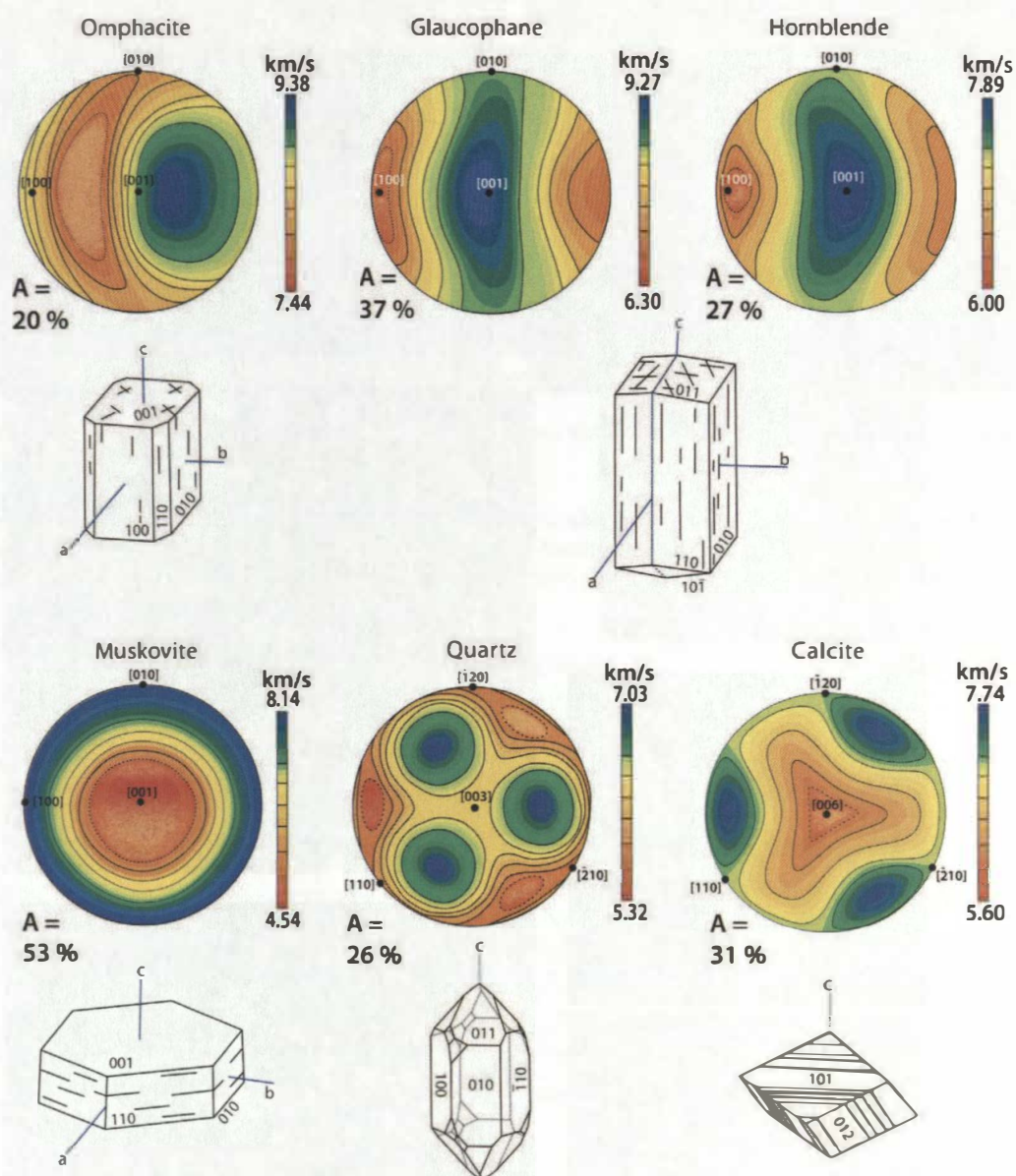


Fig. 3.3. Crystal structures and P-wave velocity distribution of important mineral phases influencing elastic anisotropy of the samples in this study. Colour bars indicate velocity ranges. $A = (V_{\max} - V_{\min}) / V_{\text{mean}}$: anisotropy. Crystallographic axes are indicated. (For interpretation of the references to colour in this figure legend, the reader is referred to the web version of this article.)

compositions of the rocks were calculated from averaged microprobe mineral analyses, and corresponding modal amounts were taken from RTA. All calculations were carried out assuming excess of a hydrous fluid. In order to reproduce the exact amount of carbonates present in the rock sample in the retrogressed state, a stoichiometric quantity of CO_2 was added to the fluid composition of sample RK4. Comparison of the retrogressed and peak-grade mineral compositions allows to assess the likely change in elastic properties and anisotropy associated with retrogressive changes during the exhumation stage.

4. Compositions and microfabrics of the samples studied

The composition of the eclogites is quite variable. Main constituents are omphacite and garnet, changing amounts of glaucophane, barroisitic hornblende, clinozoisite, quartz, phengite, paragonite, albite and minor amounts of dolomite, calcite, kyanite and rutile (Table 1). The mesoscopic and microscopic fabric of the eclogites is also highly variable (Fig. 4). There are coarse-grained and fine-

grained varieties with random mineral distribution (RK3, RK20), as well as fine grained and strongly foliated eclogites displaying compositional layering (RK1, RK4, RK49, MS112, TW33). Elongated omphacite grains define a clear lineation on the foliation plane. In mylonitic eclogites the omphacite forms aggregates of small recrystallized grains. Garnet exhibits prograde zoning and either occurs in layers or as randomly distributed cluster. Layered samples show garnet- and quartz-rich layers alternating with omphacite-rich layers of variable thickness (Fig. 4). In samples containing zoisite and dolomite, both these phases are often concentrated in distinct layers. Small and dispersed zoisite grains within omphacite-rich layers are aligned parallel to the foliation, whereas in zoisite-rich layers the grains are larger and do not show shape preferred orientation (SPO) (see RK1 in Fig. 4). Quartz grains do not exhibit SPO. In the eclogites phengitic mica (Si: 3.26–3.37) is always aligned parallel to the foliation, whereas paragonite is randomly oriented.

The metasediments investigated in this study comprise gneisses, micaschists, mica-bearing quartzites and marbles. Particular modal

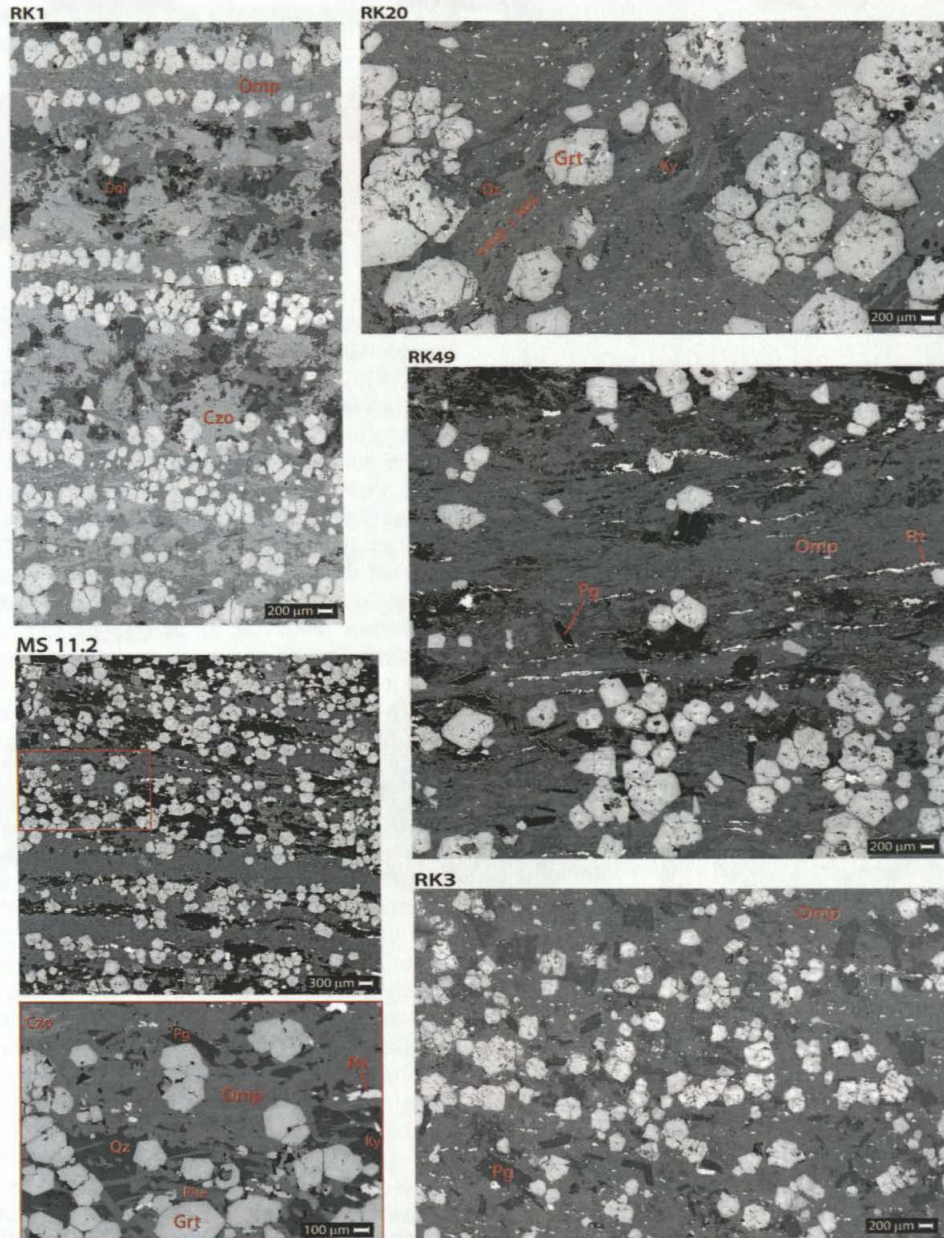


Fig. 3.4. Typical BSE microstructures of fresh (RK1 and MS112) and retrogressed (RK20, RK49 and RK3) eclogite samples. Czo = clinozoisite; Dol = dolomite; Grt = garnet; Hbl = hornblende; Ky = kyanite; Omp = omphacite; Pg = paragonite; Phe = phengite; Qz = quartz; Rt = rutile. Sections are perpendicular to the foliation and parallel to the stretching lineation. For sample descriptions see Table 1.

compositions are summarized in Table 1. The clastic metasediments exhibit a strong foliation defined by mica (Fig. 5). The phengite component of the micas is lower than in the eclogite samples (Si: 3.07–3.24). Most of the clastic metasediments contain minor amounts of clinozoisite, and the gneisses contain feldspar. The only marble sample is mainly composed of medium-grained calcite and shows a weak foliation.

5. Results

5.1. Crystallographic preferred orientations

5.1.1. Eclogites

All eclogites exhibit a distinct CPO of omphacite. Position and intensity of the pole density maxima are variable, however, (001) always displays a maximum parallel to the stretching lineation (Figs. 6 and 7). In some samples (RK1, RK3, TW33) the maximum is cluster-like,

in others, (001) forms a more or less pronounced girdle within the foliation plane (RK4, RK20, RK49, MS112). (010) not only is concentrated normal to the foliation plane, but also can be distributed in a girdle perpendicular to the lineation.

Glaucophane also displays pronounced CPO in all retrogressed eclogites (Fig. 6). As in the case of omphacite the glaucophane CPOs are variable. Glaucophane (001) mostly parallels the omphacite (001) lattice plane, however, one sample shows a clear deviation from this rule, an angular deviation of about 40° within the foliation plane is valid (sample RK20, Fig. 6). Glaucophane (100) always has the maximum pole density normal to the foliation plane. The barroisitic hornblende in sample RK4 shows girdle-like distributions of the (100) and (001) lattice planes, the latter scattering within the foliation plane. The (100) girdle is very weak and oriented perpendicular to the kinematic Z axis (Fig. 6). In this sample, there is also a pronounced (010) maximum normal to the foliation (not depicted).

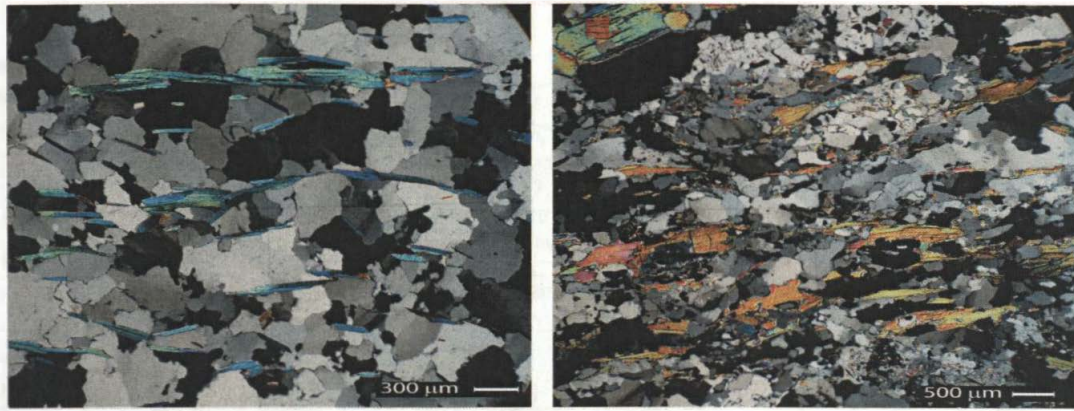


Fig.3.5. Micrographs of typical clastic metasediments. Left: mica quartzite (RK6); right: paragneiss (RK28), both exhibiting a pronounced mica foliation. Sections are perpendicular to the foliation and parallel to the stretching lineation: crossed polarizers.

With the exception of sample RK4, the phengite (006) basal planes have strong axial symmetric maxima parallel to the foliation normal. If paragonite is present in significant amounts, (006)

exhibits only a weak preferred orientation, but the maximum pole density also parallels the foliation normal (sample RK3, Fig. 6). Garnet, the acoustically isotropic constituent of the eclogites,

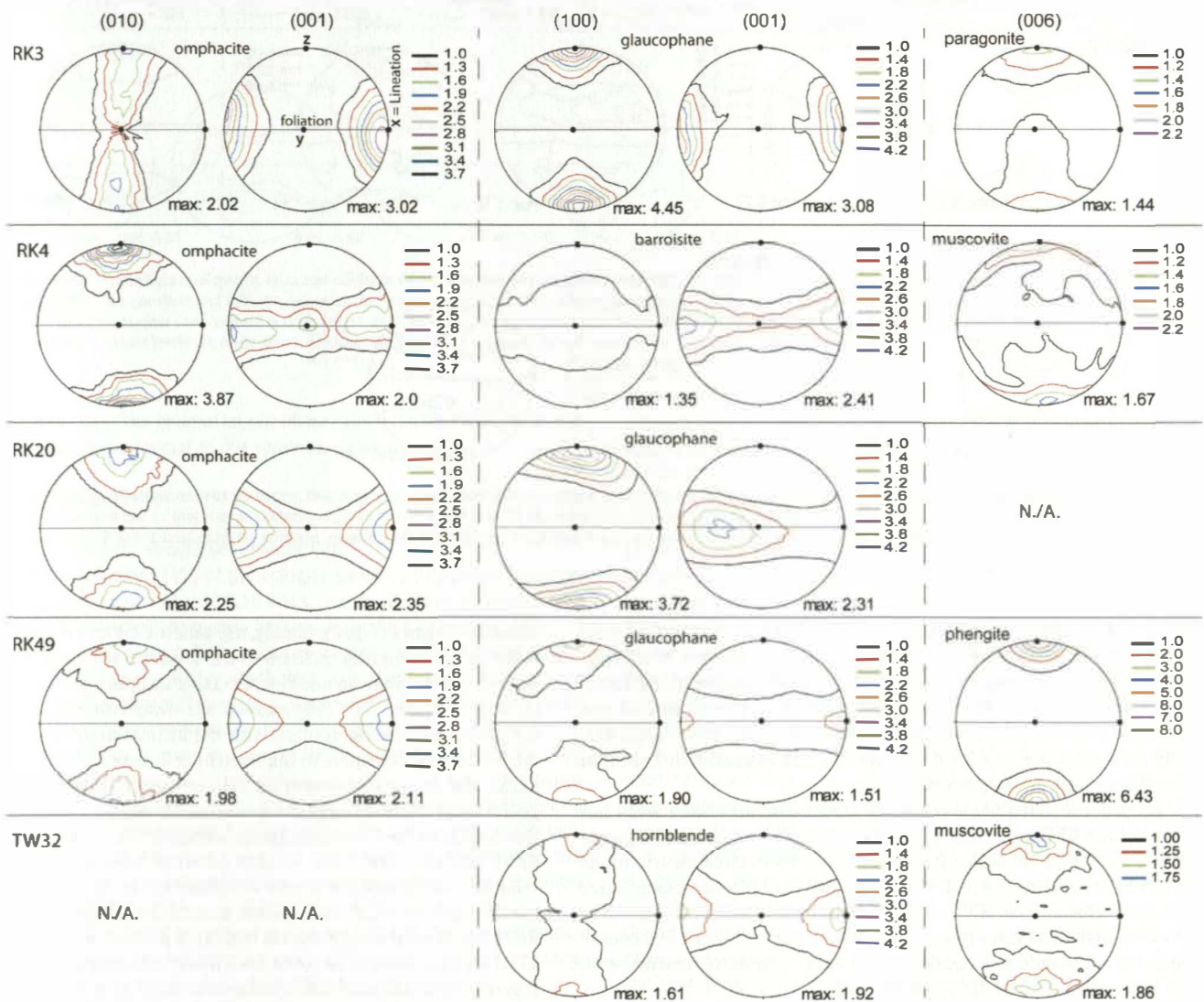


Fig. 6. Recalculated pole figures of omphacite, hornblende, and mica of the retrogressed eclogite samples. Pole figures are oriented according to omphacite lineation and foliation. The lineation (x-direction of the finite strain ellipsoid) is EW in the pole figure, the foliation normal (z-direction of the finite strain ellipsoid) is oriented NS, and the y-direction (perpendicular to x and z) lies normal to the pole figure plane. Pole figures are lower hemisphere equal area projections. Contour levels are multiples of a random distribution. Maxima are indicated at the lower right corner of the pole figure. Only significant pole figures are given. They are sufficient to illustrate the textural differences between samples. N.A. - not available.

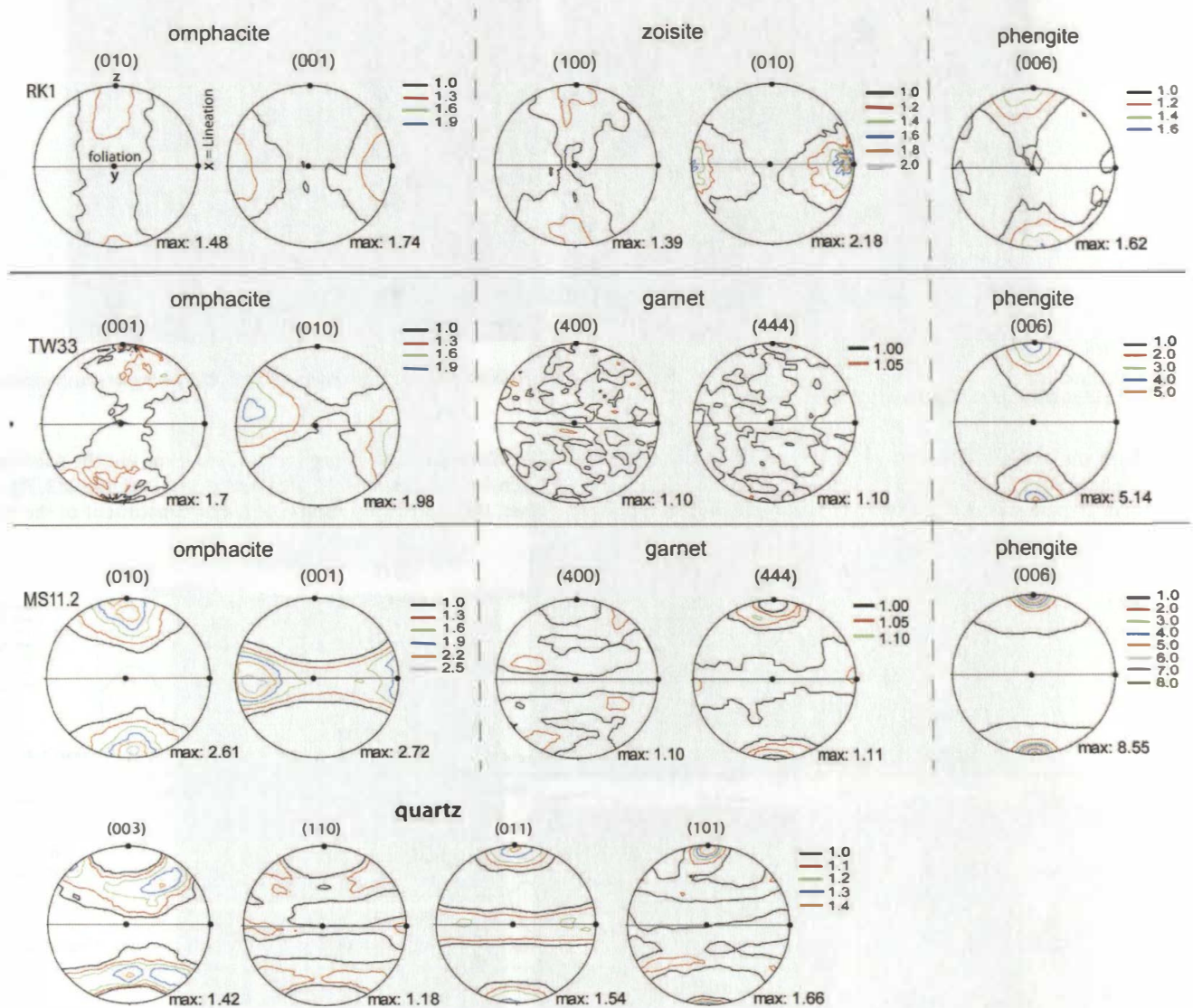


Fig. 3.7. Recalculated pole figures of omphacite, garnet, mica, and quartz of fresh eclogite samples. Pole figures are oriented according to omphacite lineation and foliation. The lineation (x-direction) is EW in the pole figure, foliation normal (z-direction) is oriented NS and the y-direction (perpendicular to x and z) lies normal to the pole figure plane. Pole figures are lower hemisphere equal area projections. Contour levels are multiples of a random distribution. Maxima are indicated at the lower right corner of the pole figure.

has nearly random distribution, as exemplified by two garnet pole figures of samples TW33 and MS11.2 (Fig. 7). The zoisite CPO of sample RK1 is of intermediate strength with (010) parallel to the lineation and a slight tendency of (100) to form a girdle around the lineation (Fig. 7). Calcite, dolomite and albite, if present, always display very weak preferred orientations close to a random distribution (for this reason not presented).

Despite the generally low volume fraction, quartz has a weak but well-defined CPO, as exemplified by sample MS 11.2 bearing 15% quartz (Table 1). The (003) lattice plane displays a small circle distributions around the foliation normal. The (011) and (101) lattice planes have intensity clusters parallel to the foliation normal, whereas (011) exhibits additional scattering in the foliation plane (Fig. 7). The overall layout corresponds to a nearly perfect axial symmetric texture with the foliation normal as the symmetry axis.

5.1.2. Metasediments

In the metasediments, the quartz CPO is more pronounced compared to the eclogites. The maximum pole densities are in the order of 2.0 [m.r.d.], except for the c-axis distribution of sample RK6, which is

two times higher (Fig. 8). Mostly, asymmetric c-axis crossed girdles or point maxima slightly inclined to the foliation normal are observed, sample RK6 exhibits an additional c-axis maximum close to the center of the pole figure. The (110) maxima are always close to the margin of the pole figures, in agreement with the inclination of the c-axis, they are inclined with respect to the stretching lineation (Fig. 8). The (100) lattice planes show pole density distributions in agreement with the geometrical relationship of the quartz lattice planes. Their outline is either similar to the (110) pole figure (sample RK6), or dissimilar (sample RK5). The (011) and (101) rhombs generally have weak preferred orientation, with maximum pole densities either within the foliation plane (RK5), on small circle girdles around the foliation pole (RK6 and RK28), or normal to the foliation (RK28). If present, albite has a random CPO (not presented). The (006) basal planes muscovite/phengite exhibit very strong maxima normal to the foliation (Fig. 8) with much higher pole densities compared to the eclogites (Figs. 6 and 7).

The calcite CPO of the marble sample RK17 is of intermediate strength. The (110) lattice planes form a girdle within the foliation plane, the maximum pole density on the girdle parallels the stretching lineation. The (006) lattice planes make a maximum parallel to the

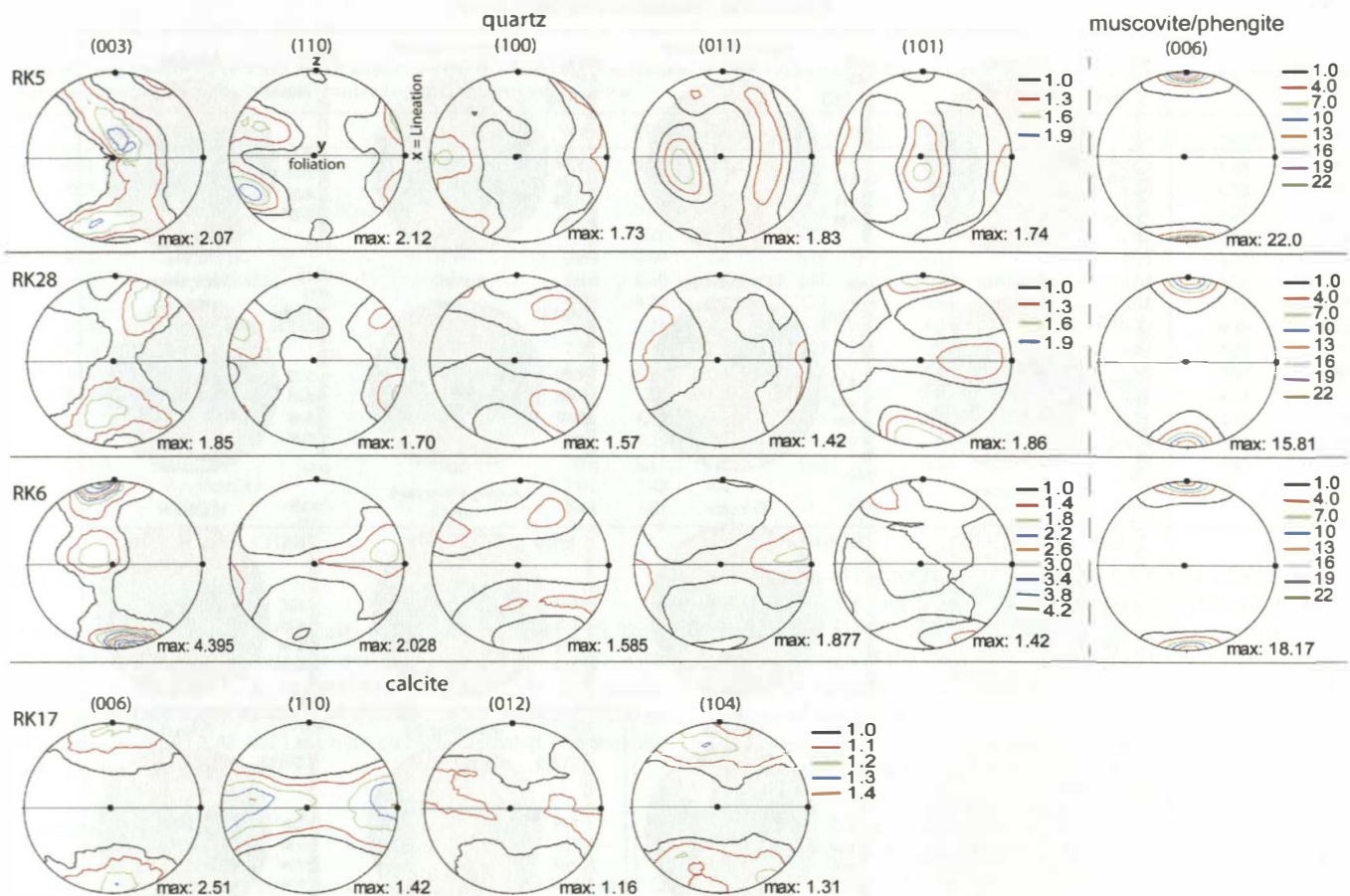


Fig. 3.8. Recalculated pole figures of quartz, mica and calcite in the metasedimentary samples. The pole figures of the elastic metasedimentary samples (RK5, RK6, and RK28) are oriented according to the mica lineation and foliation, whereas the marble sample (RK17) is aligned with respect to the calcite lineation and foliation. The lineation (x-direction) is EW in the pole figure, foliation normal (z-direction) is oriented NS and the y-direction (perpendicular to x and z) lies normal to the pole figure plane. Pole figures are lower hemisphere equal area projections. Contour levels are multiples of random distribution. Maxima are indicated at the lower right corner of the pole figure.

foliation normal. The general layout of the calcite CPO is axial symmetric with the foliation normal as the symmetry axis.

5.2. P-wave anisotropy

5.2.1. Eclogites and retrogressed counterparts

P-wave velocities (V_p) of the eclogite samples calculated from the CPOs vary between 7.45 and 8.10 km/s (Fig. 9). P-wave anisotropies of the eclogite samples are mostly low, with the highest value (3.7%) for the retrogressed sample RK20, and the lowest one (0.4%) for the non-retrogressed sample RK1, which has a high zoisite content (see Table 2). In all samples, the velocity maxima are close to the omphacite (001) pole density maximum, and, if present, the amphibole (001) pole density maximum. In sample RK20, where the pole density maxima of the two minerals exhibit an angle of about 40° within the foliation plane, the calculated velocity maximum lies between both these maxima. Lowest P-wave velocities are normal to the foliation throughout, i.e., high velocities are always located within the foliation plane. S-wave velocities in the eclogites vary between 4.82 and 4.23 km/s (V_{s1}), and between 4.81 and 4.22 km/s (V_{s2}) (Table 2). We avoided graphical representation of the S-wave velocity distributions, because the velocity differences are mostly some tenths of metres (see Table 2) and, therefore, insignificant.

P-wave velocity distributions of samples RK4 and RK20 were also calculated for the high-pressure mineral assemblages obtained from thermodynamic modelling by means of the THERIAK/DOMINO tool (RK4HP and RK20HP in particular figures and tables). The most prominent difference to the actual composition obtained from RTA is the

absence of amphibole minerals (Table 1). Fig. 10 shows an equilibrium assemblage diagram illustrating the high pressure assemblage of sample RK20, the frame in the diagram indicates the PT conditions of the EZ we used for modelling. P-wave velocities recalculated for the modelled samples are higher (RK4HP) or lower (RK20HP) compared to the retrogressed counterparts. Judging the isotropic mean V_{p300} , the velocity increase of sample RK4HP is approx. 0.7 km/s, the decrease of sample RK20HP is much less (approx. 0.2 km/s, Table 2). In both cases, however, P-wave anisotropy decreases. The already weak anisotropy of the strongly retrogressed eclogite RK4 is reduced even more and becomes insignificantly small ($<1\%$), in case of the less retrogressed eclogite RK20 anisotropy still exceeds 2%, although the decrease is remarkable (compare magnitudes in Table 2).

The experimental P-wave velocity distributions determined at moderate confining pressures of 300 MPa (amphibolite sample TW32) and 400 MPa (eclogite sample TW33) show different relationships to the crack-free (CPO-derived) counterparts. The amphibolite (TW32) has a slightly higher 'experimental' velocity level in the order of 0.1 km/s (Table 2). Since the experimental velocities should not exceed the CPO-derived ones, this is a clear indicator that the bulk error introduced by applied methods (uncertainties of the CPO estimates, inaccurate mineral elastic constants, experimental errors etc.) is 0.1 km/s to the best. Judging the velocity vs. pressure trends of the minimum and maximum velocities (Fig. 9B), further velocity increase with increasing pressure and, accordingly, a still higher error level is implied from the trends. Whether, despite these peculiarities, the calculated P-wave anisotropies are realistic will be the subject of discussion. Concerning the eclogite (TW33), the relationships are somewhat different. The

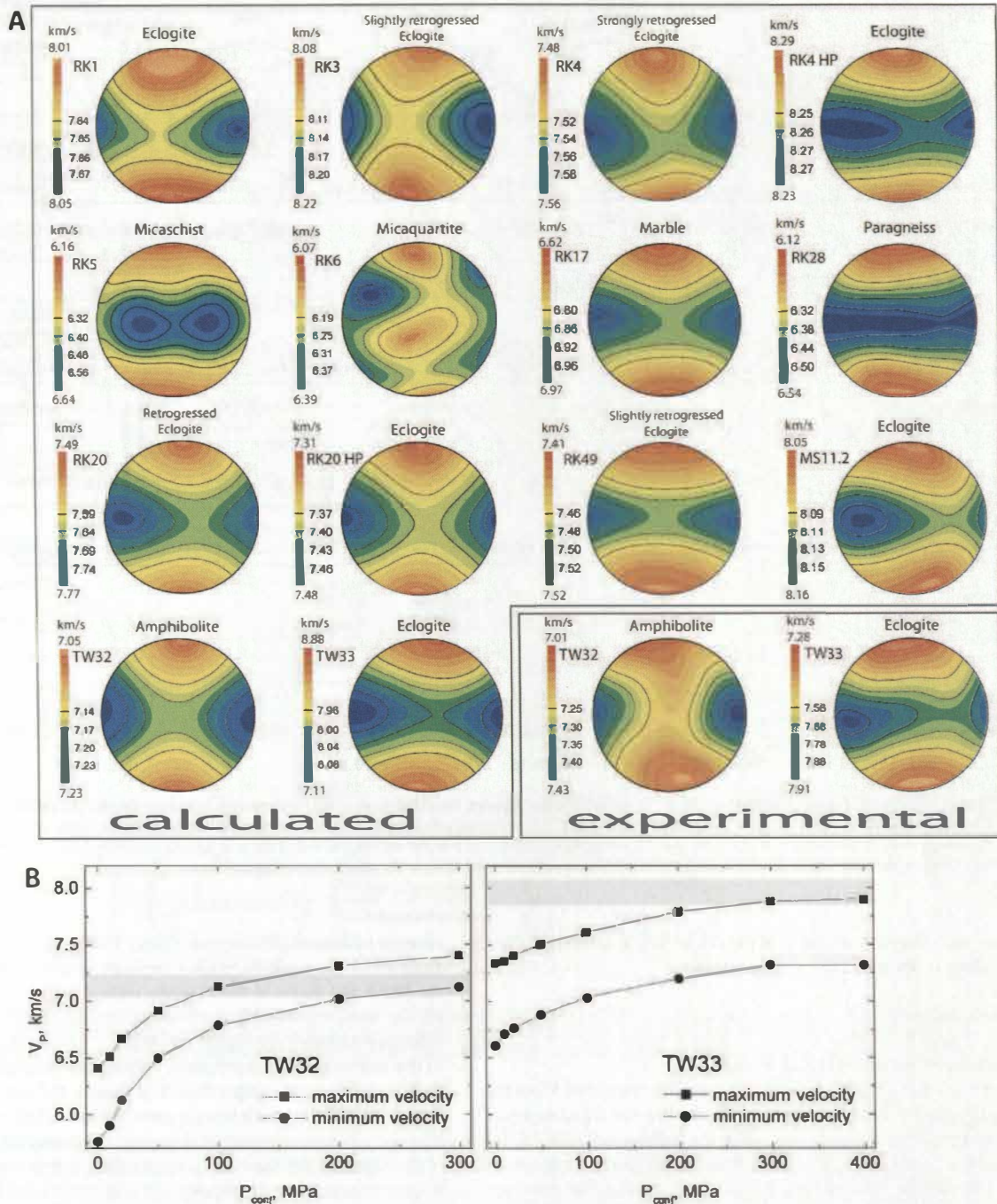


Fig. 3.9. (A) Calculated and experimental P-wave velocity distributions. The experimental data was gained at confining pressures of 300 MPa (TW32) and 400 MPa (TW33). HP: velocity distributions calculated for the corresponding high pressure assemblage of retrogressed samples RK4 and RK20. Cold colours indicate high velocities, warm colours low velocities, black lines indicate distinct contour levels and contour level spacings. (B) Minimum (circles) and maximum (squares) experimental P-wave velocity at increasing pressures. Grey bar indicates calculated P-wave velocity. (For interpretation of the references to colour in this figure legend, the reader is referred to the web version of this article.)

calculated velocities exceed the experimental velocities, as expected from theory. From the experimental velocity vs. pressure trends further velocity increase for pressures beyond 400 MPa is difficult to infer (Fig. 9B), but appears to be possible. As for the amphibolite, the 'true' level of the calculated P-wave velocities is questionable and is the subject of discussion.

5.2.2. Metasediments

In the metasediments the calculated P-wave velocities are generally lower compared to the eclogites, ranging from 6.24 to 6.86 km/s. P-wave anisotropies, on the other hand, are higher with values of up to 7.4% (Table 2). In the paragneiss sample (RK28) the

highest velocities are evenly distributed within the foliation plane and the velocity minimum parallels the foliation normal, i.e., the velocity distribution is more or less axial symmetric (Fig. 9). The micaschist sample (RK5) deviates from axial symmetry, because two velocity maxima at angles of approx. 45° with respect to the lineation are observed (Fig. 9). The micaquartzite (RK6) shows an uncommon relation to the sample reference frame with the velocity maximum apart from the foliation plane and two regions of minimum velocity (Fig. 9). The marble sample has the highest velocity roughly parallel to the lineation with some dispersion in the foliation plane, and the lowest velocity is located normal to the foliation plane.

Table 2

P-wave (V_p) and S-wave (V_s) velocities, elastic anisotropies (A) and V_p/V_s ratio of all samples. A: modelled from CPO of the samples. B: experimentally measured. Mean values for V_p and V_s were calculated by averaging the three measured or modelled principal velocities.

Sample	Lithology	V_{p50} (km/s)	Min	Max	Ap (%)	V_{s50} (km/s)	V_{s1} min	V_{s1} max	V_{s2} min	V_{s2} max	V_p/V_s
A	RK1 Eclogite	8.03	8.01	8.05	0.4	4.68	4.68	4.69	4.67	4.68	1.71
	RK3 Eclogite	8.14	8.08	8.22	1.8	4.77	4.76	4.80	4.75	4.78	1.71
	RK4 Strongly retrogressed Eclogite	7.54	7.48	7.56	1.2	4.25	4.26	4.26	4.25	4.26	1.77
	RK4HP Eclogite	8.27	8.23	8.29	0.7	4.81	4.81	4.82	4.80	4.81	1.72
	RK5 Micaschist	6.39	6.16	6.64	7.4	4.18	4.11	4.40	4.03	4.21	1.53
	RK6 Micaquartzite	6.24	6.07	6.39	5.3	4.22	4.20	4.38	4.05	4.28	1.48
	RK17 Marble	6.86	6.62	6.97	5.1	3.72	3.64	3.75	3.62	3.67	1.84
	RK20 Retrogressed Eclogite	7.57	7.49	7.77	3.7	4.38	4.36	4.43	4.35	4.39	1.73
	RK20HP Eclogite	7.40	7.31	7.48	2.3	4.23	4.23	4.26	4.22	4.24	1.75
	RK28 Paragneiss	6.37	6.12	6.54	6.8	3.98	3.93	4.10	3.88	3.97	1.60
	RK49 Eclogite	7.46	7.41	7.52	1.4	4.30	4.26	4.33	4.26	4.31	1.74
	MS11.2 Eclogite	8.12	8.05	8.16	1.5	4.78	4.73	4.78	4.72	4.76	1.70
	TW32 Amphibolite	7.14	7.05	7.23	2.6	4.01	4.00	4.05	3.98	4.02	1.78
	TW33 Eclogite	8.00	7.88	8.11	2.9	4.62	4.58	4.68	4.57	4.63	1.73
	B	TW32 Amphibolite	7.25	7.01	7.43	4.4					
TW33 Eclogite		7.56	7.28	7.91	8.3						

5.3. V_p/V_s ratios

V_p/V_s ratios of the eclogite samples are between 1.7 and 1.75. They are slightly higher for the retrogressed samples RK4 and TW32 with values of 1.77, and 1.78, respectively (Table 2). In the clastic metasedimentary samples the V_p/V_s values are significantly lower with values between 1.48 and 1.60. A much higher value of 1.85 was obtained for the marble sample.

6. Discussion

Elastic anisotropy of rocks is, to a large part, constrained by the CPO of its constituent mineral phases, which, in turn, is caused by

deformation of the rocks. As Mainprice and Ildefonse (2009) point out, only mineral percentages above 10% play an important role for rock physical properties. In this study, all mineral phases were included into calculation of the elastic anisotropy of bulk rock. Garnet does not exhibit pronounced elastic anisotropy, we, therefore, used the isotropic average of the elastic constants. This might have been possible also in the case of random textures, however, we preferred to average the contribution of particular minerals from the Orientation Distribution Function and the anisotropic mineral elastic coefficients.

The reliability of the predicted elastic anisotropy depends on accuracy of the CPO estimates and mineral elastic constants. A possible source of error is the rock modal composition delivered by RTA. Varying the volume fractions of the rock constituents can lead to the changes of anisotropy. Our observation is that modifications of a few percentages have no effect at all. Accordingly, the error contribution of the minor rock constituents is negligible. If the modification approaches 10%, the effect becomes visible, in particular for mica minerals exhibiting P-wave anisotropies in the order of 50%. The effect of erroneous CPO estimates in particular of rocks bearing many phases is much harder to assess. Methodical investigations of Keppler et al. (2014) show that, the orientational features of the CPOs of the main rock constituents can be reproduced well, but differences due to texture strength may occur.

6.1. Eclogites

6.1.1. CPO development

The omphacite CPO in the eclogites is variable, exhibiting L-type (lineation dominated), S-type (foliation dominated) or transitional (SL-type) fabrics. The transitional fabrics predominate (Figs. 6 and 7). The CPO geometry has been interpreted as relating to strain geometry (e.g. Kurz and Froitzheim, 2002), with L-type fabrics revealing constrictional strain, S-type fabrics indicating oblate strain, and transitional fabrics suggesting plain strain deformation (e.g. Helmstaedt et al., 1972).

The retrograde glaucophane – a main rock constituent of many eclogites – also exhibits variable CPO. Appearance and CPO development of glaucophane are very likely related to deformation during exhumation. As in the case of omphacite, the strain geometry may have been variable. An important result of the active deformation during exhumation is the degree of retrogression, which is reflected in different glaucophane volume fractions (Table 1). However, in most samples the layout of the glaucophane CPO corresponds to that of omphacite (Fig. 6). This indicates that the CPOs of both minerals formed during rock exhumation, and similar strain geometries persisted in the subduction channel for a long period. The retrogressed eclogite RK20 represents a significant exception, because the orientation of the

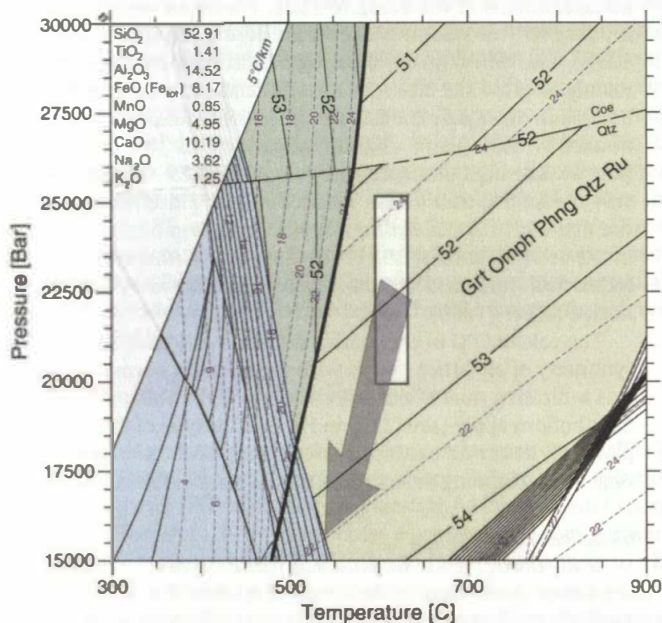


Fig. 3.10. Equilibrium assemblage diagram (pseudosection) of sample RK20, illustrating the modelled high-pressure parageneses. Whole rock chemistry is given in upper left corner. Parageneses containing glaucophane are blue-coloured, the enhanced subvertical line defines the onset of lawsonite stability towards cooler temperatures. The eclogite facies mineral assemblage Grt + Omph + Phng + Qtz + Ru occupies a large stability field and shows only minor changes in modal mineral amounts. Thin solid and short dashed lines are contours of volume percentage of omphacite and garnet, respectively. The long dashed line represents the transformation of quartz to coesite. The bright rectangle in the center outlines estimated peak metamorphic conditions of the EZ (Hoschek, 2001, 2004; Stöckhert et al., 1997), the arrow indicates the retrograde metamorphic path of the EZ (Kurz et al., 1998). (For interpretation of the references to colour in this figure legend, the reader is referred to the web version of this article.)

glaucophane lineation (direction of the pole density maximum of the (001) lattice plane) deviates from the omphacite lineation (Fig. 6). This indicates that the direction of maximum principal extension in this sample changed after formation of the omphacite CPO, but prior or simultaneously to formation of the glaucophane CPO. Passive rotation of the eclogite block as a whole within the surrounding metasediments appears to be the most probable explanation for the rotating stress field. The uncommon barroisite CPO of sample RK4 with a weak girdle tendency of (100) is unusual for amphibole (Zhang et al., 2013).

Albite as a member of the retrograde mineral assemblage formed at a late stage of exhumation. The random CPO suggests that no dislocation creep was active at this stage of exhumation. Other deformation mechanisms cannot be excluded, but, obviously, did not lead to preferred orientation of albite.

In the eclogites, phengitic mica was already present during HP deformation, as confirmed by its high silica content. Strength of the (006) basal plane maximum indicates a well-developed foliation, except for sample RK1, which has a much lower pole density maximum (Fig. 7). The more fluctuating character of the foliation is visible also on hand specimen. If quartz is present, the weak CPO is almost perfectly axial symmetric with the foliation normal as the symmetry axis (Fig. 7). Due to the crystal plastic behaviour of quartz even at low temperatures, oblate strain can be derived from this feature for the very last stages of deformation.

Generally, no correlation between compositional layering and texture strength was observed. Layered samples do not necessarily exhibit a more pronounced CPO than samples with a random grain distribution. Furthermore, no correlation between grain size and the CPO strength of the samples was found. For example strongly layered sample RK1 exhibits much lower texture values in m.r.d. than sample RK3, which exhibits a granular mineral distribution (Table 1 and Figs. 4 and 6).

6.1.2. Elastic anisotropies

The CPO-derived elastic anisotropy of the eclogites is mainly constrained by the omphacite CPO and, if present, the amphibole CPO. Phengite contributes significantly if particular volume fractions are large enough. Due to consistent CPO type with the alignment of the basal plane within the foliation, and due to very high single crystal anisotropy (Fig. 3), phengite generally decreases the velocity normal to the foliation. The contribution to the velocity level within the foliation is vice versa. Garnet is basically isotropic and does not contribute to anisotropy. Due to the high isotropic velocity in the order of 9 km/s the contribution to bulk rock velocity can be significant if large volume fractions are present.

The relationship of the kinematically significant lattice planes of omphacite ((010) and (001)) and amphibole ((100) and (001)) to the single crystal P-wave distribution is not simple. In case of the omphacite, both the (010) and (001) lattice planes occupy intermediate positions between the directions of minimum and maximum velocities (Fig. 3). The velocity in (010) direction is closer to the minimum velocity and the velocity in (001) direction is closer to the maximum velocity. In case of the amphibole, the orientation differences between (100)/minimum velocity and (001)/maximum velocity are a few degrees only (Fig. 3). Especially in case of omphacite, the P-wave velocity distributions are hard to infer directly from the pole figures. However, if the (001) lattice planes of omphacite and amphibole exhibit strong coinciding maxima parallel to the lineation (no dispersion within the foliation plane), the same applies to the velocity distribution (sample RK3 in Figs. 6 and 9). If the omphacite and amphibole (001) lattice planes are dispersed within the foliation plane, the velocity maximum also tends to form a more or less pronounced girdle within the foliation plane (sample RK49 in Figs. 6 and 9). The strongly retrogressed eclogite RK4 shows clear girdle tendencies of omphacite (001) and hornblende (001), but the velocity distribution exhibits a point maximum parallel to the lineation. The unexpected relationship is caused by the anomalous amphibole CPO with the (100) lattice plane forming a nearly

complete – but weak – girdle around the Y axis of the structural reference frame (Figs. 6 and 9). The retrogressed eclogite RK20 with different orientations of the omphacite (001) and amphibole (001) pole density maxima shows a velocity maximum between these maxima (Figs. 6 and 9).

Elastic anisotropy of the eclogites is always small with magnitudes mostly <2%, except for the retrogressed eclogite RK20 ($A = 3.7\%$), which yields the highest glaucophane volume percentage in the samples (Table 1). Elastic anisotropies of the simulated HP eclogites RK4HP and RK20HP bearing only the high-pressure mineral assemblages are dominated by the omphacite CPO due to the lacking influence of the amphibole CPO. In both cases the overall elastic anisotropy decreases. For sample RK4HP it becomes insignificantly small (0.7%), for sample RK20HP it markedly goes down to 2.3% (RK20: 3.7%, Table 2). This shows that the retrograde metamorphic overprint of eclogites during exhumation is capable of increasing the elastic anisotropy due to the formation of amphibole, provided there is a CPO-forming mechanism during exhumation.

6.2. Metasediments

6.2.1. CPO development

The asymmetric crossed girdles of quartz (003) of samples RK5 and RK28 (Fig. 8) are indicative of non-coaxial shear with combined basal <a>, prism <a> and rhomb <a> slip (e.g. Schmid and Casey, 1986). Sample RK6 exhibits a strong quartz (003) maximum at the border of the pole figure. The inclination with respect to the foliation normal indicates non-coaxial shear (Fig. 8). A weaker maximum in the foliation plane points to additional prism <a> slip. Hence, basal <a> slip is the predominant slip system (Schmid and Casey, 1986; Stipp et al., 2002). The quartz textures and observed quartz dynamic recrystallization microstructures are characteristic of dislocation creep in the metasediments of the Eclogite Zone. The asymmetry of the CPO is missing in the eclogites (see also Behrmann and Ratschbacher, 1989), i.e., non-coaxial shearing within the subduction channel mainly affected the clastic metasediments surrounding the eclogite bodies. In all clastic metasediments, the mica always shows pronounced basal plane alignment parallel to the foliation plane (Fig. 8). The high phengite component of mica indicates high pressure metamorphism of the metasediments. Since the orientation of the main foliation of the metasediments resembles the orientation in the eclogite bodies, it is likely that deformation concordantly affected both rock associations, as already assumed by Behrmann and Ratschbacher (1989).

The calcite CPO of the marble RK17 is weak and has a clear axial symmetry of all lattice planes with the foliation normal as symmetry axis indicating pure shear deformation. Slight maxima on the girdle distributions apply (see (110) in Fig. 8). This type of CPO is typical for plastically deformed marbles with combined dislocation glide and twinning as CPO forming deformation mechanisms (Wenk et al., 1987).

6.2.2. Elastic anisotropies

In the clastic metasediments, bulk rock P-wave velocity distributions are always dominated by the mica and quartz CPOs in dependence on particular volume fractions. The strongly foliated paragneiss RK28 shows clear predominance of the mica due to the very strong preferred orientation of the (006) basal planes (Fig. 8), the high single crystal anisotropy (Fig. 3) and the relatively high volume fraction approaching 19% (Table 1). As the distribution of P-wave velocities with respect to crystallographic direction in muscovite single crystals is almost biaxial, with a very strong anisotropy (see Fig. 3), representation of the basal plane textures (see Fig. 8) is sufficient to understand the textural contribution of mica to the calculated p-wave anisotropies in the metasediments. For a mica-rich mylonite, Behrmann (1984) showed that strong basal plane textures may well be accompanied by weak CPO of other reflections. Such a texture constrains the geometry of V_p

anisotropy patterns to be approximately biaxial with a V_p minimum perpendicular to the foliation, as is the case in the micaschist and paragneiss examples in Fig. 9. Due to weak CPO strength (Fig. 8), the contribution of quartz is negligible despite a volume fraction of 50% (Table 1). Albite exhibits a random preferred orientation and therefore lowers the overall anisotropy of this sample. In samples RK5 and RK6, quartz has large influence on the modelled elastic anisotropies due to a strong CPO and higher volume fractions (71% and 92%, respectively). The three-fold symmetry of the quartz single crystal velocity distribution (Fig. 3) makes it impossible to directly infer the influence of quartz on bulk rock velocity distributions. In the case of sample RK5 with clear predominance of the mica (very strong CPO and 24 vol.%), quartz causes the splitting of the mica-controlled high velocity girdle within the foliation plane into two maxima. In contrast, the effect of the mica (8 vol.%) is hardly visible in the case of sample RK6, despite the very strong preferred orientation (Fig. 8).

To some extent, the velocity distribution of the monomineralic marble RK17 can be inferred from the CPO. As expected, the direction of minimum velocity parallels the (006) maximum. The position of the velocity maximum parallel to the lineation cannot be directly inferred from the CPO, but the elongation of the maximum within the foliation plane correlates with the axial symmetric layout of the CPO.

Observed anisotropies of the metasediments range from 5.1% to 7.4%. They are considerably higher as for the eclogites (0.4%–1.8%) and the retrogressed eclogites (1.2%–3.7%; Table 2). In the case of samples RK5 and RK28, observed magnitudes of 7.4% and 6.8% can be attributed to the high volume fraction of the mica with very strong preferred orientation. The quartz textures are comparably weak and make no significant contribution. Sample RK6 also shows strong preferred orientation of the mica, but the volume fraction of 8% is too small to determine the layout of the velocity distribution and to significantly control anisotropy. The quartz CPO is rather strong compared to other samples (Fig. 8). Together with the high volume fraction of quartz (92%) this causes the observed anisotropy magnitude of 5.3%, despite the three-fold symmetry of the single crystal velocity distribution (Fig. 3). The anisotropy of the monomineralic marble RK17 corresponds to expectations from CPO strength and CPO symmetry. It appears that the much higher degree of mica preferred orientation is mainly responsible for the higher anisotropy level in most metasediments. Some eclogites/retrogressed eclogites also bear considerable amounts of mica in the order of 10%–15% (samples RK1, RK3, RK4), but the very weak degree of preferred orientation (Figs. 6 and 7) prevents significant contribution of the mica to bulk rock anisotropy. The anisotropy level of the essentially monomineralic samples is controlled by the CPO strength or the crystallography of the mineral phase.

6.3. Comparison of modelled and laboratory data

The elastic anisotropy of rocks is largely influenced by the CPO of their constituent minerals. However, other factors like oriented microcracks or an SPO of the mineral grains can further influence elastic properties. Therefore, P-wave velocities of two eclogite samples were additionally measured in the laboratory for a comparison to the modelled data. The experimental and calculated P-wave velocity distributions of samples TW32 and TW33 exhibit coinciding maxima and minima, the outlines of the patterns are slightly different (Fig. 9A). Such a principal agreement, which has been observed also by Mauler et al. (2000) and Ábalos et al. (2010) indicates that the influence of the crack fabric is mainly due to quantities. The much larger decrease of the experimental minimum velocity compared to the experimental maximum velocity indicates that the influence of microcracks is anisotropic, and that the microcracks essentially parallel the mica basal planes. Differences are due to anisotropy, which is generally higher for the experimental velocity distributions (Table 2). We already described the considerably lower velocity level of the calculated velocity distribution of sample TW32 compared to the experimental one (Fig. 9B). The

most probable explanation is that the elastic constants of hornblende used for the averaging do not fit the actual ones. Microprobe analyses revealed that the amphibole composition of this sample does not match the composition of glaucophane as for all other eclogites and retrogressed eclogites. Hence, we used elastic constants of Aleksandrov and Ryzhova (1961) for the averaging. Compared to glaucophane, the P-wave velocities recalculated from the elastic constants are lower (hornblende: 5.98–7.86 km/s; glaucophane: 6.30–9.27 km/s), and this may explain the surprisingly low velocity level of the calculated P-wave distribution. Simply shifting the calculated velocity pattern as a whole to higher velocities would not change anisotropy significantly, so we suppose that the estimated anisotropy magnitude is affected by some error but realistic. In conclusion, the comparison indicates a remarkable anisotropy difference for the eclogite (TW33), at intermediate crustal depths it is approximately three times higher as for the crack-free (CPO-derived) sample. For the retrogressed eclogite (TW32) it is roughly 1.5 times higher. Such raw estimates give an idea about the increasing influence of the crack fabric during exhumation. According to Christensen (1974) the influence of microcracks is nonexistent at pressures exceeding about 1 GPa, which means for rocks in deeper levels of the subduction channel (e.g. more than 30 km), the modelled anisotropies are expected to be realistic.

Measured elastic anisotropies of gneisses and micaschists are likewise higher than those modelled from compositions and CPO (cf. Meltzer and Christensen, 2001; Punturo et al., 2005; Zappone et al., 2000). Generally the discrepancies are larger than in case of the eclogites. Again, this indicates that preferentially oriented mica exerts a strong influence on velocity anisotropy. In samples RK5 and RK6 of this study, the quartz CPO largely controls the modelled elastic anisotropies and not the mica CPO. Because of the effects induced by microcrack fabric the modelled anisotropy values from this study need to be considered as lower bound estimates. The same is true for the 5.1% anisotropy modelled for the marble sample with a weak CPO (RK17; Table 2), which is at the lower bound for experimentally measured anisotropies of marble (6–12%, depending on the strength of the foliation; Zappone et al., 2000; Punturo et al., 2005).

6.4. V_p/V_s ratios

Calculated V_p/V_s ratios of the fresh eclogite samples are about 1.70–1.75 (Table 2). These values are somewhat lower than those obtained by Kern et al. (1999), or Worthington et al. (2013), who modelled V_p and V_s . Laboratory investigations of Gao et al. (2001), on the other hand, produced a wide spread of V_p/V_s ratios between 1.70 and 1.86 for fresh eclogite samples, and values of up to 1.87 for retrogressed samples. Considering the suite of samples in the present study retrogression of eclogite, ultimately leading to amphibolite, has the effect of increasing the V_p/V_s ratios, to values of up to 1.78. This can be seen when examining V_p/V_s ratios in samples RK20, RK4 and TW32 (Table 2). In principle, this allows to differentiate between portions of fresh and retrogressed eclogite in subduction channels.

The V_p/V_s values of eclogite appear lower than those of peridotites of the lithospheric mantle of a downgoing slab, quoted for global earth models (1.79; e.g. Kennett et al., 1995), those of peridotites from experimental studies (e.g. Karato et al., 2008), or those from studies that take compositional differences into account (e.g. Alfonso et al., 2010). High-resolution tomographic analysis of subducting slabs (Northern Honshu; Zhang et al., 2004) shows that the peridotite slab has V_p/V_s ratios of 1.80–1.85 at depths between 60 and 85 km. A zone of lower V_p/V_s ratios (1.70–1.80) in the upper layer of the slab is interpreted to reflect subducted meta-gabbros of the oceanic crust that are transformed to blueschists and/or eclogites. The V_p/V_s values from Zhang et al. (2004) are in good accordance with those derived from the present study, and show that subducted oceanic crust can be imaged and identified by seismic tomography.

The metasediments, however, have much lower V_p/V_s ratios (Table 2), with the exception of the marble sample RK17, which has a V_p/V_s ratio of 1.85. The micaceous rocks and the paragneiss, show V_p/V_s ratios between 1.48 and 1.60, making them typical equivalents of subducted terrigenous sediments deposited in a deep sea trench setting, with V_p/V_s around 1.60 at a V_p velocity of 5 km/s (e.g. Fig. 7 of Tsuji et al., 2011). When large packets of such sediments are subducted, they should be clearly visible as low V_p/V_s features in seismic tomographic images at convergent margins. This signature may be modified by high fluid pressures (e.g. Eberhart-Phillips et al., 2005; Nugraha and Mori, 2006), but based on only the composition of subducted sediments V_p/V_s ratios would be low and coupled with high V_p and V_s anisotropies. For marble, the combination of high V_p/V_s ratio, as well as high V_p anisotropy, and V_p velocities much lower than those of peridotite or eclogite, may constrain a very specific signal for marble, which is a characteristic of subducted carbonate platforms (see e.g. Urai et al., 1990; Behrmann and Seckel, 2007, for a fossil geological example).

6.5. Seismic imaging of subduction channel rocks

The EZ is a good example for a fossilized subduction channel and the data discussed in the previous sections yield important information on the elastic properties of rocks within such a tectonic regime. Nevertheless, no serpentinite is found in this unit, which occurs in several other exhumed subduction channels (e.g. the Voltri Massif in the Western Alps; Frederico et al., 2007, or the Sierra del Convento in Cuba; Blanco-Quintero et al., 2010). Therefore the EZ represents a subduction channel, in which the viscous matrix surrounding the eclogite boudins is purely made up of high pressure metasediments.

Our results demonstrate that in this kind of subduction channel a matrix of highly anisotropic (up to 7.5%) metasediments with low V_p (6.2–6.4 km/s) and low V_p/V_s ratios (1.48–1.60) can be expected. At depth of over 45–50 km, where eclogite high pressure assemblages are stable, the eclogite boudins in the subduction channel exhibit low anisotropy (~1.5%), high V_p (8.0–8.3 km/s) and a relatively high V_p/V_s ratio (~1.70). At higher levels in the subduction channel, retrogression of the eclogites increases their anisotropy to up to 3.7%, mostly lowers their velocity (7.1–7.6 km/s) and somewhat increases their V_p/V_s ratio (~1.78). This shows that retrogression of eclogite boudins in the subduction channel may be detectable. Marbles in the subduction channel, which originate from subducted carbonate platforms (e.g. e.g. Urai et al., 1990; Behrmann and Seckel, 2007), yield an anisotropy of about 5% and a V_p of about 6.9 km/s. Further, their V_p/V_s ratio is very high with values of 1.85, constraining a specific seismic signal for marble.

The present state of instrumental techniques only permits relatively low resolution images at depths in which high pressure subduction channels are active. Yet, substantial progress was made improving the resolution of seismic imaging in the last decades and it is assumable that a detection of the internal structures within subduction channels will be possible in the future.

In addition, the expected signal of subduction channels can be evaluated by numerical modelling of seismic waves. Essen et al. (2009) modelled subduction channels as a layer of intermediate velocity above the downgoing slab to predict the seismic signal, and showed that high amplitudes of guided waves could indicate the existence of a subduction channel. However, no internal structure within this layer was incorporated in their model. Recent numerical simulations of Friederich et al. (2014) included a more detailed subduction channel structure with eclogite blocks in a serpentinite matrix. The authors demonstrated that this internal structure leads to very specific seismic signatures. In their model, elastic anisotropy of the rocks was neglected, since the large-scale anisotropy of the subduction channel was considered insignificantly small. Our results show that anisotropy of subduction channel rocks can be significant in case of the metasedimentary matrix surrounding the eclogite blocks. An incorporation of anisotropy

in numerical simulations could, therefore, help to make the resulting images more realistic.

7. Conclusion

We use crystallographic preferred orientations (CPO) of a comprehensive suite of rocks from the Tauern Eclogite Zone in southern Austria as a petrophysical analogue for a subduction channel between the downgoing and overriding plates at modern convergent margins. Using this analogy we show in particular that:

1. Time-of-flight neutron diffraction studies on large polymineralic rock samples and the application of full pattern fit methods are a valuable quantitative tool to assess CPO and resulting elastic anisotropy and V_p/V_s ratios of mineralogically complex rocks.
2. P-wave anisotropies of fresh deformed eclogites are fairly low, with an average of about 1.5%, and mainly constrained by pronounced omphacite CPO. Growth and deformation of retrograde amphibole also produces a pronounced CPO, raising P-wave velocity anisotropy to up to 3.7%, and possibly changing the orientations of velocity maxima.
3. Elastic anisotropies of the once subducted metasediments are higher (up to 7.4%) and constrained by quartz and mica CPO in clastic sediments.
4. Most rock types of such subduction channels have distinct signatures of V_p/V_s ratios. Fresh eclogites can be distinguished from retrogressed ones, and both rock types can in turn be distinguished from mantle peridotites and metasediments of the downgoing lithospheric slab.
5. Subducted terrigenous sediments are not only strongly anisotropic, but also have low V_p/V_s ratios. This makes them detectable at depth in active subduction channels using seismic tomography. Marbles, which may constitute subducted marine carbonates, are distinguishable from terrigenous clastics by high anisotropy, but also high V_p/V_s ratios.

Acknowledgements

Funding by the German Federal Ministry of Education and Research (BMBF) through grants 05K09FKA and 05K13FKB is gratefully acknowledged. We kindly thank Dr. Tatiana Ivankina and the anonymous reviewer for their constructive and helpful comments. We are also grateful to the Frank Laboratory of Neutron Physics (FLNP) at Dubna (Russia) for support in the texture measurements.

References

- Ábalos, B., Fountain, D.M., Gil Ibarra, J.I., Puelles, P., 2010. Eclogite as a seismic marker in subduction channels: seismic velocities, anisotropy, and petrofabric of Cabo Ortegal eclogite tectonites (Spain). *GSA Bull.* 123 (3/4), 439–456.
- Agard, P., Yamato, P., Jolivet, L., Burov, E., 2009. Exhumation of oceanic blueschists and eclogites in subduction zones: timing and mechanisms. *Earth Sci. Rev.* 92, 53–79.
- Aleksandrov, K.S., Ryzhova, T.V., 1961. The elastic properties of rock forming minerals. *Izvestija Academy of Science USSR. Geophys. Ser.* 12, 1799–1804.
- Aleksandrov, K.S., Alchikov, U.V., Belikov, B.P., Zaslavski, B.I., Krupny, A.I., 1974. Elastic wave velocities in minerals at atmospheric pressure and increasing precision of elastic constants by means of EVM. *Izvestija Academy of Science USSR. Geol. Ser.* 10, 15–24.
- Anozkiewicz, R., Platt, J.P., Thirlwall, M.F., Wakabayashi, J., 2004. Franciscan subduction off to a slow start: evidence from high-precision Lu–Hf garnet ages on high grade-blocks. *Earth Planet. Sci. Lett.* 225, 147–161.
- Angiboust, S., Agard, P., Jolivet, L., Beyssac, O., 2009. The Zermatt–Saas ophiolite: the largest (60–km wide) and deepest (c. 70–80 km) continuous slice of oceanic lithosphere detached from a subduction zone? *Terra Nova* 21, 171–180.
- Babuska, V., Fiala, J., Kumazawa, M., Ohno, I., Sumino, Y., 1978. Elastic properties of garnet solid-solution series. *Phys. Earth Planet. Inter.* 16, 157–176.
- Barruol, G., Kern, H., 1996. Seismic anisotropy and shear-wave splitting in lower-crustal and upper-mantle rocks from the Ivrea Zone experimental and calculated data. *Phys. Earth Planet. Inter.* 95, 175–194.
- Bascou, J., Barruol, G., Vauchez, A., Mainprize, D., Eglydio-Silva, M., 2001. EBSD-measured lattice preferred orientations and seismic properties of eclogites. *Tectonophysics* 342, 61–80.
- Behrmann, J.H., 1984. Microstructure and chemistry of white mica in a low grade mylonite. *J. Struct. Geol.* 6, 283–292.

- Behrmann, J.H., Ratschbacher, L., 1989. Archimedes revisited: a structural test of eclogite emplacement models in the Austrian Alps. *Terra Nova* 1, 242–252.
- Behrmann, J.H., Seckel, C., 2007. Structural analysis of the Small Cyclades Iraklia and Schinoussa (Aegean Sea, Greece). *Geotecton. Res.* 95, 1–11.
- Bezacier, L., Reynard, B., Bass, J.D., Wang, J., Mainprice, D., 2010. Elasticity of glaucophane, seismic velocities and anisotropy of the subducted oceanic crust. *Tectonophysics* 494, 201–210.
- Bhagat, S.S., Bass, J.D., Smyth, J.R., 1992. Single-crystal elastic properties of omphacite-C2/C by Brillouin spectroscopy. *J. Geophys. Res. Solid Earth* 97, 6843–6848.
- Blanco-Quintero, I.F., García-Casco, A., Gerya, T.V., 2010. Tectonic blocks in serpentinite mélange (eastern Cuba) reveal large-scale convective flow of the subduction channel. *Geology* 39, 79–82.
- Bousquet, R., 2008. Metamorphic heterogeneities within a single HP unit: overprint effect or metamorphic mix? *Lithos* 103, 46–69.
- Brown, J.M., Abramson, E.H., Angel, R.J., 2006. Triclinic elastic constants for low albite. *Phys. Chem. Miner.* 33, 256–265.
- Christensen, N.L., 1974. Compressional wave velocities in possible mantle rocks to pressures of 30 kbars. *J. Geophys. Res.* 79, 407–412.
- Christoffel, E.B., 1874. Über die Fortpflanzung von Stößen durch elastische, feste Körper. *Annali di Matematica* 8, 193–243.
- Cloos, M., Shreve, R.L., 1988. Subduction-channel model of prism accretion, mélange formation, sediment subduction, and subduction erosion at convergent plate margins: implications and discussion. *Pure Appl. Geophys.* 128 (314), 501–545.
- Dachs, E., 1990. Geothermobarometry in metasediments of the southern Grossvenediger area (Tauern Window, Austria). *J. Metamorph. Geol.* 8, 217–230.
- Dandekar, D.P., 1968. Variation in the elastic constants of calcite with pressure. *Am. Geophys. Union Trans.* 49 (323 pp.).
- De Capitani, C., Brown, T.H., 1987. The computation of chemical equilibrium in complex systems containing non-ideal solutions. *Geochim. Cosmochim. Acta* 51, 2639–2652.
- De Capitani, C., Petrakakis, K., 2010. The computation of equilibrium assemblage diagrams with Theriak/Domino software. *Am. Mineral.* 95, 1006–1016.
- De Franco, R., Govers, R., Wortel, R., 2008. Nature of the plate contact and subduction zones diversity. *Earth Planet. Sci. Lett.* 271, 245–253.
- Eberhart-Phillips, D., Reyners, M., Chadwick, M., Chiu, J.-M., 2005. Crustal heterogeneity and subduction processes: 3-D Vp, Vp/Vs and Q in the southern North Island, New Zealand. *Geophys. J. Int.* 162, 270–288.
- Essen, K., Braatz, M., Ceranna, L., Friederich, W., Meier, T., 2009. Numerical modelling of seismic wave propagation along the plate contact of the Hellenic Subduction Zone—the influence of a deep subduction channel. *Geophys. J. Int.* 179, 1737–1756.
- Frederico, L., Crispini, L., Scambelluri, M., Capponi, G., 2007. Ophiolite mélange zone records exhumation in a fossil subduction channel. *Geology* 35, 499–502.
- Frederich, W., Lambrecht, L., Stöckhert, B., Wassmann, S., Moos, C., 2014. Seismic visibility of a deep subduction channel – insights from numerical simulation of high-frequency seismic waves emitted from intermediate depth earthquakes. *Solid Earth* 5, 141–159.
- Gao, S., Kern, H., Jin, Z., Popp, T., Jin, S., Zhang, H., Zhang, B., 2001. Poisson's ratio of eclogite: the role of retrogression. *Earth Planet. Sci. Lett.* 102, 523–531.
- Glodny, J., Ring, U., Kühn, A., Gleissner, P., Franz, G., 2005. Crystallization and very rapid exhumation of the youngest Alpine eclogites (Tauern Window, Eastern Alps) from Rb/Sr mineral assemblage analysis. *Contrib. Mineral. Petrol.* 149, 699–712.
- Guillot, S., Hattori, K., Sigoyer, J., Nägler, T., Auzende, A.L., 2001. Evidence of hydration of the mantle wedge and its role in the exhumation of eclogites. *Earth Planet. Sci. Lett.* 193, 115–127.
- Helmsstaedt, H., Anderson, D.L., Gavasci, A.T., 1972. Petrofabric studies of eclogite, spinel websterite, and spinel-lherzolite xenoliths from kimberlite-bearing breccia pipes in southeastern Utah and northeastern Arizona. *J. Geophys. Res.* 77, 4350–4365.
- Heyliger, P., Ledbetter, H., Kim, S., 2003. Elastic constants of natural quartz. *J. Acoust. Soc. Am.* 114, 644–650.
- Hill, R., 1952. The elastic behavior of a crystalline aggregate. *Proc. Phys. Soc. A65*, 349–354.
- Holland, T.J.B., Powell, R., 1998. An internally-consistent thermodynamic dataset for phases of petrological interest. *J. Metamorph. Geol.* 16, 309–344.
- Hoschek, G., 2001. Thermobarometry of metasediments and metabasites from the Eclogite zone of the Hohe Tauern, Eastern Alps, Austria. *Lithos* 59, 127–150.
- Hoschek, G., 2004. Comparison of calculated P-T pseudosections for a kyanite eclogite from the Tauern Window, Eastern Alps, Austria. *Eur. J. Mineral.* 16, 59–72.
- Ivankina, T.I., Kern, H.M., Nikitin, A.N., 2005. Directional dependence of P- and S-wave propagation and polarization in foliated rocks from the Kola superdeep well: evidence from laboratory measurements and calculations based on TOF neutron diffraction. *Tectonophysics* 407, 25–42.
- Karato, S., Jung, H., Katayama, I., Skemer, P., 2008. Geodynamic significance of seismic anisotropy of the upper mantle: new insights from laboratory studies. *Annu. Rev. Earth Planet. Sci.* 36, 59–95.
- Kennett, B.L.N., Engdahl, E.R., Buland, R., 1995. Constraints on seismic velocities in the Earth from travel times. *Geophys. J. Int.* 122, 108–124.
- Keppler, R., Ullemeyer, K., Behrmann, J.H., Stipp, M., 2014. Potential of full pattern fit methods for the texture analysis of geological materials: implications from texture measurements at the recently upgraded neutron time-of-flight diffractometer SKAT. *J. Appl. Crystallogr.* 47. <http://dx.doi.org/10.1107/S1600576714015830>.
- Kern, H., Gao, S., Jin, Z., Popp, T., Jin, S., 1999. Petrophysical studies on rocks from the Dabie ultrahigh-pressure (UHP) metamorphic belt, Central China: implications for the composition and delamination of the lower crust. *Tectonophysics* 301, 191–215.
- Kern, H., Jin, Z., Gao, S., Popp, T., Xu, Z., 2002. Physical properties of ultrahigh-pressure metamorphic rocks from the Sulu terrain, eastern central China: implications for the seismic structure at the Donghai (CCSD) drilling site. *Tectonophysics* 354, 315–330.
- Kern, H., Ivankina, T.I., Nikitin, A.N., Lokajčiček, T., Pros, Z., 2008. The effect of oriented microcracks and crystallographic and shape preferred orientation on bulk elastic anisotropy of a foliated biotite gneiss from Outokumpu. *Tectonophysics* 457, 143–149.
- Kitamura, K., 2006. Constraint of lattice-preferred orientation (LPO) on Vp anisotropy of amphibole-rich rocks. *Geophys. J. Int.* 165, 1058–1065.
- Kurz, W., Froitzheim, N., 2002. The exhumation of eclogite-facies metamorphic rocks – a review of models confronted with examples from the Alps. *Int. Geol. Rev.* 44 (8), 702–743.
- Kurz, W., Neubauer, F., Genser, J., Dachs, E., 1998. Alpine geodynamic evolution of passive and active continental margin sequences in the Tauern Window (eastern Alps, Austria, Italy): a review. *Int. J. Earth Sci.* 87, 225–242.
- Llana-Fúnez, S., Brown, D., 2012. Contribution of crystallographic preferred orientation to seismic anisotropy across a surface analog of the continental Moho at Cabo Ortegal, Spain. *GSA Bull.* 124 (9/10), 1495–1513.
- Lutterotti, L., Matthies, S., Wenk, H.-R., Schultz, A.J., Richardson, J.W., 1997. Combined texture and structure analysis of deformed limestone from time-of-flight neutron diffraction spectra. *J. Appl. Phys.* 81, 594–600.
- Mainprice, D., Humbert, M., 1994. Methods of calculating petrophysical properties from lattice preferred orientation data. *Surv. Geophys.* 15, 575–592.
- Mainprice, D., Ildefonse, B., 2009. Seismic anisotropy of subduction zone minerals – contribution of hydrous phases. In: Lallemand, S., Funicello, F. (Eds.), *Subduction Zone Geodynamics*. Springer-Verlag, Berlin Heidelberg, pp. 63–84.
- Matthies, S., 2011. GEO-MIX-SELF calculation of the elastic properties of a textured graphite sample at different hydrostatic pressures. *J. Appl. Crystallogr.* 45, 1–16.
- Matthies, S., Humbert, M., 1995. On the principle of a geometric mean of even-rank symmetric tensors for textured polycrystals. *J. Appl. Crystallogr.* 28, 254–266.
- Matthies, S., Lutterotti, L., Wenk, H.R., 1997. Advances in Texture Analysis from Diffraction Spectra. *J. Appl. Cryst.* 30, 31–42.
- Mauler, A., Burlini, L., Kunze, K., Philippot, P., Burg, J.-P., 2000. P-wave anisotropy in eclogites and relationship to the omphacite crystallographic fabric. *Phys. Chem. Earth* 15, 119–126.
- Meltzer, A., Christensen, N., 2001. Nanga Parbat crustal anisotropy: implications for interpretation of crustal velocity structure and shear-wave splitting. *Geophys. Res. Lett.* 28 (10), 2129–2132.
- Montagner, J.-P., Guillot, L., 2003. Seismic anisotropy and global geodynamics. *Mineral. Soc. Am.* 51, 353–385.
- Montagner, J.-P., Tanimoto, T., 1990. Global anisotropy in the upper mantle inferred from the regionalization of phase velocities. *J. Geophys. Res.* 95 (B4), 4797–4819.
- Nagel, T.J., Herwartz, D., Rexroth, S., Munker, C., Froitzheim, N., Kurz, W., 2013. Lu-Hf dating, petrography, and tectonic implications of the youngest Alpine eclogites (Tauern Window, Austria). *Lithos* 170–171, 179–190.
- Neufeld, K., Ring, U., Heidelbach, F., Dietrich, S., Neuser, R.D., 2008. Omphacite textures in eclogites of the Tauern Window: implications for the exhumation of the Eclogite Zone, Eastern Alps. *J. Struct. Geol.* 30, 976–992.
- Nugraha, A.D., Mori, J., 2006. Three-dimensional velocity structure in the Bungo Channel and Shikoku area, Japan, and its relationship to low-frequency earthquakes. *Geophys. Res. Lett.* 33. <http://dx.doi.org/10.1029/2006GL028479>.
- Platt, J.P., 1986. Dynamics of orogenic wedges and the uplift of high pressure metamorphic rocks. *Bull. Geol. Soc. Am.* 97, 1037–1053.
- Pros, Z., Lokajčiček, T., Klíma, K., 1998. Laboratory study of elastic anisotropy on rock samples. *Pure Appl. Geophys.* 151, 619–629.
- Pros, Z., Lokajčiček, T., Prikryl, R., Klíma, K., 2003. Direct measurement of 3D elastic anisotropy on rocks from the Ivrea Zone (Southern Alps, NW Italy). *Tectonophysics* 370, 31–47.
- Punturo, R., Kern, H., Cirrincione, R., Mazzoleni, P., Pezzino, A., 2005. P- and S-wave velocities and densities in silicate and calcite rocks from the Peloritani mountains, Sicily (Italy): the effect of pressure, temperature and the direction of wave propagation. *Tectonophysics* 409, 55–72.
- Raith, M., Mehrens, C., Thöle, W., 1980. Gliederung, tektonischer Bau und metamorphe Entwicklung der penninischen Serien im südlichen Venediger-Gebiet. *Osttiroler Jahrb. Geol. Bundesanst.* 123, 1–37.
- Ratschbacher, L., Dingeldey, C., Miller, C., Hacker, B.R., McWilliams, M.O., 2004. Formation, subduction, and exhumation of Penninic oceanic crust in the Eastern Alps: time constraints from 40Ar/39Ar geochronology. *Tectonophysics* 394, 155–170.
- Reuss, A., 1929. Berechnung der Fließgrenze von Mischkristallen auf Grund der Plastizitätsbedingung für Einkristalle. *Z. Angew. Math. Mech.* 9, 49–58.
- Schmid, S.M., Casey, M., 1986. Complete fabric analysis of some commonly observed quartz c-axis patterns. *Geophys. Monogr.* 36, 263–286.
- Schmid, S.M., Scharf, A., Handy, M.R., Rosenberg, C.L., 2013. The Tauern Window (Eastern Alps, Austria): a new tectonic map, with cross-sections and a tectonometamorphic synthesis. *Swiss J. Geosci.* 106, 1–32.
- Shreve, R.L., Cloos, M., 1986. Dynamics of sediment subduction, mélange formation, and prism accretion. *J. Geophys. Res.* 91 (B10), 10229–10245.
- Silver, P.G., 1996. Seismic anisotropy beneath the continents: probing the depths of geology. *Annu. Rev. Earth Space Sci.* 24, 385.
- Stipp, M., Stünitz, H., Heilbronner, R., Schmid, S.M., 2002. The eastern Tonale fault zone: a natural laboratory for crystal plastic deformation of quartz over a temperature range from 250 to 700 °C. *J. Struct. Geol.* 24, 1861–1884.
- Stöckhert, B., Massonne, H.-J., Nowlan, E.U., 1997. Low differential stress during high-pressure metamorphism: the microstructural record of a metapelite from the Eclogite Zone, Tauern Window, Eastern Alps. *Lithos* 41, 103–118.
- Tsuji, T., Dvorkin, J., Mavko, G., Nakata, N., Matsuoka, T., Nakanishi, A., Kodaira, S., Nishizawa, O., 2011. Vp/Vs ratio and shear-wave splitting in the Nankai Trough seismicogenic zone: insights into effective stress, pore pressure, and sediment consolidation. *Geophysics* 76, WA71–WA82. <http://dx.doi.org/10.1190/1.3560018>.

- Ullemeyer, K., Spalthoff, P., Heinicz, J., Isakov, N.N., Nikitin, A.N., Weber, K., 1998. The SKAT texture diffractometer at the pulsed reactor IRR-2 at Dubna: experimental layout and first measurements. *Nucl. Inst. Methods Phys. Res.* 412, 80–88.
- Ullemeyer, K., Siegesmund, S., Rasolofosaon, P.N.J., Behrmann, J.H., 2006. Experimental and texture-derived P-wave anisotropy of principal rocks from the TRANSALP traverse: an aid for the interpretation of seismic field data. *Tectonophysics* 414, 97–116.
- Ullemeyer, K., Leiss, B., Stipp, M., 2010. Textures and microstructures in peridotites from the Finero complex (Ivrea Zone, Alps) and their influence on the elastic rock properties. *Solid State Phenom.* 160, 183–188.
- Ullemeyer, K., Nikolayev, D.I., Christensen, N.I., Behrmann, J.H., 2011. Evaluation of intrinsic velocity–pressure trends from low-pressure P-wave velocity measurements in rocks containing microcracks. *Geophys. J. Int.* 185, 1312–1320.
- Urai, J.L., Schuiling, R.D., Jansen, J.B.H., 1990. Alpine deformation on Naxos (Greece). In: Knipe, R.J., Rutter, E.H. (Eds.), *Deformation Mechanisms, Rheology and Tectonics*. Spec. Publ. Geol. Soc. London 54, pp. 509–522.
- Vaughan, M.T., Guggenheim, S., 1986. Elasticity of muscovite and its relationship to crystal structure. *J. Geophys. Res.* 91, 4657–4664.
- Voigt, W., 1928. *Lehrbuch der Kristallphysik*. Teubner, Leipzig.
- Von Dreele, R.B., 1997. Quantitative texture analysis by rietveld refinement. *J. Appl. Cryst.* 30, 517–525.
- Wenk, H.R., Takeshita, T., Bechler, E., Erskine, B.G., Matthies, S., 1987. Pure shear and simple shear calcite textures. Comparison of experimental, theoretical and natural data. *J. Struct. Geol.* 9, 731–745.
- Wenk, H.-R., Lutterotti, L., Vogel, S.C., 2010. Rietveld texture analysis from TOF neutron diffraction data. *Powder Diffract.* 25 (3), 283–296.
- Wenk, H.-R., Vasin, R.N., Kern, H., Matthies, S., Vogel, S.C., Ivankina, T.I., 2012. Revisiting elastic anisotropy of biotite gneiss from the Outokumpu scientific drill hole based on new texture measurements and texture-based velocity calculations. *Tectonophysics* 570–571, 123–134.
- Worthington, J.R., Hacker, B.R., Zandt, G., 2013. Distinguishing eclogite from peridotite: EBSD-based calculations of seismic velocities. *Geophys. J. Int. Seism.* <http://dx.doi.org/10.1093/gji/ggt004>.
- Zappone, A., Fernández, M., García-Duenas, V., Burlini, L., 2000. Laboratory measurements of seismic P-wave velocities on rocks from the Betic chain (southern Iberian Peninsula). *Tectonophysics* 317, 259–272.
- Zhang, H., Thurber, C.H., Shelly, D., Ide, S., Beroza, G.C., Hasegawa, A., 2004. High-resolution subducting-slab structure beneath northern Honshu, Japan, revealed by double-difference tomography. *Geology* 42, 361–364. <http://dx.doi.org/10.1130/G202612>.
- Zhang, X.L., Hu, L., Ji, M., Liu, J.L., Song, H.L., 2013. Microstructures and deformation mechanisms of hornblende in Guandi complex, the Western Hills, Beijing. *Sci. China Earth Sci.* 56 (9), 1510–1518.

MANUSKRIFT # 3

**Deformation of subduction channel rocks - Insights from
crystallographic preferred orientations and
microstructures of eclogites and metasediments from the
Eclogite Zone of the Tauern Window, Austria**

In preparation to be submitted

Deformation of subduction channel rocks - Insights from crystallographic preferred orientations and microstructures of eclogites and metasediments from the Eclogite Zone of the Tauern Window, Austria

ABSTRACT

The Eclogite Zone (EZ) of the Tauern Window is an exhumed subduction channel of the Eastern Alps consisting of kilometer sized eclogite lenses wrapped in a matrix of metasediments. The eclogites show variable grades of retrogression, from fresh eclogites still exhibiting their high pressure mineral assemblage to those that were severely retrogressed during exhumation. In this study, microfabrics of both fresh and retrogressed eclogites, as well as the metasediments surrounding the eclogite lenses were investigated. EBSD analysis of fresh eclogites shows omphacite porphyroclasts with local subgrains, as well as small recrystallized omphacite grains. The porphyroclasts exhibit increasing jadeite content from core to rim, whereas highest jadeite contents are observed for the recrystallized grains. This points to omphacite growth and dynamic recrystallization during subduction at increasing pressure. Bulk omphacite CPO of fresh eclogites exhibits an SL-type fabrics pointing to plane strain during subduction. EBSD analysis of retrogressed eclogites also showed omphacite porphyroclasts with local subgrains as well as small recrystallized grains. In the retrogressed eclogites the porphyroclasts mainly display decreasing jadeite content from core to rim. The recrystallized grains show lower jadeite contents than the porphyroclast cores pointing to dynamic recrystallization during the exhumation at decreasing pressure. Omphacite CPO of the retrogressed eclogites mainly exhibits SL-type fabrics pointing to plane strain during exhumation. L-type fabrics and S-type fabrics also occur indicating local strain variations in the prolate and oblate strain field. The CPO of retrograde glaucophane always matches the omphacite CPO, which suggests that the local strain variations persisted from eclogite facies to the exhumation to blueschist facies. Quartz CPO of the metasediments is also pronounced. Deformation of the metasediments outlasted that of the eclogite lenses, as confirmed by lower Si-contents of mica. The metasediments therefore record the final stages of deformation in the EZ.

1. Introduction

Subduction channels comprising a mélange of sediments and oceanic crust represent shear zones of up to a few km thickness on top of the downgoing oceanic plate in subduction zones. The concept of material transport and specifically the exhumation processes within subduction channels have first been established by Shreve and Cloos (1986). Originally applied to the circulation of sedimentary material within a crustal wedge reaching depths of 30 km, this model has been extended to the exhumation of oceanic crust and its sedimentary cover from depths of more than 70 km in recent models (e.g., Angiboust et al., 2009; Agard et al., 2009). At this greater depth the subduction channel rocks are subjected to high-pressure metamorphism leading to the formation of eclogites and high pressure metasediments (e.g., Ernst, 1970; Goffé and Chopin, 1986).

Eclogites from exhumed subduction channels can show a pronounced crystallographic preferred orientation (CPO) of omphacite, their main constituent, e.g., Monviso ophiolitic complex in the Western Alps (Mauler et al., 2000a), Les Essarts complex in France (Mauler et al., 2001), the Cabo Ortegal complex in Spain (Abalos et al., 2010), Adula Nappe in the Central Alps and Eclogite Zone in the Eastern Alps (Kurz et al., 2004). The deformation mechanisms leading to such pronounced omphacite CPOs, however, are not completely understood. Godard and Van Roermund determined the activity of three slip systems of omphacite $[001]\{100\}$, $\frac{1}{2}\langle 110 \rangle\{-110\}$, and $[001]\{110\}$ using transmission electron microscopy (TEM). With the activity of three slip systems alone, strain cannot be fully accommodated according to Von Mises criterion (von Mises, 1928) and the authors concluded that other deformation mechanisms must be involved. Mauler et al. (2000) investigated microstructures and crystallographic preferred orientations (CPOs) of experimentally deformed omphacite. Their study indicated that anisotropic growth of omphacite is the main CPO forming mechanism. Helmstedt et al. (1979) identified two principal types of omphacite CPO: L-type fabrics characterized by alignment of $[001]$ parallel to the lineation and $[010]$ girdles perpendicular to the lineation, and S-type fabrics, in which $[001]$ exhibits girdles within the foliation plane and $[010]$ is aligned with the foliation normal. According to Brenker et al. (2002) the formation of S-type and L-type fabrics is determined by cation ordering of omphacite, which is in turn defined by its formation temperature and jadeite content. Abalos (1997) and Kurz et al. (2004) on the other hand, studied omphacite CPO in naturally deformed eclogites and infer a strain induced CPO development leading to L-fabrics due to prolate strain and S-fabrics due to oblate strain. Another question is the timing of CPO development in eclogites, i.e., does it take place mainly during subduction of the rocks, during their exhumation, or is it a continuous process? Based on omphacite CPO data of eclogites, Neufeld et al. (2008)

assume that CPO formation in eclogites occurs during prograde metamorphism of subduction due to a higher fluid availability. However, deformation related retrogression of eclogites is well documented (e.g. Abalos and Puelles, 2003), and Kurz (2005) relates CPO formation of eclogites with both, subduction and exhumation.

The Eclogite Zone (EZ) of the Tauern Window offers the great opportunity to study deformation during both prograde and retrograde metamorphism stages of subduction channel rocks. The EZ is an exhumed high pressure unit of the Eastern Alps exhibiting a subduction channel structure with eclogite lenses in a metasedimentary matrix (e.g. Smye et al. 2011). Several aspects make the EZ an ideal study area for subduction channel deformation and CPO formation. The eclogite lenses reach sizes of several kilometres (Raith et al., 1980) and it is unlikely that these large and partly irregularly shaped lenses rotated much within the metasediments. Both metasedimentary matrix and eclogite lenses experienced high pressure metamorphism up to 2.5 GPa (e.g. Holland, 1979, Dachs, 1986; Selverstone, 1992; Stöckhert et al., 1997; Hoschek, 2001; 2004) and were exhumed as a coherent unit (Dachs, 1990; Behrmann and Ratschbacher, 1989). The eclogites of the EZ comprise the complete spectrum from prograde blueschist facies relicts, over fresh eclogites, to eclogites, which were severely retrogressed under blueschists facies conditions.

The main aims of the present study are the determination of CPO forming mechanisms in eclogites, as well as the timing of their deformation. Furthermore, we want to determine, which rock units accommodate strain at different stages in the subduction channel. For this purpose, we investigate the microfabrics of fresh and retrogressed eclogites, as well as metasediments from the EZ to unravel their deformation from subduction to peak pressures and back to the exhumation to crustal levels. Our results give insights into CPO formation and deformation mechanisms of eclogites and their operation within the Tauern window subduction channel.

2. Geological overview

The EZ is a high pressure unit in the southern Tauern Window (Fig. 1 A and B), which is a tectonic window exposing European continental units and Penninic oceanic units beneath the Adria-derived Austroalpine. It developed through crustal scale folding, EW extension, and an indentation of the Southern Alps (Laubscher, 1988; Ratschbacher et al., 1989; Behrmann and Frisch, 1990; Selverstone, 1993; Rosenberg et al., 2004; Schmid et al., 2013). The EZ is located in the southern Tauern Window and originates from transitional crust between the distal European margin to the north and the Penninic ocean to the south. It is assumed to have developed from a volcano-sedimentary sequence, which formed during rifting of the Penninic ocean in the Jurassic (Kurz et al., 1998b). The EZ entered the subduction channel during the subduction of the Penninic

ocean beneath the Adriatic microcontinent and reached PT conditions of 2.0-2.5 GPa and 600 +/- 30°C (Holland, 1979, Dachs, 1986; Selverstone, 1992; Stöckhert et al., 1997; Hoschek, 2001; 2004). Recent Rb-Sr and Lu-Hf dating revealed an Oligocene age for peak conditions in the EZ and a fast exhumation within 1-2 Ma (Glodny et al., 2005; Nagel et al., 2013). Initial exhumation of the EZ occurred under relatively low temperature (Fig. 2A) and part of the unit was retrogressed under blueschist facies conditions (Dachs, 1986; Behrmann and Ratschbacher, 1989; Zimmermann et al., 1994; Kurz et al., 1998a). Furthermore, the EZ was subjected to a late stage high temperature overprint (Holland and Richardson, 1979). However, due to the fast exhumation large parts of the unit escaped retrogression.

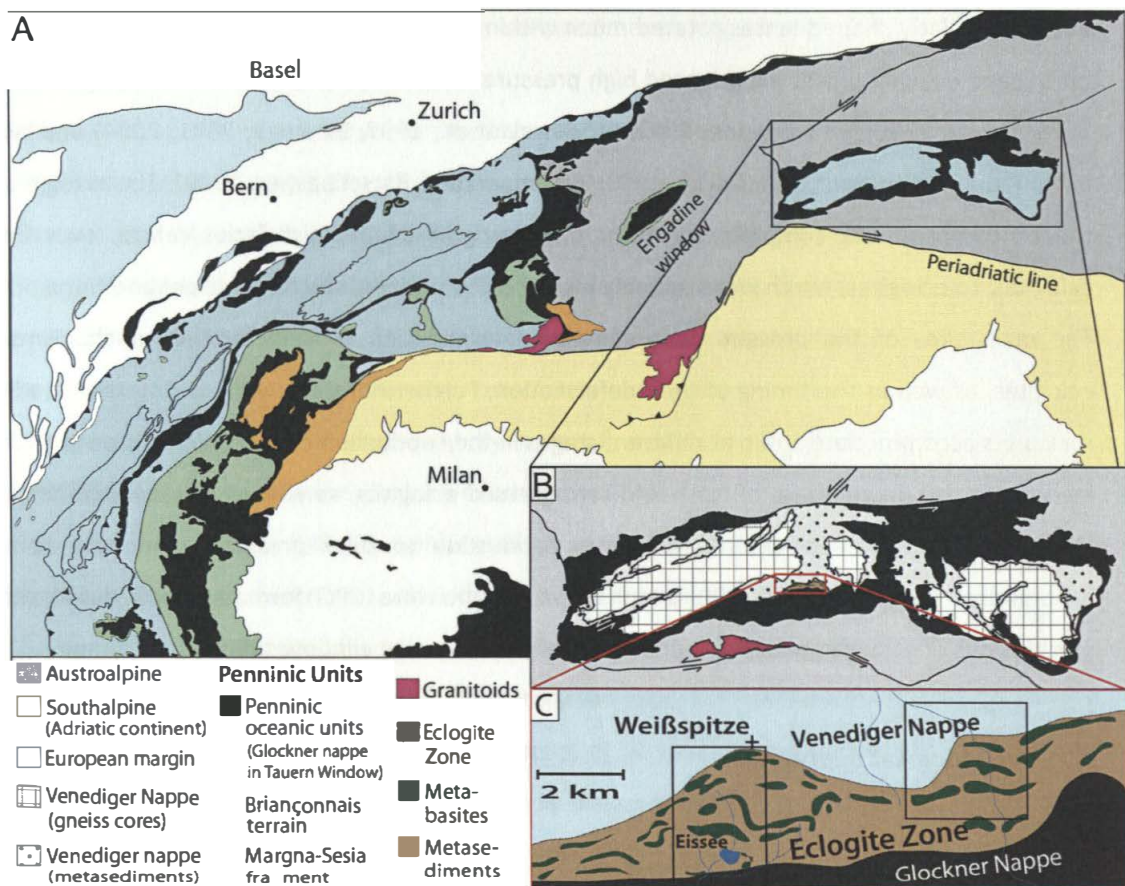


Figure 4.1: Tectonic maps of (A) the Alps, (B) the Tauern Window (after Froitzheim et al., 1996; Schmid et al., 2013) and (C) the Eclogite Zone (after Neufeld et al., 2008). Insets indicates locations of field areas shown in figure 2B and C.

Today, the EZ is steeply dipping to the SSE and sandwiched between the Venediger nappe in its footwall, which was part of the European basement and the Glockner nappe in its hangingwall, which originates from Penninic oceanic crust (Fig 1C). Under- and overlying nappes are of lower metamorphic conditions than the EZ. The Venediger nappe reached a metamorphic peak of 10-12 kbar and 550°C, which corresponds to the blueschist facies event of the EZ. This indicates an

emplacement of the EZ on the Venediger nappe under blueschist facies metamorphic conditions (Franz et al., 1991; Selverstone, 1993). Geothermobarometric data of Dachs (1990) indicate peak conditions of 7.5 ± 1 kbar and $525 \pm 25^\circ\text{C}$ for the overlying Glockner nappe.

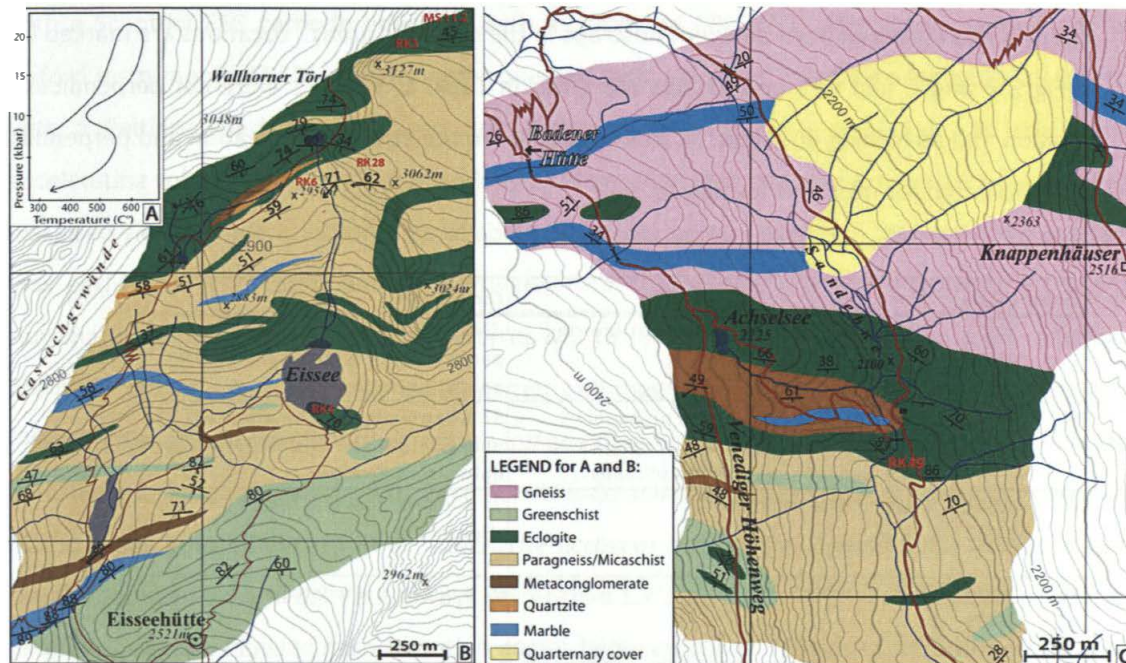


Figure 4.2: (A) PT-path of the EZ after Holland, 1979; Dachs, 1986; Spear and Franz 1986; Dachs, 1990; Zimmermann et al., 1994; Kurz et al., 1998a. Geologic maps of the Timmeltal (B), constructed from own work and completed with map of Raith et al., (1980) and the Frosnitzal (C). Marked in red are sample locations. Main foliation and stretching lineation are indicated.

Previous field studies covering the entire EZ revealed a steeply S to SE-dipping foliation and a subhorizontal stretching and mineral lineation preferentially dipping gently to the W and SW (e.g., Behrmann and Ratschbacher, 1989; Fig. 2A, B). The EZ consists of lenses of eclogites, with thicknesses between a few meters and several hundreds of meters. They are enclosed in a matrix of paragneisses, micaschists, quartzites, metaconglomerates, and marbles (Fig. 2B and C), which were part of the high pressure mélangé in the subduction channel (Spear and Franz, 1986; Dachs, 1990).

2. Methods

A detailed field mapping was performed in the areas of the Timmeltal and Frosnitzal (Fig. 2 B and C) and a set of rock samples including fresh eclogites, retrogressed eclogites, and metasediment samples was collected from different outcrops in the two field areas. Locations are marked in red in Fig 2 B and C and GPS coordinates are given in Table 1. Samples were cut perpendicular to foliation and stretching lineation, as well as parallel to the stretching lineation and perpendicular to the foliation for microfabric analysis.

Sample	Location	Description	Composition
RK3	30193/ 21692	Fine grained eclogite with weak layering	43 % omphacite, 22 % garnet, 15 % paragonite, 10 % glaucophane, 9 % quartz, 1 % rutile
RK4	30157/ 21550	Retrogressed eclogite with pronounced carbonate rich layers. Medium grain size and layers of about 1-5 mm thickness.	37 % barroisite, 25 % omphacite, 12 % phengite, 9 % garnet, 8 % albite, 6 % dolomite, 3 % calcite
RK5	30104/ 21542	Layered micaschist	71 % quartz, 24 % muscovite, 5 % clinozoisite
RK6	30136/ 21639	Mica-quartzite	92 % quartz, 8 % muscovite
RK28	30147/ 21637	Paragneiss with strong mica foliation	50% quartz, 31 % albite, 19 % muscovite
RK49	30636/ 21642	Layered, retrogressed eclogite	25 % omphacite, 33 % albite, 14 % garnet, 12 % phengite, 8 % quartz, 8 % glaucophane
MS11.2		Fine grained, mylonized eclogite with pronounced layering of omphacite and garnet. Layers are 0.5-2 mm thick	45 % omphacite, 24 % almandine, 15 % quartz, 6 % phengite, 5 % albite, 4 % glaucophane, 1 % rutile

Table 3.1: Location, description and composition of the samples investigated in this study. Mineral phases were determined by microprobe analysis. Volume percentages of different mineral phases were determined by Rietveld texture analysis.

Mineral assemblages and chemical compositions of the eclogites and metasedimentary samples were determined by microprobe analyses at a JEOL JXA 8200 Electron Probe of GEOMAR, Kiel. Natural and synthetic silicates were used as standard materials. Single point analyses were performed at 15 kV accelerating voltage and 20 nA beam current. Volume percentages of mineral phases in the investigated samples were determined by 'Rietveld Texture Analysis' using the MAUD software (Table 1; Lutterotti et al., 1997). Microstructures of both the eclogites and the metasedimentary rocks were investigated using optical light microscopy.

For the fabric analysis, sample surfaces perpendicular to foliation and stretching lineation were mechanically polished with a minimum grain size of 0.25 μm and subsequently chemo-

mechanically polished with a high-pH silica solution. Additionally, the sample surface was coated with about 3nm of carbon to prevent charging in the SEM. Microfabrics of two eclogite samples were analyzed with electron backscatter diffraction (EBSD) in the scanning electron microscope (SEM) of the Bayerisches Geoinstitut, Universität Bayreuth. The SEM is a Leo (Zeiss) Gemini 1530 with a Schottky FEG cathode equipped with a combined EBSD/EDS detection system made by Oxford Instruments. EBSD patterns were collected with a Nordlys 2 CCD camera and EDS spectra with a Peltier-cooled X-MAX silicon drift detector with 20 mm² chip size. In the scans, accelerating voltage was 20 keV at a working distance of 19 mm and a beam current of about 2 nA was used yielding an acquisition time of about 50 ms per point. Analysis of indexed EBSD patterns was performed with the Channel 5 software from Oxford Instruments (Schmidt et al., 1991). Automatic indexing of the diffraction patterns was carried out with 5-7 reflections and a reference file of 75 reflections of the omphacite, garnet and magnesiohornblende structure, respectively. The use of magnesiohornblende structure instead of glaucophane, which is the amphibole in the investigated samples, is warranted since hornblende and glaucophane are structurally equivalent (C2/m space group; Reynard et al., 1989). The accuracy between individual EBSD orientations is usually between 0.5 and 0.8°, but always better than 1.3°.

Orientation maps showing misorientation angles between crystal lattices of different grains were produced and color-coded with respect to the Euler angles. Sudden changes in color do not necessarily represent large changes in orientation. Boundaries related to different misorientation intervals are presented as colored lines on the orientation maps. Black and red lines define misorientations above 10° and between 1 and 10°, respectively.

Misorientation angle distributions were calculated for correlated as well as uncorrelated omphacite grains by selecting the minimum misorientation angle and its corresponding axis from all possible symmetric variants (Wheeler et al., 2001). Uncorrelated grains are random, non-neighboring pairs of grains, whereas correlated grains are neighboring pairs of grains (e.g. Mainprice et al. 1993). For comparison, in all histograms the misorientation angle distribution for random distributions of crystals, e.g. no crystallographic distribution, was plotted (Mackenzie 1958).

Misorientation axes express the rotation that transfers one crystal lattice into the other and can be illustrated in pole figures and inverse pole figures. An analysis of the distribution of misorientation axes of neighboring or nearby grains can highlight the deformation process that led to the misorientation (e.g. Lloyd et al., 1997; Wheeler et al., 2001). In this study, the distribution of misorientation axes was determined for misorientations of 2-10°, 10-30° and 30-50° and plotted with respect to the sample reference system, as well as the crystallographic reference system.

Energy dispersive spectroscopy (EDX) was performed in parallel to the EBSD scans with an exposure time of 30 ms per point. X-ray fluorescence counts in the positions of the Mg-, Na-, and Ca-K lines were collected within a window of 90, 95 and 134 eV width respectively. In addition, CPO was investigated by time-of-flight (tof) neutron diffraction texture analysis at the SKAT diffractometer at the Frank Laboratory of Neutron Physics at JINR, Dubna, Russia (Ullemeyer et al., 1998; Keppler et al. 2014). This method allows the investigation of large sample volumes leading to representative bulk CPO. The application of full pattern fit methods makes it possible to determine the CPO of all mineral phases in the investigated samples.

4. Microfabrics

4.1. Eclogites

The studied eclogites are relatively fine-grained (< 1 mm) and can be subdivided into rocks that were retrogressed during exhumation and those that do not show significant signs of retrogression. The high-pressure assemblage of the eclogites contains omphacite, garnet, phengite, quartz and minor amounts of rutile (Table 1). For samples not overprinted by later retrogression we will use the term ‘fresh eclogites’ in the following. Most fresh eclogites are strongly layered displaying omphacite rich layers alternating with layers that are rich in garnet, phengite and quartz. A few samples, however, exhibit a more or less random grain fabric. Omphacite is the main constituent in all eclogites and mostly displays a well-developed foliation (Fig. 3A). Frequently a distinct stretching lineation is observed, but there are also samples, in which it is only weakly developed (Fig. 3B). Phengite is always aligned within the foliation. Garnet is either distributed within layers or forms clusters within the omphacite matrix. Quartz is mostly found in the pressure shadows of garnets.

Eclogite samples, which were overprinted by blueschist facies conditions further contain amphibole and paragonite (Table 1). The amphibole is either glaucophane or barroisitic hornblende. For these we will use the term ‘retrogressed eclogites’ in the following. Likewise, the samples mostly exhibit strong layering with omphacite and garnet rich layers, whereas the amphibole can be found within the omphacite layers, as well as the pressure shadows of garnet. The retrogressed eclogites also display a distinct omphacite foliation and in some samples a stretching lineation is observed (Fig. 3 C and D). The retrograde amphibole foliation is parallel to the omphacite foliation and in most samples the amphibolite stretching lineation is aligned with that of omphacite. Paragonite is not so well aligned in the foliation as phengite and frequently displays a nearly random orientation.

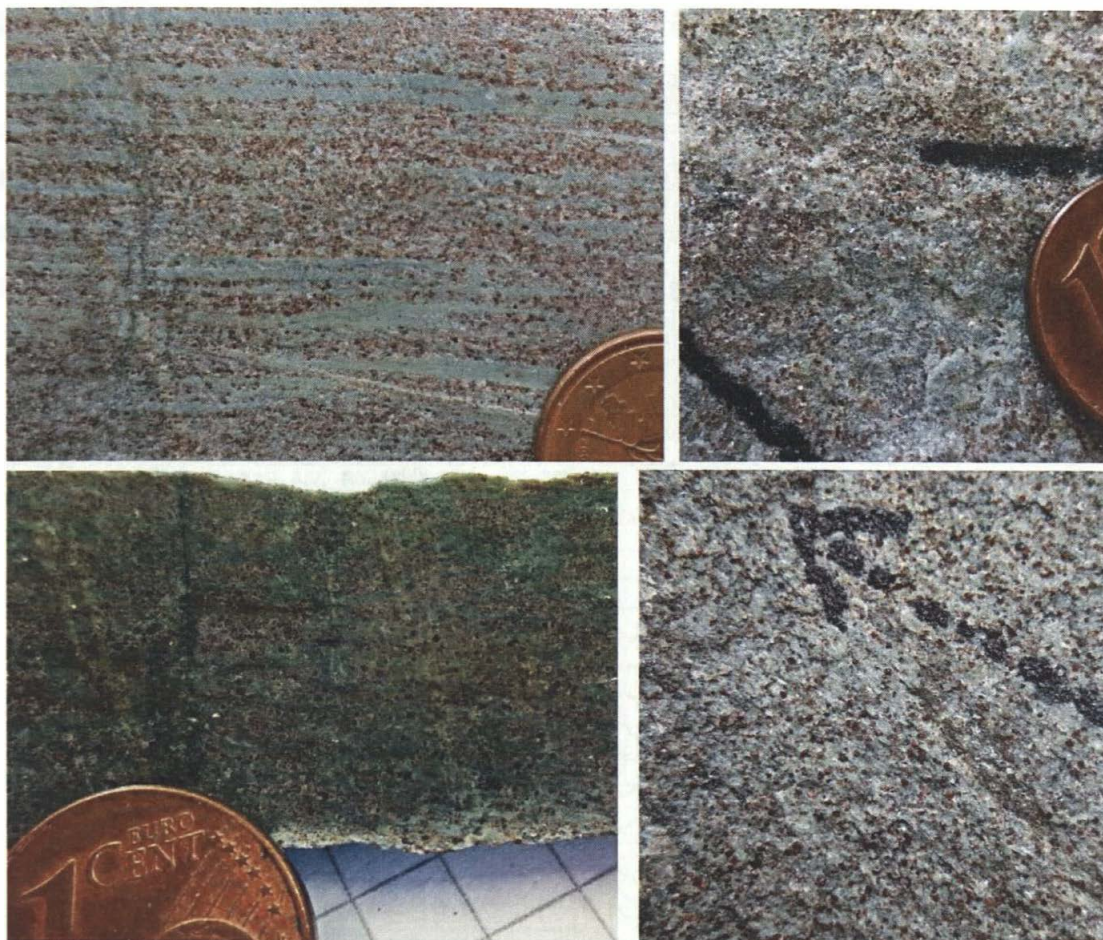


Figure 4.3: (A) Fresh eclogite mylonite sample MS112 cut perpendicular to foliation and parallel to lineation; note the distinct omphacite rich and alternating garnet rich layers. (B) foliation plane of sample MS112; note that lineation is only weakly developed. (C) retrogressed eclogite sample RK3 cut perpendicular to foliation and parallel to lineation. Alternating omphacite rich and garnet rich layers are visible but less distinct. (D) Foliation plane of retrogressed sample RK19; note the clear stretching lineation.

Tof neutron diffraction texture analysis shows a variable omphacite CPO of both fresh and retrogressed eclogites (Fig. 4A and Keppler et al., 2015). (001) is strongly aligned with the omphacite stretching lineation in some samples and more or less distributed within the foliation plane in others. (010) displays girdle structures perpendicular to the omphacite stretching lineation in samples where (001) is aligned with the lineation (RK3 in Fig 4A). This CPO is a clear L-fabric after Helmstedt (1974). In samples where (001) is distributed within the foliation plane, (010) shows point maxima aligned with the foliation normal (RK4 in Fig. 4A), which would be described as a typical S-fabric after Helmstedt (1974). Most samples, however, exhibit SL-fabrics, where (001) is aligned with the omphacite stretching lineation with some distribution in the foliation plane and (010) displays point maxima normal to the foliation (RK49 and MS112 in Fig. 4A and Keppler et al., 2015). In the retrogressed samples, (001) of amphibole mostly matches that

of omphacite. Likewise, it can either be strongly aligned with the omphacite stretching lineation (RK3 in Fig. 4A) or more or less distributed within the foliation plane with some alignment in lineation direction (RK4 and RK49 in Fig. 4A). Glaucophane (100) is always aligned with the foliation normal, whereas (100) of barroisite shows a very weak girdle distribution in the foliation plane. Phengite in the eclogites always exhibits a strong alignment of its basal plane (001) in the foliation (see RK49 and MS112 in Fig. 4A). (001) of muscovite and paragonite, on the other hand, only shows a weak alignment in the foliation plane (RK3 and RK4 in Fig. 4A).

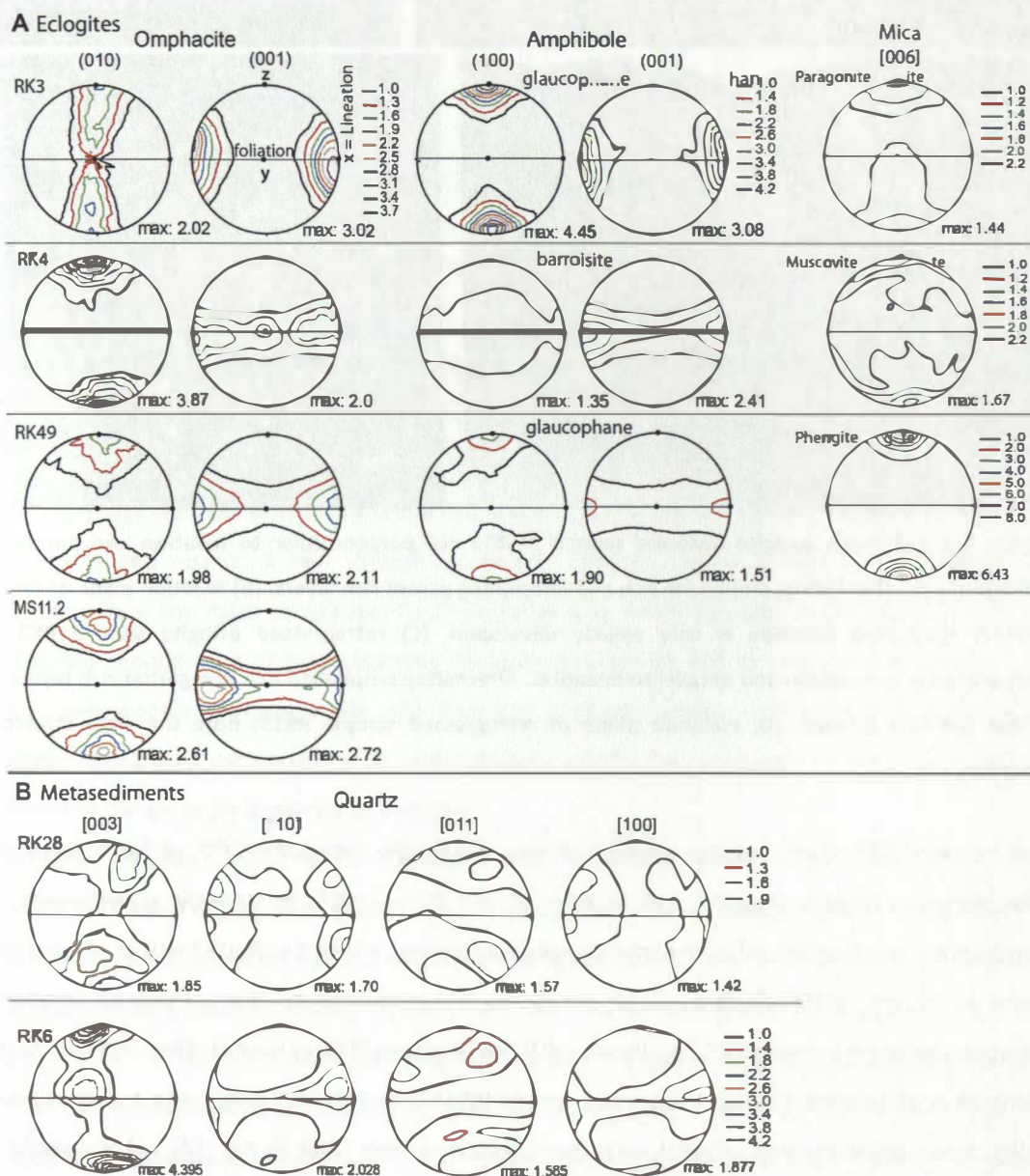


Figure 4.4: (A) Omphacite and amphibole CPO of fresh and retrogressed eclogites. (B) Quartz CPO of metasediments. All pole figures are lower hemisphere equal area projections. Coloured lines are multiples of a random distribution with maxima (max) indicated at the lower right of each pole figure. CPO is derived from tof neutron diffraction.

A Omphacite													Glaucophane												
Sample	MS112 (fresh eclogite)								RK49 (retrogressed eclogite)								RK3 (retrogressed eclogite)								
	# 1	# 2	# 3	# 4	# 5	# 6	# 7	# 8	representative profile through omphacite grain								# 9	# 10	# 11	# 12	# 13				
SiO2	56.67	57.19	57.23	57.84	56.85	57.04	57.42	57.83	57.04	57.71	57.49	57.46	57.51	57.80	57.60	57.49	57.46	58.16	58.91	59.43	59.21				
TiO2	0.06	0.05	0.05	0.07	0.05	0.05	0.05	0.07	0.05	0.05	0.06	0.05	0.04	0.05	0.05	0.05	0.04	0.05	0.04	0.03	0.02				
Al2O3	9.18	10.96	11.35	13.34	10.13	10.98	12.93	13.05	13.00	13.06	14.25	13.48	13.84	14.44	14.38	13.07	9.84	13.69	13.46	12.98	12.99				
FeO	6.25	4.95	4.81	1.95	5.29	4.67	2.29	2.25	2.24	4.00	1.83	2.03	3.04	2.31	2.17	2.30	5.84	2.39	4.37	4.40	4.44				
MnO	0.02	0.03	0.00	0.00	0.01	0.00	0.00	0.00	0.00	0.08	0.04	0.07	0.00	0.01	0.03	0.00	0.00	0.07	0.03	0.01	0.02				
MgO	8.77	8.14	8.21	8.54	8.93	8.53	8.44	8.44	9.29	7.83	8.49	8.68	7.63	7.70	7.85	8.93	8.32	8.19	12.07	12.88	13.04				
CaO	14.19	12.85	12.87	12.51	13.91	13.27	12.39	12.34	13.35	11.77	11.99	12.55	11.22	11.27	11.41	13.07	13.65	12.17	1.71	0.50	0.98				
Na2O	5.72	6.45	6.60	6.85	5.96	6.45	6.85	6.87	6.58	7.47	7.31	6.96	7.61	7.63	7.57	6.57	6.18	6.97	6.67	7.06	6.87				
K2O	0.00	0.02	0.00	0.00	0.00	0.00	0.00	0.00	0.02	0.01	0.01	0.00	0.00	0.01	0.00	0.01	0.01	0.00	0.02	0.01	0.02				
Sum	100.9	100.6	101.1	101.1	101.1	101	100.4	100.9	101.6	102	101.5	101.3	100.9	101.2	101.1	101.5	101.3	101.7	97.28	97.3	97.59				
jd-content	0.38	0.46	0.47	0.53	0.42	0.46	0.53	0.53	0.45	0.52	0.51	0.50	0.55	0.56	0.55	0.49	0.41	0.55							
Si	8.07	8.06	8.05	8.05	8.02	8.05	8.03	7.98	7.89	7.98	7.91	7.94	7.98	7.97	7.95	7.94	8.10	7.99	8.27	8.28	8.25				
Ti	0.01	0.00	0.01	0.01	0.01	0.00	0.01	0.01	0.01	0.01	0.01	0.01	0.01	0.01	0.01	0.01	0.00	0.005	0.01	0.00	0.00				
Al	1.63	1.49	2.23	1.90	1.38	0.78	1.92	2.22	2.12	2.13	2.31	2.20	2.26	2.35	2.34	2.13	2.06	2.22	2.11	2.13	2.13				
Fe	0.68	0.72	0.28	0.53	0.70	0.85	0.51	0.28	0.26	0.46	0.21	0.24	0.35	0.27	0.25	0.27	0.69	0.28	0.51	0.51	0.52				
Mn	0.00	0.00	0.00	0.00	0.00	0.00	0.00	0.00	0.00	0.01	0.01	0.01	0.00	0.00	0.00	0.00	0.00	0.008	0.00	0.00	0.00				
Mg	1.79	1.91	1.58	1.69	2.07	2.55	1.72	1.67	1.91	1.61	1.74	1.79	1.58	1.58	1.62	1.84	1.75	1.68	2.70	2.68	2.71				
Ca	2.11	2.22	1.73	1.92	2.41	2.87	1.91	1.77	1.98	1.74	1.77	1.86	1.67	1.67	1.69	1.93	2.06	1.79	0.12	0.07	0.15				
Na	1.64	1.56	1.91	1.78	1.38	0.90	1.81	1.98	1.77	2.00	1.95	1.86	2.05	2.04	2.03	1.76	1.69	1.86	1.88	1.91	1.86				
K	0.00	0.00	0.00	0.00	0.00	0.00	0.00	0.00	0.00	0.00	0.00	0.00	0.00	0.00	0.00	0.00	0.00	0.00	0.00	0.00	0.00				
Sum	15.92	15.97	15.79	15.89	15.98	16.01	15.91	15.90	15.93	15.95	15.91	15.89	15.9	15.88	15.89	15.87	15.93	15.82	15.61	15.60	15.62				
O	24.0	24.0	24.0	24.0	24.0	24.0	24.0	24.0	24.0	24.0	24.0	24.0	24.0	24.0	24.0	24.0	24.0	24.0	24.00	24.00	24.00				

B Phengite										C Phengite						
Sample	MS112 (fresh eclogite)					RK1					RK28 (paragneiss)					
SiO2	51.00	49.64	50.90	50.12	50.71	50.75	50.17	50.51	51.58	48.59	48.28	48.33				
TiO2	0.20	0.22	0.16	0.25	0.23	0.21	0.22	0.25	0.26	0.38	0.40	0.35				
Al2O3	27.87	30.42	27.71	30.07	28.88	29.44	30.02	28.91	29.49	31.56	31.43	32.11				
FeO	1.00	1.10	1.00	0.71	2.02	1.85	1.96	2.16	2.33	3.25	3.37	3.01				
MnO	0.04	0.00	0.01	0.00	0.00	0.00	0.00	0.00	0.00	0.00	0.01	0.01				
MgO	4.49	3.77	4.44	3.88	3.82	3.76	3.45	4.16	3.74	2.19	2.23	2.10				
CaO	0.01	0.01	0.02	0.00	0.00	0.00	0.00	0.03	0.04	0.00	0.00	0.00				
Na2O	0.33	0.67	0.38	0.69	0.66	0.73	0.73	0.66	0.76	0.59	0.58	0.68				
K2O	10.80	10.06	10.70	10.31	10.51	10.43	10.45	10.23	10.23	10.49	10.48	10.37				
Sum	95.74	95.89	95.32	96.03	96.83	97.18	97.00	96.91	98.43	97.06	96.78	96.95				
Si ratio:	3.37	3.27	3.38	3.29	3.33	3.32	3.29	3.31	3.33	3.20	3.20	3.19				
Si	6.74	6.54	6.59	6.75	6.66	6.63	6.63	6.57	6.63	6.32	6.32	6.32	6.27			
Ti	0.02	0.02	0.02	0.02	0.02	0.02	0.02	0.02	0.03	0.03	0.04	0.04	0.03			
Al	4.34	4.72	4.66	4.33	4.47	4.54	4.54	4.64	4.47	5.16	5.14	5.14	5.24			
Fe	0.12	0.12	0.08	0.12	0.24	0.22	0.22	0.23	0.26	0.26	0.25	0.25	0.25			
Mn	0.00	0.00	0.00	0.00	0.00	0.00	0.00	0.00	0.00	0.00	0.00	0.00	0.00			
Mg	0.89	0.74	0.76	0.88	0.82	0.80	0.80	0.74	0.89	0.34	0.36	0.37	0.32			
Ca	0.00	0.00	0.00	0.00	0.00	0.00	0.00	0.00	0.00	0.00	0.00	0.00	0.00			
Na	0.08	0.17	0.18	0.10	0.18	0.20	0.20	0.20	0.18	0.15	0.21	0.20	0.22			
K	1.82	1.69	1.73	1.81	1.76	1.74	1.74	1.75	1.71	1.76	1.70	1.72	1.72			
Sum	14.02	14.01	14.01	14.01	14.05	14.04	14.04	14.05	14.05	14.02	14.03	14.04	14.05			
O	22.00	22.00	22.00	22.00	22.00	22.00	22.00	22.00	22.00	22.00	22.00	22.00	22.00			

Table 3.2: Mineral analysis of the investigated samples. (A) Omphacite in fresh and retrogressed eclogites (MS112, RK3 and RK49) and glaucophane in a retrogressed eclogite (RK3). Jd=Jadeite. (B) Phengite in fresh (MS112) and retrogressed (RK49) eclogites. (C) Phengite and feldspar in a in a paragneiss (RK28). (D) Garnet in fresh (MS112) and retrogressed (RK49) eclogites.

D Garnet															
Sample	MS112 (fresh eclogite)														
SiO2	37.56	37.52	37.20	37.13	36.80	36.75	36.42	36.24	36.31	37.11	36.76	37.17	37.41	37.58	
TiO2	0.04	0.06	0.09	0.13	0.05	0.15	0.10	0.15	0.23	0.14	0.25	0.09	0.04	0.02	
Al2O3	21.97	22.13	21.65	21.54	21.82	21.53	21.52	21.24	21.25	22.16	21.78	22.13	22.10	22.44	
FeO	25.88	28.57	29.13	28.61	26.42	25.11	25.58	22.31	21.00	26.04	29.64	29.36	29.19	26.81	
MnO	0.12	0.22	0.56	0.84	2.04	1.81	4.59	7.50	8.19	0.67	0.50	0.36	0.13	0.16	
MgO	6.86	5.21	3.52	3.15	2.92	2.85	1.00	0.88	0.65	5.46	3.40	4.22	4.97	6.33	
CaO	6.69	6.65	8.29	8.76	9.74	11.56	11.29	11.91	12.23	8.05	8.28	7.27	6.41	6.13	
Na2O	0.04	0.02	0.02	0.02	0.00	0.04	0.03	0.04	0.03	0.01	0.03	0.02	0.04	0.02	
K2O	0.00	0.00	0.00	0.00	0.00	0.00	0.00	0.00	0.00	0.00	0.00	0.00	0.00	0.01	
Cr2O3	0.00	0.02	0.02	0.03	0.05	0.05	0.00	0.01	0.01	0.00	0.02	0.00	0.00	0.03	
Sum	99.16	100.39	100.49	100.21	99.84	99.84	100.54	100.28	99.91	99.64	100.66	100.62	100.29	99.52	
Alman															
dine:	54.32	60.66	61.53	60.89	56.23	51.89	53.39	45.31	43.65	54.62	62.10	62.28	62.35	57.94	
Pyrope:	26.70	20.27	13.82	12.41	11.54	11.25	3.98	3.52	2.61	21.31	13.37	16.49	19.39	24.59	
Si	5.88	5.88	5.86	5.88	5.89	5.85	5.84	5.86	5.82	5.84	5.83	5.82	5.85	5.84	
Ti	0.00	0.01	0.01	0.01	0.02	0.01	0.02	0.01	0.02	0.03	0.02	0.03	0.01	0.01	
Al	4.06	4.09	4.09	4.03	4.03	4.09	4.03	4.08	4.02	4.03	4.10	4.06	4.10	4.13	
Fe	3.39	3.74	3.77	3.85	3.80	3.51	3.34	3.47	3.00	2.83	3.42	3.92	3.86	3.75	
Mn	0.02	0.03	0.05	0.08	0.11	0.27	0.24	0.18	1.02	1.12	0.09	0.07	0.05	0.04	
Mg	1.60	1.22	1.05	0.83	0.75	0.69	0.68	1.03	0.21	0.16	1.28	0.80	0.99	1.14	
Ca	1.12	1.12	1.25	1.40	1.49	1.66	1.97	1.47	2.05	2.10	1.36	1.41	1.23	1.16	
Na	0.01	0.01	0.02	0.01	0.01	0.00	0.01	0.01	0.01	0.01	0.00	0.01	0.01	0.01	
K	0.00	0.00	0.00	0.00	0.00	0.00	0.00	0.00	0.00	0.00	0.00	0.00	0.00	0.00	
Cr	0.00	0.00	0.00	0.00	0.00	0.01	0.01	0.00	0.00	0.00	0.00	0.00	0.00	0.00	
Total	16.09	16.08	16.09	16.10	16.09	16.10	16.13	16.10	16.15	16.12	16.10	16.12	16.10	16.09	
O	24.00	24.00	24.00	24.00	24.00	24.00	24.00	24.00	24.00	24.00	24.00	24.00	24.00	24.00	
Sample	RK49 (retrogressed eclogite)														
SiO2	38.29	38.42	38.13	37.97	37.40	38.16	37.44	37.43	37.42	37.16	37.45	37.45	37.60	38.14	38.22
TiO2	0.04	0.04	0.02	0.02	0.04	0.05	0.04	0.04	0.09	0.05	0.05	0.05	0.04	0.03	0.04
Al2O3	22.45	22.49	22.22	22.29	21.75	22.26	21.77	21.83	21.52	21.76	21.67	21.85	22.04	22.32	22.33
FeO	23.16	22.83	24.48	24.80	27.67	24.45	28.84	28.31	29.33	29.88	30.07	29.70	28.56	26.07	23.31
MnO	0.14	0.56	0.25	0.27	0.35	0.42	0.38	0.53	0.37	0.37	0.27	0.24	0.24	0.29	0.19
MgO	8.45	8.46	7.34	7.29	5.40	7.33	4.49	4.35	3.98	4.22	4.20	4.92	5.81	6.78	8.31
CaO	6.66	6.78	6.92	6.73	6.73	6.83	7.22	7.81	7.74	6.82	6.63	6.22	5.50	6.35	6.56
Na2O	0.03	0.03	0.03	0.05	0.02	0.03	0.01	0.04	0.01	0.02	0.02	0.04	0.02	0.05	0.05
K2O	0.01	0.00	0.00	0.00	0.00	0.00	0.00	0.00	0.00	0.01	0.00	0.00	0.00	0.01	0.01
Cr2O3	0.00	0.02	0.00	0.00	0.01	0.01	0.02	0.02	0.00	0.00	0.00	0.00	0.00	0.01	0.01
Sum	99.22	99.63	99.39	99.42	99.37	99.54	100.21	100.36	100.47	100.30	100.37	100.47	99.81	100.05	99.03
Alman															
dine:	48.97	47.88	51.97	52.60	59.07	51.94	61.27	59.89	61.76	63.34	64.24	62.81	61.38	55.68	49.52
Pyrope:	32.38	32.30	28.30	28.14	21.18	28.22	17.57	17.00	15.60	16.57	16.47	19.21	22.66	26.11	31.94
Si	5.91	5.91	5.92	5.90	5.90	5.91	5.90	5.88	5.90	5.88	5.91	5.89	5.90	5.91	5.91
Ti	0.00	0.00	0.00	0.00	0.00	0.01	0.00	0.00	0.01	0.01	0.01	0.01	0.00	0.00	0.00
Al	4.08	4.07	4.07	4.08	4.05	4.07	4.04	4.05	4.00	4.05	4.03	4.05	4.08	4.08	4.07
Fe	2.99	2.93	3.18	3.22	3.65	3.17	3.80	3.72	3.87	3.95	3.97	3.90	3.75	3.38	3.02
Mn	0.02	0.07	0.03	0.04	0.05	0.06	0.05	0.07	0.05	0.05	0.04	0.03	0.03	0.04	0.03
Mg	1.94	1.94	1.70	1.69	1.27	1.70	1.05	1.02	0.94	0.99	0.99	1.15	1.36	1.57	1.92
Ca	1.10	1.12	1.15	1.12	1.14	1.13	1.22	1.32	1.31	1.16	1.12	1.05	0.93	1.06	1.09
Na	0.01	0.01	0.01	0.01	0.01	0.01	0.00	0.01	0.00	0.01	0.01	0.01	0.00	0.17	0.01
K	0.00	0.00	0.00	0.00	0.00	0.00	0.00	0.00	0.00	0.00	0.00	0.00	0.00	0.00	0.00
Cr	0.00	0.00	0.00	0.00	0.00	0.00	0.00	0.00	0.00	0.00	0.00	0.00	0.00	0.00	0.00
Total	16.05	16.06	16.05	16.06	16.07	16.50	16.08	16.09	16.09	16.10	16.07	16.09	16.06	16.05	16.05
O	24.00	24.00	24.00	24.00	24.00	24.00	24.00	24.00	24.00	24.00	24.00	24.00	24.00	24.00	24.00

Table 3.2 (continued)

4.1.1. Fresh eclogites

The mylonitic eclogite sample MS11.2 represents a fresh eclogite, which has not been overprinted by later retrogression. It exhibits a pronounced omphacite foliation and a weakly developed stretching lineation (Fig. 3 A and B). The omphacite grain size is variable with larger grains (~100-300 μm) and smaller grains with sizes <20 μm (Fig. 5A).

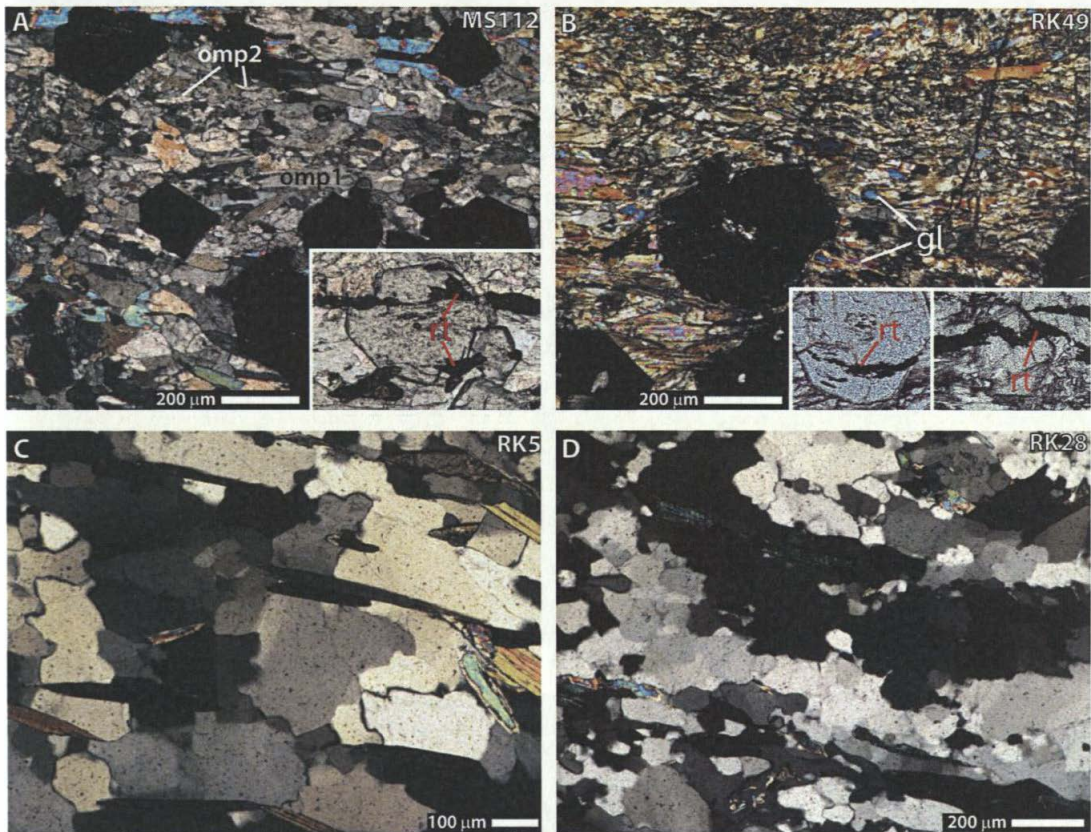


Fig. 4.5: Characteristic sample micrographs under crossed polarizers of thin sections perpendicular to the main foliation and parallel to the stretching lineation. (A) fresh eclogite, showing elongated omphacite grains of both larger grains (omp1) and smaller recrystallized grains (omp2). Inset shows rutile (rt) inclusions in garnet through transmitted light. (B) Retrogressed eclogite with glaucophane (gl) growing in the pressure shadows of garnet, and alignment of omphacite within the foliation. Insets show rutile (rt) inclusions in garnet through transmitted light. (C) Mica-schist with quartz grains displaying variable grain size (50-300 μm), irregular shapes, and lobate boundaries, pointing to grain boundary migration. (D) Paragneiss with large, slightly elongated quartz grains (100-400 μm) and smaller recrystallized grains (30-60 μm).

The grain boundaries of the omphacite porphyroclasts, i.e. the larger grains, are frequently lobate, resulting in dissection microstructures and island grains (Fig. 6A), characteristic of grain boundary migration recrystallization (e.g., Guillopé and Poirier, 1979; Means, 1983; Urai et al., 1986).

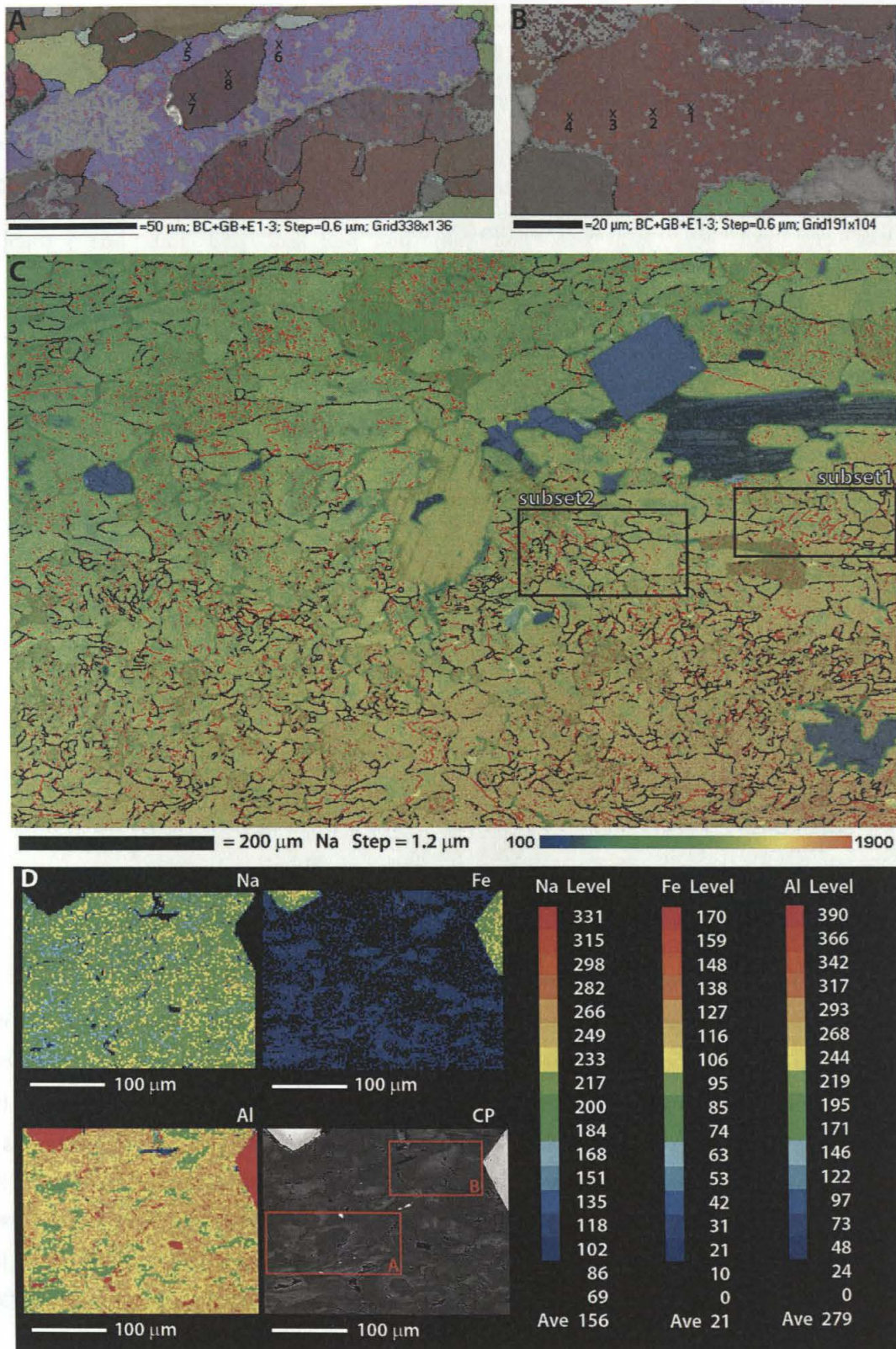


Figure 4.6: A and B) Orientation maps of omphacite. Numbers indicate locations of quantitative point measurements listed in Table 2. Location of maps A and B are marked by red squares in D. C) EDX map showing Na-content of omphacite matrix of a fresh eclogite. Warmer colours indicate higher content. Black lines show misorientation angles over 10° , red lines indicate boundaries with misorientation angles below 10° . D) Microprobe maps showing contents of Na, Fe, and Al in omphacite matrix and BSE picture of the same area. All images are perpendicular to foliation and lineation.

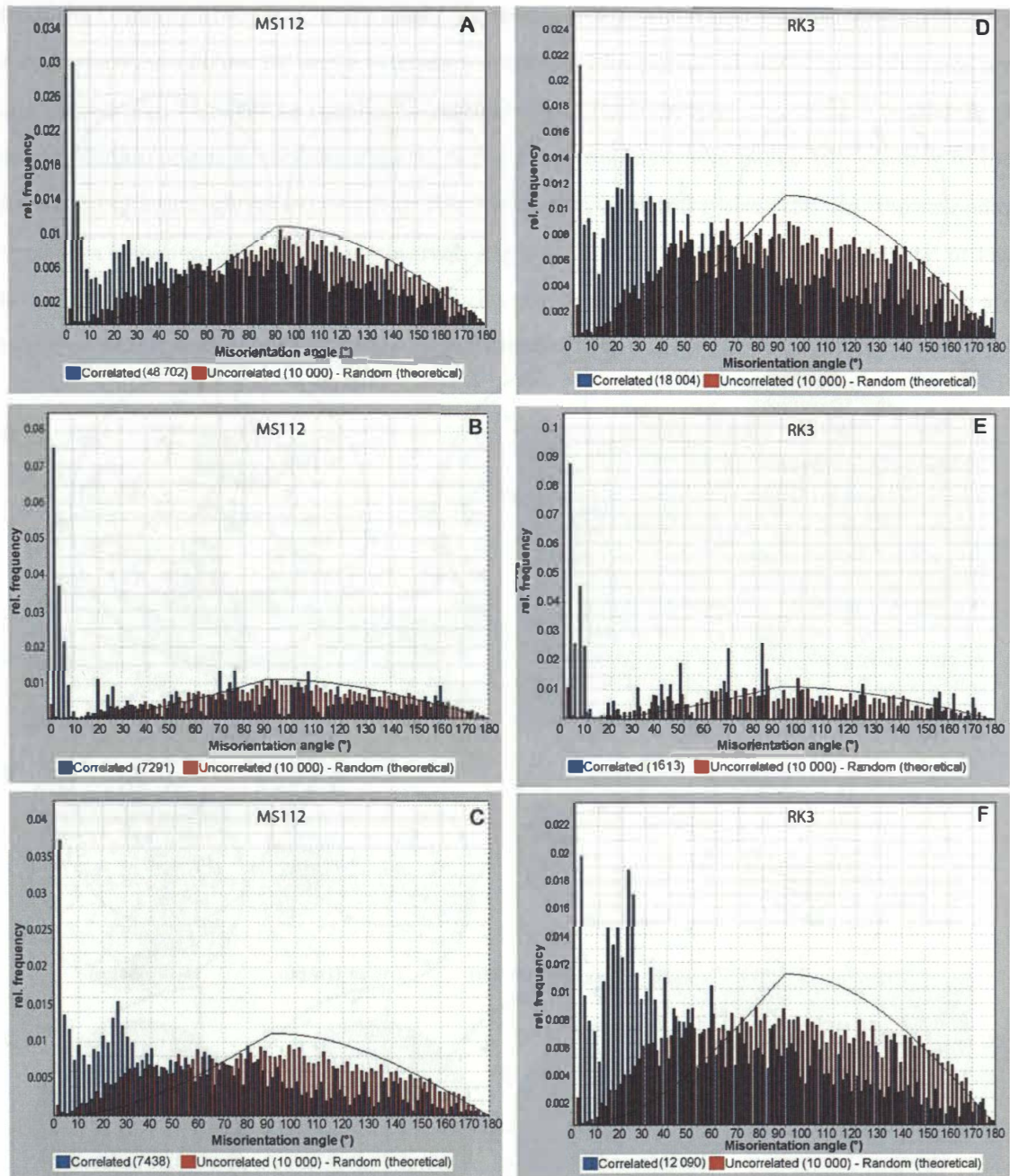


Fig. 4. 7: Distribution of misorientation angles of correlated and uncorrelated omphacite grains. (A-C) are from the fresh aclogite sample MS11.2 and (D-F) are from the retrogressed sample RK3. (A and D) all omphacite grains, (B and E grains $>20\ \mu\text{m}$, (C and F) grains $<20\ \mu\text{m}$.

The porphyroclasts show some intracrystalline deformation features like undulose extinction and subgrains, but the subgrain density is relatively low. There are, however, also some porphyroclasts without any subgrains, showing little variability in misorientation angles. Subgrain boundaries in omphacite are defined by misorientation angles of less than 10° , following Buatier et al. (1991). Many of the subgrains (Fig. 6C subset 1) are about the same size as the smaller grains $<20\ \mu\text{m}$ (Fig 6C subset 2), which we interpret as recrystallized grains. These subgrains and related

recrystallized grains are indicative of the operation of subgrain rotation recrystallization (e.g., Hobbs, 1968; Guillopé and Poirier, 1979; Urai et al., 1986).

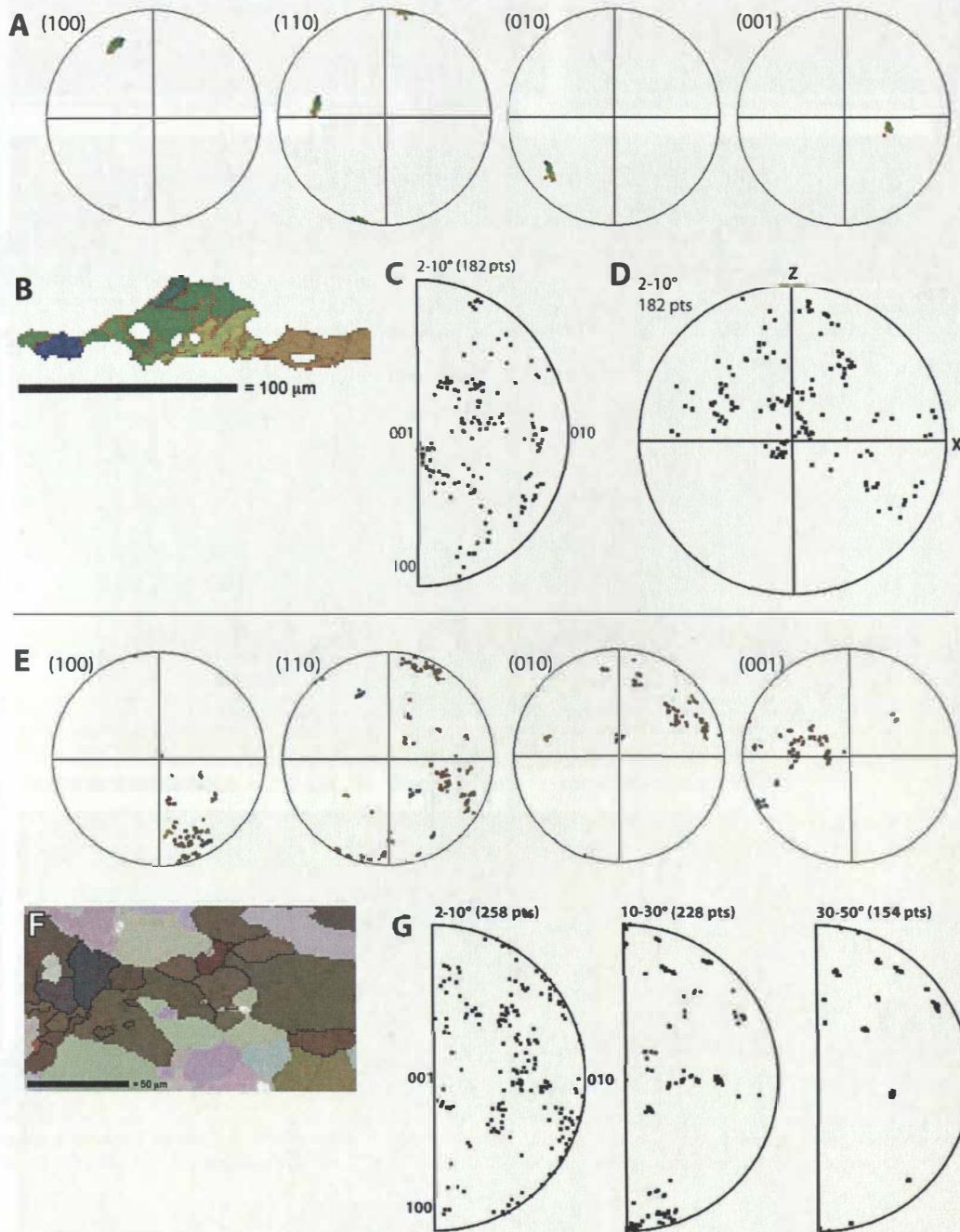


Fig. 4.8: (A) Pole figures of relevant hkl of omphacite porphyroclast in subset 1 (B). For location of subset see Fig. 5. (C) Inverse pole figure and (D) pole figure of misorientation axes of small angle boundaries (2-10°) of the omphacite porphyroclast. (E) Pole figures of relevant hkl of omphacite porphyroclast and recrystallized grains in subset 2 (F). For location of subset see Fig. 5. Inverse pole figures of misorientation axes of small angle boundaries (2-10°) and large angle boundaries (>10°) of omphacite porphyroclast and recrystallized grains.

Misorientation angle data analysis of sample MS11.2 shows a deviation of uncorrelated grains from the random distribution, which can be attributed to a pronounced CPO. For correlated grains a main maximum below 10° and a secondary maximum between 20 and 30° , when all grains are considered (Fig. 7A). For the omphacite porphyroclasts (100 - $300\ \mu\text{m}$), the relative frequency of misorientation angles in correlated grains displays only the maximum below 10° , pointing to the formation of low angle boundaries (Fig. 7B). For the recrystallized grains ($<20\ \mu\text{m}$) the secondary maximum between 20° and 30° is observed (Fig. 7C). The main maximum characteristic of low angle grain boundaries below 10° as well as this secondary maximum of recrystallized grains are together indicative of subgrain rotation recrystallization (Fig. 7C).

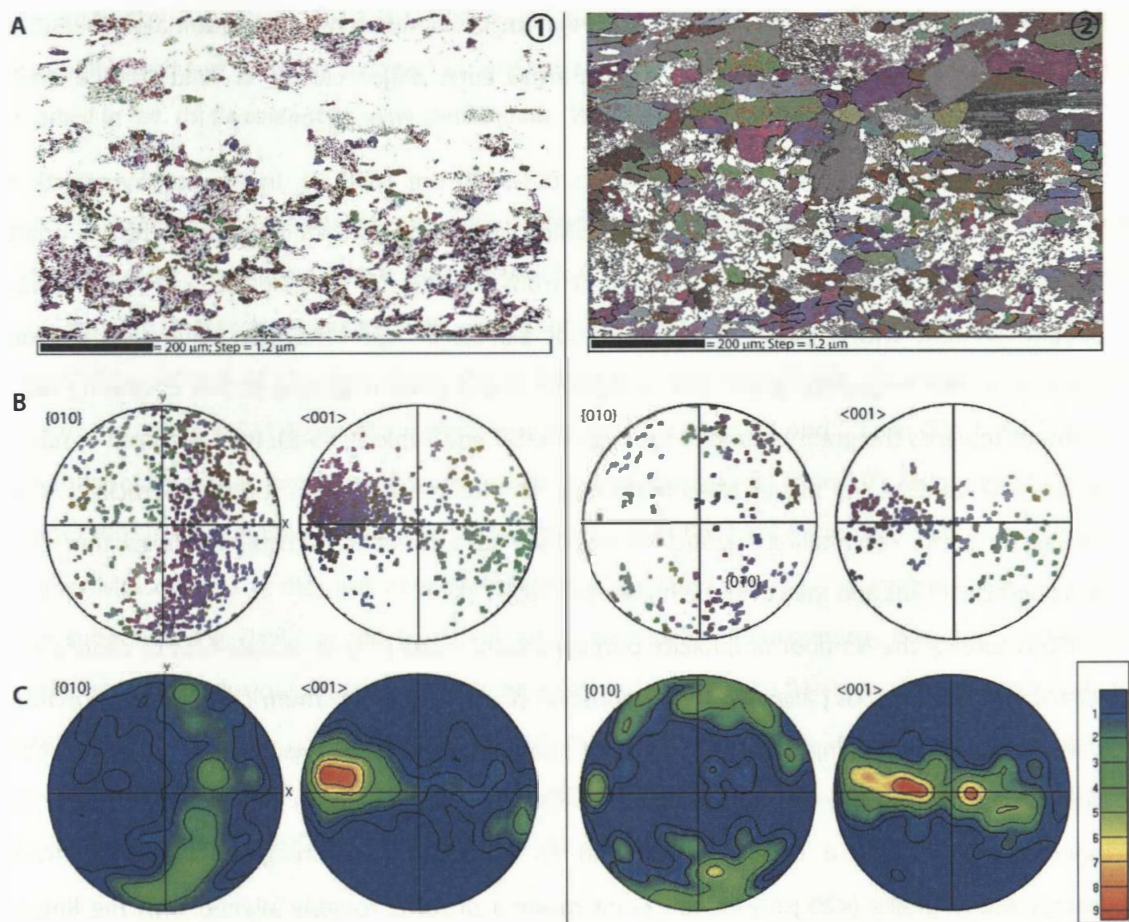


Fig. 4.9: (A1) Orientation map of the omphacite matrix of a fresh eclogite (MS112) showing grains $<20\ \mu\text{m}$. (B1) Pole figures and (C1) related contour pole figures of omphacite $[010]$ and $[001]$ of grains $<20\ \mu\text{m}$. (A2) Orientation map of the omphacite matrix of a fresh eclogite (MS112) showing grains $>20\ \mu\text{m}$. (B2) Pole figures and (C2) related contour pole figures of omphacite $[010]$ and $[001]$ of grains $>20\ \mu\text{m}$. Maps are perpendicular to foliation and lineation. Black lines indicate misorientation angles over 10° , red lines indicate misorientation angles between 1 and 10° . Contour levels in pole figures represent multiples of a random distribution and are indicated to the right.

Pole figures of an omphacite porphyroclast with a high subgrain density showed a continuous misorientation of the crystal lattice from subgrain to subgrain (subset 1 in Fig. 8A and B). A misorientation axis analysis across the subgrain boundaries yielded a relatively scattered distribution of the misorientation axes with some clustering in pole figures and inverse pole figures (Fig. 8C and D). The clusters can usually be related to individual subgrain boundaries. In the pole figure of Fig. 8D a prominent cluster is found around the Y-direction. Pole figures of several porphyroclast and surrounding recrystallized grains (subset 2 in Fig. 8E and F) exhibit a more distributed orientation of the crystals, forming several clusters around a main maximum. The misorientation axis analysis of this section yielded patchy distributions. Low angle misorientation axes ($2-10^\circ$) show some clustering in the inverse pole figure (Fig. 8G), but less clear than for the subgrains of subset 1 (Fig. 8C). High angle boundary misorientation axes ($10-30^\circ$ and $30-50^\circ$) display some distinct clustering whereas each major cluster is related to a distinct recrystallized grain (Fig. 8G).

Omphacite exhibits variable jadeite contents (38-53%, see Table 2). In the porphyroclasts, the jadeite-content increases from core to rim, which goes along with an increase of the Na- and the Al-content and a decrease of the Fe-content from core to rim (see Fig. 6B and Table 2, #1-4). Jadeite content within island grains does not exhibit a high variability, whereas the jadeite content in the omphacite grain, into which the island grain migrated shows decreasing jadeite content towards the grain boundary (see Fig. 6A, 5D and Table 2, #5-8). Recrystallized omphacite grains always display a higher Na-content (e.g. Jadeite content) than the porphyroclasts. Color-coding of some recrystallized grains corresponds to a Na-content comparable to that of the porphyroclast rims and may even be higher (Fig. 6C).

EBSD results of the Na-poor omphacite porphyroclasts ($>100\ \mu\text{m}$) of sample MS112 show a girdle distribution of the [001] axes within the foliation plane with a maximum close to the direction of the omphacite stretching lineation and point maxima of the [010] axes normal to the omphacite foliation of the sample (Fig 9B and C). This CPO concurs well with the SL-fabric of the hand specimen, displaying a clear foliation and an omphacite stretching lineation. The Na-rich recrystallized grains ($<20\ \mu\text{m}$) exhibit point maxima of [001] roughly aligned with the lineation direction and girdle structures of [010] perpendicular to the lineation (Fig. 9B and C). The CPO of porphyroclasts coincides with the one derived from neutron diffraction texture analysis (compare MS11.2 in Fig. 9 and Fig. 4A).

Quartz in sample MS112 shows an irregular grain shape and frequently displays straight grain boundaries and it is mostly found in pressure shadows of garnet. Phengite display a strong alignment parallel to the omphacite foliation. It exhibits high Si-contents (3.27-3.39, see Table 2) and is mostly found within garnet rich layers, but locally also within omphacite rich layers.

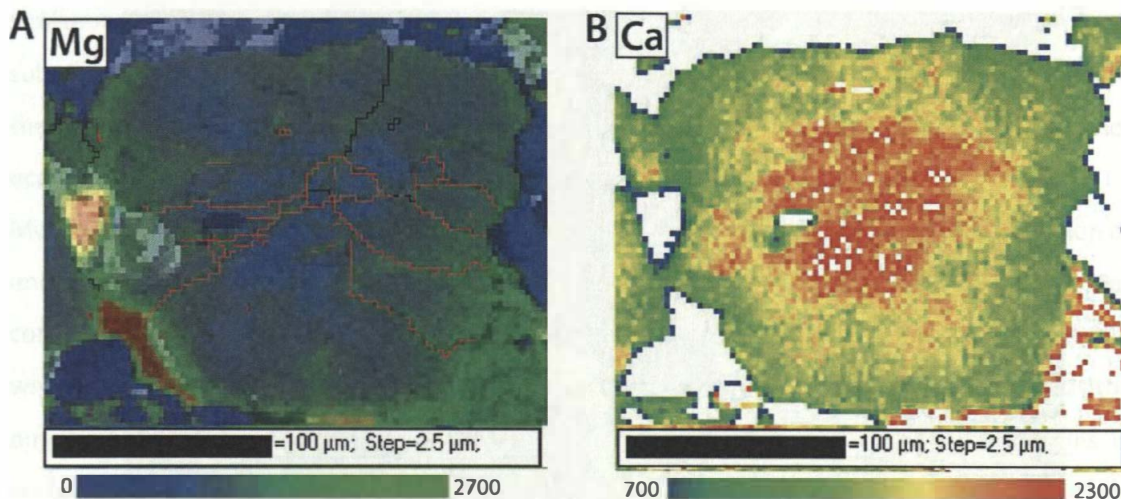


Fig. 4.10: EDX map of a garnet grain in the fresh eclogite sample MS112 (A) Mg content. Misorientation boundary angles of over 10° are marked in black and misorientation boundary angles of over 2° are marked in red. (B) Ca content of same garnet grain. Warmer colours indicate higher contents.

Garnets in the fresh eclogites are generally euhedral and display grain sizes of about 100-500 μm . They are mostly intact, but some grains show fractures. In sample MS11.2 they display prograde zoning with increasing pyrope and almandine contents from core to rim. A small drop in almandine content at the very outer rim is frequently observed (Table 2D MS11.2). The garnet grains in sample MS11.2 contain subgrains with sizes between 20 and 50 μm (Fig 10B). Subgrain boundaries in garnet are defined by misorientation angles of less than 10° , following Storey and Prior (2005). The subgrain formation is locally reflected in the Mg-content of the grains, exhibiting higher Mg-contents at the rims of subgrains (Fig. 10A). The Ca-content of garnet is not related to the subgrains (Fig. 10B). In the fresh eclogites, omphacite, glaucophane, phengite, quartz and rutile occur as inclusions in garnet. Rutile needles and white mica flakes in garnets show a shape preferred orientation corresponding to the main foliation (inset in Fig. 5A). Most of the glaucophane and omphacite inclusions are aligned in the foliation, too, but some exhibit an irregular or random distribution as do the quartz inclusions.

4.1.2. Retrogressed eclogites

Sample RK3 is a retrogressed eclogite representing a protomylonite. It exhibits a pronounced omphacite lineation, whereas the omphacite foliation is only weakly developed (Fig 3D). Omphacite exhibits two sets of grain sizes in this sample – larger grains of $\sim 100\text{-}400\ \mu\text{m}$ and smaller grains of $<20\ \mu\text{m}$ (Fig. 5B).

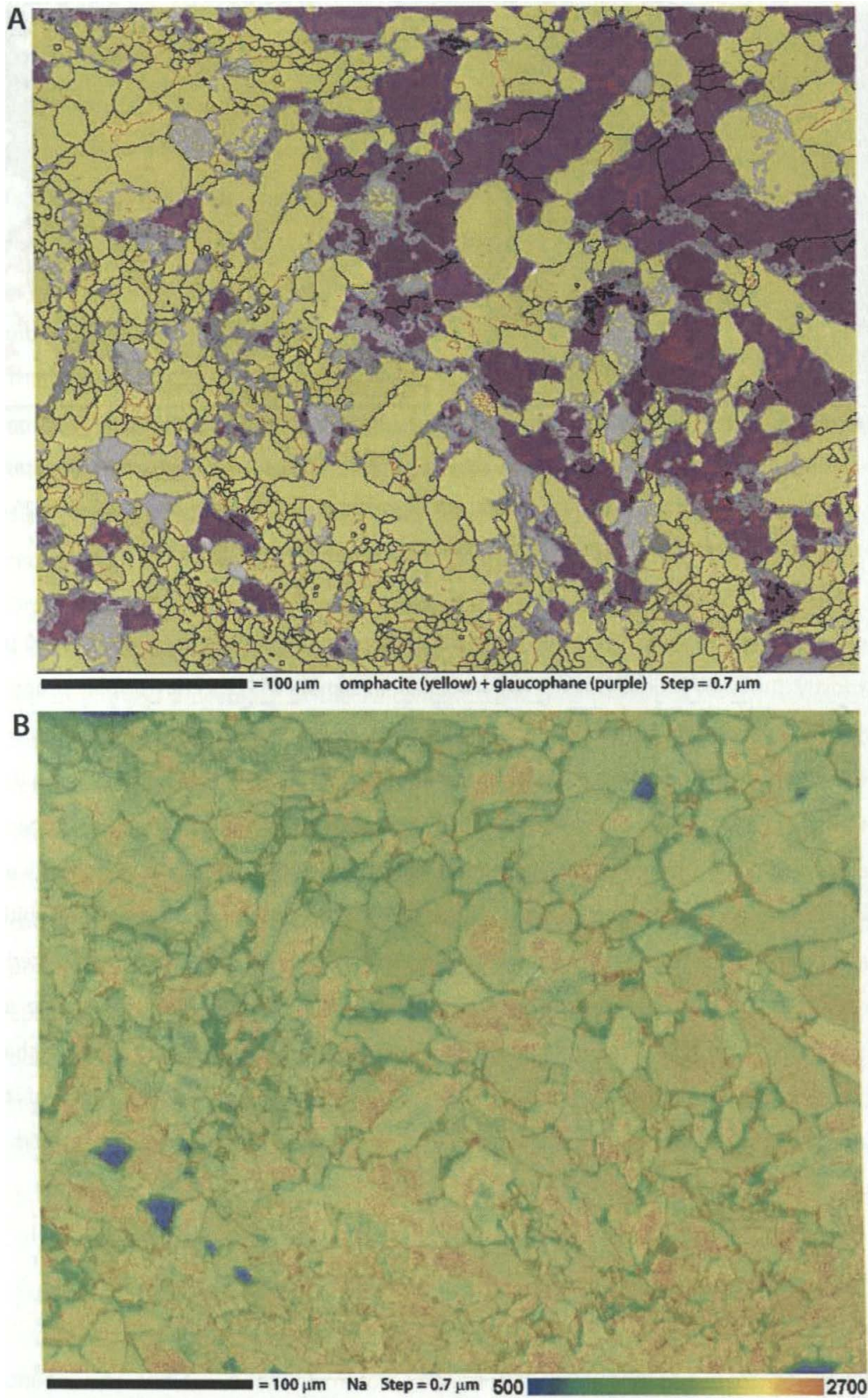


Fig. 4.11: A) Orientation map of a retrograde eclogite sample consisting of omphacite (yellow) and glaucophane (purple). Black and red lines indicate misorientation angles over 10° and between 1 and 10°, respectively. B) EDX map showing Na-content of the same section. Section is perpendicular to foliation and stretching lineation.

Similar to the fresh eclogite sample MS11.2, the large omphacite grains frequently exhibit subgrains, which are similar in size to the smaller grains (Fig. 11A). The smaller grains are therefore considered recrystallized grains. Lobate grain boundaries of the porphyroclasts do not occur as frequently as in the fresh eclogite sample MS11.2 and island grains are not observed.

Misorientation angle data analysis of the eclogite protomylonite sample RK3 reveals a deviation of uncorrelated grains from a random distribution, which indicates a pronounced CPO. For correlated grains a main maximum below 10° and a secondary maximum between 15° and 30° , when all grains are considered (Fig. 7D) similar to the eclogite mylonite sample MS11.2. For the omphacite porphyroclasts (100-400 μm), the relative frequency of misorientation angles in correlated grains displays only the maximum below 10° , pointing to the formation of small angle boundaries (Fig. 7D). For the small grains (<20 μm) the secondary maximum of misorientation angles between 15° and 25° is observed, pointing to a recrystallization of grains (Fig. 7E). The main maximum characteristic of low angle grain boundaries below 10° as well as this secondary maximum of recrystallized grains are together indicative of subgrain rotation recrystallization (Fig. 7F).

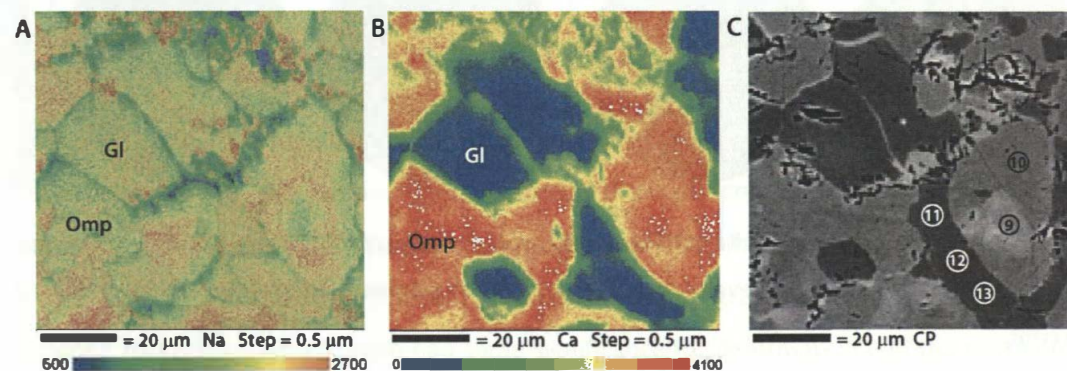


Fig. 12: (A) EDX map of Na-content of retrogressed eclogite sample RK3. Gl = glaucophane; Omp = omphacite (B) EDX map of Mg-content. C) Back scatter electron map. Numbers indicate location of quantitative point measurements listed in Table 2. Section is perpendicular to foliation and lineation.

In contrast to the fresh eclogite mylonite sample MS11.2, porphyroclasts of the retrogressed mylonites mainly display Na-rich cores and a decreasing Na-content towards the rim (subset in Fig. 11B and Fig. 12A). Locally, a few omphacite porphyroclasts yield Na-poor inner cores (#9 in Fig. 12C and Table 2), Na-rich outer cores (#10 in Fig. 12C and Table 2) and a decreasing Na-content towards the rim (subset in Fig. 12A). A decrease of Na is always associated with an increase of Ca in the omphacite grains (Fig. 12A and B and Table 2 #9 and #10). Color-coding of the recrystallized grains indicates an intermediate Na-content, i.e. generally lower than the Na-

rich cores, but higher than the Na-poor rims of the porphyroclasts. They also show some zoning with decreasing Na-content towards the rim.

Glaucofane in the eclogites formed during retrogression, illustrated by its frequent occurrence in pressure shadows of garnet grains (Fig 5B). Furthermore boudinaged omphacite grains with glaucofane-filled gaps can be observed. The glaucofane also occurs within the omphacite matrix and its stretching lineation is aligned with that of omphacite. Glaucofane likewise exhibits two sets of grain sizes – larger grains with ($> 100 \mu\text{m}$) and smaller grains ($< 10 \mu\text{m}$) and a few of the glaucofane grains exhibit subgrains (Fig. 11A). There are two different groups of subgrains, one with a size of 3-10 μm , the other one with a size of 20-50 μm (Fig. 11A). The small glaucofane grains are of similar size as the small set of subgrains indicating that they are recrystallized grains. Relatively low Na- and Mg-contents and high Fe-contents of up to 4.4% show that the amphibole in sample RK3 is not the pure glaucofane end-member, but a solid solution between glaucofane and ferroglaucophane (Table 2 #11-13).

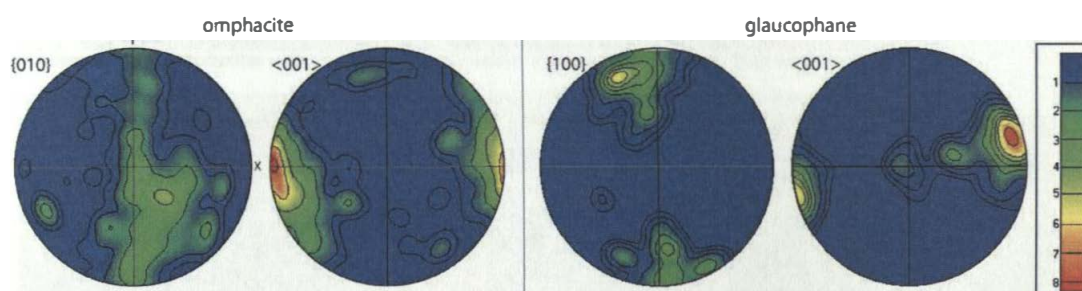


Fig. 4.13: Pole figures of omphacite [010] and [001] and glaucofane [100] and [001] of a retrogressed eclogite sample (RK3). Contour levels represent multiples of a random distribution and are indicated on the right.

EBSO CPO analysis of sample RK3 showed that both, the omphacite CPO, and the glaucofane CPO display [001] point maxima parallel to the X-direction of the pole figure which is aligned in accordance with the omphacite lineation (Fig. 13). The [010] axes of omphacite, and the [100] of glaucofane, respectively, form girdle structures perpendicular to the omphacite stretching lineation in sample RK3 (Fig. 13). This is in accordance with the pronounced stretching lineation observed in the hand specimen. The CPOs of both the omphacite and the glaucofane coincide with those derived from neutron diffraction (compare RK3 in Fig. 4A and Fig. 13).

Paragonite in sample mostly exhibits a random distribution, as well as orientation in the sample. Its random orientation is confirmed by the CPO obtained by tof neutron diffraction, which shows a weak alignment of the paragonite basal plane (001) within the foliation plane (RK3 Fig. 4A).

Garnet grain sizes are about 80-500 μm in the fine-grained retrogressed samples. The grains are mostly euhedral and fractures are frequent. In the retrogressed eclogite sample RK49, the pyrope content increases from core to rim, whereas the almandine content decreases (Table 2). Garnet inclusions in retrogressed eclogites are omphacite, glaucophane, phengite, epidote, quartz and rutile. Omphacite, glaucophane and phengite are mostly aligned within the main foliation, but locally also exhibit an irregular orientation. Rutile needles are ubiquitous and are always aligned in a foliation, (inset Fig. 5B). Quartz and epidote inclusions always display an irregular or random distribution.

4.2. Metasediments

4.2.1. Micaquartzites

The micaquartzites contain quartz (71-92 vol.-%), white mica (8-24 vol.-%) and some minor amounts of clinozoisite. The rocks are relatively massive and exhibit a weak mica foliation and a well-defined quartz foliation and quartz stretching lineation. Quartz grains are variable in size with smaller grains and larger grains of a few hundred μm and display irregular grain shapes, which can be influenced by pinning of mica flakes and other second phases. They exhibit lobate grain boundaries and form together dissection microstructures indicative of grain boundary migration recrystallization (Fig. 5C). Some of the large grains show intracrystalline deformation features like undulose extinction, deformation bands and subgrains. As the small grains (~30-100 μm) are similar in size as the subgrains within some of the larger grains, it can be assumed that also subgrain rotation recrystallization had some significance for deformation and the microstructural development. Locally, there are straight grain boundaries and 120° triple junctions, which suggest that the quartz microstructure was affected by some annealing after deformation.

White mica in the micaquartzites is phengitic with Si-contents of 3.22-3.24 (Table 2). Mica grains are between 100 μm and 1 mm in length. There are individual mica grains between quartz grains and also some thin mica layers. Most mica grains are aligned in the foliation, but some grains, especially the individual ones are irregularly oriented.

4.2.2. Paragneisses

The gneisses consist of quartz (~50 vol.-%), feldspar (~30 vol.-%), white mica (~20 vol.-%) and some accessory minerals. A pronounced foliation is defined by alternating quartz-rich and mica-rich layers with thicknesses of a few mm. Some of the quartz layers vary in thickness and either

thinn-out or reach thicknesses of up to 1 cm. Quartz grains display irregular shapes and a variable grain size. There are larger porphyroclasts with sizes of 100-500 μm and recrystallized grains with sizes of 30-80 μm (Fig. 5D). The large grains contain some optical subgrains which are about the same size as the recrystallized grains. Locally bulges with sizes of 10-20 μm are also observed. Signs of annealing of the porphyroclasts are not clearly visible.

Mica in the paragneiss is phengitic with Si-contents of 3.19-3.20 (Table 2). Mica grain sizes are between 150 μm and 2 mm in length. They show some alignment within the foliation, but occur also at small angles to the foliation.

The feldspar in the gneisses has a grain size of 100-400 μm and mostly displays an irregular shape. Most deformation was taken up by quartz and mica; albite grains represent clasts with some internal fractures, embedded in the weaker matrix of quartz and mica.

5. Discussion

5.1 Deformation mechanisms of eclogites

Omphacite and garnet are the major constituents of eclogites. Since garnets generally behave as rigid bodies, omphacite accommodates most of the deformation in eclogites. Omphacite in naturally deformed eclogites frequently develops a pronounced CPO (e.g. Abalos, 1997; Kurz et al., 2004; Neufeld et al., 2008; Llana-Funez et al., 2012), but the CPO forming deformation mechanisms are not completely understood. Trans electron microscopy (TEM) studies of naturally deformed omphacite revealed dislocation glide and climb by activation of three slip systems: $[001]\{100\}$; $\frac{1}{2}\langle 110 \rangle\{-110\}$; $[001]\{110\}$ (Godard and Van Roermund, 1995). Three active slip systems alone, however, cannot fully accommodate strain, which means other deformation mechanisms are likely to operate in addition. Mauler et al. (2001) consider anisotropic growth and anisotropic elastic moduli as most important mechanisms for CPO formation in omphacite. The eclogite mylonite MS112 and the retrogressed eclogite RK3 of the present study both display a pronounced omphacite CPO (Figs. 4, 9 and 13). In both samples, the omphacite grains exhibit zoning, which has an equal thickness along individual grains (e.g. zoning is not thicker in any growth direction of omphacite grains). This shows that anisotropic growth of omphacite was not the CPO forming mechanism of the eclogites in this study. EBSD analysis revealed large omphacite porphyroclasts with subgrains, as well as small grains, which are of similar size as the subgrains in the porphyroclasts in both fresh eclogites (Fig. 6C) and retrogressed eclogites (Fig. 11A). The porphyroclasts in the eclogite mylonite MS112 frequently exhibit lobate grain boundaries, which points to grain boundary migration (GBM) and indicates relatively low strain rates (Fig. 6A).

Misorientation angles of the omphacite porphyroclasts of both fresh eclogites (Fig. 7B) and retrogressed eclogites (Fig. 7E) exhibit a maximum below 10°, which indicates subgrain rotation (SGR) and higher strain rates. The recrystallized grains display a maximum between 10 and 30° in addition to the maximum below 10° (Fig. 7 C and F), which points to an ongoing rotation of the recrystallized grains in both fresh and retrogressed eclogites.

The analysis of misorientation axes of subgrains within a porphyroclast of the eclogite mylonite MS112 yielded a relatively scattered distribution (Fig. 8 C and D). The observed clusters are formed by individual subgrain boundaries and indicate that several different slip systems operated. The prominent cluster in Y-direction of the pole figure could indicate a rotation around the Y-axis and shows the kinematic influence on the deformation (Fig. 8 D). When subgrains of several porphyroclasts, as well as recrystallized grains, are considered in the analysis of misorientation axes, the distribution is even more scattered (Fig. 8G). However, clustering is still observed even for high angle boundaries. This confirms SGR and dynamic recrystallization of omphacite. The generally scattered distribution of misorientation axes however, indicates that other deformation mechanisms were active. Grain boundary sliding has been well documented in other minerals like calcite (Bestmann and Prior, 2003), quartz (Stipp et al., 2006; Halfpenny et al. 2006), plagioclase (Jiang et al., 2000) and garnet (Terry and Heidelbach, 2004), and could be an explanation for the randomization of misorientation axes of omphacite in MS112.

EBSD analysis of retrograde glaucophane in sample RK3 revealed subgrains in large porphyroclasts and smaller grains, which are of similar size as the subgrains in the porphyroclasts (Fig. 11A). Deformation of naturally deformed glaucophane by dislocation creep at temperatures between 550 and 600° has been documented by Reynard et al. (1989), who identified the activity of 5 independent slip systems through TEM: (010)[100]; (100)[001]; {110}[001]; $\{110\}^{1/2}\langle 1-10 \rangle$; $(001)^{1/2}\langle 110 \rangle$. It is therefore likely that glaucophane in the retrogressed eclogite sample RK3, which formed at similar temperatures deformed by dynamic recrystallization (Fig. 2A).

5.2 Deformation from subduction to peak conditions

Prograde blueschist facies conditions during subduction of the EZ are documented by glaucophane inclusions in garnet (Droop, 1985; Frank et al., 1987; Kurz et al., 1998a). The garnets in the eclogite mylonite MS112 exhibit prograde zoning and contain numerous glaucophane inclusions, which are aligned in a foliation. This shows that a foliation forming deformation took place at blueschist facies conditions on the prograde path. A foliation forming deformation at eclogite facies conditions is confirmed by the alignment of omphacite inclusions. The folded rutile

foliation in garnets of the eclogite sample RK49 points to a rotation of some of the garnets during their syn-deformational growth (Fig. 4B).

Deformation of the omphacite matrix of the eclogites was analysed by EBSD analysis of sample MS112 (section 6.1). Omphacite porphyroclasts, which exhibit a prograde zoning, were deformed by GBM, indicating relatively low strain rates and a distributed deformation during subduction at lower eclogite facies conditions. The recrystallized omphacite grains exhibit higher jadeite contents than the porphyroclasts (Fig. 5C), which shows that dynamic recrystallization became the main deformation mechanism at higher pressures. Hence, with increasing depth strain rates increased and deformation became more localized, which is unusual for shear zones, where generally the opposite effect is observed (e.g. the Simplon fault in the Central Alps: Campani et al., 2010 or the Northern Shear Belt at the Cap de Creus peninsula: Füsseis and Handy, 2008).

On the basis of quartz inclusions in garnet of a metasediment from the EZ, which displayed a foam structure and random CPO, Stöckert et al. (1997) and Stöckert (2002) concluded that stress in the EZ was too low for dislocation creep of quartz during peak conditions. Experimental studies revealed that high stress is required for dislocation creep pyroxene (Boland and Tullis, 1986). The fact that omphacite in the eclogite mylonite MS112 of the present study deformed by dislocation creep shows that stress in the EZ was in fact high during peak conditions.

The eclogites of the EZ exhibit a pronounced omphacite CPO (Fig. 9 and Kurz et al., 2004; Neufeld et al., 2008; Keppler et al., 2015). CPO analysis of Kurz et al. (2004) yielded an S to SL fabric of omphacite in coarse grained eclogites containing jadeite poor omphacite and an L-fabric in fine grained eclogites containing jadeite rich omphacite. According to the authors this indicates oblate strain conditions during subduction and prolate strain during peak conditions and the first stages of exhumation. In contrast, CPO analysis of Neufeld et al. (2008) exclusively yielded SL and S-fabrics of omphacite in the eclogites. The CPO forming deformation was assigned to the prograde path of the EZ by the authors and interpreted to have occurred during the accretion of the EZ to the upper plate. Bulk CPO of the eclogite mylonite MS112 of the present study yielded an SL fabric for omphacite (Fig. 9 and Keppler et al., 2015), which indicates plane strain during subduction of the EZ at eclogite facies conditions. This concurs well with the pronounced macroscopic foliation and well-defined stretching lineation of the eclogites in the EZ (Fig. 3 A and B of this study and Behrmann and Ratschbacher, 1989). The L-fabric of the recrystallized jadeite rich omphacite grains in this sample indicates a transition towards more prolate strain conditions with increasing pressure in this sample. Brenker et al. (2002) attributed the formation of S-fabrics and L-fabrics, respectively, to the cation ordering in omphacite, which is in turn determined by jadeite content and formation temperature. According to this model, at temperatures of up to 750°, an increase in jadeite content causes a transition from a C2/c to a P2/n structure of omphacite leading to a

switch from S-type fabrics to the formation of L-type fabrics. This concurs with the SL-fabric of jadeite-poor porphyroclasts and the L-type fabric of jadeite-rich recrystallized grains of sample MS112. However, this concept is refuted by the SL-fabric yielded for sample RK49 (Fig. 9A), in which omphacite exhibits high jadeite contents (Table 2) and should therefore exhibit an L-type fabric according to the model of Brenker et al., (2002).

Keppler et al. (2015) showed that garnets in the eclogites of the EZ generally exhibit a nearly random CPO. However, the formation of subgrains in garnet of the mylonite eclogite MS112, indicates that strain was high enough for ductile deformation of garnet. The Mg highs along subgrain boundaries could be explained by short-range vacancy diffusion increasing the concentration of the pyrope end member in the distorted regions (Strorey and Prior, 2005). This indicates garnet deformation at increasing pressures coeval with the deformation of the omphacite matrix of this sample on the prograde path (see discussion above).

5.3 Deformation during exhumation

The decreasing jadeite content from core to rim of most omphacite porphyroclasts in the retrogressed eclogite RK3 confirms their continuous growth at decreasing pressures during the exhumation of the eclogites (Fig. 11 and 12). A few omphacite porphyroclasts exhibit Jadeite poor inner cores, Jadeite-rich outer cores and a decreasing Jadeite-content towards the rim (Fig. 11 and 12), indicating that the inner core is a remnant from the prograde path of the rock, while the outer core and the rim grew during exhumation at decreasing pressure. EBSD analysis of this sample suggests SGR and dynamic recrystallization of omphacite (section 6.1). Neufeld et al. (2008) performed CPO analysis of the eclogites from the EZ and found that all CPO forming deformation of omphacite occurred on the prograde path during eclogitization. However, the retrograde zoning of the omphacite porphyroclasts and the low jadeite content of the recrystallized grains in sample RK3 of the present study demonstrate that the dynamic recrystallization occurred on the retrograde path and that CPO forming deformation of the eclogites in the EZ continued during exhumation. Kurz et al. (2004) and Kurz (2005) found L-type fabrics to be dominant in the eclogites during decreasing pressures at eclogite facies conditions, which led Kurz (2005) to the conclusion that constrictional strain was prevalent during early stages of exhumation of the EZ. Neutron diffraction CPO analysis, however, mostly yielded SL-fabrics of omphacite in the retrogressed eclogite samples, which indicate plane strain during exhumation at eclogite facies conditions (Fig. 9A and Keppler et al. 2015). In addition, Keppler et al. (2015) yielded a few S-type fabrics and L-type fabrics of omphacite, which are most likely caused by strain variations towards prolate strain and oblate strain within the subduction

channel. Local strain variability is frequently observed in high strain shear zones, like for example the simplon fault in the Central Alps (REF).

Glaucophane in the retrogressed eclogite sample RK3 shows signs of dynamic recrystallization (section 6.1). Like omphacite, glaucophane CPO mostly yields SL-type fabrics, which shows that plane strain was still dominant at blueschist facies conditions (Fig. 9A and Keppler et al., 2015). A few L-type fabrics and SL-type fabrics of glaucophane are also found, suggesting ongoing local strain variabilities during exhumation to blueschist facies conditions. The CPO of glaucophane always matches that of omphacite (Fig. 9A). If omphacite yields L-type, SL-type, or S-type fabrics, glaucophane correspondingly produces L-type, SL-type, and S-type fabrics, respectively. Heidelberg and Terry (2013) showed that CPO of retrogressive amphibole can be inherited from a preexisting omphacite CPO. In their study, the [100] and [010] axes of amphibole match those of omphacite, if the amphibole CPO is inherited from the omphacite CPO. In the eclogites of the present study, on the other hand, the [010] axes of omphacite preferably align normal to the foliation, or form girdles normal to the lineation according to a more oblate or prolate strain regime, respectively, whereas glaucophane [100] is always aligned normal to the foliation and glaucophane [010] is usually aligned in γ -direction (Fig. 9A and Keppler et al. 2015). This shows that in the eclogites of the EZ, glaucophane CPO formed due to ongoing strain as opposed to statically overgrowing a preexisting omphacite CPO. This shows that the same strain was constant from eclogite facies conditions towards the exhumation to blueschist facies conditions.

Phengite in the eclogites always exhibits a pronounced alignment in the foliation, whereas paragonite is not so well aligned. This points to foliation forming deformation at higher pressures during the growth of phengite, which decreased by the time of paragonite growth at a later stage of the exhumation of the eclogites.

In the metasediments, on the other hand, a pronounced mica foliation and lower Si-contents of mica, as compared to the eclogites (Table 2), demonstrate an ongoing foliation forming deformation during exhumation of the metasediments surrounding the eclogite lenses. Deformation of the metasediments is further documented by quartz microstructures. Quartz grains in the micaquartzites display a variable grain size and irregular shapes. The grain boundaries are frequently lobate (Fig. 4C), which indicates grain boundary migration recrystallization and points to a deformation at high temperatures. 120° triple junctions show that temperatures were high enough for a local annealing. Quartz grains in the paragneisses display large porphyroclasts, as well as small recrystallized grains (Fig. 4D). Furthermore, visual subgrains are observed, indicating subgrain rotation recrystallization.

Quartz CPO in both the paragneisses and the micaquartzites exhibits an asymmetry (Fig. 9B). The asymmetric type I crossed girdle of the quartz c-axes of the paragneiss sample RK28 is indicative

of combined basal $\langle a \rangle$, rhomb $\langle a \rangle$ and prism $\langle a \rangle$ slip. The maxima of the c-axes close to the periphery of the pole figure at an angle to the foliation normal show that rhomb $\langle a \rangle$ slip was most dominant. Quartz c-axes of the mica quartzite are aligned at a small angle to the foliation normal, indicating basal $\langle a \rangle$ slip. The secondary maximum in the center of the pole figure points to additional prism $\langle a \rangle$ slip.

In summary, the eclogites and metasediments document ongoing deformation during the complete exhumational path of the EZ. Dynamic recrystallization and formation of a pronounced CPO of both, omphacite, and glaucophane revealed deformation from peak conditions at eclogite facies up to the exhumation to blueschist facies. Si-contents of the metasediments are lower than those of the eclogites and show that deformation in the metasediments outlasted that of the eclogites.

3. Summary

In this study, metasediments, fresh eclogites and retrogressed eclogites from the EZ, an exhumed subduction channel of the Tauern Window, were examined in terms of microstructures and CPO to draw conclusions on their deformation during subduction, peak conditions and exhumation. Our results showed that CPO forming deformation in the eclogites took place both during their subduction and their exhumation. Dynamic recrystallization of omphacite occurred at eclogite facies conditions on the prograde path, as well as during the exhumation. The analysis of misorientation axes confirmed that dislocation creep was the main CPO forming mechanism in the eclogites, although other mechanisms must have been active in addition.

During subduction of the eclogites plane strain was dominant with some variations towards prolate and oblate strain (Fig. 14). During exhumation plane strain was likewise prevailing in the eclogites and the same strain variations are also observed. This strain lasted from eclogite facies towards the exhumation to blueschist facies, which is confirmed by matching CPO of omphacite and glaucophane in the eclogites (Fig. 14). Si-contents of white mica in the metasediments are lower than in the eclogites, which shows that deformation in the metasediments outlasted that of the eclogites. The metasediments record deformation during the final stages of exhumation of the EZ (Fig. 14). Signs of annealing are observed in the metasediments, which likely occurred during the late stage high temperature overprint of the EZ. This recovery shows that by the time of the high temperature overprint, deformation of the metasediments had also ceased.

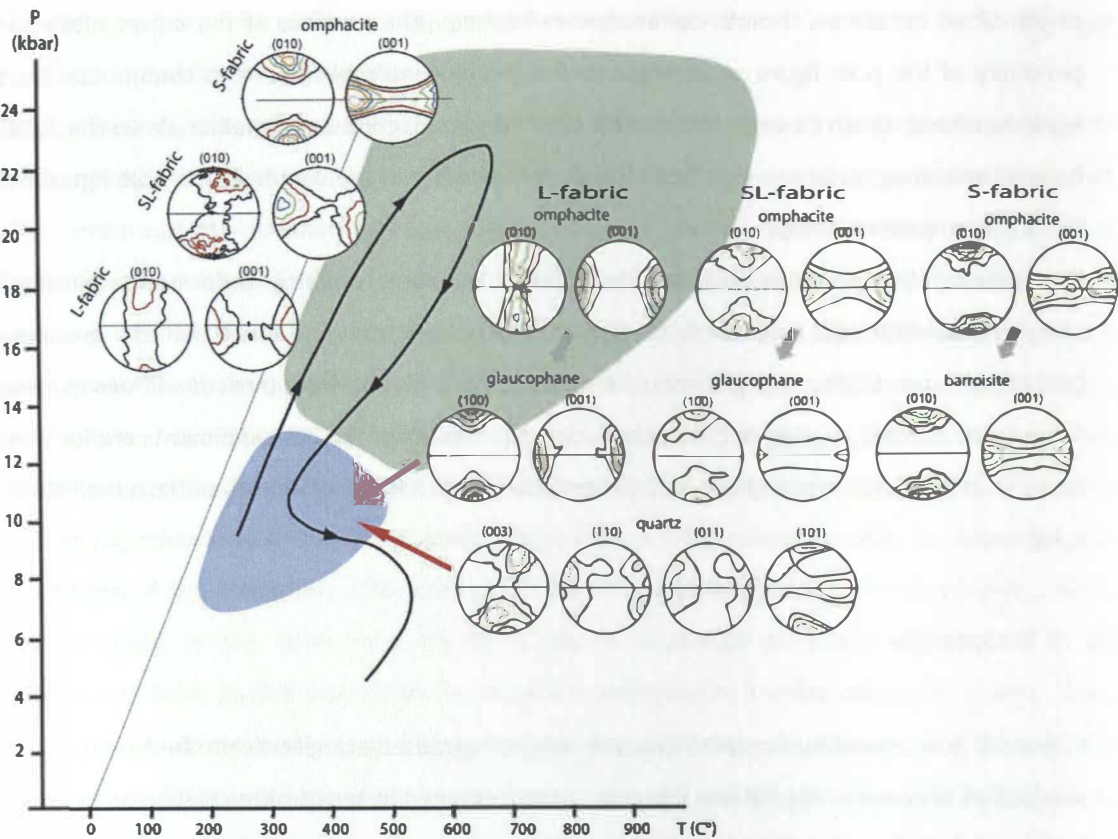


Fig. 4.14: PT-path of the EZ after Holland, 1979; Dachs, 1986; Spear and Franz 1986; Dachs, 1990; Zimmermann et al., 1994; Kurz et al., 1998 , including omphacite and amphibole CPO of the eclogites and quartz CPO of the metasediments at the approximate stage of CPO formation.

4. Conclusions

1. The oldest observed foliation formed during prograde blueschist facies conditions, documented by glaucophane inclusions in garnet grains of eclogites.
2. Deformation of omphacite close to peak pressure is characterized by subgrain rotation and subsequent recrystallization, i.e. dominated by dislocation creep.
3. Strain during subduction and exhumation of the eclogites was close to plane strain with some local variations in the prolate and oblate strain field. Plane strain deformation corresponds to the macroscopic foliation and lineation of the eclogites.
4. The same strain persisted in the eclogites during exhumation from eclogite facies to blueschist facies, demonstrated by matching CPO of omphacite and glaucophane.
5. Deformation of the metasediments outlasted that of the eclogites as illustrated by their lower Si-contents of white mica. CPO and microstructures of the metasediments document the last stages of exhumational deformation.

6. Ongoing deformation during subduction, peak pressure, as well as the exhumation of the EZ was demonstrated, offering insights into the deformational processes within subduction channels.

REFERENCES:

- Adams, B.L., Wright, S.I., Kunze, K., 1993. Orientation imaging and the emergence of a new microscopy. *Metallurgical and Materials Transactions, A* 24, 819-831.
- Agard, P., Yamato, L., Jolivet, E., and Burov (2009), Exhumation of oceanic blueschists and eclogites in subduction zones: Timing and mechanisms, *Earth Science Review*, 92, 53–79.
- Behrmann, J. H. a. Frisch, W., 1990. Sinistral Ductile Shearing Associated with Metamorphic Decompression in the Tauern Window, Eastern Alps. *Jahrbuch der Geologischen Bundesanstalt*, 133, 2, 135-146.
- Behrmann, J.H., Ratschbacher, L., 1989. Archimedes revisited: a structural test of eclogite emplacement models in the Austrian Alps. *Terra Nova* 1, 242–252.
- Bestmann, M., Habler, G., Heidelbach, F., Thöni, M., 2008. Dynamic recrystallization of garnet and related diffusion processes. *Journal of Structural Geology*, 30, 777-790.
- Bestmann, M. and Prior, D.J., 2003. Intragranular dynamic recrystallization in naturally deformed calcite marble: diffusion accommodated grain boundary sliding as a result of subgrain rotation recrystallization. *Journal of Structural Geology*, 25, 1597–1613.
- Blanco-Quintero, I.F., Garcia-Casco, A., Gerya, T.V., 2011. Tectonic blocks in serpentinite mélangé (eastern Cuba) reveal large-scale convective flow of the subduction channel. *Geology* 39, 79–82.
- Buatier, M., Van Roermund, H.L.M., Drury, M.R., Lardeaux, J.M., 1991. Deformation and recrystallization mechanisms in naturally deformed omphacites from the Sesia-Lanzo zone: geophysical consequences. *Tectonophysics* 195, 11-27.
- Burov, E., Jolivet, A., Le Pourhiet, L., Poliakov, A., 2001. A thermomechanical model of exhumation of high pressure (HP) and ultra-high pressure (UHP) metamorphic rocks in Alpine-type collision belts. *Tectonophysics* 342, 113– 136.
- Dachs, 1986. High pressure mineral assemblage and their breakdown products in metasediments of the southern Großvenediger, Tauern Window, Austria. *Schweizer Mineralogische und Petrologische Mitteilungen*, 66, 145-161.
- Dachs, E., 1990. Geothermobarometry in metasediments of the southern Grossvenediger area (Tauern Window, Austria). *Journal of Metamorphic Geology*, 8, 217–230.
- Díaz Aspiroz, M., Lloyd, G.E., Fernández, C., 2007. Development of lattice preferred orientation in clinoamphiboles deformed under low-pressure metamorphic conditions. A SEM/EBSD study of metabasites from the Aracena metamorphic belt (SW Spain). *Journal of Structural Geology* 29, 629–645.

- Droop, G.T.R., 1985. Alpine metamorphism in the south-eastern Tauern Window, Austria. P-T variations in space and time. *Journal of Metamorphic Geology*, 3, 371-401.
- Frank, W., Höck, V., and Miller, C., 1987. Metamorphic and tectonic history of the central Tauern Window. *Geodynamics of the Eastern Alps*, Deuticke Vienna, 34-54.
- Franz, G., Mosburger, V., and Menge, R., 1991. Carbo-Permian pteridophyll leaf fragments from an amphibolite facies basement, Tauern Window, Austria. *Terra Nova*, 3, 137-141.
- Froitzheim, N., Schmid, S.M., and Frey, M., 1996. Mesozoic paleogeography and the timing of eclogite-facies metamorphism in the Alps: A working hypothesis. *Eclogae Geologicae Helveticae*, 89, 1.
- Gerya, T.V., Stöckhert, B. and Perchuk, A.L., 2002. Exhumation of high-pressure metamorphic rocks in a subduction channel – a numerical simulation. *Tectonics*, 21, 6-16-19.
- Glodny, J., Ring, U., Kühn, A., Gleissner, P., Franz, G., 2005. Crystallization and very rapid exhumation of the youngest Alpine eclogites (Tauern Window, Eastern Alps) from Rb/Sr mineral assemblage analysis. *Contributions to Mineralogy and Petrology*, 149, 699 – 712.
- Godard, G., Van Roermund, H.L.M., 1995. Deformation-induced clinopyroxene fabrics from eclogites. *Journal of Structural Geology* 17 (10), 1425–1443.
- Halfpenny, A., Prior, D.J. and Wheeler, J., 2006. Analysis of dynamic recrystallization and nucleation in a quartzite mylonite. *Tectonophysics*, 427, 3-14.
- Holland, T. J. B., and Richardson, S. W., 1979. Amphibole zonation in metabasites as a guide to the evolution of metamorphic conditions. *Contributions to Mineralogy and Petrology*, 70, 143-148.
- Hoschek, G., 2001. Thermobarometry of metasediments and metabasites from the Eclogite zone of the Hohe Tauern, Eastern Alps, Austria. *Lithos*, 59, 127-150.
- Hoschek, G., 2004. Comparison of calculated P-T pseudosections for a kyanite eclogite from the Tauern Window, Eastern Alps, Austria. *European Journal of Mineralogy* 16, 59-72.
- Jiang, Z., Prior, D.J., and Wheeler, J., 2000. Albite crystallographic preferred orientation and grain misorientation distribution in a low-grade mylonite: implications for granular flow. *Journal of Structural Geology*, 22, 1663-1674.
- Keppler, R., Ullemeyer, K., Behrmann, J. H., Stipp, M., 2014. Potential of full pattern fit methods for the texture analysis of geological materials: implications from texture measurements at the recently upgraded neutron time-of-flight diffractometer SKAT. *Journal of Applied Crystallography*, 47, doi:10.1107/S1600576714015830.

Keppler, R., Ullemeyer, K., Behrmann, J. H., Stipp, M., Kurzwski, R. M., (in press). Crystallographic preferred orientations and elastic anisotropies of exhumed subduction channel rocks: an example from the Eclogite Zone (Tauern Window, Austria). *Tectonophysics*

Kleinschrodt, R., Duyster, J.P., 2002. HT-deformation of garnet: an EBSD study on granulites from Sri Lanka, India and the Ivrea Zone. *Journal of Structural Geology* 24, 1829–1844.

Kurz, W., 2005. Constriction during exhumation: Evidence from eclogite microstructures. *Geology*, 33, 1, 37-40.

Kurz, W., Jansen, E., Hundenborn, R., Pleuger, J., Schäfer, W., a. Unzog, W., 2004. Microstructures and crystallographic preferred orientations of omphacite in Alpine eclogites: implications for the exhumation of (ultra-) high-pressure units. *Journal of Geodynamics*, 37, 1-55.

Kurz, W., Neubauer, F. a. Dachs, E., 1998a. Eclogite meso- and microfabrics: implications for the burial and exhumation history of eclogites in the Tauern Window (Eastern Alps) from P-T-d paths. *Tectonophysics*, 285, 183-209.

Kurz, W., Neubauer, F., Genser, J., Dachs, E. 1998b. Alpine geodynamic evolution of passive and active continental margin sequences in the Tauern Window (eastern Alps, Austria, Italy): a review. *International Journal of Earth Sciences*, 87, 225–242.

Laubscher, H., 1988. Material balance in Alpine orogeny. *Geological Society of America Bulletin*, 100, 1313-1328.

Nagel, T. J., Herwartz, D., Rexroth, S., Münker, C., Froitzheim, N., Kurz, W., 2013. Lu-Hf dating, petrography, and tectonic implications of the youngest Alpine eclogites (Tauern Windo, Austria). *Lithos* 170-171, 179-190.

Neufeld, K., Ring, U., Heidelbach, F., Dietrich, S., and Neuser, R.D., 2008. Omphacite textures in eclogites of the Tauern Window: Implications for the exhumation of the Eclogite Zone, Eastern Alps. *Journal of Structural Geology*, 30, 976–992.

Raith, M., Mehrens, C., and Thöle W., 1980. Gliederung, tektonischer Bau und metamorphe Entwicklung der penninischen Serien im südlichen Venediger-Gebiet, Osttiroler Jahrbuch der Geologischen Bundesanstalt, 123, 1–37.

Reynard, B., Gillet, P., Willaime, C., 1989. Deformation mechanisms in naturally deformed glaucophanes: a TEM and HREM study. *European Journal of Mineralogy*. 1, 11-624.

Ratschbacher, L., Frisch, W., Neubauer, F., Schmid, S. M. a. Neugebauer, J., 1989. Extension in compressional orogenic belts: The eastern Alps. *Geology*, 17, 404-407.

Rosenberg, C.L. ,2004. Shear zones and magma ascent: a model based on a review of the Tertiary magmatism in the Alps. *Tectonics*, 23, 997-1000.

- Schmid, S. M., Pfiffner, O. A., Froitzheim, N., Schönborn, G., and Kissling, E., 1996. Geophysical-geological transect and tectonic evolution of the Swiss-Italian Alps. *Tectonics*, 15, 1036–1064.
- Schmid, S.M., Scharf, A., Handy, M.R., and Rosenberg, C.L., 2013. The Tauern Window (Eastern Alps, Austria): a new tectonic map, with cross-sections and a tectonometamorphic synthesis. *Swiss Journal of Geoscience*, 106, 1-32.
- Selverstone, J., 1993. Micro- to macroscale interactions between deformational and metamorphic processes, Tauern Window, Eastern Alps. *Schweizerische Mineralogische Mitteilung*, 7, 229-239.
- Selverstone, J., Franz, G., Thomas, S., a. Getty, S., 1992. Fluid variability in 2 Gpa eclogites as an indicator of fluid behaviour during subduction. *Contributions to Mineralogy and Petrology*, 112, 341-357.
- Smye, A.J., Bickle, M.J., Holland, T.J.B., Parrish, R.R., Condon, D.J., 2011. Rapid formation and exhumation of the youngest Alpine eclogites: a thermal conundrum to Barrovian metamorphism. *Earth and Planetary Science Letters* 306, 193–204.
- Spear and Franz, 1986. P-T evolution of metasediments from the Eclogite one, south-central Tauern Window, Austria. *Lithos* 19, 219-234.
- Stipp, M., Tullis, J. and Behrens, H., 2006. Effect of water on the dislocation creep microstructure and flow stress of quartz and implications for the recrystallized grain size piezometer, *Journal of Geophysical Research*, 111, B04201, doi:10.1029/2005JB003852.
- Stöckhert, B., 2002. Stress and deformation in subduction zones: insight from the record of exhumed metamorphic rocks. *Geological Society of London* 200, 255-274.
- Stöckhert, B., Massonne, H.-J., Nowlan, E. U., 1997. Low differential stress during high-pressure metamorphism: the microstructural record of a metapelite from the Eclogite Zone, Tauern Window, Eastern Alps. *Lithos*, 41, 103-118.
- Storey, C.D., Prior, D.J., 2005. Plastic deformation and recrystallization of garnet: a mechanism to facilitate diffusion creep. *Journal of Petrology* 46, 2593–2613.
- Terry, M.P., Heidelbach, F., 2004. Superplasticity in garnet from eclogite facies shear zones in the Haram Gebbro, Haramsøya. Norway. *Geology* 32, 281–284.
- Ullemeyer, K., Spalhoff, P., Heinitz, J., Isakov, N. N., Nikitin, A. N., Weber, K., 1998. The SKAT texture diffractometer at the pulsed reactor IBR-2 at Dubna: Experimental layout and first measurements. *Nuclear Instruments and Methods of Physical Research*, 412, 80–88.
- Vollbrecht, A., Pawlowski, J., Leiss, B., Heinrichs, T., Seidel, M., Kronz, A. 2006. Ductile deformation of garnet in mylonitic gneisses from the Münchberg Massif (Germany). *Tectonophysics*, 427, 153-170.

Wenk, H.-R. & Christie, J. M. 1991. Comments on the interpretation of deformation textures in rocks. *Journal of Structural Geology* 13, 1091-1110.

Zimmermann, R., Hammerschmidt, K., Franz, G., 1994. Eocene high pressure metamorphism in the Penninic units of the Tauern Window (Eastern Alps): evidence from ^{40}Ar - ^{39}Ar dating and petrological investigations. *Contributions to Mineralogy and Petrology*, 117, 175–186.

5. Discussion, conclusions and outlook

This PhD thesis presents the results of CPO analysis of high pressure rocks from the EZ of the Tauern Window, an exhumed subduction channel of the Eastern Alps. The EZ has a typical structure and composition of a subduction channel and the conclusions drawn from this work can be directly transferred to other exhumed high pressure units as well as recent subduction channels around the world. This study provides new information on the physical properties and the deformational processes of these highly complex shear zones and offers valuable insights into the method of tof neutron diffraction for CPO investigations. In the following sections, the results of the three individual studies are summarized and discussed. In addition, an outlook on possible future work in this research area is given.

5.1. Manuscript #1

Tof neutron diffraction texture analysis of polymineralic rock samples was performed at the SKAT diffractometer of the Frank Laboratory of Neutron Physics at JINR, Dubna, Russia (Ullemeyer et al., 1996). The SKAT was recently upgraded and provides three different detector-collimator rings at variable theta angles to adapt resolution and accessible d-range to the investigated samples. In this study, the effect of counting statistics and number of peak overlaps was analyzed by comparison of results from 'Rietveld texture analysis' (RTA), using different d-ranges in the tof spectra for the calculation. Additionally, a possible reduction of exposition time was tested by progressively reducing the number of measured sample positions.

Our results indicate that peak overlaps represent the most limiting factor in texture analysis of polymineralic rock samples. Considering d-ranges at higher d-spacings leads to better results, despite lower counting statistics. A higher resolution allows for a better separation of peaks and strongly increases the quality of texture results.

RTA of a four phase sample, which was artificially created by summing up spectra of three individual samples, showed that fairly good results can be achieved for samples of medium complexity, despite overlapping peaks in the spectra. Maxima in pole figures of relevant hkl always coincide with maxima of reference pole figures, which were

calculated from tof spectra of the three individual samples and are therefore considered true texture. Small differences in texture strength in comparison to the reference are observed. The differences are fairly minor, however, and the RTA results for the four phase sample are considered reliable for the calculation of rock physical properties, as well as for geological interpretations.

RTA of an eclogite sample containing seven mineral phases with medium or low symmetry yielded more difficulties. Nevertheless, when the mineral phases constitute a high volume percentage (>10%) and texture is strong ($f_2 > 1.4$), eligible results are achieved, provided that the detector-collimator configuration with highest resolution is used for the measurement.

RTA results from a successively thinned out measuring grid were evaluated by comparison to reference textures calculated from a fully covered grid. The results demonstrate that the number of measured sample orientations can be severely reduced without the loss of CPO quality. In samples with an intermediate amount of mineral phases, the limit for high quality texture is the use of about 300-340 spectra for the calculation. Concerning monophasic samples, the lower limit applies to about 150 spectra. When larger step sizes (e.g. fewer spectra) are used, missing points on the grid can lead to a reduction in texture strength, if the maximum of the pole figure is very precise. Locations of maxima, however, still coincide with the reference, illustrating that the number of spectra could be further reduced, if texture is needed for geological interpretations, only. These results show that bulk exposition time for tof neutron diffraction can be severely reduced without loss of information.

5.2. Manuscript #2

In this study, CPOs of eclogites and metasediments from the EZ were measured by means of tof neutron diffraction at the SKAT. As illustrated in Manuscript #1, this method allows the investigation of large polymineralic rock samples and the application of full pattern fit methods for texture evaluation. 3D models for P-wave velocity were calculated using the CPO and known single crystal elastic properties of the constituent minerals (Mainprice and Humbert, 1994). In addition V_p/V_s ratios were calculated for all samples.

Eclogites preserving their high-pressure assemblage Grt + Omph ± Phe ± Qtz ± accessories yield a pronounced omphacite and mica CPO. Anisotropies of these fresh eclogites are fairly low with an average of 1.5%. The location of P-wave maxima is determined by the distribution of omphacite [001], which is mostly aligned with the lineation and sometimes distributed in the foliation plane. Mica basal planes always exhibit a strong alignment in the foliation and high mica contents additionally increase P-wave velocities within the foliation plane of the eclogites.

Retrogressed eclogites further contain glaucophane, which likewise displays a pronounced CPO. Frequently it matches the CPO of omphacite concerning the distribution of [001] axes. The growth and deformation of glaucophane raises the elastic anisotropy of the eclogites to up to 3.7%. If the glaucophane CPO deviates from that of omphacite, it furthermore effects the location of P-wave velocity maxima. These results illustrate a large impact of retrogression during subduction on the physical properties of eclogites.

In addition to modeling the elastic properties, P-wave velocities were measured on spherical samples of a retrogressed and a fresh eclogite in 132 directions in a pressure vessel filled with hydraulic oil (Pros et al., 1998). Pressure can be increased to up to 400 MPa, simulating conditions at depth. The experimentally derived P-wave velocities are lower than those calculated from the CPO, but the locations of maxima coincide. The elastic anisotropy is 40-65% higher, when calculated from the measured P-wave velocities, which confirms previous experimental studies (e.g. Fountain et al., 1994). This difference is caused by the presence of a shape preferred orientation of the grains and by microcracks in the rocks, which are still partially present despite high-pressure conditions (e.g. Siegesmund et al., 1993). Microcracks are particularly important in mica rich samples, since microcracks are mostly oriented parallel to the mica foliation. The studied eclogite samples contain high amounts of phengite and the discrepancy between measured and modeled P-wave velocities is best explained this way.

CPO analysis of the metasedimentary samples yielded a relatively weak calcite CPO in the marble sample. The a-axes show an alignment in lineation direction, while the c-axes are mostly found normal to the foliation plane. The clastic metasediments exhibit a pronounced quartz and mica CPO. As in the eclogites, the mica basal plane is strongly aligned in the foliation plane. The modeled elastic anisotropy of the metasediments is

higher than that of the eclogites. The marble sample yields an anisotropy of 5%, determined by the distribution of calcite a-axes, whereas elastic anisotropies of the clastic metasediments reach values of up to 7.5%, mostly induced by a pronounced mica CPO. Correspondingly the mica rich metasediments yield high velocities within the foliation plane. In quartz-rich samples (50-90%), on the other hand, the anisotropy is further influenced by a pronounced quartz CPO.

Calculated V_p/V_s ratios of the fresh eclogites are about 1.70-1.75, whereas in retrogressed samples this value increases to up to 1.78. This shows that a distinction between fresh and retrogressed eclogites in the subduction channel might be possible. The metasediments have much lower V_p/V_s ratios of 1.5-1.6 with the exception of the marble, which has a V_p/V_s ratio of 1.85. These distinctly different values show the potential for detecting subducted clastic sediments or carbonate platforms within subduction channels at depth.

5.3. Manuscript #3

In this study, the microfabrics of metasediments, as well as fresh and retrogressed eclogites, were investigated by means of EBSD analysis and light optical microscopy to determine the deformational history of the EZ.

Light optical microscopy of eclogite thin sections showed aligned glaucophane inclusions in garnet grains, which point to foliation forming deformation during prograde blueschist facies conditions. SEM studies displayed an increasing jadeite content from core to rim in omphacite grains of fresh eclogites, illustrating their prograde growth during eclogite facies conditions. EBSD analyses revealed the formation of subgrains and small recrystallized grains. The recrystallized grains exhibit the highest jadeite content, which points to recrystallization close to peak pressure. The analysis of misorientation axes revealed the activity of several different slip systems indicating dislocation creep. However other deformation mechanisms were active in addition, as confirmed by a relatively scattered distribution of misorientation axes. Bulk omphacite CPO of fresh eclogites show an SL-type fabric pointing to plane strain during subduction. The jadeite rich recrystallized grains, on the other hand, exhibit an L-type CPO pointing to a change of the deformational regime towards prolate strain during the final stages of subduction.

Furthermore, the formation of subgrains in garnet indicates that strain was high enough for ductile deformation of garnet during subduction (Terry and Heidelbach, 2004).

In the retrogressed eclogites, omphacite porphyroclasts mostly display Jadeite-rich cores and a decreasing Jadeite-content towards the rim, indicating their growth on the retrograde path. They also show signs of subgrain formation and dynamic recrystallization. The recrystallized grains exhibit lower jadeite contents than the porphyroclasts, confirming recrystallization during exhumation. CPO of omphacite of the retrogressed eclogite samples displays S-type, SL-type and L-type fabrics pointing to oblate, plain strain, and prolate strain, respectively. SL-type fabrics are most common, which indicates that plain strain was dominant. The CPO of glaucophane always matches that of omphacite, which shows that despite the strain variability within the shear zone, locally the same strain regime was constant from eclogite facies conditions towards the exhumation to blueschist facies conditions. This contradicts the study of Neufeld et al. (2008), who suggested that all CPO forming deformation of the eclogites took place on the prograde path.

Microstructural investigation of micaquartzites revealed irregular shapes and lobate grain boundaries of quartz, which indicates grain boundary migration recrystallization and points to a deformation at high temperatures. Furthermore, 120° triple junctions suggest a local annealing. Quartz grains in the paragneisses show signs of subgrain formation, bulging and recrystallization, which points to deformation at low to medium temperatures (e.g. Stipp et al, 2002). This shows that some of the metasediments might have been overprinted by the late stage high temperature pulse that took place in the EZ, while others escaped this Barrovian overprint. Quartz CPO in both the paragneisses and the micaquartzites exhibits an asymmetry, indicating simple shear deformation. This asymmetry is in contrast to the omphacite and glaucophane CPO in the eclogites, which is generally symmetric. The non-coaxial deformation of the metasediments is likely due to their higher viscosity, which led to a more prevalent accommodation of strain compared to the competent eclogite lenses.

5.4. Synopsis

In this PhD thesis a complete deformational history of subduction channel rocks is provided. The study includes both fresh eclogites still exhibiting their high pressure mineral assemblage and eclogites that were retrogressed during exhumation. This allowed conclusions on the different deformation stages at various depths, e.g. a correlation to subduction related and exhumation related processes in the subduction channel, respectively. In addition, the metasediments surrounding the eclogite lenses in the subduction channel were part of the investigation, permitting a reconstruction of the evolution of subduction channels as a whole. Data from neutron diffraction texture analysis and EBSD analysis revealed that the eclogite lenses in subduction channels undergo continuous deformation from blueschist facies during subduction, over peak conditions at eclogite facies to the exhumation back to blueschist facies conditions. Previous studies investigating textures of subduction channel rocks focused on fresh eclogites and analysed only omphacite CPO (e.g. Abalos et al., 2010; Mauler et al., 2001; Kurz et al., 2004; Neufeld et al., 2008). In the present study, retrogressed eclogites were included and it was revealed that CPO forming deformation does not only take place during subduction, but continuous during the exhumation in large parts of the eclogite lenses. For the first time the CPO of retrograde glaucophane in the eclogites was investigated and showed a match with the omphacite CPO, which confirms a constant strain regime from eclogite facies to the exhumation to blueschist facies in the subduction channel. Microprobe analysis of white mica (phengite and muscovite) in both eclogites and metasediments showed lower silica contents in the metasediments as compared to the eclogites. This indicates that deformation in the metasediments outlasted deformation in the eclogites. Quartz CPO of the metasediments is strongly asymmetric, which is in contrast to the eclogite lenses. This shows that simple shear was dominant during the final stages of subduction and was accommodated by the metasedimentary matrix of the subduction channel.

Many recent subduction channels are active today, however, an examination at depth is only possible through seismic imaging. Although low velocity layers of a few km thickness are frequently observed above the downgoing lithospheric plate (Langston, 1981; Helffrich and Stein, 1993; Abers et al., 1996; Audet et al., 2010), pointing to the existence

of active subduction channels, a deconvolution of the internal structures within these zones was not possible so far. In part, seismic investigations are hampered by a lack of knowledge regarding the velocity structure and elastic anisotropies of the rocks comprising the subduction channel. In the present study, the elastic properties of a large set of different subduction channel rocks were calculated from the CPO of their constituent mineral phases. As mentioned above, previous studies investigating CPO of eclogites focused on rocks, which still exhibit their high pressure mineral assemblage. Therefore, only elastic properties of fresh eclogites have been examined so far. On the basis of the data presented in this PhD thesis it was revealed that retrogression has in fact a strong influence on the elastic properties of subduction channel rocks, both lowering their P-wave velocity and increasing their elastic anisotropy. Furthermore, it was illustrated that the combination of P-wave velocity, elastic anisotropy and V_p/V_s ratio is specific to different rock types found in subduction channels, which illustrates that each rock type yields a very specific seismic signal. This makes it possible to differentiate between fresh and retrogressed eclogites and to distinguish both from the metasediments in the subduction channel based on their elastic properties. Even a distinction between clastic metasediments and subducted carbonate platforms is feasible. Although, at present, resolution of seismic imaging is not high enough to reveal the internal structure of these shear zones, which have a thickness of only a few kilometers, the instrumental techniques tremendously improved in the last decades and it is assumable that a detection will be possible in the future. Even today, the data presented here is highly useful. The seismic signal expected from subduction channels can be evaluated by numerical modeling of seismic waves (e.g. Essen et al., 2009; Friedrich et al., 2014). An incorporation of elastic anisotropy in these models will highly improve the preciseness of the modeled signal.

To guaranty the quality of elastic properties calculated from CPO of rocks, precise CPO data is essential. Subduction channel rocks are generally mineralogically complex and contain a high number of phases. In this PhD thesis the accuracy of CPO analysis of complex rock samples using *in situ* neutron diffraction was proven. This is not only useful for the CPO investigation of subduction channel rocks, but in fact all crustal rocks, which are mostly polymineralic and highly complex.

5.5. Outlook

While this PhD thesis provides useful information on the physical properties of subduction channel rocks and offers insights into their deformational history, it also raises new questions and reveals some existing gaps in this research area.

Knowledge of elastic wave velocities and anisotropies of rocks are extremely useful for seismic data processing and their interpretation (Lin et al. 2010). In our work, detailed information on elastic anisotropies of subduction channel rocks was presented, however, the resolution of seismic imaging is currently too low to clearly image the internal structures of deep subduction channels. Yet, enormous progress in the technology was made in the last decade and numerical simulations of seismic waves can use the data on elastic properties of high pressure rocks to explore a possible detection of subduction channel rocks in the future. Friedrich et al., (2014) for example modeled the seismic signals produced by a deep subduction channel with a block in matrix structure. In their study, the seismic anisotropies of the rocks were neglected. Our investigations, however, show that anisotropy of subduction channel rocks can be considerably high in case of the metasedimentary matrix. An incorporation of this anisotropy data in numerical simulations could highly increase the precision of their results.

Besides modeling the elastic anisotropies of subduction channel rocks, we performed experimental measurements on two eclogite samples for comparison. The P-wave velocity of the spherical samples was determined in a pressure vessel filled with hydraulic oil. This enables measurements in several different sample directions, which allows a three dimensional illustration of P-wave anisotropy in the samples. This method, however, precludes the measurement of S-waves. To completely cover experimental data on elastic anisotropies of subduction channel rocks the samples should additionally be measured in a triaxial press apparatus, which allows the investigation of S-wave velocities. This would further allow a comparison between modeled and experimental V_p/V_s ratios, which were revealed to be an important factor for the distinction of different rocks in the subduction channel.

The work presented in this study covers the seismic properties of a wide range of subduction channel rocks. Serpentinite is another rock type, which frequently occurs in subduction channels, though it is not found in the EZ. It occurs in other exhumed subduction channels of the Alps, like Monviso and Zermatt Saas, where samples could be collected for investigation. Together with the data presented in this work, modeled elastic properties of serpentinites would cover the complete spectrum of subduction channel rocks.

In this study, CPO analysis of retrogressed eclogites demonstrated that strain during the exhumation of the EZ was highly variable. Investigation of a fresh eclogite sample, on the other hand, revealed a switch from oblate to prolate strain during final stages of subduction. EBSD analysis of a larger set of fresh eclogite samples could show if this specific change in strain regime applied to all eclogites of the EZ during subduction, or if strain was actually as variable as during the exhumation of the rocks.

REFERENCES:

Ábalos, B., Fountain, D.M., Gil Ibarguchi, J.I., Puellas, P., 2010. Eclogite as a seismic marker in subduction channels: Seismic velocities, anisotropy, and petrofabric of Cabo Ortegal eclogite tectonites (Spain). *GSA Bulletin*, 123, 3/4, 439–456.

Abers, G.A., Sarker, G., 1996. Dispersion of regional body waves at 100-150 km depth beneath Alaska: in situ constraints on metamorphism of subducted crust. *Geophysical Research Letters* 23, 1171–1174.

Audet, P., Bostock, M.G., Christensen, N.I. and Peacock, S.M., 2009. Seismic evidence for overpressured subducted oceanic crust and megathrust fault sealing. *Nature*, 457, 76-78.

Fountain, D.M., Boundy, T.M., Austrheim, H., and Rey, P., 1994. Eclogite–facies shear zones—deep crustal reflectors? *Tectonophysics*, 232, 411– 424.

Friederich, W., Lambrecht, L., Stöckhert, B., Wassmann, S. and Moos, C., 2014. Seismic visibility of a deep subduction channel – insights from numerical simulation of high-frequency seismic waves emitted from intermediate depth earthquakes. *Solid Earth*, 5, 141–159.

Helfrich, G., Stein, S., 1993. Study of the structure of the slab-mantle interface using reflected and converted seismic waves. *Geophysical Journal International* 115, 14–4072.

Kurz, W., Jansen, E., Hundenborn, R., Pleuger, J., Schäfer, W., a. Unzog, W., 2004. Microstructures and crystallographic preferred orientations of omphacite in Alpine eclogites: implications for the exhumation of (ultra-) high-pressure units. *Journal of Geodynamics*, 37, 1-55.

Langston, C.A., 1981. Evidence for the subducting lithosphere under southern Vancouver island and western Oregon from teleseismic P wave conversion. *J. Geophys. Res.* 86, 3857–3866.

Lin, G., Thurber, C.H., Zhang, H., Hauksson, E., Shearer, P.M., Waldhauser, F., Brocher, T.M. and Hardebeck, J., 2010. A California statewide three-dimensional seismic velocity model from both absolute and differential times. *Bulletin of the Seismological Society of America*, 100, 225–240.

Mainprice, D., and Humbert, M., 1994. Methods of calculating petrophysical properties from lattice preferred orientation data. *Surveys in Geophysics*, 15, 575–592.

Mauler, A., Godard, G., and Kunze, K., 2001. Crystallographic fabrics of omphacite, rutile and quartz in Vendée eclogites (Armorican Massif, France). Consequences for deformation mechanisms and regimes. *Tectonophysics*, 342, 81–112.

Neufeld, K., Ring, U., Heidelbach, F., Dietrich, S., and Neuser, R.D., 2008. Omphacite textures in eclogites of the Tauern Window: Implications for the exhumation of the Eclogite Zone, Eastern Alps. *Journal of Structural Geology*, 30, 976–992.

Pros, Z., Lokajíček, T., Klíma, K., 1998. Laboratory study of elastic anisotropy on rock samples. *Pure Applied Geophysics*, 151, 619–629.

Siegesmund, S., Vollbrecht, A., Chlupac, T., Nover, G., Dürrast, H., Müller, J. & Weber, K., 1993. Fabric-controlled anisotropy of petrophysical properties observed in KTB core samples, *Sci. Drill.*, 4, 31–54.

Stipp, M., Stunitz, H., Heilbronner, R. and Schmid, S.M., 2002. The eastern Tonale fault zone: a 'natural laboratory' for crystal plastic deformation of quartz over a temperature range from 250 to 700 degrees C°. *Journal of Structural Geology*, 24, 12, 1861–1884.

Terry, M.P., Heidelbach, F., 2004. Superplasticity in garnet from eclogite facies shear zones in the Haram Gebro, Haramsøya, Norway. *Geology* 32, 281–284.

Ullemeyer, K., Spalhoff, P., Heinitz, J., Isakov, N. N., Nikitin, A. N., Weber, K., 1998. The SKAT texture diffractometer at the pulsed reactor IBR-2 at Dubna: Experimental layout and first measurements. *Nuclear Instruments and Methods of Physical Research*, 412, 80–88.

APPENDIX A

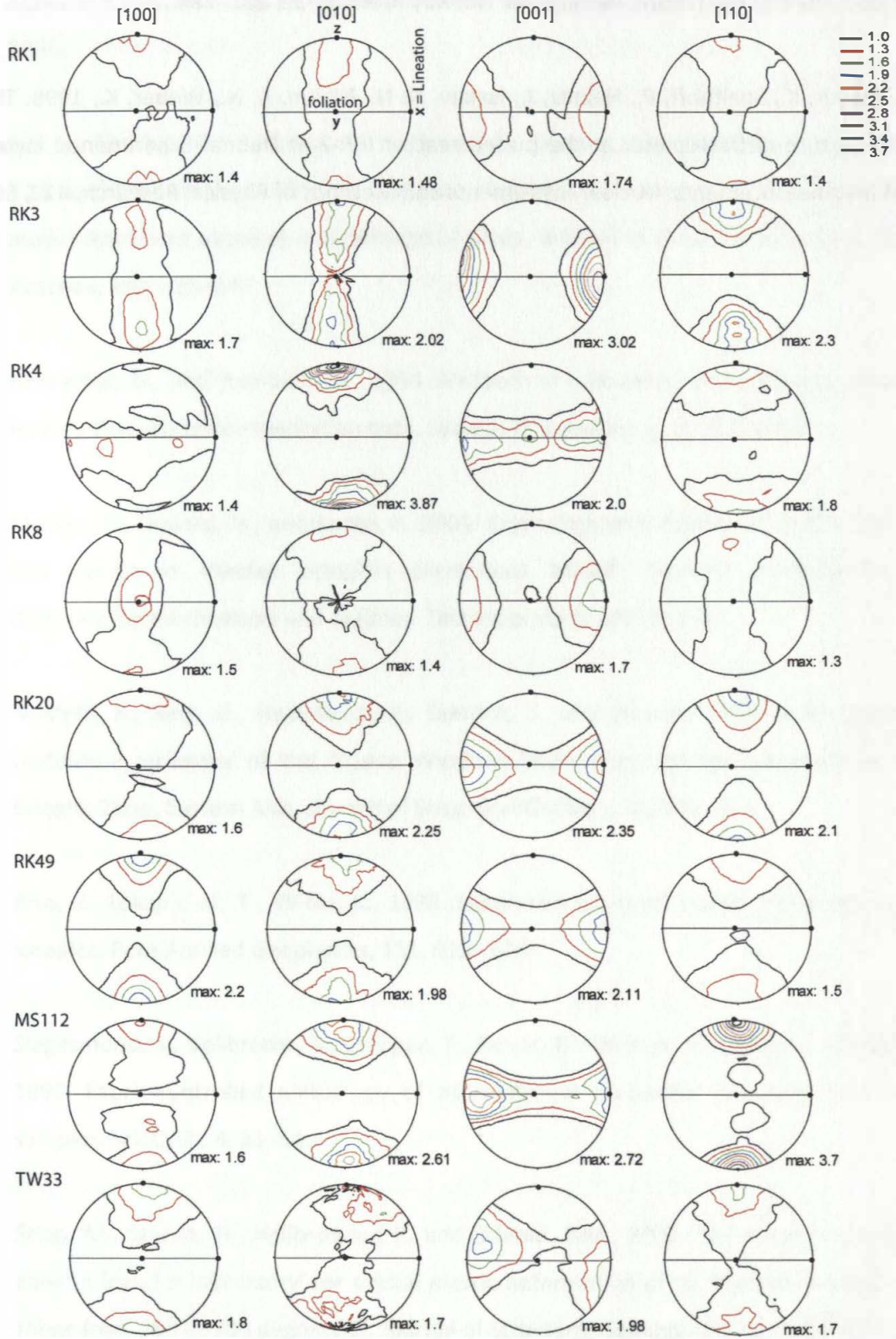


Fig. 1: Pole figures of relevant omphacite hkl of all investigated samples.

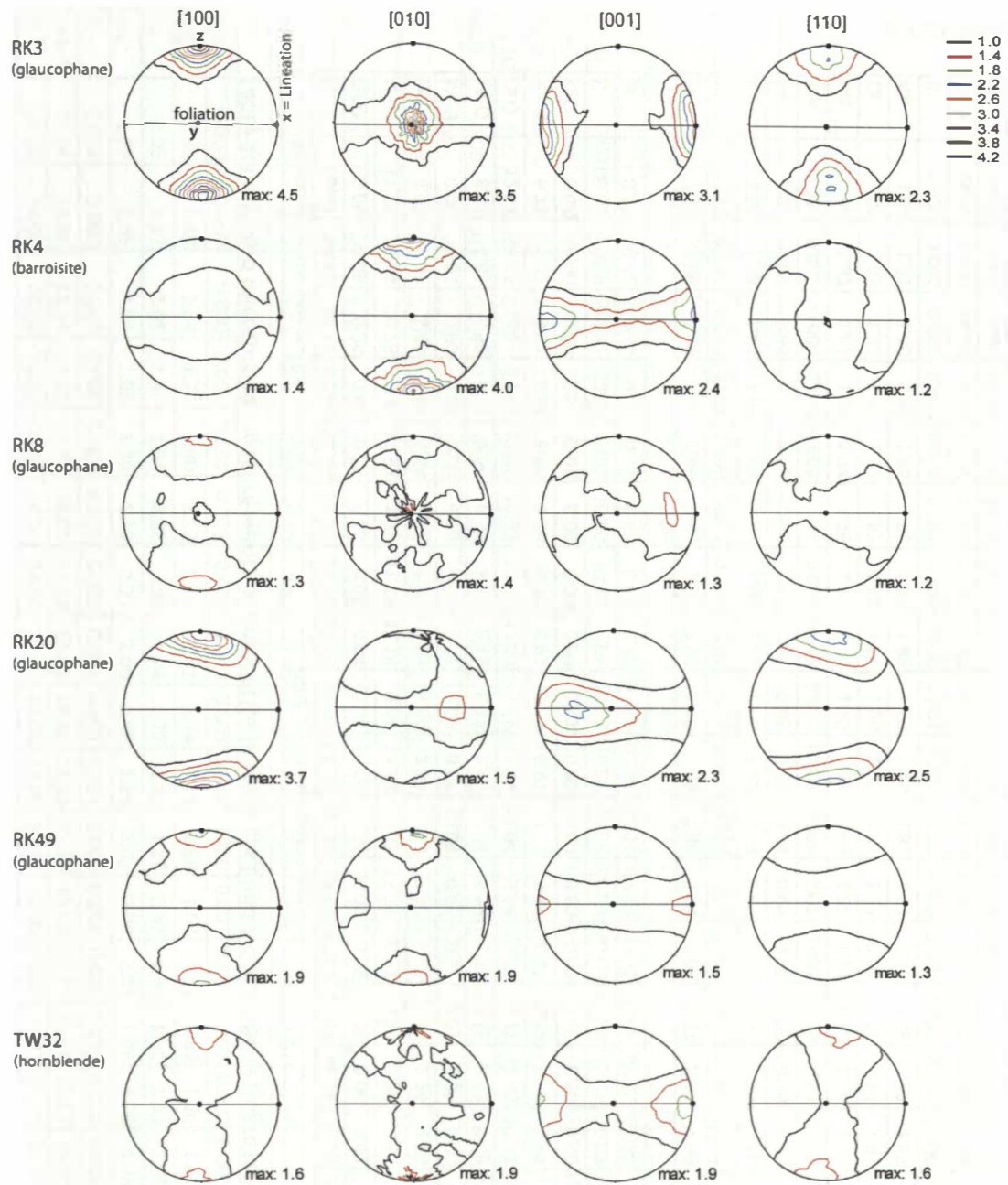


Fig. 1: Pole figures of relevant amphibole hkl of all investigated samples.

APPENDIX B

Table 1: Collected microprobe measurements of omphacite in fresh (RK1 and MS112) and retrogressed (RK3, RK20 and RK49) eclogites. Jd = jadeite

	RK1 point measurements										RK3 point measurements													
	RK1 profile					RK3 profile					RK1 profile					RK3 profile								
SiO2	56.63	56.40	56.22	56.67	56.45	56.12	56.51	56.66	57.46	58.16	58.10	58.58	57.17	57.32	58.28	58.29	58.41	58.36	57.63	58.53	57.02	58.00	58.41	57.09
TiO2	0.05	0.05	0.06	0.04	0.05	0.06	0.06	0.04	0.04	0.05	0.04	0.05	0.05	0.05	0.06	0.07	0.06	0.04	0.04	0.07	0.03	0.06	0.04	0.03
Al2O3	11.78	10.34	10.78	11.38	11.93	11.76	11.83	12.18	9.84	13.69	13.83	15.29	10.37	9.84	13.25	13.51	13.30	15.12	12.12	15.61	9.82	12.81	13.63	9.26
FeO	4.48	5.63	5.49	5.04	4.64	4.62	4.56	4.83	5.84	2.39	2.10	3.86	5.77	5.76	2.24	2.68	4.66	3.49	5.29	2.22	6.81	4.31	2.22	6.82
MnO	0.00	0.01	0.00	0.07	0.00	0.05	0.05	0.02	0.00	0.07	0.04	0.01	0.01	0.02	0.03	0.00	0.01	0.01	0.01	0.00	0.15	0.04	0.05	0.00
MgO	8.48	8.85	8.52	8.35	8.26	8.30	8.34	8.11	8.32	8.19	8.24	6.12	8.24	8.65	8.52	8.39	6.85	6.47	7.31	7.01	7.95	7.33	8.36	8.46
CaO	12.53	13.36	12.61	12.63	12.36	12.32	12.48	12.00	13.65	12.17	12.04	9.34	13.26	13.71	12.50	12.31	10.74	9.97	11.78	10.27	13.61	11.62	12.17	13.94
Na2O	6.73	6.22	6.51	6.58	6.81	6.76	6.76	6.92	6.18	6.97	7.11	8.43	6.47	6.17	6.82	6.97	7.77	8.17	7.27	8.06	6.21	7.16	6.98	6.01
K2O	0.00	0.00	0.00	0.00	0.01	0.01	0.00	0.00	0.01	0.00	0.00	0.00	0.00	0.00	0.00	0.00	0.01	0.00	0.01	0.00	0.00	0.00	0.00	0.00
Σ	100.69	100.9	100.2	100.8	101	100.0	100.6	101	101.3	101.7	101.5	101.7	101.3	101.5	101.7	102.2	101.8	101.6	101.5	101.8	101.6	101.3	101.9	101.6
Jd	0.47	0.42	0.45	0.47	0.47	0.46	0.47	0.48	0.409	0.548	0.551	0.619	0.431	0.408	0.536	0.532	0.54	0.61	0.50	0.618	0.409	0.525	0.55	0.39
Si	7.97	7.99	7.99	7.99	7.96	7.96	7.96	7.97	8.10	7.99	7.98	8.04	8.05	8.07	8.01	7.98	8.08	8.02	8.05	7.98	8.06	8.06	8.00	8.07
Ti	0.005	0.005	0.007	0.005	0.006	0.007	0.006	0.004	0.004	0.005	0.005	0.006	0.005	0.006	0.006	0.007	0.006	0.005	0.005	0.007	0.003	0.006	0.004	0.004
Al	1.95	1.73	1.81	1.89	1.98	1.97	1.97	2.02	2.06	2.22	2.24	2.47	1.72	1.63	2.15	2.18	2.17	2.45	2.00	2.51	1.64	2.10	2.20	1.54
Fe	0.53	0.67	0.65	0.60	0.55	0.55	0.54	0.57	0.69	0.28	0.24	0.44	0.68	0.68	0.26	0.31	0.54	0.40	0.62	0.25	0.81	0.50	0.26	0.81
Mn	0.000	0.002	0.000	0.008	0.000	0.006	0.006	0.003	0.000	0.008	0.004	0.002	0.001	0.003	0.003	0.000	0.001	0.002	0.001	0.000	0.018	0.005	0.006	0.000
Mg	1.78	1.87	1.81	1.76	1.74	1.76	1.75	1.70	1.75	1.68	1.69	1.25	1.73	1.82	1.74	1.71	1.41	1.33	1.52	1.43	1.68	1.52	1.71	1.78
Ca	1.90	2.03	1.92	1.91	1.87	1.87	1.88	1.81	2.06	1.79	1.77	1.37	2.00	2.07	1.84	1.81	1.59	1.47	1.76	1.50	2.06	1.73	1.79	2.11
Na	1.84	1.71	1.80	1.80	1.86	1.86	1.85	1.89	1.69	1.86	1.89	2.24	1.77	1.68	1.82	1.85	2.08	2.18	1.97	2.13	1.70	1.93	1.85	1.65
K	0.001	0.001	0.001	0.000	0.001	0.001	0.000	0.000	0.001	0.001	0.000	0.000	0.000	0.000	0.001	0.010	0.000	0.001	0.000	0.000	0.000	0.000	0.000	0.000
Total	15.97	16.00	16.00	15.96	15.97	15.98	15.97	15.96	15.93	15.82	15.84	15.84	15.96	15.95	15.82	15.85	15.88	15.84	15.93	15.82	15.97	15.85	15.82	15.97
O	24.00	24.00	24.00	24.00	24.00	24.00	24.00	24.00	24.00	24.00	24.00	24.00	24.00	24.00	24.00	24.00	24.00	24.00	24.00	24.00	24.00	24.00	24.00	24.00

Table 1 (continued)

	RK20 point meas.				RK20 inclusions in garnet				RK49 profile				RK49 inclusions in garnet				MS112 individual measurements						
SiO2	56.95	57.62	57.16	57.11	56.74	55.46	57.04	57.71	57.49	57.46	57.51	57.80	57.60	56.87	57.49	57.21	56.45	56.52	56.60	57.96	58.12	57.72	57.48
TiO2	0.04	0.05	0.05	0.05	0.06	0.04	0.05	0.05	0.06	0.05	0.04	0.05	0.05	0.03	0.05	0.05	0.06	0.04	0.05	0.07	0.05	0.05	0.06
Al2O3	10.84	13.10	12.39	13.68	13.21	8.86	13.00	13.06	14.25	13.48	13.84	14.44	14.38	13.04	13.07	11.82	10.16	10.94	10.84	12.13	13.08	13.33	12.62
FeO	4.57	2.41	3.06	2.45	2.60	6.36	2.24	4.00	1.83	2.03	3.04	2.31	2.17	2.36	2.30	4.06	6.48	6.64	4.82	1.97	2.29	1.96	2.25
MnO	0.00	0.00	0.00	0.03	0.01	0.02	0.00	0.08	0.04	0.07	0.00	0.01	0.03	0.00	0.00	0.00	0.09	0.10	0.05	0.01	0.02	0.00	0.00
MgO	8.85	8.74	8.89	8.41	8.68	9.96	9.29	7.83	8.49	8.68	7.63	7.70	7.85	9.12	8.93	9.04	8.59	7.71	9.32	9.25	8.59	8.45	8.75
CaO	13.63	12.61	13.06	12.59	12.98	15.18	13.35	11.77	11.99	12.55	11.22	11.27	11.41	13.08	13.07	13.28	13.77	12.59	13.82	13.76	12.62	12.34	12.93
Na2O	6.22	6.90	6.70	6.82	6.64	5.04	6.58	7.47	7.31	6.96	7.61	7.63	7.57	6.43	6.57	6.44	6.32	6.88	6.19	5.66	6.74	6.85	6.46
K2O	0.00	0.01	0.01	0.00	0.00	0.00	0.02	0.01	0.01	0.00	0.00	0.01	0.00	0.12	0.01	0.00	0.00	0.00	0.00	0.01	0.00	0.00	0.01
Σ	101.1	101.4	101.3	101.1	100.9	100.9	101.6	102.0	101.5	101.3	100.9	101.2	101.1	101.1	101.5	101.9	101.9	101.4	101.7	100.8	101.5	100.7	100.6
jd	0.45	0.50	0.47	0.49	0.46	0.31	0.45	0.52	0.51	0.50	0.55	0.56	0.55	0.46	0.49	0.45	0.39	0.45	0.40	0.50	0.53	0.54	0.52
Si	8.00	7.96	7.95	7.91	7.89	7.92	7.89	7.98	7.91	7.94	7.98	7.97	7.95	7.90	7.94	7.95	7.96	7.99	7.93	8.03	8.01	8.00	8.00
Ti	0.005	0.005	0.005	0.006	0.006	0.004	0.006	0.007	0.005	0.005	0.005	0.006	0.005	0.004	0.005	0.005	0.006	0.005	0.005	0.007	0.005	0.005	0.006
Al	1.80	2.13	2.03	2.23	2.17	1.49	2.12	2.13	2.31	2.20	2.26	2.35	2.34	2.14	2.13	1.94	1.69	1.82	1.79	1.98	2.12	2.18	2.07
Fe	0.54	0.28	0.36	0.28	0.30	0.76	0.26	0.46	0.21	0.24	0.35	0.27	0.25	0.27	0.27	0.47	0.77	0.79	0.57	0.23	0.26	0.23	0.26
Mn	0.000	0.000	0.000	0.003	0.001	0.002	0.001	0.010	0.005	0.008	0.000	0.002	0.004	0.000	0.000	0.000	0.011	0.012	0.006	0.001	0.002	0.001	0.000
Mg	1.85	1.80	1.84	1.74	1.80	2.12	1.91	1.61	1.74	1.58	1.58	1.62	1.62	1.89	1.84	1.87	1.81	1.63	1.95	1.91	1.77	1.75	1.82
Ca	2.05	1.87	1.95	1.87	1.94	2.32	1.98	1.74	1.77	1.86	1.67	1.67	1.69	1.95	1.93	1.98	2.08	1.91	2.08	2.04	1.86	1.83	1.93
Na	1.69	1.85	1.81	1.83	1.79	1.40	1.77	2.00	1.95	2.05	2.04	2.03	2.03	1.73	1.76	1.74	1.73	1.89	1.68	1.52	1.80	1.84	1.74
K	0.001	0.000	0.002	0.000	0.001	0.001	0.003	0.001	0.002	0.001	0.000	0.001	0.000	0.021	0.002	0.000	0.000	0.000	0.000	0.002	0.001	0.000	0.001
Total	15.94	15.89	15.94	15.88	15.91	16.02	15.93	15.95	15.91	15.89	15.90	15.88	15.89	15.91	15.87	15.95	16.05	16.04	16.01	15.73	15.83	15.83	15.83
O	24.00	24.00	24.00	24.00	24.00	24.00	24.00	24.00	24.00	24.00	24.00	24.00	24.00	24.00	24.00	24.00	24.00	24.00	24.00	24.00	24.00	24.00	24.00

Table 2: Collected microprobe measurements of amphibole in retrogressed (RK3, RK4, RK20 and RK49) eclogites and garnet inclusions in both fresh (MS112) and retrogressed (RK20) eclogites.

	RK 3 glaucophane individual measurements								RK4 barroisitic hornblende individual measurements								RK20 glaucophane profile				
SiO ₂	59.67	59.50	59.40	59.92	59.97	58.91	59.43	59.21	49.34	48.78	49.27	49.63	50.12	49.85	48.11	50.67	57.35	57.56	57.85	56.79	57.57
TiO ₂	0.06	0.07	0.02	0.01	0.02	0.04	0.03	0.02	0.21	0.21	0.21	0.19	0.17	0.18	0.18	0.17	0.08	0.05	0.06	0.07	0.07
Al ₂ O ₃	13.01	12.36	12.43	12.90	13.02	13.46	12.98	12.99	10.51	11.36	10.84	10.63	10.29	10.18	11.83	9.76	13.68	13.65	13.41	13.85	13.50
FeO	4.28	4.50	4.36	4.27	4.64	4.37	4.40	4.44	11.91	13.02	12.00	12.42	11.63	11.75	10.55	11.29	4.03	4.16	3.85	4.36	4.12
MnO	0.01	0.01	0.00	0.01	0.01	0.03	0.01	0.02	0.08	0.13	0.13	0.13	0.10	0.14	0.11	0.11	0.04	0.04	0.05	0.07	0.01
MgO	12.98	13.24	13.40	12.48	12.39	12.07	12.88	13.04	12.05	11.90	12.11	12.46	12.70	12.44	13.27	13.10	14.07	14.00	14.40	13.87	14.11
CaO	0.40	0.70	0.64	0.41	0.42	1.71	0.50	0.98	8.09	8.34	8.43	7.96	8.35	7.93	8.52	7.77	2.09	2.14	1.99	1.99	2.15
Na ₂ O	7.15	6.98	7.03	7.16	7.17	6.67	7.06	6.87	3.56	3.58	3.40	3.68	3.45	3.62	3.66	3.74	6.22	6.28	6.20	6.32	6.32
K ₂ O	0.00	0.04	0.04	0.02	0.02	0.02	0.01	0.02	0.20	0.24	0.25	0.22	0.18	0.20	0.31	0.17	0.07	0.05	0.06	0.07	0.06
Cr ₂ O ₃	0.009	0.038	0.028	0.014	0.003	0.032	0.016	0.013	0.010	0.010	0.047	0.037	0.048	0.033	0.017	0.015	0.000	0.000	0.000	0.000	0.000
Σ	97.56	97.43	97.35	97.20	97.66	97.31	97.32	97.60	95.97	97.57	96.68	97.36	97.03	96.33	96.55	96.80	97.63	97.94	97.87	97.38	97.91
Si	8.29	8.30	8.29	8.35	8.33	8.27	8.28	8.25	7.50	7.35	7.45	7.46	7.52	7.54	7.26	7.60	7.35	7.36	7.38	7.31	7.36
Ti	0.006	0.007	0.002	0.001	0.002	0.007	0.004	0.002	0.024	0.024	0.024	0.022	0.019	0.021	0.020	0.019	0.007	0.006	0.006	0.006	0.007
Al	2.13	2.03	2.04	2.12	2.13	2.11	2.13	2.13	1.88	2.02	1.93	1.88	1.82	1.81	2.10	1.73	2.07	2.06	2.02	2.10	2.03
Fe	0.50	0.53	0.51	0.50	0.54	0.51	0.51	0.52	1.51	1.64	1.52	1.56	1.46	1.49	1.33	1.42	0.43	0.45	0.41	0.47	0.44
Mn	0.001	0.000	0.000	0.001	0.001	0.001	0.001	0.003	0.011	0.017	0.016	0.017	0.012	0.018	0.014	0.015	0.004	0.005	0.005	0.007	0.001
Mg	2.69	2.75	2.79	2.59	2.57	2.70	2.68	2.71	2.73	2.67	2.73	2.79	2.84	2.80	2.98	2.93	2.69	2.67	2.74	2.66	2.69
Ca	0.06	0.10	0.10	0.06	0.06	0.12	0.07	0.15	1.32	1.35	1.37	1.28	1.34	1.29	1.38	1.25	0.29	0.29	0.27	0.27	0.29
Na	1.93	1.89	1.90	1.94	1.93	1.88	1.91	1.86	1.05	1.05	1.00	1.07	1.00	1.06	1.07	1.09	1.55	1.56	1.53	1.58	1.57
K	0.001	0.007	0.007	0.004	0.003	0.004	0.002	0.003	0.039	0.046	0.048	0.026	0.034	0.038	0.060	0.033	0.011	0.008	0.009	0.011	0.010
Cr	0.001	0.004	0.003	0.002	0.000	0.001	0.002	0.002	0.001	0.001	0.006	0.004	0.006	0.004	0.002	0.002	0.000	0.000	0.000	0.000	0.000
Total	15.61	15.62	15.64	15.57	15.57	15.61	15.60	15.62	16.08	16.16	16.09	16.13	16.07	16.08	16.24	16.08	14.39	14.39	14.37	14.43	14.41
O	24.00	24.00	24.00	24.00	24.00	24.00	24.00	24.00	24.00	24.00	24.00	24.00	24.00	24.00	24.00	24.00	22.00	22.00	22.00	22.00	22.00

Table 2 (continued)

	RK20 glaucophane individual measurements										RK49 glaucophane individual measurements									
SiO2	57.34	58.16	58.00	57.89	59.44	59.38	58.68	57.70	57.97	57.72	58.97	58.46	58.81	58.79	58.73	59.09	58.48	58.69	58.27	57.91
TiO2	0.07	0.04	0.05	0.05	0.02	0.03	0.04	0.05	0.06	0.07	0.03	0.04	0.05	0.05	0.05	0.03	0.06	0.06	0.05	0.05
Al2O3	13.13	13.11	13.04	12.76	12.66	12.76	12.79	12.67	13.09	12.96	13.00	12.92	12.90	13.18	13.07	12.89	12.98	13.00	12.86	12.71
FeO	4.22	4.01	3.98	3.94	4.12	3.82	3.85	3.84	4.32	4.15	4.13	4.37	3.86	4.29	4.42	3.96	4.23	4.18	4.10	4.33
MnO	0.01	0.04	0.03	0.01	0.00	0.01	0.00	0.03	0.00	0.02	0.04	0.03	0.04	0.04	0.04	0.02	0.03	0.00	0.05	0.02
MgO	13.70	13.36	13.59	14.17	13.36	13.32	13.75	14.56	13.37	13.32	13.32	13.29	13.38	13.47	13.33	13.26	13.51	12.79	13.12	13.54
CaO	2.25	1.53	1.93	2.03	0.67	0.64	1.23	2.24	1.97	2.11	1.09	1.83	1.00	1.72	1.83	1.00	1.56	1.45	1.50	2.06
Na2O	6.39	6.60	6.40	6.35	6.98	6.98	6.64	6.41	6.63	6.55	6.82	6.62	6.92	6.55	6.63	6.80	6.66	6.68	6.60	6.31
K2O	0.05	0.03	0.05	0.07	0.03	0.01	0.04	0.07	0.06	0.06	0.02	0.03	0.03	0.02	0.02	0.01	0.04	0.02	0.03	0.04
Cr2O3	0.019	0.000	0.000	0.000	0.016	0.026	0.029	0.034	0.033	0.057	0.097	0.040	0.109	0.062	0.019	0.002	0.062	0.008	0.311	0.311
Σ	97.18	96.88	97.08	97.27	97.28	96.97	97.05	97.61	97.51	97.02	97.52	97.63	97.10	98.16	98.14	97.07	97.61	96.88	96.88	97.27
Si	8.06	8.17	8.14	8.11	8.29	8.29	8.21	8.07	8.09	8.12	8.22	8.17	8.21	8.16	8.16	8.26	8.16	8.23	8.19	8.13
Ti	0.007	0.004	0.006	0.005	0.002	0.003	0.004	0.006	0.007	0.007	0.004	0.004	0.006	0.005	0.005	0.004	0.006	0.006	0.005	0.005
Al	2.18	2.17	2.16	2.11	2.08	2.10	2.11	2.09	2.16	2.15	2.13	2.13	2.12	2.16	2.14	2.12	2.14	2.15	2.13	2.10
Fe	0.50	0.47	0.47	0.46	0.48	0.45	0.45	0.45	0.51	0.49	0.48	0.51	0.45	0.50	0.51	0.46	0.49	0.49	0.48	0.51
Mn	0.001	0.004	0.003	0.001	0.000	0.001	0.001	0.003	0.000	0.003	0.005	0.004	0.004	0.004	0.005	0.003	0.004	0.000	0.006	0.002
Mg	2.87	2.80	2.84	2.96	2.78	2.77	2.87	3.04	2.85	2.80	2.77	2.77	2.79	2.79	2.76	2.76	2.81	2.68	2.75	2.84
Ca	0.34	0.23	0.29	0.31	0.10	0.10	0.18	0.34	0.29	0.32	0.16	0.27	0.18	0.26	0.27	0.15	0.23	0.22	0.23	0.31
Na	1.74	1.80	1.74	1.73	1.89	1.89	1.80	1.74	1.80	1.79	1.84	1.80	1.87	1.76	1.79	1.84	1.80	1.82	1.80	1.72
K	0.010	0.006	0.010	0.012	0.005	0.002	0.006	0.013	0.011	0.120	0.003	0.005	0.005	0.003	0.003	0.002	0.007	0.003	0.005	0.006
Cr	0.002	0.000	0.000	0.000	0.001	0.003	0.003	0.004	0.004	0.006	0.011	0.004	0.012	0.007	0.002	0.000	0.006	0.000	0.035	0.035
Total	15.72	15.65	15.65	15.70	15.62	15.60	15.64	15.75	15.72	15.69	15.63	15.66	15.66	15.64	15.66	15.60	15.67	15.60	15.62	15.66
O	24.00	24.00	24.00	24.00	24.00	24.00	24.00	24.00	24.00	24.00	24.00	24.00	24.00	24.00	24.00	24.00	24.00	24.00	24.00	24.00

Table 3: Collected microprobe measurements of garnete in retrogressed (RK20 and RK49) and fresh (RK1 and MS112) eclogites.

Alm = almandine, Prp = pyrope, Sps = spessartine, GAU = grossular + andradite + uvarovite.

	RK1 garnet profile 1										RK1 garnet profile 2										
SiO2	37.60	37.06	36.79	37.01	37.05	37.57	37.35	36.70	36.67	36.39	36.48	36.46	36.49	36.56	36.75	36.70	37.08	37.18	37.43	37.53	37.86
TiO2	0.06	0.06	0.10	0.10	0.08	0.05	0.05	0.05	0.06	0.07	0.11	0.09	0.11	0.08	0.08	0.08	0.06	0.04	0.04	0.04	0.04
Al2O3	21.90	21.30	21.18	21.13	21.23	21.90	21.75	21.35	21.04	20.96	20.99	20.91	20.84	21.02	21.00	21.01	21.35	21.73	21.98	22.09	22.16
FeO	24.91	30.35	31.04	30.10	30.51	26.67	23.21	28.47	30.18	30.70	31.10	30.88	30.62	30.03	29.44	30.45	27.33	26.65	25.45	24.33	23.33
MnO	0.38	0.75	0.73	0.86	0.83	0.55	0.33	0.72	0.66	0.77	0.73	0.76	0.72	0.75	0.72	0.70	0.80	0.52	0.46	0.39	0.41
MgO	5.92	3.50	2.75	3.07	2.98	4.53	6.39	3.84	3.27	2.82	2.69	2.82	2.69	3.13	3.48	3.55	4.03	4.78	5.33	6.43	6.68
CaO	8.17	7.20	7.63	7.90	7.65	8.43	8.40	7.87	7.29	7.41	7.61	7.55	7.80	7.84	7.54	7.21	8.39	8.26	8.66	7.89	8.00
Na2O	0.010	0.022	0.045	0.012	0.011	0.022	0.031	0.023	0.023	0.001	0.011	0.013	0.031	0.013	0.019	0.027	0.014	0.013	0.000	0.025	0.019
K2O	0.010	0.006	0.001	0.000	0.003	0.004	0.003	0.006	0.000	0.000	0.001	0.004	0.000	0.002	0.000	0.001	0.000	0.000	0.009	0.005	0.005
Cr2O3	0.050	0.009	0.020	0.006	0.000	0.000	0.024	0.042	0.004	0.038	0.011	0.006	0.001	0.000	0.039	0.009	0.007	0.026	0.024	0.012	0.000
Σ	99.0	100.3	100.3	100.2	100.3	99.7	97.5	99.1	99.2	99.2	99.7	99.5	99.3	99.4	99.1	99.7	99.1	99.2	99.4	98.7	98.5
Alm	53.2	64.0	65.7	63.4	64.6	57.4	50.4	60.6	64.5	65.5	65.7	65.2	65.1	63.3	62.8	63.7	58.4	56.7	53.9	52.0	50.8
Prp	23.1	13.8	10.9	12.2	11.8	17.7	25.1	15.3	13.1	11.3	10.8	11.3	10.8	12.5	13.9	14.1	16.0	18.8	20.8	25.1	26.0
Sps	0.8	1.7	1.6	1.9	1.9	1.2	0.7	1.6	1.5	1.7	1.7	1.7	1.6	1.7	1.6	1.6	1.8	1.2	1.0	0.9	0.9
GAU	22.9	20.5	21.8	22.5	21.8	23.7	23.8	22.5	20.9	21.4	21.9	21.7	22.5	22.5	21.6	20.6	23.9	23.4	24.3	22.1	22.4
Si	5.91	5.90	5.88	5.90	5.90	5.91	5.92	5.88	5.90	5.88	5.87	5.88	5.89	5.88	5.91	5.88	5.91	5.89	5.88	5.89	5.93
Ti	0.007	0.008	0.012	0.012	0.009	0.006	0.006	0.006	0.008	0.009	0.013	0.011	0.014	0.010	0.010	0.009	0.008	0.005	0.005	0.004	0.004
Al	4.05	3.99	3.99	3.97	3.99	4.06	4.06	4.03	3.99	3.99	3.98	3.98	3.97	3.98	3.98	3.97	4.01	4.06	4.07	4.09	4.09
Fe	3.27	4.04	4.15	4.01	4.07	3.51	3.07	3.81	4.06	4.15	4.19	4.17	4.14	4.04	3.96	4.08	3.64	3.53	3.35	3.19	3.05
Mn	0.050	0.10	0.098	0.116	0.113	0.073	0.045	0.097	0.090	0.105	0.100	0.010	0.099	0.102	0.098	0.095	0.108	0.069	0.061	0.051	0.054
Mg	1.39	0.83	0.66	0.73	0.71	1.06	1.51	0.92	0.79	0.68	0.65	0.68	0.65	0.75	0.83	0.85	0.96	1.13	1.25	1.51	1.56
Ca	1.38	1.23	1.31	1.35	1.31	1.42	1.43	1.35	1.26	1.28	1.31	1.31	1.35	1.35	1.30	1.24	1.43	1.40	1.46	1.33	1.34
Na	0.003	0.007	0.014	0.004	0.004	0.007	0.010	0.007	0.007	0.000	0.003	0.004	0.010	0.004	0.006	0.009	0.004	0.004	0.000	0.008	0.006
K	0.001	0.001	0.000	0.000	0.001	0.001	0.001	0.001	0.000	0.000	0.000	0.001	0.000	0.000	0.000	0.000	0.000	0.000	0.002	0.002	0.001
Cr	0.007	0.001	0.003	0.001	0.000	0.000	0.003	0.005	0.001	0.005	0.001	0.001	0.000	0.000	0.005	0.001	0.001	0.003	0.003	0.002	0.000
Total	16.06	16.10	16.12	16.10	16.10	16.06	16.05	16.10	16.10	16.11	16.12	16.12	16.12	16.12	6.10	16.13	16.08	16.08	16.07	16.03	
O	24.00	24.00	24.00	24.00	24.00	24.00	24.00	24.00	24.00	24.00	24.00	24.00	24.00	24.00	24.00	24.00	24.00	24.00	24.00	24.00	24.00

Table 3 (continued)

	RK20 profile																							
SiO2	38.38	38.25	37.91	38.21	38.11	35.34	37.77	37.40	37.57	37.71	37.72	37.42	37.59	37.65	37.83	37.71	37.79	38.06	37.77	37.74	37.85	38.23	38.45	38.82
TiO2	0.05	0.06	0.05	0.07	0.08	0.05	0.08	0.08	0.07	0.09	0.09	0.10	0.07	0.08	0.07	0.09	0.06	0.07	0.05	0.06	0.05	0.03	0.04	0.03
Al2O3	22.16	22.42	22.09	22.23	22.04	20.56	22.00	21.77	21.71	21.68	21.52	21.77	21.78	22.10	21.86	21.76	22.00	22.14	22.06	21.94	22.03	22.30	22.46	22.75
FeO	25.64	26.02	27.88	28.22	28.10	28.59	28.46	28.68	29.60	28.57	27.63	28.67	28.48	28.13	27.47	27.25	28.43	28.02	28.77	28.60	28.47	26.96	24.93	24.27
MnO	0.08	0.28	0.19	0.17	0.17	0.22	0.24	0.41	0.28	0.27	0.20	0.28	0.23	0.28	0.38	0.26	0.24	0.25	0.20	0.17	0.23	0.16	0.09	0.10
MgO	6.89	6.66	5.05	5.14	4.64	5.19	4.26	3.87	3.54	3.28	4.04	3.31	3.55	4.46	4.58	4.54	4.58	5.21	4.87	5.20	5.52	6.68	7.49	8.48
CaO	6.67	6.93	7.07	7.29	7.66	7.47	7.71	8.06	8.22	9.26	8.93	9.02	8.56	7.97	8.34	8.44	7.70	7.41	7.36	6.86	6.56	6.15	6.40	6.07
Na2O	0.02	0.03	0.02	0.03	0.05	0.01	0.02	0.01	0.04	0.03	0.03	0.04	0.01	0.04	0.02	0.03	0.02	0.03	0.01	0.02	0.03	0.04	0.03	0.01
K2O	0.000	0.003	0.000	0.000	0.000	0.003	0.001	0.007	0.004	0.000	0.005	0.003	0.004	0.003	0.000	0.009	0.000	0.004	0.005	0.000	0.002	0.000	0.005	0.006
Cr2O3	0.02	0.01	0.03	0.00	0.02	0.01	0.03	0.02	0.01	0.05	0.02	0.03	0.06	0.04	0.07	0.04	0.03	0.01	0.03	0.00	0.00	0.03	0.02	0.00
Σ	99.9	100.7	100.3	101.4	100.9	97.4	100.6	100.3	101.0	100.9	100.2	100.6	100.3	100.7	100.6	100.1	100.9	101.2	101.1	100.6	100.7	100.6	99.9	100.5
Alm	54.9	54.8	60.3	59.7	60.4	56.7	61.3	61.2	62.5	60.6	58.7	61.1	61.5	59.8	58.1	58.1	60.2	58.9	60.2	60.3	59.9	57.0	53.5	51.2
Prp	26.5	25.5	19.6	19.8	17.9	21.1	16.6	15.2	13.8	12.8	15.8	13.0	13.9	17.3	17.8	17.7	17.8	20.1	18.8	20.2	21.4	25.7	28.7	32.1
Sps	0.2	0.6	0.4	0.4	0.4	0.5	0.5	0.9	0.6	0.6	0.4	0.6	0.5	0.6	0.8	0.6	0.5	0.5	0.5	0.5	0.4	0.5	0.4	0.2
GAU	18.4	19.1	19.7	20.1	21.3	21.8	21.6	22.7	23.1	26.0	25.1	25.4	24.1	22.2	23.3	23.6	21.5	20.5	20.5	19.1	18.3	17.0	17.6	16.5
Si	5.94	5.90	5.92	5.91	5.93	5.77	5.92	5.90	5.90	5.92	5.93	5.89	5.92	5.89	5.91	5.92	5.90	5.90	5.88	5.90	5.90	5.90	5.90	5.92
Ti	0.005	0.007	0.006	0.008	0.009	0.006	0.009	0.009	0.008	0.010	0.011	0.012	0.008	0.009	0.008	0.011	0.008	0.008	0.006	0.007	0.006	0.003	0.005	0.003
Al	4.05	4.07	4.07	4.06	4.04	3.96	4.06	4.05	4.02	4.01	3.99	4.04	4.04	4.07	4.03	4.02	4.05	4.05	4.05	4.04	4.05	4.06	4.08	4.09
Fe	3.32	3.36	3.64	3.65	3.66	3.90	3.73	3.78	3.89	3.75	3.64	3.78	3.75	3.68	3.59	3.58	3.71	3.63	3.75	3.74	3.71	3.49	3.21	3.09
Mn	0.011	0.037	0.025	0.022	0.023	0.031	0.031	0.055	0.038	0.037	0.027	0.037	0.031	0.037	0.051	0.035	0.032	0.033	0.027	0.022	0.030	0.021	0.011	0.012
Mg	1.59	1.53	1.18	1.19	1.08	1.26	1.00	0.91	0.83	0.77	0.95	0.04	0.83	1.04	1.07	1.06	1.07	1.20	1.13	1.21	1.28	1.54	1.72	1.93
Ca	1.11	1.15	1.18	1.21	1.28	1.31	1.29	1.36	1.38	1.56	1.51	1.52	1.45	1.34	1.40	1.42	1.29	1.23	1.23	1.15	1.10	1.02	1.06	0.99
Na	0.007	0.009	0.007	0.008	0.014	0.004	0.007	0.004	0.012	0.008	0.009	0.013	0.003	0.012	0.005	0.010	0.007	0.008	0.003	0.006	0.010	0.012	0.009	0.003
K	0.000	0.001	0.000	0.000	0.000	0.001	0.000	0.001	0.001	0.000	0.001	0.001	0.001	0.001	0.000	0.002	0.000	0.001	0.001	0.000	0.000	0.000	0.001	0.001
Cr	0.002	0.002	0.004	0.000	0.003	0.001	0.004	0.002	0.001	0.006	0.003	0.004	0.008	0.004	0.009	0.005	0.003	0.001	0.004	0.000	0.000	0.004	0.002	0.001
Total	16.03	16.06	16.04	16.05	16.04	16.25	16.05	16.07	16.09	16.07	16.06	16.08	16.05	16.07	16.06	16.06	16.07	16.08	16.08	16.08	16.08	16.06	16.03	16.04
O	24.00	24.00	24.00	24.00	24.00	24.00	24.00	24.00	24.00	24.00	24.00	24.00	24.00	24.00	24.00	24.00	24.00	24.00	24.00	24.00	24.00	24.00	24.00	24.00

Table 3 (continued)

	RK49 profile 1														RK49 profile 2													
SiO2	38.22	38.29	38.42	38.13	37.97	37.40	38.16	37.44	37.43	37.30	37.42	37.16	37.45	37.45	37.60	38.14	38.22	38.74	38.61	37.82	37.85	37.63	37.64	37.27	37.20			
TiO2	0.02	0.04	0.04	0.02	0.02	0.04	0.05	0.04	0.04	0.09	0.09	0.05	0.05	0.05	0.04	0.03	0.04	0.01	0.04	0.03	0.03	0.05	0.04	0.04	0.08			
Al2O3	22.46	22.45	22.49	22.22	22.29	21.75	22.26	21.77	21.83	21.77	21.52	21.76	21.67	21.85	22.04	22.32	22.33	22.70	22.63	22.20	22.11	21.96	21.90	21.89	21.85			
FeO	22.64	23.16	22.83	24.48	24.80	27.67	24.45	28.84	28.31	28.90	29.33	29.88	30.07	29.70	28.56	26.07	23.31	22.41	24.76	26.83	27.90	28.85	29.24	29.30	28.93			
MnO	0.89	0.14	0.56	0.25	0.27	0.35	0.42	0.38	0.53	0.53	0.37	0.37	0.27	0.24	0.24	0.29	0.19	11.49	0.24	0.24	0.23	0.32	0.21	0.40	0.45			
MgO	8.82	8.45	8.46	7.34	7.29	5.40	7.33	4.49	4.35	3.96	3.98	4.22	4.20	4.92	5.81	6.78	8.31	8.72	7.92	6.41	5.76	5.36	5.00	4.74	4.59			
CaO	5.73	6.66	6.78	6.92	6.73	6.73	6.83	7.22	7.81	8.02	7.74	6.82	6.63	6.22	5.50	6.35	6.56	6.03	6.26	6.21	6.26	6.11	6.06	6.69	7.10			
Na2O	0.021	0.031	0.032	0.028	0.047	0.018	0.029	0.014	0.042	0.057	0.012	0.024	0.024	0.042	0.016	0.049	0.045	0.037	0.022	0.013	0.015	0.025	0.002	0.018	0.028			
K2O	0.041	0.009	0.003	0.000	0.000	0.001	0.000	0.000	0.000	0.000	0.000	0.008	0.003	0.000	0.000	0.006	0.014	0.012	0.000	0.000	0.000	0.000	0.000	0.000	0.008			
Cr2O3	0.010	0.000	0.020	0.000	0.000	0.008	0.007	0.016	0.018	0.006	0.000	0.000	0.000	0.003	0.000	0.010	0.013	0.007	0.018	0.003	0.010	0.007	0.006	0.018	0.014			
Σ	98.8	99.2	99.6	99.4	99.4	99.4	99.5	100.2	100.4	100.6	100.5	100.3	100.4	100.5	99.8	100.0	99.0	110.2	100.5	99.8	100.2	100.3	100.1	100.4	100.3			
Alim	48.4	49.0	47.9	52.0	52.6	59.1	51.9	61.3	59.9	60.8	61.8	63.3	64.2	62.8	61.4	55.7	49.5	47.9	52.2	57.3	59.7	61.3	63.0	61.8	61.0			
Ppp	33.9	32.4	32.3	28.3	28.1	21.2	28.2	17.6	17.0	15.5	15.6	16.6	16.5	19.2	22.7	26.1	31.9	33.2	30.1	24.8	22.3	20.9	19.5	18.5	18.0			
Sps	1.9	0.3	1.2	0.6	0.6	0.8	0.9	0.8	1.2	1.2	0.8	0.8	0.6	0.5	0.5	0.6	0.4	2.5	0.5	0.5	0.5	0.5	0.7	0.5	0.9	1.0		
GAU	15.8	18.3	18.6	19.2	18.7	19.0	18.9	20.3	21.9	22.6	21.8	19.3	18.7	17.5	15.4	17.6	18.1	16.5	17.1	17.3	17.5	17.1	17.0	18.8	20.0			
Si	5.91	5.91	5.91	5.92	5.90	5.90	5.91	5.90	5.88	5.87	5.90	5.88	5.91	5.89	5.90	5.91	5.91	5.93	5.91	5.90	5.91	5.90	5.92	5.87	5.87			
Ti	0.002	0.004	0.004	0.003	0.002	0.004	0.006	0.005	0.005	0.010	0.011	0.006	0.006	0.006	0.004	0.004	0.004	0.001	0.005	0.004	0.004	0.006	0.004	0.005	0.010			
Al	4.09	4.08	4.07	4.07	4.08	4.05	4.07	4.04	4.05	4.00	4.05	4.03	4.03	4.05	4.08	4.08	4.07	4.09	4.08	4.08	4.07	4.06	4.06	4.06	4.06			
Fe	2.93	2.99	2.93	3.18	3.22	3.65	3.17	3.80	3.72	3.81	3.87	3.95	3.97	3.90	3.75	3.38	3.02	2.87	3.17	3.50	3.64	3.78	3.85	3.86	3.82			
Mn	0.116	0.018	0.073	0.033	0.035	0.047	0.056	0.050	0.070	0.070	0.050	0.050	0.037	0.032	0.033	0.038	0.025	0.149	0.031	0.032	0.030	0.042	0.028	0.054	0.060			
Mg	2.03	1.94	1.94	1.70	1.69	1.27	1.70	1.05	1.02	0.93	0.94	0.99	0.99	1.15	1.36	1.57	1.92	1.99	1.81	1.49	1.34	1.25	1.17	1.11	1.08			
Ca	0.95	1.10	1.12	1.15	1.12	1.14	1.13	1.22	1.32	1.35	1.31	1.16	1.12	1.05	0.93	1.06	1.09	0.99	1.03	1.04	1.05	1.03	1.02	1.13	1.20			
Na	0.006	0.009	0.009	0.009	0.014	0.006	0.009	0.004	0.013	0.017	0.004	0.007	0.008	0.013	0.005	0.174	0.014	0.011	0.006	0.004	0.005	0.008	0.001	0.006	0.009			
K	0.008	0.002	0.001	0.001	0.000	0.000	0.000	0.000	0.000	0.000	0.000	0.002	0.001	0.000	0.000	0.001	0.003	0.002	0.000	0.000	0.000	0.000	0.000	0.000	0.002			
Cr	0.001	0.000	0.002	0.000	0.002	0.001	0.001	0.001	0.002	0.001	0.000	0.000	0.000	0.000	0.000	0.001	0.002	0.001	0.002	0.000	0.001	0.001	0.001	0.002	0.002			
Total	16.05	16.05	16.06	16.05	16.06	16.07	16.50	16.08	16.09	16.10	16.09	16.10	16.07	16.09	16.06	16.05	16.05	16.03	16.05	16.06	16.05	16.87	16.05	16.10	16.10			
O	24.00	24.00	24.00	24.00	24.00	24.00	24.00	24.00	24.00	24.00	24.00	24.00	24.00	24.00	24.00	24.00	24.00	24.00	24.00	24.00	24.00	24.00	24.00	24.00	24.00			

Table 3 (continued)

	RK49 profile 2 continued										MS112 profile															
SiO2	37.29	37.28	37.29	37.33	37.18	36.97	36.97	37.30	37.18	37.66	37.56	37.52	37.20	37.13	36.80	36.75	36.42	37.29	36.24	36.31	37.11	36.76	37.17	37.41	37.58	
TiO2	0.06	0.06	0.07	0.08	0.06	0.08	0.07	0.07	0.05	0.05	0.04	0.06	0.09	0.13	0.05	0.15	0.10	0.07	0.15	0.23	0.14	0.25	0.09	0.04	0.02	
Al2O3	21.82	21.62	21.66	21.74	21.72	21.86	21.71	21.95	21.92	22.03	21.97	22.13	21.65	21.54	21.82	21.53	21.52	22.03	21.24	21.25	22.16	21.78	22.13	22.10	22.44	
FeO	30.21	29.25	30.29	29.49	30.05	29.95	30.19	28.69	29.02	26.49	25.88	28.57	29.13	28.61	26.42	25.11	25.58	26.40	22.31	21.00	26.04	29.64	29.36	29.19	26.81	
MnO	0.43	0.41	0.46	0.49	0.46	0.47	0.29	0.32	0.28	0.25	0.12	0.22	0.56	0.84	2.04	1.81	4.59	1.32	7.50	8.19	0.67	0.50	0.36	0.13	0.16	
MgO	3.62	3.92	3.67	3.95	3.96	4.00	4.03	4.79	4.99	6.70	6.86	5.21	3.52	3.15	2.92	2.85	1.00	4.37	0.88	0.65	5.46	3.40	4.22	4.97	6.33	
CaO	7.07	7.77	7.69	7.60	7.07	7.59	6.99	7.09	6.44	6.29	6.69	6.65	8.29	8.76	9.74	11.56	11.29	8.70	11.91	12.23	8.05	8.28	7.27	6.41	6.13	
Na2O	0.000	0.015	0.017	0.026	0.026	0.052	0.040	0.023	0.022	0.025	0.038	0.017	0.024	0.023	0.001	0.039	0.032	0.047	0.036	0.034	0.009	0.032	0.023	0.042	0.018	
K2O	0.000	0.000	0.004	0.000	0.000	0.007	0.000	0.000	0.001	0.009	0.003	0.004	0.000	0.003	0.002	0.000	0.002	0.001	0.000	0.001	0.002	0.000	0.000	0.001	0.009	
Cr2O3	0.000	0.000	0.004	0.014	0.000	0.000	0.005	0.004	0.002	0.003	0.000	0.016	0.021	0.027	0.048	0.049	0.000	0.021	0.014	0.010	0.003	0.017	0.002	0.000	0.026	
Σ	100.5	100.3	101.2	100.7	100.5	101.0	100.3	100.2	99.9	99.5	99.2	100.4	100.5	100.2	99.8	99.8	100.5	100.3	100.3	99.9	99.6	100.7	100.6	100.3	99.5	
Alm	64.9	61.8	63.0	62.1	63.5	61.9	63.7	60.6	61.7	55.9	54.3	60.7	61.5	60.9	56.2	51.9	53.4	55.6	45.3	43.6	54.6	62.1	62.3	62.4	57.9	
Prp	14.2	15.4	14.4	15.5	15.5	15.7	15.9	18.7	19.6	26.0	26.7	20.3	13.8	12.4	11.5	11.2	4.0	17.1	3.5	2.6	21.3	13.4	16.5	19.4	24.6	
Sps	1.0	0.9	1.0	1.1	1.0	1.0	0.6	0.7	0.6	0.5	0.3	0.5	1.3	1.9	4.6	4.1	10.4	2.9	17.0	18.6	1.5	1.1	0.8	0.3	0.4	
GAU	20.0	21.9	21.6	21.4	19.9	21.4	19.8	19.9	18.1	17.6	18.7	18.6	23.4	24.8	27.7	32.8	32.3	24.4	34.2	35.1	22.6	23.4	20.4	18.0	17.1	
Si	5.89	5.89	5.87	5.88	5.88	5.83	5.86	5.87	5.87	5.89	5.88	5.88	5.86	5.88	5.89	5.85	5.84	5.83	5.86	5.82	5.84	5.83	5.82	5.82	5.85	5.84
Ti	0.007	0.008	0.009	0.010	0.007	0.010	0.009	0.006	0.006	0.006	0.004	0.007	0.009	0.011	0.015	0.006	0.018	0.012	0.009	0.018	0.028	0.017	0.029	0.010	0.009	
Al	4.07	4.03	4.02	4.04	4.05	4.06	4.05	4.07	4.08	4.06	4.06	4.09	4.09	4.03	4.03	4.09	4.03	4.06	4.08	4.02	4.03	4.10	4.06	4.10	4.13	
Fe	3.99	3.87	3.99	3.88	3.97	3.94	4.00	3.78	3.83	3.47	3.39	3.74	3.77	3.85	3.80	3.51	3.34	3.42	3.47	3.00	2.83	3.42	3.92	3.86	3.75	
Mn	0.057	0.054	0.062	0.066	0.062	0.062	0.039	0.043	0.037	0.033	0.016	0.029	0.046	0.075	0.113	0.270	0.240	0.620	0.176	1.020	1.120	0.089	0.067	0.048	0.040	
Mg	0.85	0.92	0.86	0.93	0.09	0.94	0.95	1.12	1.17	1.56	1.60	1.22	1.05	0.83	0.75	0.69	0.68	0.24	1.03	0.21	0.16	1.28	0.80	0.99	1.14	
Ca	1.20	1.32	1.30	1.28	1.20	1.28	1.19	1.20	1.09	1.06	1.12	1.12	1.25	1.40	1.49	1.66	1.97	1.94	1.47	2.05	2.10	1.36	1.41	1.23	1.16	
Na	0.000	0.005	0.005	0.008	0.008	0.016	0.012	0.007	0.007	0.008	0.012	0.005	0.015	0.007	0.007	0.000	0.012	0.010	0.015	0.011	0.011	0.003	0.010	0.007	0.009	
K	0.000	0.000	0.001	0.000	0.000	0.002	0.000	0.000	0.000	0.002	0.001	0.001	0.000	0.000	0.001	0.000	0.000	0.001	0.000	0.000	0.000	0.001	0.000	0.000	0.000	
Cr	0.000	0.000	0.001	0.002	0.000	0.000	0.001	0.001	0.000	0.000	0.000	0.002	0.001	0.003	0.003	0.006	0.006	0.000	0.003	0.002	0.001	0.000	0.002	0.000	0.002	
Total	16.07	16.09	16.11	16.10	16.10	16.14	16.11	16.09	16.09	16.08	16.09	16.08	16.09	16.10	16.09	16.10	16.13	16.14	16.10	16.15	16.12	16.10	16.12	16.10	16.09	
O	24.00	24.00	24.00	24.00	24.00	24.00	24.00	24.00	24.00	24.00	24.00	24.00	24.00	24.00	24.00	24.00	24.00	24.00	24.00	24.00	24.00	24.00	24.00	24.00	24.00	

Table 4: Collected microprobe measurements of white mica in retrogressed (RK49) and fresh (RK1 and MS112) eclogites and metasediments (RK5 and RK28).

	RK1 phengite point measurements					RK5 phengite profile 1										RK5 phengite profile 1					RK28 phengite profile				
SiO2	50.71	50.75	50.17	50.51	51.58	49.20	47.86	48.78	47.73	48.90	49.63	46.71	49.13	49.30	48.60	48.94	48.94	49.06	49.44	47.87	47.99	47.92	47.55		
TiO2	0.23	0.21	0.22	0.25	0.26	0.32	0.30	0.30	0.28	0.26	0.25	0.26	0.29	0.26	0.28	0.15	0.22	0.33	0.27	0.31	0.37	0.37	0.27		
Al2O3	28.88	29.44	30.02	28.91	29.49	31.45	30.83	31.14	31.86	32.58	32.03	33.16	31.38	32.24	31.09	31.77	31.15	31.77	31.61	33.18	33.14	33.10	33.73		
FeO	2.02	1.85	1.96	2.16	2.33	2.08	1.92	2.14	1.96	2.02	2.12	2.02	2.03	1.92	2.00	2.40	2.24	1.94	2.06	2.34	2.27	2.24	2.24		
MnO	0.000	0.000	0.001	0.000	0.000	0.000	0.000	0.013	0.000	0.026	0.017	0.000	0.019	0.000	0.000	0.000	0.015	0.001	0.000	0.000	0.003	0.015	0.018		
MgO	3.82	3.76	3.45	4.16	3.74	2.62	2.67	2.59	2.51	2.57	2.65	1.93	2.60	2.63	2.61	2.53	2.42	2.69	2.72	1.73	1.85	1.90	0.99		
CaO	0.00	0.00	0.00	0.03	0.04	0.01	0.01	0.05	0.02	0.01	0.00	0.02	0.01	0.00	0.04	0.00	0.04	0.00	0.00	0.01	0.00	0.00	0.00		
Na2O	0.66	0.73	0.73	0.66	0.76	0.41	0.38	0.30	0.54	0.54	0.49	0.54	0.34	0.49	0.27	0.27	0.26	0.40	0.39	0.59	0.81	0.77	0.85		
K2O	10.51	10.43	10.45	10.23	10.23	10.83	10.46	11.08	10.68	10.73	10.79	10.31	10.98	10.80	11.03	11.00	10.89	10.92	10.79	10.42	10.14	10.25	10.20		
Σ	96.83	97.18	97.00	96.91	98.43	96.92	94.43	96.39	95.57	97.63	97.97	94.94	96.78	97.64	95.92	97.06	96.18	97.11	97.28	96.45	96.57	96.57	95.84		
Si	3.33	3.32	3.29	3.31	3.33	3.23	3.22	3.23	3.18	3.19	3.22	3.13	3.23	3.21	3.23	3.22	3.24	3.22	3.23	3.16	3.16	3.16	3.15		
Si	6.66	6.63	6.63	6.57	6.63	6.46	6.44	6.46	6.37	6.38	6.45	6.26	6.47	6.42	6.46	6.43	6.48	6.43	6.47	6.32	6.32	6.32	6.27		
Ti	0.024	0.022	0.023	0.023	0.027	0.031	0.030	0.030	0.028	0.026	0.024	0.026	0.029	0.025	0.028	0.015	0.022	0.032	0.027	0.031	0.036	0.037	0.026		
Al	4.47	4.54	4.54	4.64	4.47	4.87	4.89	4.86	5.01	5.01	4.90	5.24	4.87	4.95	4.87	4.92	4.86	4.91	4.87	5.16	5.14	5.14	5.24		
Fe	0.24	0.22	0.22	0.23	0.26	0.23	0.22	0.24	0.22	0.22	0.23	0.23	0.22	0.21	0.22	0.26	0.25	0.21	0.23	0.26	0.25	0.25	0.25		
Mn	0.000	0.000	0.000	0.000	0.000	0.000	0.000	0.002	0.000	0.003	0.002	0.000	0.002	0.000	0.000	0.000	0.002	0.000	0.000	0.000	0.000	0.002	0.002		
Mg	0.82	0.80	0.80	0.74	0.89	0.51	0.54	0.51	0.50	0.50	0.51	0.39	0.51	0.51	0.52	0.50	0.48	0.53	0.53	0.34	0.36	0.37	0.32		
Ca	0.001	0.000	0.000	0.000	0.004	0.001	0.002	0.007	0.002	0.001	0.000	0.002	0.002	0.000	0.006	0.001	0.006	0.000	0.000	0.002	0.000	0.000	0.000		
Na	0.183	0.203	0.203	0.204	0.183	0.105	0.126	0.078	0.139	0.136	0.123	0.139	0.087	0.124	0.070	0.070	0.067	0.101	0.099	0.151	0.207	0.197	0.217		
K	1.76	1.74	1.74	1.75	1.71	1.82	1.80	1.87	1.82	1.79	1.79	1.76	1.84	1.80	1.87	1.84	1.84	1.83	1.80	1.76	1.70	1.72	1.72		
Σ	14.05	14.04	14.04	14.05	14.05	14.03	14.04	14.06	14.08	14.05	14.03	14.05	14.04	14.04	14.05	14.05	14.02	14.04	14.02	14.02	14.03	14.04	14.05		
O	22.00	22.00	22.00	22.00	22.00	22.00	22.00	22.00	22.00	22.00	22.00	22.00	22.00	22.00	22.00	22.00	22.00	22.00	22.00	22.00	22.00	22.00	22.00		

Table 4 (continued)

	RK28 phengite profile					RK49 paragonite individual measurements					MS112 phengite profile				
SiO ₂	47.76	45.15	47.67	47.46	47.63	45.98	45.83	46.28	46.95	46.95	51.00	49.64	50.12	50.90	
TiO ₂	0.25	0.33	0.30	0.20	0.27	0.10	0.10	0.07	0.09	0.05	0.20	0.22	0.25	0.16	
Al ₂ O ₃	32.89	31.17	33.62	32.71	33.01	42.44	42.85	42.60	43.26	43.27	27.87	30.42	30.07	27.71	
FeO	3.16	5.78	2.77	2.62	2.91	0.23	0.18	0.20	0.10	0.17	1.00	1.10	0.71	1.00	
MnO	0.016	0.011	0.011	0.000	0.006	0.000	0.000	0.029	0.014	0.001	0.039	0.000	0.000	0.010	
MgO	1.72	2.71	1.77	1.79	1.72	0.38	0.22	0.25	0.21	0.16	4.49	3.77	3.88	4.44	
CaO	0.02	0.04	0.01	0.00	0.00	0.31	0.30	0.34	0.33	0.44	0.01	0.01	0.00	0.02	
Na ₂ O	0.66	0.37	0.77	0.70	0.83	6.39	6.42	6.58	6.90	6.91	0.33	0.67	0.69	0.38	
K ₂ O	10.38	10.72	10.27	10.21	10.20	1.29	1.06	0.96	0.52	0.39	10.80	10.06	10.31	10.70	
Σ	96.85	96.28	97.19	95.70	96.58	97.13	96.97	97.31	98.37	98.34	95.74	95.89	96.02	95.32	
Si	3.15	3.07	3.13	3.16	3.15	2.89	2.88	2.89	2.90	2.90	3.37	3.27	3.29	3.38	
Si	6.31	6.13	6.26	6.32	6.30	5.77	5.75	5.79	5.79	5.79	6.74	6.54	6.59	6.75	
Ti	0.025	0.034	0.029	0.021	0.027	0.009	0.010	0.007	0.008	0.004	0.020	0.022	0.024	0.016	
Al	5.12	5.00	5.20	5.14	5.15	6.28	6.34	6.28	6.29	6.29	4.34	4.72	4.66	4.33	
Fe	0.35	0.66	0.30	0.29	0.32	0.025	0.020	0.021	0.012	0.018	0.12	0.12	0.08	0.12	
Mn	0.002	0.001	0.001	0.000	0.001	0.000	0.000	0.000	0.001	0.000	0.004	0.000	0.000	0.001	
Mg	0.34	0.55	0.35	0.36	0.34	0.072	0.042	0.046	0.038	0.030	0.89	0.74	0.76	0.88	
Ca	0.002	0.006	0.001	0.000	0.000	0.042	0.041	0.045	0.044	0.058	0.001	0.001	0.000	0.002	
Na	0.168	0.098	0.197	0.182	0.213	1.55	1.56	1.60	1.65	1.65	0.084	0.172	0.176	0.097	
K	1.75	1.86	1.72	1.74	1.72	0.21	0.17	0.15	0.08	0.06	1.82	1.69	1.73	1.81	
Σ	14.07	14.32	14.07	14.05	14.07	13.96	13.93	13.94	13.92	13.91	14.02	14.01	14.01	14.01	
O	22.00	22.00	22.00	22.00	22.00	22.00	22.00	22.00	22.00	22.00	22.00	22.00	22.00	22.00	

Acknowledgements

I would kindly like to thank...

... Jan Behrmann for the scientific input, support and criticism throughout the last years and the opportunity for free development on the scientific directions of this thesis.

... Klaus Ullemeyer and Michael Stipp for guidance, scientific input and the discussions throughout the past three years.

... Florian Heidelbach for his help with the EBSD analysis and the discussions.

... Robert Kurzawski for high help with the thermodynamic modeling.

... all colleagues who contributed to this work for the discussions and constructive criticism throughout the thesis.

... all my friends at GEOMAR for the positive atmosphere.

... finally I would like to thank my parents for their everlasting support.

CURRICULUM VITAE

Ruth Keppler

Address:

Marienwerderstr. 44
24148 Kiel

Email:

rkeppler@geomar.de

Personal Information:

Date of birth: March 21st, 1985

Place of birth: Ulm

Nationality: German

Status: single

Education:

• "Abitur" at the St. Hildegard Gymnasium, Zinglerstr. 90, 89077 Ulm: **24. Juni, 2004**

• Diploma Study of Geology at the Steinmann Institut der Rheinischen Friedrich- Wilhelms-Universität Bonn, Poppelsdorfer Schloss, 53115 Bonn **October 2005-February, 2011**

• Doctorate student at the department of geosciences of the Christian Albrechts Universität zu Kiel, Ludwig-Meyn-Str. 10, 24118 Kiel **March 2012-March 2015**